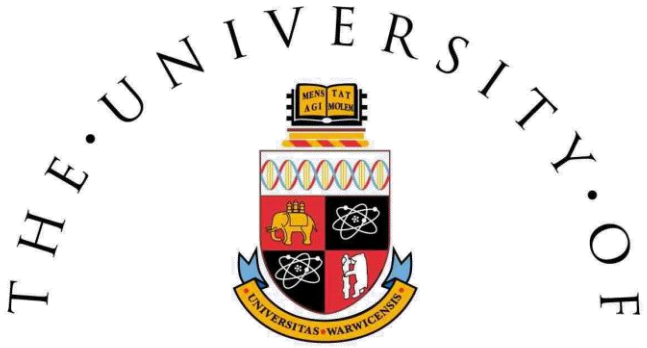

Quantification of Microstructure During the Phase Transformation of Dynamically Cooled Steels Using the EMspec® Sensor

William Jacobs

A thesis submitted to the University of Warwick for the degree of Doctor of Philosophy

Warwick Manufacturing Group

Steels Processing Group

University of Warwick

January 2020

Abstract

Electromagnetic (EM) sensor signals are sensitive to changes in permeability and resistivity in steel, where both are determined by microstructure, chemical composition and temperature. EM sensors are currently being used in the steel industry to monitor the phase transformation of hot strip on the runout table. However, there are factors still not fully understood when it comes to the EM signal such as relationship between phase fraction transformed at high temperatures and the EM signal. The purpose of this research is to quantitatively relate the EM of zero crossing frequency to microstructure and more specifically phase fraction during transformation of steels at high temperature.

The EMspec® industrial EM sensor which is currently used in industrial conditions on the run-out table of a hot strip mill has been installed into a run out table simulator that consists of a furnace and roller run out table. This system has been designed and constructed to allow the EMspec® sensor to be able to monitor various steels through transformation during dynamic cooling on a lab-based scale.

A full 3D finite element model of the EMspec® sensor has been developed in a parallel project and is able to use permeability and resistivity values to predict zero crossing frequency. This model has been used in this project to along with measured resistivities and extrapolated permeabilities from the literature to predict zero crossing frequency. The power law was used along with the permeability values, resistivities and phase fraction obtained from dilatometry to predict zero crossing frequency.

The EMspec® industrial sensor has been used to monitor the full phase transformation of various carbon steels including mild steels of 3, 6 and 10mm in thickness, a high carbon steel and medium carbon steel. The EMspec® sensor was able to distinguish between the mild steels of different thickness due to their different cooling rates in air and therefore transformation trajectory. The EMspec® sensor was also used to successfully monitor a 2.25 Cr- 1 Mo steel to measure the full transformation to bainite below the Curie temperature. The magnetic transformation of the duplex stainless steel was also monitored by the EMspec® as it cools through the Curie temperature. The EMspec® sensor was shown to be sensitive to the formation of sigma phase as a result of heat treatment of the duplex stainless steel. The sample with higher amount of sigma phase had a lower zero crossing frequency.

When relating the ZCF to phase percentage transformed obtained from dilatometry, the 6mm and 10mm mild steels, the high carbon and the 2.25 Cr- 1Mo steel all needed to be approximately 30-40% transformed before an increase in ZCF would occur due to the need for ferromagnetic phase connectivity before permeability significantly increases. This agrees well with the literature for room temperature ferrite fractions however there is room for discrepancies when taking into the temperature difference between a dilatometry sample and a larger sample cooling on the ROT. For the mild steels, the ZCF would peak before dilatometry predicts the steels to be 100% transformed.

The modelling data agreed well with the experimental data for steels that consisted of lower permeability phases such as the 2.25Cr-1Mo and high carbon steels. For the 3mm, 6mm and 10mm thick mild steels, the model could not solve for the high permeabilities which may be due to a more refined mesh being required. The model was able to solve for the duplex stainless steel however the modelled data did not agree with the experimental data due to the nature of the calculation of effective permeability. Power law was used however this does not consider the microstructural parameters such as the connectivity of ferrite. The permeabilities at lower phase fractions is higher as a result of this.

The work in this project shows that the EMspec® industrial sensor can monitor the full transformation of multiple steels below the Curie temperature and the EMspec® signal can be related quantitatively to phase percentage transformed although the discrepancy between a dilatometry sample and a large sample with inhomogeneity in temperature cannot be ignored.

List of Publications

1. W. Jacobs, J. Shen, L. Zhou, C. Davis, P. Hunt, and J. Hinton, “Measurement and modelling of the EMspec® sensor response to phase transformation in a 2.25 Cr-Mo steel,” in *BINTD*, 2018.

2. J. Shen, L. Zhou, W. Jacobs, P. Hunt, and C. Davis, “Real-time in-line steel microstructure control through magnetic properties using an EM sensor,” *J. Magn. Magn. Mater.*, vol. 490, no. March, p. 165504, 2019, doi: 10.1016/j.jmmm.2019.165504.

3. J. Shen, L. Zhou, W. Jacobs, P. Hunt, and C. Davis, “Use of COMSOL® AC/DC module to model a commercial electromagnetic sensor deployed to monitor steel transformation during cooling from high temperatures,” *COMSOL Conf.*, pp. 22–24, 2018.

4. J. Shen, L. Zhou, W. Jacobs, P. Hunt, and C. Davis, “Real-time microstructure control using EMspecTM sensor,” in *IOM3*, Warwick University, 2017.

Acknowledgements

There are many that I would like to give my sincere thanks for their enormous contribution to my research to this PhD research, but for also making my experience while at Warwick an enjoyable one.

First and foremost, a huge thank you to my amazing academic supervisor Professor Claire Davis. Words do not do justice to how great of a lady she is. She is a pure scientist, so enthusiastic about her work and a very nice and understanding human being. Her dedicated supervision, technical guidance and her advice on life has moulded me into the scientist and man that I am today. It is fair to that I had a lot of low points during my PhD due to issues in my personal life, and there was a time that I did not think I would be able to finish. But with Claire's understanding, advice on life, and encouragement towards my work, I was able to fight through my lows and submit my thesis on time. I have felt very privileged to have had her as my supervisor and will be forever grateful for everything she has done for me.

A big thank you goes to my co supervisor Dr Lei (Frank) Zhou. He would always challenge me and keep me on my toes whenever I presented my work to him and he taught me to be logical and to be able to justify my results. I am eternally grateful to Frank for, his technical guidance, his extensive help with modelling work, and for being a dedicated co-supervisor. Maybe I will beat him at singles badminton one day…..

My sincerest thanks goes to my other co supervisor Dr Russ Hall. His experimental expertise and his technical guidance were an incredible help to me, and I would not have been able to achieve the results I did in my experiments without him. I am forever grateful for his dedicated supervision, but also his understanding, advice and encouragement to me when I was going through a low period in my life. I cannot thank him enough for his help with my CV which ultimately aided me in getting my current job. Pretty sure I owe him about 400 pints for everything he has done for me.

I was lucky to be able to have a wonderful working relationship with my industrial supervisor's Dr John Hinton, Peter Hunt and Mark Dolby. Their technical guidance was a massive help to me on my PhD and I am ecstatic that I am still able to work with them now. A huge thank you to them.

It was a pleasure to work alongside Jialong Shen who did the modelling on a project parallel to my PhD. A big thank you for making my PhD an enjoyable experience but also for his support and advice.

I am indebted to Dr Carl Slater for his help with MATLAB coding that saved my hours of extracting data. As well as that he took time out of his valuable working hours to help me with my gleeble tests at the university of Birmingham. I am forever grateful to him for not only his advice and support, but also for being a good friend and making my PhD experience an enjoyable one. I am also indebted to Dr Aimee Goodall for her extensive help with my gleeble experiments. It was a pleasure to work alongside her and we always had great talks. My sincerest thanks goes to Professor Anthony Peyton from the university of Manchester for his continued support of my work. I am forever grateful to Numan Aslan for his help with showing me how to use the dilatometer. My phase fraction transformed results would not have been possible without his help. A big thankyou to Dr Jun Liu for his help with modelling and for offering his technical expertise.

A big thanks to the United Kingdom Engineering and Physical Sciences Research Council (EPSRC) and Primetals Technologies Ltd for financially funding this research.

I am hugely appreciative of my colleagues and friends from WMG: Mohsen Jolfaei-Aghadavoudi, Akalya Raviraj, James Whiston, Dr Stephen Spooner, Dr Sarah Conolly, Tonia Betzou, Arun Sengupta, Cameron Bee, Darbaz Khasraw, Lucky Osarogiagbon, Fanfu Wu, Jenny Rolls, Lewis Yule, Martin Olowe, Michael Zhang, Dr Mo Ji, Dr Raul Chinchilla Adell, Sharhid Jabar and Mir Hamza Khan. They all made my PhD a hugely enjoyable experience and I will forever be grateful.

My sincere thanks goes to one of my best mates Jack Isaacs. We go back as far as doing our undergrad and living together in Portsmouth. We were lucky enough to get to do our PhD together at Warwick and I am grateful to him for continuing to be a good mate, housemate and making my PhD experience an enjoyable one.

I will always be eternally grateful to my parents Alison and Philip Jacobs for always supporting me. I would not be the man I am today without them and words cannot describe how much I am indebted to and love them.

Finally, I am lucky that I got to have a lovely relationship for the duration of my PhD with Cheuk Sze (Cherish) Ng. I am so grateful for all her support and love, and although we cannot be together anymore, I will never forget the wonderful times we spent together.

Table of Contents

Abstract 5

List of Publications 7

Acknowledgements 8

Table of Contents 10

List of Figures 14

List of Tables 25

List of Common Abbreviations 25

1. Introduction 26

1.1 Overview 26

1.2 Aims and Objectives 26

2. Magnetism and Electrical Resistivity 29

2.1 Magnetic field 29

2.2 Origins of a Magnetic Moment 30

2.3 Paramagnetism 30

2.4 Ferromagnetism 31

2.5 B-H Curve 32

2.6 Magnetic Domain Theory 33

2.7 Relationship of Permeability with Steel Microstructure 36

2.7.1 Grain size 36

2.7.2 Phase Type 37

2.7.3 Phase Balance 39

2.8 Relationship Between Permeability and Temperature 43

2.9 Electrical Resistivity and Relationship with Temperature 45

2.9 Chapter Summary 50

3. EM Fundamentals and EM sensors 51

3.1 EM Sensor Design 51
3.2 Inductance 52
3.3 Eddy Current Theory 54
3.4 Impedance 55
3.5 EM Sensor Function 56
3.5.1 Real Mutual Inductance 56
3.5.2 Phase Angle of Impedance Spectra 58
3.6 Summary 59
4. Non-Destructive Testing Methods of Measuring the Phase Transformation in Steels 60
4.1 X-ray Diffraction 60
4.2 Ultrasonic Techniques 64
4.3 EM Techniques 68
4.3.1 Magnetic Bakhausen Noise (MBN) 69
4.3.2 Magnetic Hysteresis Loop Measurement 73
4.3.3 Laboratory EM Sensors 77
4.3.4 Commercially Available Systems 80
4.4 EM Modelling 83
4.5 Summary 87
5. Materials and Experimental Procedure 90
5.1 Materials 90
5.1.1 Materials for Edge Effect and Lift off Testing 90
5.1.2 Materials for EMspec® Sensor Testing on ROT and Furnace System 91
5.2 Sample Preparation, Microscopy and Image Analysis 92
5.3 Resistivity Measurements 92
5.3.1 Room Temperature 92
5.3.2 High Temperature 93
5.4 Dilatometry 93

5.5 EM Sensor Measurement 95
5.5.1 Lab Based U-Shaped Sensor 95
5.5.2 EMspec® Sensor Measurements 97
5.5.3 EMspec® Model 102
6. Measurement of EMspec® Sensor Sensitivity to Non-Microstructural Parameters 104
6.1 EMspec® Sensor Sensitivity to Edge Effect 104
6.2 EMspec® Sensor Sensitivity to Changes in Lift Off 106
6.3 Modelled Effect of Sample Thickness on the EMspec® Sensor Signal 107
6.4 Sensitivity of the EMspec® Sensor to the ROT Surrounding Structures 108
6.5 Summary 109
7. Materials for ROT Information 111
7.1 Room Temperature Permeabilities and Resistivities of Materials for ROT... 111
7.2 Resistivity with Temperature 112
7.3 Summary 113
8. Measurement and Modelling of the EMspec® Sensor Response to the Phase Transformation in Dynamically Cooled Steels 114
8.1 Carbon Steels 114
8.1.1 3mm Mild Steel 114
8.1.2 6mm Mild Steel 126
8.1.3 10mm Mild Steel 140
8.1.4 Comparison of the EMspec® Sensor Response to Phase Transformation in Mild Steel Plates of Different Thickness 152
8.1.5 High Carbon Steel 156
8.1.6 Medium Carbon Steel 166
8.1.7 Comparison of the EMspec® Sensor Response to Steels of Different Carbon Content 173
8.2 2.25Cr - 1Mo Steel 175
8.2.1 Microstructural Characterisation 175

8.2.2 Cooling Trajectories 179
8.2.3 EMspec® Sensor Results and Relation to Phase Fraction Transformed and EMspec® Sensor Model 180
8.3 Duplex Stainless Steel 182
8.3.1 Microstructural Characterisation 182
8.3.2 Cooling Trajectories 186
8.3.3 EMspec® Sensor Results and Modelling 186
8.4 Chapter Summary 188
8.4.1 Industrial Relevance of this Research 189
9. Conclusions 191
10. Future Works 194
11. References 196
Appendix A. Phase Angle at 8 Frequencies with Temperature 10mm Medium Carbon Steel 204

Word count = 35488

List of Figures

Figure 1. Associated magnetic moments for (a) electron orbiting an atomic nucleus creating a microscopic current loop and (b) electron spinning on its axis [13] 30
Figure 2. B-H curve for iron. Dashed line shows the hysteresis loop while the solid line shows the magnetisation curve.μi is the initial permeability, μm is the maximum permeability, μΔ is the incremental permeability, Hm is the applied field at saturation, B_m is magnetic flux at saturation, B_r is the residual magnetic flux density (also known as remenance), H_c is the coercivity, H_Δ and delta B_Δ are the applied incremental magnetic fields and magnetic flux respectively [11]. 32
Figure 3. Schematic of the gradual change of magnetic moment orientation across a domain boundary with 180° angular displacement [13] 34
Figure 4. Domain wall motion for a ferromagnetic material at different stages of magnetisation with the size and direction of the blue arrows describing the applied field (a) unmagnetised sample (b) weak applied field so the mutually aligned domain is growing at the expense of the other domains not aligned with the applied field (c) stronger magnetic field applied and starting to see rotation of domains (reproduced from [14]. . 35
Figure 5. Relative permeability predicted from EM sensor measurements plotted with ferrite grain size for a 0.17 wt% carbon steel [35]. 37
Figure 6. Predicted permeability inferred from EM sensor measurements for a pure iron (ferrite) and a 0.8 wt% C steel (pearlite). Reproduced from [4]. 38
Figure 7. B-H Loops for ferrite, pearlite, martensite and ferrite + cementite [36]. 39
Figure 8. Maximum relative permeability as a function of carbon content in ferrite pearlite steels [26]. 40
Figure 9. Initial permeability as a function of carbon content in ferrite pearlite steels [26]. 40
Figure 10. Relative permeability predicted from EM sensor measurements with ferrite fraction compared with power law and FEM models [4]. 41
Figure 11. Permeability from EM measurements and FEM model as a function of ferrite fraction in austenite ferrite steels made from stainless steel powders [37]. 42
Figure 12. The effects of temperature on permeability for iron at varying constant field strengths. The Curie temperature is labelled and is shown as Tc [11]. 43

Figure 13. Permeability with temperature for pure iron and 0.80C carbon steel inferred from high temperature cylindrical EM sensor measurements [40]. 44
Figure 14. Effect of alloying elements on the Curie temperature of iron. The alloying elements plotted are chromium (Cr), silicon (Si), aluminium (Al), manganese (Mn), gold (Au), tin (Sn) and vanadium (v). [11] 45
Figure 15. Relationship between electrical resistivity and addition of alloying elements in iron at 20℃ [11]..... 46
Figure 16. Dependence of change in resistivity on alloying elements in a low carbon steel. The alloying elements plotted are sulphur (S), nickel (Ni), copper (Cu), chromium (Cr), Manganese (Mn), silicon (Si) and phosphorus (P) [41]. 47
Figure 17. Resistivity with temperature for commercial sheet iron. The points on the plot where BCC ferrite and FCC austenite microstructures are expected have been labelled [11]. 48
Figure 18. Resistivity with temperature for a range of steels reproduced from the ASM handbook [42] 50
Figure 19. Schematic of an H shaped EM sensor measuring a ferromagnetic target [43]. 52
Figure 20. Interaction of a coil probe with a conductive material showing the primary and secondary magnetic fields and eddy currents [44]. 54
Figure 21. Real inductance with frequency for a steel being measured at different lift offs [45]. 57
Figure 22. Schematic of phase response to a non-conductive magnetic material (top), a paramagnetic material (middle) and a ferromagnetic material (bottom). The grey x-axis represents the background signal [7]. 58
Figure 23. Schematic of x-ray diffraction technique [13]. 61
Figure 24. X-ray diffraction showing peaks and positions for microstructural phases in a martensitic stainless-steel during tempering. Martensite (101) and (110) has 2 peaks, ferrite (110) has 1 peak, the presence of retained austenite (111) is also detected [50]. 62
Figure 25. Number of ferrite and pearlite grains transformed as a function of temperature derived from x-ray reflections on a structural steel specimen. The increases in grain size to due to ferrite and pearlite transformations are labelled [51]. 63
Figure 26. Basic principles of an ultrasonic measuring system [56] 64
Figure 27. Comparison of grain size analysis between metallographic (dmet) and ultrasonic (dus) method [60] 65

Figure 28. Fractional velocity change with time at temperature. Open triangles =500°C, Open diamonds = 730°C, Open squares = 800°C [61] 66
Figure 29. (a) Ultrasonic velocities with temperature for ferrite (solid line), austenite (dotted line) and measured data low alloy steel (line and symbol) and (b) austenite fraction with temperature from the ultrasonic velocities shown in (a) [63]. 67
Figure 30. Steps associated with increased magnetisation responsible for MBN [11]. .. 69
Figure 31. Relationship between MBN peak height (a) and MBN peak position (b) and martensite percentage (%) [70]. 70
Figure 32. MBN peak amplitude response to annealing times at various temperatures in an extra low carbon steel [73]. 71
Figure 33. MBN voltage output (mV) for 4 tensile loads (0N, 8825N, 9316N and 9806N) on a 304 austenitic stainless steel [74]. 72
Figure 34. MBN voltage outputs measured at 4 different temperatures during quench of AISI D2 steel [75]. 72
Figure 35. Magnetic hysteresis loops for a 0.2 wt% carbon steel (a) and a 0.45 wt% carbon steel (b) [78]. 74
Figure 36. Coercivity (Hc) plotted with respect to annealing time at different annealing temperatures for an IF steel [79]. 75
Figure 37. B-H curves for austenitic stainless steel after (a) polishing and cutting (hollow squares) and after annealing at 1127°C for 30 minutes and cooling to room temperature (solid circles) (b) after performing an array of nano indentations with a lateral size of 1µm and (c) after dragging nano-indenter along the steel with a line width of 1.8µm [81]. .. 76
Figure 38. Inductance (H) plotted against time for IF steels at different annealing temperatures (365°C, 420°C, 650°C and 700°C). The arrows mark critical points of recovery and recrystallisation. The black vertical line indicates the end of the heating process, data shown before this shows inductance changes related to changes in temperature [10]. 78
Figure 39. Imaginary impedance at 12.5Hz for a low, medium and high carbon steel during cooling from 1000°C [97]. 79
Figure 40. Diagram of IMPOC system measuring a steel strip [98]. 81
Figure 41. Plots of real (a) and imaginary (b) HACOM system signal with increasing percentage elongation [98]. 82
Figure 42. Modelled flux distribution though a ferrite-austenite microstructure with 30 % ferrite (a) and a ferrite-pearlite microstructure with 30 % ferrite (b) [4, 35]. 84

Figure 43. U-shaped EM sensor on a steel sample (a) and the 3D FE model of the same sensor and steel strip (b) The colours represent the modelled magnetic flux intensity [100]. 85
Figure 44. Calibration curves relating low frequency (10 Hz) real inductance with permeability for different thickness samples. The dashed lines represent modelling results (for 1 mm–4 mm strip thickness) and experimental data for commercial DP samples of different thicknesses are indicated by different points [100]. 86
Figure 45. Model of an H shaped EM sensor between rollers with a steel strip sample above the sensor. The model was built to show effect of rollers on the EM signal while measuring a steel [45]. 87
Figure 46. Modelled ZCF as a function of relative permeability [45]. 87
Figure 47. Change in length with temperature during cooling cycle for 6mm mild steel. Transformation start and finish temperatures are marked and shown in red. Tangent lines (black straight lines) drawn against the measured data (blue line) for transformed fraction calculation. Values on the tangent lines are change in length values (from initial room temperature value). 94
Figure 48. U shaped sensor with bridge =100mm, legs= 56mm and thickness of 25mm. The sensor consists of an exciting coil with 100 turns, and 2 sensing coils each with 86 turns [100]. 96
Figure 49. Schematic of EMspec® industrial H shaped sensor measuring a steel target [7]. 97
Figure 50. (a) Picture of ROT and furnace system and (b) EMspec® integrated between the ROT rollers in its protective housing. 100
Figure 51. Position of the thermocouples on the samples used for high temperature EMspec® testing. The position of the back of the furnace and the direction of sample movement on the ROT is also shown. The position of the sensor feet and the x and y direction with respect to the sensor is also indicated. 101
Figure 52. Modelled EMspec® sensor positioned at the centre of a 500 x 500 mm^2 sample. The canister is shown lifted above the sensor for clarity [102]. 103
Figure 53. ZCF plotted against distance of sensor to sample edge in X direction 105
Figure 54. ZCF plotted against distance of sensor to sample edge in Y direction 105
Figure 55. ZCF plotted with varying sample lift offs. Blue triangles represent low carbon (LC) data while orange circle represents dual phase (DP) 107
Figure 56. Percentage change in ZCF for 1.5mm and 3mm thickness samples when compared with 6mm thickness [103]. 108

Figure 57. Comparison of EMspec® measurements from the lab (no ROT) and when installed on the ROT. 109
Figure 58. Room temperature permeabilities and resistivities for steels to be tested using EMspec® sensor. 112
Figure 59. Resistivity with temperature for low carbon steel, high carbon steel, austenite (extrapolated), duplex stainless steel, and Cr-Mo steel (extrapolated). 113
Figure 60. Optical microstructure at 20× magnification of 3mm mild steel in as received condition. Areas of ferrite, bainite and pearlite have been labelled. 115
Figure 61. Optical microstructure at 20× magnification of 3mm mild steel following heat treatment for test 1. An area of bainite has been labelled. 116
Figure 62. Optical microstructure at 20× magnification of 3mm mild steel following heat treatment for test 2. Some areas of bainite have been labelled. 116
Figure 63. Optical microstructure at 20× magnification of 3mm mild steel following heat treatment for test 3. An area of bainite has been labelled. 117
Figure 64. Optical microstructures at 20× magnification looking at top surface (a) and bottom surface (b) of the 3mm mild steel used in test 1. 117
Figure 65. Optical microstructures at 20× magnification looking at top surface (a) and bottom surface (b) of the 3mm mild steel used in test 2. 118
Figure 66. Optical microstructures at 20× magnification showing evidence of decarburisation at top surface (a) and bottom surface (b) of the 3mm mild steel used in test 3. 118
Figure 67. Optical microstructure at 20× magnification of 3mm mild steel following dilatometry heat treatment. Areas of bainite have been indicated using label and arrows. 119
Figure 68. Cooling trajectory for 3mm steel during test 1. Thermocouple 1 (T1) and thermocouple 2 (T2) are plotted along with temperature difference between the two thermocouples (T1-T2). The points at which thermocouples 1 and 2 leave the furnace are indicated on the T1-T2 graph. 120
Figure 69. Cooling trajectory for 3mm steel during test 2. Thermocouple 1 (T1) and thermocouple 2 (T2) are plotted along with temperature difference between the two thermocouples (T1-T2). The points at which thermocouples 1 and 2 leave the furnace are indicated on the T1-T2 graph. 121
Figure 70. Cooling trajectory for 3mm steel during test 3. Thermocouple 1 (T1) and thermocouple 2 (T2) are plotted along with temperature difference between the two

thermocouples (T1-T2). The points at which thermocouples 1 and 2 leave the furnace are indicated on the T1-T2 graph. 122
Figure 71. Average temperature of 3mm mild steel (tests 1-3) with time during cooling in air. An expanded view is also shown. 123
Figure 72. Measured and modelled ZCF with temperature. Transformed percentage also plotted with temperature on the second Y axis. The points at which the steel is paramagnetic and ferromagnetic are indicated on the ZCF graph. 124
Figure 73. Modelled phase angle with frequency for 3mm mild and 3mm high carbon at their peak effective permeability during transformation (calculated by power law). Error in 3mm mild steel data is indicated. 126
Figure 74. Optical microstructure at 20× magnification of 6mm mild steel in the as received condition. Bainitic regions have been indicated using arrows. 127
Figure 75. Optical microstructure at 20× magnification of the 6mm mild steel after heat treatment for test 1. 128
Figure 76. Optical microstructure at 20× magnification of a 6mm mild steel after heat treatment for test 2. 128
Figure 77. Optical microstructure at 20× magnification of a 6mm mild steel after heat treatment for test 3. 129
Figure 78. Optical microstructures at 10× magnification for (a) 6mm mild steel test 1 and (b) 6mm mild steel test 3. Regions with ferrite/bainite microstructure marked using yellow arrows. 129
Figure 79. Optical microstructure at 20× magnification of the 6mm mild steel following dilatometry heat treatment 130
Figure 80. Optical microstructures at 20× magnification looking at top surface (a) and bottom surface (b) of the 6mm mild steel used in test 1. Decarburisation and sample surface are indicated using the coloured arrows. 130
Figure 81. Optical microstructures at 20× magnification looking at top surface (a) and bottom surface (b) of the 6mm mild steel used in test 2. Decarburisation and the sample surface are indicated using the coloured arrows. 131
Figure 82. Optical microstructures at 20× magnification looking at top surface (a) and bottom surface (b) of the 6mm mild steel used in test 3. Decarburisation and sample surface are indicated. 131
Figure 83. Cooling trajectory for 6mm steel during test 1. Thermocouple 1 (T1) and thermocouple 2 (T2) are plotted along with temperature difference between the two

thermocouples (T1-T2). The points at which thermocouples 1 and 2 leave the furnace, and latent heating occurs are indicated on the T1-T2 graph. 133
Figure 84. Cooling trajectory for 6mm steel during test 2. Thermocouple 1 (T1) and thermocouple 2 (T2) are plotted along with temperature difference between the two thermocouples (T1-T2). The point where thermocouples 1 and 2 leave the furnace and latent heating occurs is indicated on the T1-T2 graph. 134
Figure 85. Cooling trajectory for 6mm steel during test 3. Thermocouple 1 (T1) and thermocouple 2 (T2) are plotted along with temperature difference between the two thermocouples (T1-T2). The point at which thermocouples 1 and 2 leave the furnace and latent heating occurs is indicated on the T1-T2 graph. 135
Figure 86. Average temperature of 6mm mild steel with time during cooling in air for EMspec® tests 1, 2 and 3. Expanded view is also shown at higher temperatures. The latent heating is indicated with the arrows. 136
Figure 87. Measured and modelled ZCF with temperature for 6mm mild steel. Transformed percentage obtained from dilatometry also plotted with temperature on the second Y axis. The points at which the steel is paramagnetic and ferromagnetic are indicated. 137
Figure 88. Modelled phase angle with frequency for 6mm mild and 3mm high carbon at their peak effective permeability during transformation (calculated by power law). The error in the data in indicated..... 139
Figure 89. Optical microstructure at 20× magnification of a 10mm mild steel in the as received condition. Areas of bainite are indicated. 141
Figure 90. Optical microstructure at 20× magnification of a 10mm mild steel after heat treatment for test 1. 141
Figure 91.Optical microstructure at 20× magnification of a 10mm mild steel after heat treatment for test 2. 142
Figure 92. Optical microstructure at 20× magnification of a 10mm mild steel after heat treatment for test 3. 142
Figure 93. Optical microstructures at 20× magnification looking at top surface (a) and bottom surface (b) of the 10mm mild steel used in test 1. Sample surface and decarburisation regions are indicated using coloured arrows. 143
Figure 94. Optical microstructures at 20× magnification looking at top surface (a) and bottom surface (b) of the 10mm mild steel used in test 2. Sample surface and decarburisation regions are indicated using coloured arrows. 143

Figure 95. Optical microstructures at 20× magnification looking at top surface (a) and bottom surface (b) of the 10mm mild steel used in test 3. Sample surface and decarburisation regions are indicated using coloured arrows. 144
Figure 96. Optical microstructures at 20× magnification of a 10mm mild steel following dilatometry heat treatment..... 144
Figure 97. Cooling trajectory for 10mm steel during test 1. Thermocouple 1 (T1) and thermocouple 2 (T2) are plotted along with temperature difference between the two thermocouples (T1-T2). The points at which thermocouples 1 and 2 leave the furnace is indicated. 146
Figure 98. Cooling trajectory for 10mm steel during test 2. Thermocouple 1 (T1) and thermocouple 2 (T2) are plotted along with temperature difference between the two thermocouples (T1-T2). The points at which thermocouples 1 and 2 leave the furnace are indicated. 147
Figure 99. Cooling trajectory for 10mm steel during test 3. Thermocouple 1 (T1) and thermocouple 2 (T2) are plotted along with temperature difference between the two thermocouples (T1-T2). The point at which thermocouples 1 and 2 leave the furnace are indicated. 148
Figure 100. Average temperature of 10mm mild steel with time during cooling in air for EMspec® tests 1, 2 and 3. Expanded view is also shown at higher temperatures. The points at which latent heating occur are indicated. 149
Figure 101. Measured and modelled ZCF with temperature for 10mm mild steel. Transformed percentage obtained from dilatometry also plotted with temperature on the second Y axis. Points where the steel is paramagnetic and ferromagnetic are indicated on the ZCF graph. 150
Figure 102. Modelled phase angle with frequency for 10mm mild and 3mm high carbon at their peak effective permeability during transformation (calculated by power law). The error in the data is indicated. 152
Figure 103. ZCF with temperature for 3mm mild steel tests 1-3, 6mm mild steel tests 1-3 and finally the 10mm mild steel tests 1-3. 154
Figure 104. Average cooling trajectories for the 3mm mild steel, 6mm mild steel and the 10mm mild steel during EMspec® sensor measurements. Cooling rates between 980°C and 500°C also stated for each sample. 155
Figure 105: Phase percentage transformed for 3mm mild steel, 6mm mild steel and 10mm mild steel. Obtained from dilatometry tests. 155

Figure 106. Optical microstructure at 100× magnification of a 3mm high carbon steel in the as received condition. Regions of pearlite and spheroidised carbides have been indicated. 157
Figure 107. Optical microstructure at 50× magnification of a 3mm high carbon steel after heat treatment for test 1. 157
Figure 108. Optical microstructure at 50× magnification of a 3mm high carbon steel after heat treatment for test 2. 158
Figure 109. Optical microstructure at 50× magnification of a 3mm high carbon steel after heat treatment for test 3. 158
Figure 110. Optical microstructures at 20× magnification looking at top surface (a) and bottom surface (b) of the high carbon steel used in test 1. 159
Figure 111. Optical microstructures at 20× magnification looking at top surface (a) and bottom surface (b) of the high carbon steel used in test 2. 159
Figure 112. Optical microstructures at 20× magnification looking at top surface (a) and bottom surface (b) of the high carbon steel used in test 3. 160
Figure 113. Optical microstructure at 50× magnification of 3mm high carbon steel following dilatometry heat treatment. 160
Figure 114. Cooling trajectory for 3mm high carbon steel during test 2. Thermocouple 1 (T1) and thermocouple 2 (T2) are plotted along with temperature difference between the two thermocouples (T1-T2). The points at which thermocouples 1 and 2 leave the furnace and latent heating occurs have been indicated on the T1-T2 graph. 162
Figure 115. Temperature of thermocouple 1 (closer to furnace entrance) for 3mm high carbon steel with time during cooling in air for EMspec® tests 1, 2 and 3. The point where latent heating occurs is indicated. The noise in test 3 potentially caused by poor thermocouple contact in test 3 is also indicated. 163
Figure 116. Measured and modelled ZCF with temperature for 10mm mild steel. Transformed percentage obtained from dilatometry also plotted with temperature on the second Y axis. The points at which the steel is paramagnetic and ferromagnetic are indicated on the ZCF graph. 164
Figure 117. Optical microstructure of a C45 steel sourced from [104]. 166
Figure 118. Cooling trajectory for 10mm medium carbon steel during test 1. Thermocouple 1 (T1) and thermocouple 2 (T2) are plotted along with temperature difference between the two thermocouples (T1-T2). The points at which thermocouples 1 and 2 leave the furnace are indicated on the T1-T2 graph. 168

Figure 119. Cooling trajectory for 10mm medium carbon steel during test 2. Thermocouple 1 (T1) and thermocouple 2 (T2) are plotted along with temperature difference between the two thermocouples (T1-T2). The points at which thermocouples 1 and 2 leave the furnace are indicated on the T1-T2 graph. 169
Figure 120. Cooling trajectory for 10mm medium carbon steel during test 3. Thermocouple 1 (T1) and thermocouple 2 (T2) are plotted along with temperature difference between the two thermocouples (T1-T2). The points at which thermocouples 1 and 2 leave the furnace are indicated on the T1-T2 graph. 170
Figure 121. Average cooling trajectories for 10mm medium carbon steel test 1-3. The latent heating caused by the ferrite and pearlite transformations are indicated. 171
Figure 122. ZCF plotted with temperature for 10mm medium carbon steel tests 1-3. . 172
Figure 123. Average cooling trajectory of 3mm mild steel and 3mm high carbon steel. Cooling rates between 950℃ and 650℃ have been indicated. 174
Figure 124. Phase percentage transformed with temperature for 3mm mild and 3mm high carbon steels obtained from dilatometry. 174
Figure 125. ZCF with temperature for 3mm mild steel tests 1-3 and 3mm high carbon steel tests 1-3. 175
Figure 126. Optical microstructure at 50× magnification of a 3mm 2.25 Cr - 1 Mo steel in the as received condition. 176
Figure 127. Optical microstructure at 50× magnification of a 3mm 2.25 Cr - 1 Mo steel following heat treatment for EMspec® test 1. 177
Figure 128. Optical microstructure at 50× magnification of a 3mm 2.25 Cr - 1 Mo steel following heat treatment for EMspec® test 2. 177
Figure 129. Optical microstructures at 20× magnification looking at top surface (a) and bottom surface (b) of the 3mm 2.25 Cr – 1 Mo steel used in test 1. 178
Figure 130. Optical microstructures at 20× magnification looking at to surface (a) and bottom surface (b) of the 3mm 2.25 Cr - 1 Mo steel used in test 2. 178
Figure 131. Optical microstructure at 50× magnification of a 3mm 2.25Cr-1Mo steel following dilatometry heat treatment. 179
Figure 132. Cooling trajectories for 2.25Cr-1Mo steel following heat treatment for EMspec® sensor tests 1 and 2. The point where latent heating occurs for both tests is indicated. 180
Figure 133. Measured and modelled ZCF with temperature for 3mm 2.25 Cr – 1 Mo Steel. Transformed percentage also plotted with temperature on the second Y axis. 181
Figure 134. EBSD image of the duplex stainless steel in the as received condition. ... 183

Figure 135. Optical microstructure at 50× magnification of a duplex stainless-steel following heat treatment for EMspec® test 1. Regions of sigma phase are indicated. 184
Figure 136. Optical microstructure at 50× magnification of a duplex stainless-steel following heat treatment for EMspec® test 2. Regions of sigma phase are indicated. 184
Figure 137. Optical microstructure at 50× magnification of a duplex stainless-steel following heat treatment for EMspec® test 3. Regions of sigma phase are indicated. 185
Figure 138. Kinetics of different phase in a duplex stainless steel [106]. 185
Figure 139. Cooling trajectories for duplex stainless-steel tests 1-3. 186
Figure 140. ZCF with temperature for duplex stainless-steel tests 1-3 and modelled ZCF. 188
Figure 141. Phase angles at 0.375-48kHz with temperature. Error in phase angle indicated on graph..... 204

List of Tables

Table 1. Chemical composition and previous heat treatment for steels reported in the ASM handbook [42].....49
Table 2. IF steel chemical composition in wt%. 90
Table 3. DP steel chemical composition in wt%. 90
Table 4. Dimensions and Chemical compositions of steels used for ROT and Furance system in wt%. 91
Table 5. Ferrite fractions in % for 3mm mild steel in as received condition, after 3 heat treatments following EMspec® sensor measurements and following dilatometry heat treatment.....119
Table 6. Ferrite fractions in % for 6mm mild steel in as received condition, after 3 heat treatments following EMspec® sensor measurements and dilatometry heat treatment. 132
Table 7. Ferrite fractions in % for the 10mm mild steel in the as received condition and after heat treatments (Tests 1 – 3) following EMspec® sensor measurements. 145

List of Common Abbreviations

Zero Crossing Frequency = ZCF

Run-out table = ROT

Finite Element Model = FEM

Electromotive Force =EMF

Electromagnetic = EM

1. Introduction

1.1 Overview

Steel is one of the most extensively used engineering materials in the world today, since it can be manufactured cheaply and in great quantities to very precise specifications. Additionally, steel provides a wide range of mechanical properties, which vary depending on the composition and processing history, and can be tailored for specific applications [1]. These mechanical properties are dependent on microstructural parameters, such as phase balance, grain size and precipitates, which are developed in steel mills using hot rolling and controlled cooling [2].

EM sensors provide a cheap, non-contact, non-destructive method of measuring changes in microstructure. This is because the EM signal is sensitive to changes in the relative permeability and electrical resistivity of steels, which vary with steel chemistry and microstructure. EM sensors have been shown to be able to detect microstructural parameters offline, such as pearlite inter-lamellae spacing and quantifying phase fraction [3, 4]. Online EM sensors have shown to be able to detect phase transformation in rod and strip steels during cooling after hot rolling [5-7]. A newly commercialized EM sensor is currently being used on the ROT of a hot strip mill [8]. They have also been applied in optimization of steel processing by means of monitoring the austenite transformation of advanced high strength steels on-line and have been shown to be able to dynamically monitor recovery and recrystallization during heat treatment in a furnace [9, 10]. However, there are still several factors that are not fully characterized in terms of EM sensor signal interpretation, such as validated EM signal – phase fraction relationships at high temperature.

1.2 Aims and Objectives

EM sensors have been shown to be able to successfully detect and monitor phase transformation in steels both offline and in industrial conditions. They have been used to

monitor product uniformity of advanced high strength strip steels during hot and cold processing and correlations exist to predict tensile strength from cold EM measurements. Whilst the current phase transformation sensor (EMspec®) measurements have been related to the phase balance, a robust full quantitative approach is required with validation. Consequently, the aim of this project is to relate the EM signal measured by the EMspec sensor to phase fraction transformed at high temperature and how this is determined by changes in the relevant materials parameters of resistivity and low magnetic field permeability. This will include:

- Extrapolation of changes in permeability with temperature for a range of steels using a combination of literature data and the power law.

- Measurement of the changes in resistivity with temperature for a range of steels.

- Development of a furnace-roller ROT with embedded EMspec® system to allow dynamic measurement of EMspec® signal with temperature for steel samples during cooling.

- Determination of the effect of environment (lift off, positioning in the ROT) and sample geometry (thickness, edge effect) on the EMspec® signal.

- Measurement of the transformation characteristics (transformation fraction) for selected steels using cooling rates observed for samples on the furnace-roller ROT using dilatometry

- EMspec® sensor measurements of a range of steel samples on the furnace-roller ROT during dynamic cooling

- Establish the relationship between the EMspec® sensor signal and phase fraction during transformation for a range of steels.

- Relate the experimentally determined relationship between EMspec® signal and phase transformation to that determined using an FEM developed in a parallel project.

2. Magnetism and Electrical Resistivity

Most steels are ferromagnetic and will boast a body centred cubic (BCC) or body centred tetragonal (BCT) crystal structure at room temperature. After hot rolling in a strip mill, steels will be cooled along a ROT before coiling and here, a solid-state transformation from face centred cubic (FCC) austenite to BCC ferrite/pearlite/bainite or BCT martensite or a mixture of these, will occur depending on the cooling rates applied and chemical composition. Understanding magnetic behaviour of different steels during phase transformation during cooling is integral to the research presented in this thesis. This chapter will discuss relevant magnetic characteristics to this research.

2.1 Magnetic field

A piece of iron will be attracted to a magnet despite the two not being in contact. This is caused by the interaction of the magnetic field with the piece of iron. A magnetic field can be thought of as endless lines as described by Faraday. This can be explored by sprinkling iron filings around a magnet. The lines formed by the fillings are due to the magnetic field converging on the poles. The poles of magnets exert forces on each other with the north and south poles attracting, while like poles repel. A magnetic field can be generated by either a current carrying coil (such as a solenoid) or a permanent magnet [11]. The magnetic field strength of a current carrying coil, H in A/m can be calculated by equation 1 [12]:

$$H = \frac{N}{l} I \qquad \text{Equation 1}$$

Where N is the number of turns of the coiled wire, l is the length of the wire in meters (m) and I is the current in Amps (A).

2.2 Origins of a Magnetic Moment

Magnetic properties of materials result from the magnetic moments of each individual atom. Atoms that make up all matter have moving electrons, which themselves form microscopic current loops when orbiting the nucleus (figure 1a). These microscopic current loops produce magnetic fields of their own. Electrons also have intrinsic angular momentum, known as spin (not related to orbital motion) and can be pictured as an electron spinning on an axis. This angular momentum also has an associated magnetic moment in either an up or antiparallel down direction [12]. A schematic showing an electron spinning on an axis is shown in figure 1b.

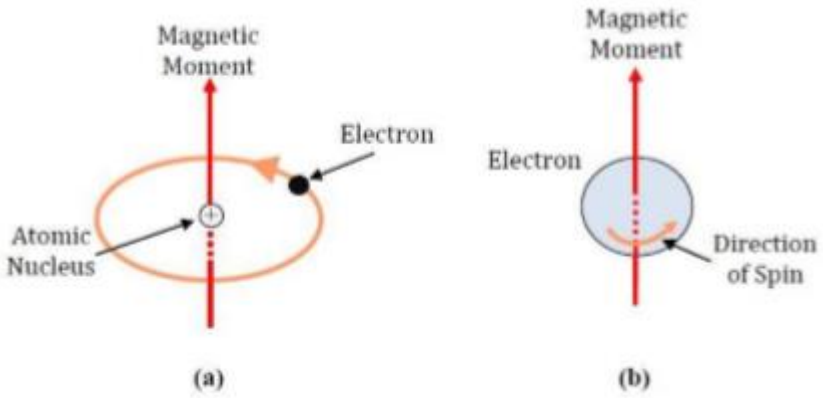

Figure 1. Associated magnetic moments for (a) electron orbiting an atomic nucleus creating a microscopic current loop and (b) electron spinning on its axis [13]

2.3 Paramagnetism

Following hot rolling and before cooling on a ROT in a hot strip mill, a steel will be above the Curie temperature, fully austenitic and, therefore paramagnetic. For this study it is important to understand paramagnetism and how effects magnetic permeability and therefore EM sensor signal, therefore it will be discussed here. In many materials, their atoms will have complete electron shells, therefore the magnetic moments (due to electron orbit or spin) will add up to 0. However, in some materials (such as platinum), the atoms have incomplete shells and therefore have a small net magnetic moment. When there is no external magnetic field present, these magnetic moments will be randomly aligned due

to thermal agitation. When the material is placed in an external magnetic field, the field exerts a torque on each magnetic moment. These toques tend to align the magnetic moments with the external field. Paramagnetic materials have a low relative permeability (explained later in this chapter) between 1 and 1.003 (except at -273.15℃ where they may be larger). They also do not show any hysteresis (explained later in this chapter) [12].

2.4 Ferromagnetism

Materials which exhibit similar magnetic properties to iron (such as nickel and cobalt their alloys) fall into a category of materials known as ferromagnetic materials. As previously discussed, ferromagnetic materials such as iron will be attracted to objects that have their own magnetic field such as permanent magnets or electromagnets. Like paramagnetic materials, ferromagnetic materials also have incomplete electron shells which results in a net magnetisation of an atom. However, this is only one contributing factor to a material being ferromagnetic. The electron orbits of neighbouring atoms overlap each-other in ferromagnetic materials; therefore, the neighbouring electrons can affect each other's spins. This is known as the exchange interaction and causes the net spin magnetic moments to line up parallel with one another even in the absence of an external magnetic field. Mutual spin alignments occur over relatively large volumes throughout the crystal known as magnetic domains [11].

Ferromagnetic materials do not generate their own magnetic field when there is no external field present as the magnetic domains are randomly oriented. However, when an external field is present, these domains tend to align themselves parallel to the external field; domains that are oriented favourably with the magnetic field grow while domains oriented in other directions shrink (explained further later in this chapter). The magnetic moment of a domain is specified by the magnitude and direction of its magnetisation and by its volume. A domain magnetic moment may be many thousands of times greater than an individual magnetic moment of an atom. Therefore, the torques that tend to align the domains with the external field are far greater than in paramagnetic materials. The ease at which domain boundaries (also known as Bloch walls) move are a very important factor in the use of non-destructive methods such as EM sensors. Ferromagnetic materials lose their ferromagnetic properties and become paramagnetic when they hit a critical temperature known as the Curie temperature (discussed later in this chapter).

The magnetic field strength (H) and the magnetic flux density (B), are related to each other and the magnetic property of the medium, also known as the magnetic permeability (μ). The relative permeability relates the magnetic permeability of the material to the permeability of free space (4×10^{-7} N/A^2) and is very useful when classifying different materials in comparison to one another. Relative permeability values for ferromagnetic materials are greater than 1 while paramagnetic materials have a permeability close to 1 (except at -273.15℃ where they may be larger) [11].

2.5 B-H Curve

If an external field H is applied to a ferromagnetic material a magnetic field, B, is induced in the material. The relationship between B and H can be shown on a magnetization curve known as a B-H curve or hysteresis loop. An example of a hysteresis loop is shown in figure 2

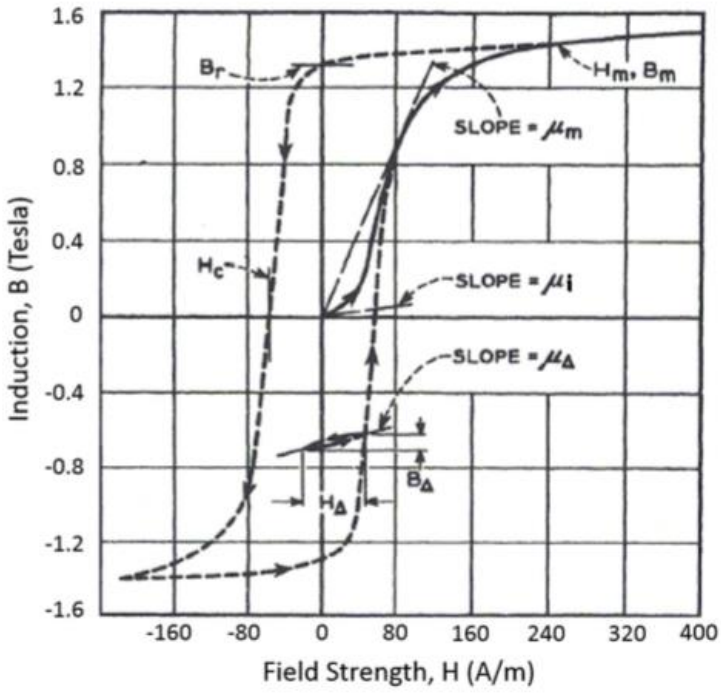

Figure 2. B-H curve for iron. Dashed line shows the hysteresis loop while the solid line shows the magnetisation curve. μi is the initial permeability, μm is the maximum permeability, μΔ is the incremental permeability, Hm is the applied field at saturation, B_m is magnetic flux at saturation, B_r is the residual magnetic flux density (also known as remanence), H_c is the coercivity, $H_Δ$ and delta $B_Δ$ are the applied incremental magnetic fields and magnetic flux respectively [11].

In ferromagnetic materials, the magnetic flux density (B) and the applied field (H) are not directly proportional. The magnetic permeability is given by the ratio of B over H. The initial slope of the B-H curve is known as the initial permeability (μ_i). At the point on the magnetization curve where the slope is at its steepest gradient, this is known as the maximum permeability (μ_m). If a biasing magnetic field is applied, and another applied in the opposite direction and alternated cyclically (H_Δ), this gives rise to an alternating magnetic flux (B_Δ). The incremental permeability (μ_Δ) is given by the slope of the incremental magnetic flux over the incremental applied field (B_Δ/H_Δ).

When the applied field H is increased, this brings about a shift in the magnetic domain boundaries, with the domains already orientated parallel to the external field increasing in size at the expense of the domains oriented in other directions. This process will continue, and the number of domains will decrease as the applied field increases until the macroscopic specimen becomes one domain orientated parallel to the H field. This point is known as saturation and is shown by the tips of the hysteresis loop in figure 2 at the highest and lowest applied fields. More detail on the magnetic domains and their motions at different points of the magnetization process will be discussed on greater detail later in this chapter.

When the applied field H is decreased after the materials has been saturated, a hysteresis is observed in which the magnetic flux lags the applied field. This occurs because the microstructural parameters in ferromagnetic materials can oppose the movement of domain walls (pinning). When H is reduced to H=0, some residual magnetization of the material remains. The magnitude of the remaining magnetisation is known as the remanence and is shown as point B_r in figure 2 [11]. The coercivity (H_c) describes the demagnetizing field required to bring the magnetisation to 0. Materials with high coercivities are described as magnetically hard materials while low coercivity materials are magnetically soft [11].

2.6 Magnetic Domain Theory

The phenomena of the B-H curve and magnetic hysteresis loops can be described using domain theory. A magnetic domain is a region in a ferromagnetic material where the atom magnetic moments are mutually aligned. If all the atom magnetic moments were aligned in the same direction, the magnetic energy of the material would be very high and

unstable. To reduce this energy, magnetic domains orientated in different directions form naturally. Magnetic domains are separated by boundaries known as Bloch walls and this is where the direction of magnetisation of each magnetic moment changes. The change in direction of magnetic moments is gradual and occurs over many planes as appose to one discontinuous step. Typically, 90° or 180° is the angular displacement across a domain boundary. A diagram of a domain boundary with a displacement of 180° is shown in figure 3 [11].

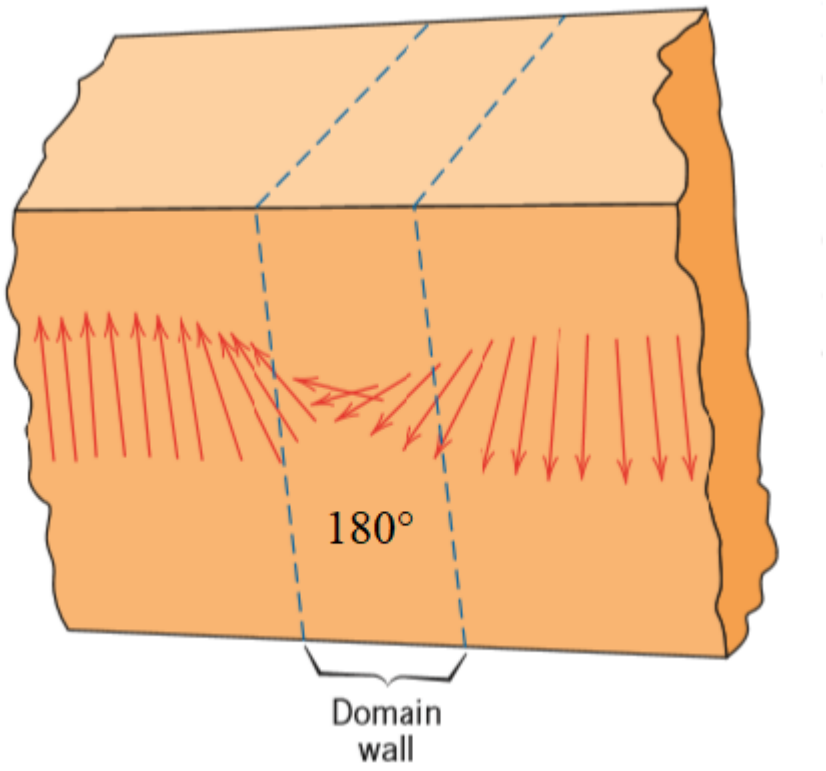

Figure 3. Schematic of the gradual change of magnetic moment orientation across a domain boundary with 180° angular displacement [13]

Domain walls play a significant part in the magnetisation/demagnetisation of a ferromagnetic material. When there is no external magnetic field present, the magnetic domains are oriented at random and the net magnetisation of the material is 0. When an external field is applied, the domains that are aligned mutually with the external field grow at the expense of the domains that are not aligned mutually with the external field. As domains grow, the number of magnetic moments that are aligned with the magnetic field increase. Domain wall motion must occur to allow domains to grow. In terms of the initial magnetisation curve, there are 3 main processes of domain wall motion; reversible

boundary displacement, irreversible boundary displacement and reversable rotation. At relatively weak applied fields, the domain wall motion is reversable and the domain walls will return to their original position if the applied field is removed. If the applied field is increased, then the domain walls can overcome crystalline imperfections such as dislocations, grain boundaries and precipitates. When the magnetic field is removed, the imperfections prevent the domain boundaries from moving back to their original position causing the material to remain magnetised. This is known as irreversible boundary displacement. When the applied field is high enough that the material approaches saturation, the magnetic domains that are not aligned favourably with the applied field rotate to align with the applied field and with the domains that have already grown in size to form one macroscopic domain. This is known as saturation and at this point the material is fully magnetised. If the applied field is removed, the domains that rotated to align favourable with the applied field will rotate back to their original position. This is known as reversable rotation. Figure 4 shows a schematic of domain wall motion with increasing magnetic field strength in 1 direction [11].

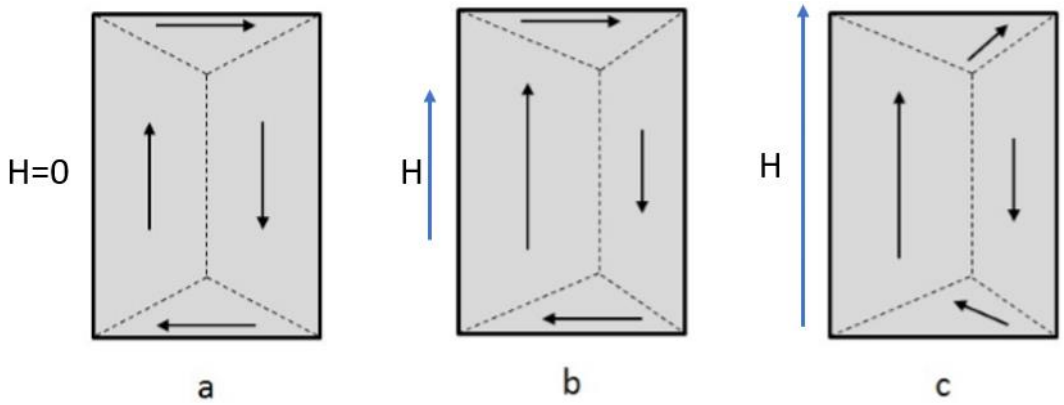

Figure 4. Domain wall motion for a ferromagnetic material at different stages of magnetisation with the size and direction of the blue arrows describing the applied field (a) unmagnetised sample (b) weak applied field so the mutually aligned domain is growing at the expense of the other domains not aligned with the applied field (c) stronger magnetic field applied and starting to see rotation of domains (reproduced from [14].

2.7 Relationship of Permeability with Steel Microstructure

Studies have been conducted using different steel grades to explore the relationship between steel microstructure and magnetic permeability. It has been shown that different microstructural parameters such as grain size, phase balance, texture and plastic deformation have a direct effect on magnetic permeability [16-34]. As different microstructural parameters have a significant effect on the permeability, it is important that the magnitude of the relationships is understood when considering the use of EM techniques for online assessment of steel during production. This section summarises the effects of the different microstructural parameters on magnetic permeability in steels.

2.7.1 Grain size

Magnetic permeability of steel is linked to its magnetic domain structure and domain wall motion under an applied magnetic field. In a study by Zhou [35], a 0.17 wt% C steel was annealed at different temperatures to give samples with varying average ferrite grain size. At these grain sizes, they were shown to have 1 domain per grain. The samples were measured with a cylindrical EM sensor and the permeability was predicted from these measurements using a model for the sensor (figure 5). The relative permeability increases with increasing grain size in this range. This is to be expected, as if the grains only have 1 domain, then the domain will increase with increasing grain size.

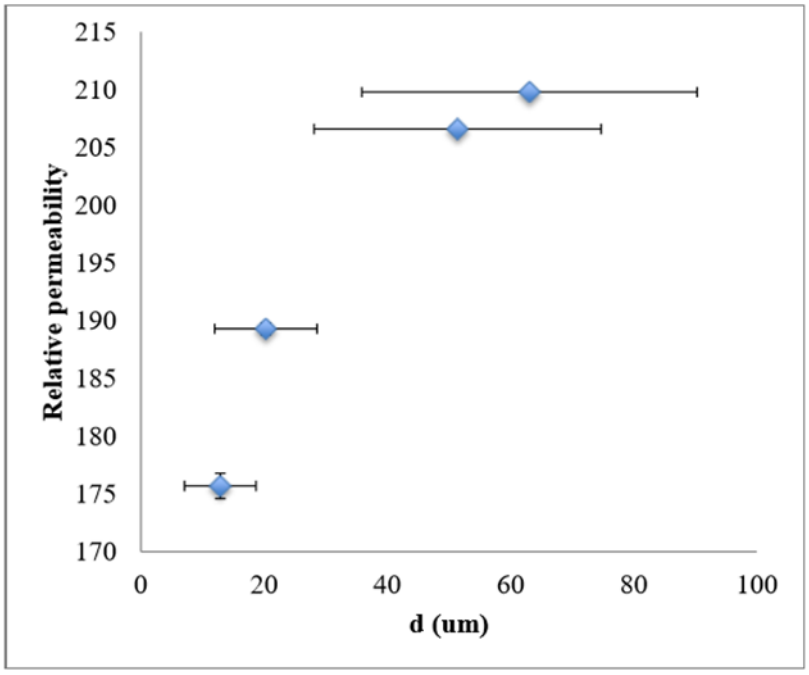

Figure 5. Relative permeability predicted from EM sensor measurements plotted with ferrite grain size for a 0.17 wt% carbon steel [35].

2.7.2 Phase Type

In a study by Zhou et al. [4], a multifrequency EM sensor was used to measure C-Mn steels of varying carbon content (0.17-0.8 wt%) and a pure iron. A FEM of this sensor was created in COMSOL Multiphysics and verified. This model was used along with the experimental results (low frequency real inductance) to infer predicted permeabilities. Figure 6 shows the predicted permeability for pure iron (ferrite) and 0.8 wt% C steel. The EM sensor and FEM model can clearly distinguish between a fully ferritic and fully pearlitic microstructure, with the fully ferritic pure iron exhibiting a higher predicted permeability than for the fully pearlite 0.8 wt% C steel. This is due to the pearlite lamellae in the microstructure of the 0.8 wt% C steel providing more pinning to the domain wall motion which results in a lower relative permeability and therefore low frequency real inductance than for the pure iron [4]

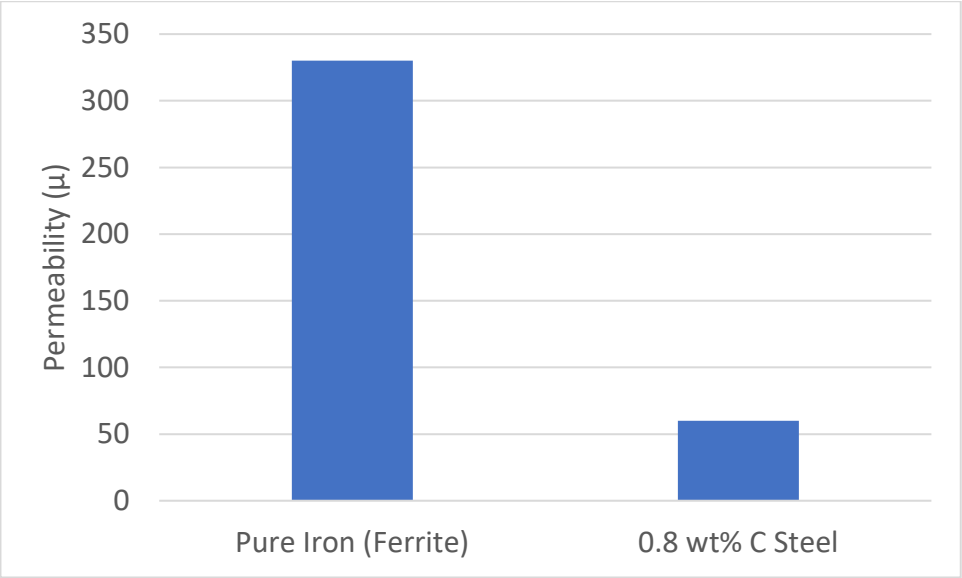

Figure 6. Predicted permeability inferred from EM sensor measurements for a pure iron (ferrite) and a 0.8 wt% C steel (pearlite). Reproduced from [4].

Saquet et al. [36] measured the B-H loops of a range of plain carbon steels with different microstructural phases. The measured steels were a ferritic steel (0.1wt% C), a pearlitic steel (0.8wt% C), a martensitic steel (0.55wt% C) and a steel with a ferrite and cementite microstructure (0.55wt% C). Figure 7 shows the respective B-H curves for the steel samples. While the effect of different microstructural parameters on the magnetic permeability is not discussed, it can be seen from figure 7 that these microstructural phases show a coercivity with an order of magnitude of the following; ferrite > pearlite > tempered martensite > martensite. This agrees with the study by Zhou et al. [4]. The measured B-H curves can distinguish between ferrite and pearlite but also martensite and tempered martensite. It can also be seen that the loops have different gradients which corresponds to having different permeabilities [36].

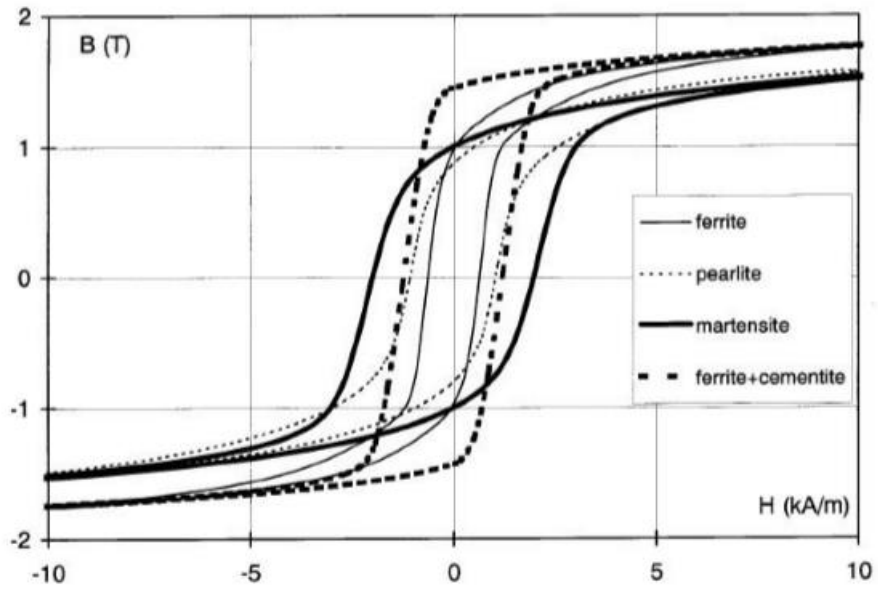

Figure 7. B-H Loops for ferrite, pearlite, martensite and ferrite + cementite [36].

2.7.3 Phase Balance

A study by Thomson et al. [26] investigated the effect of phase balance on the magnetic properties of ferrite pearlite steels. Figure 8 and figure 9 show initial and maximum permeability as a function of carbon content respectively. Initial and maximum permeability values are shown to decrease with increasing carbon content. This is to be expected, as the higher content means a higher amount of pearlite phase which has a lower maximum and initial permeability than ferrite [26].

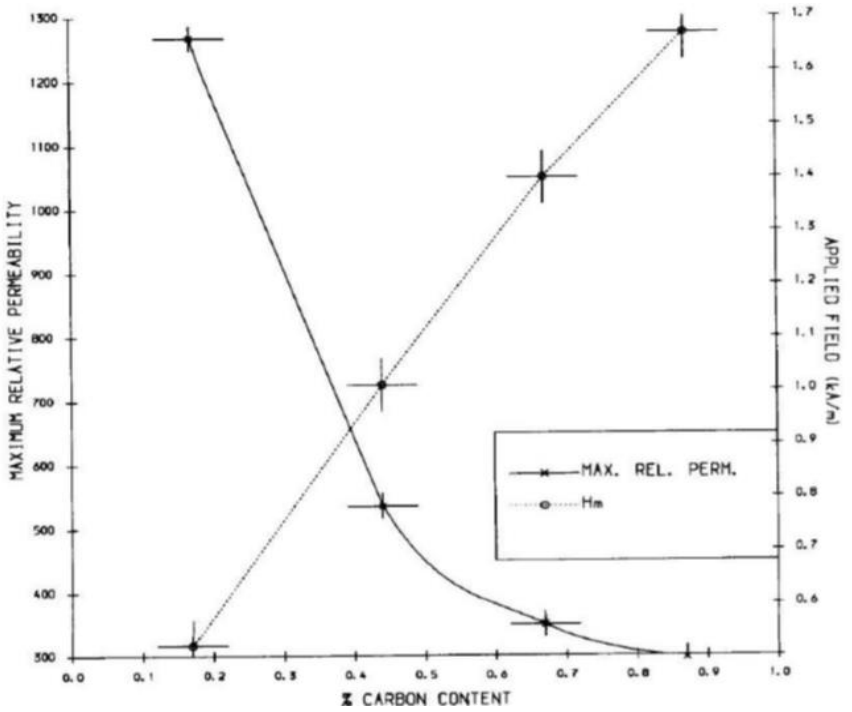

Figure 8. Maximum relative permeability as a function of carbon content in ferrite pearlite steels [26].

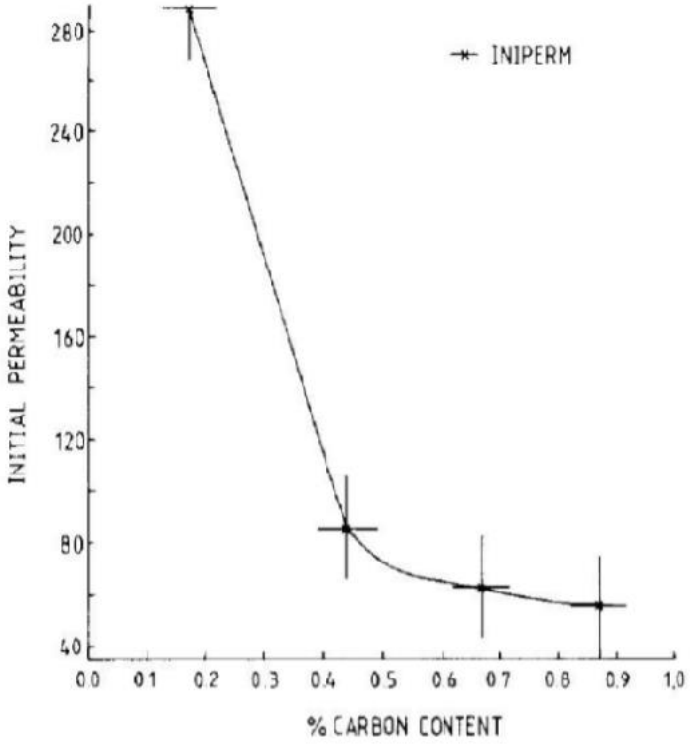

Figure 9. Initial permeability as a function of carbon content in ferrite pearlite steels [26].

A study by Zhou et al. [4] used an EM sensor to measure pure iron and ferrite pearlite steels with varying ferrite fractions as a result of their carbon content. An EM sensor was used to measure the steels, this sensor was modelled to predict permeability. Power laws using fitting factors of 1/2, 1/3 and 1/5 were used to calculate effective permeability for the same ferrite pearlite steels measured using the EM sensor. Power law has been popularly used to predict magnetic and electrical properties of 2 phase microstructures, where the microstructural phases have contrasting magnetic and electrical properties [37-39] A finite element microstructure model was also developed to predict permeability for the ferrite fractions of the ferrite pearlite steels. Figure 10 shows permeability with ferrite fraction for the 3 techniques. Firstly, the relative permeability increases with increasing ferrite fraction. The FEM model agrees well with the experimental data. At approximately 0.15 ferrite fraction and below for the EM sensor model and FEM model, there is little effect on the permeability, and this is due to there being no connected ferrite in this region. This causes a lack of a favourable path for the flux to travel, so there is little effect on the relative permeability at this ferrite fraction and below. The power law model with a fitting factor of 1/5 fits the EM model best. The power law models do not consider ferrite connectivity, so there is a small discrepancy between the power law models, the FEM and EM sensor measured data at lower ferrite fractions (0.2 and below) [4].

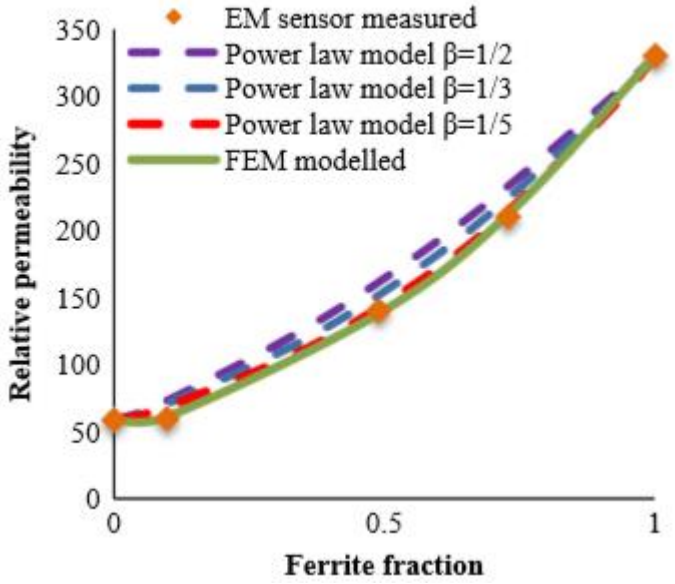

Figure 10. Relative permeability predicted from EM sensor measurements with ferrite fraction compared with power law and FEM models [4].

In a study by Hao et al. [37], EM sensors were used to measure steel samples (produced from stainless steel powders) of varying ferrite/austenite phase balances. The EM sensor was modelled and used to predict permeability of the different ferrite austenite phase balances. An FEM for microstructure, modelling the different austenite ferrite phase balances was produced to predict permeability. Permeability with ferrite fraction predicted from both the EM sensor model and FEM model is plotted in figure 11. Firstly, the graph shows that the FEM and inferred from EM sensor measurements permeabilities with phase fractions agree well with each other. The graph also shows that the permeability remains low up to 35% ferrite fraction despite the presence of ferromagnetic ferrite. Similarly, to the study by Zhou et al. [4], this is due to the lack of ferrite connectivity at these ferrite fractions however the effect is greater for austenite ferrite phase balances, as austenite is paramagnetic, and therefore has a larger effect on the effective permeability of the steel than for pearlite which is ferromagnetic [37].

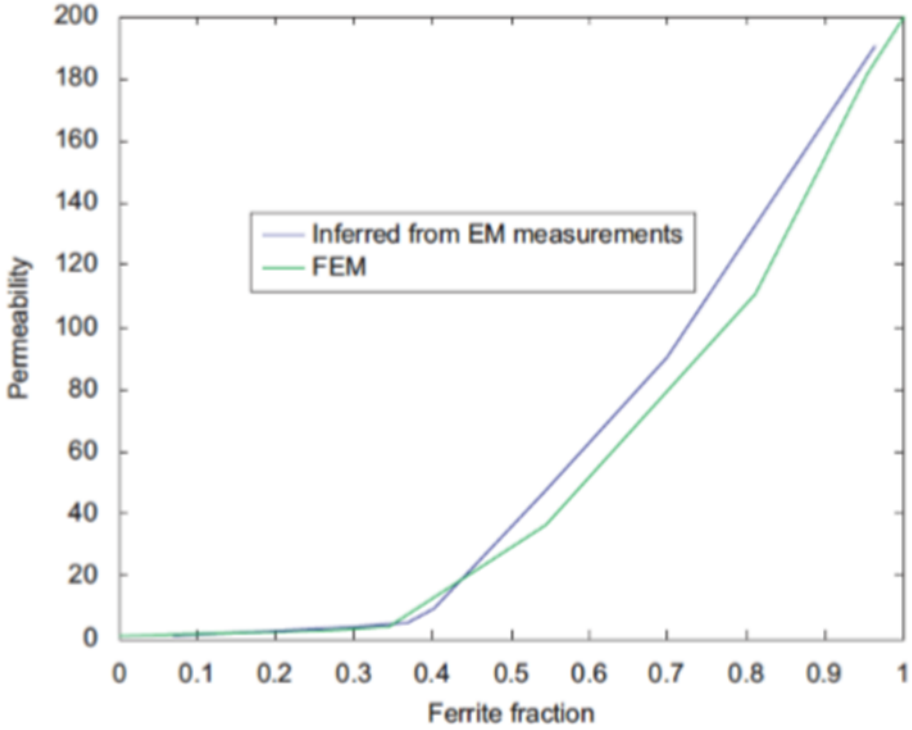

Figure 11. Permeability from EM measurements and FEM model as a function of ferrite fraction in austenite ferrite steels made from stainless steel powders [37].

2.8 Relationship Between Permeability and Temperature

Temperature is one of the biggest factors affecting permeability of ferromagnetic materials. A ferromagnetic material will become more responsive to an applied magnetic field as it's temperature increases, that is to say, its permeability increases with temperature. This is because the atomic spacing changes as the temperature increases due to thermal expansion. Thus, the ease at which the electron shells can interact with each other decreases. As a result of this, the electron spins are more easily affected by an external field. The increase in permeability with temperature is not linear. Figure 12 shows that at low applied magnetic fields (16 or 40 A/m), the permeability of iron will only increase with temperature until it reaches its Curie temperature (Tc) [11].

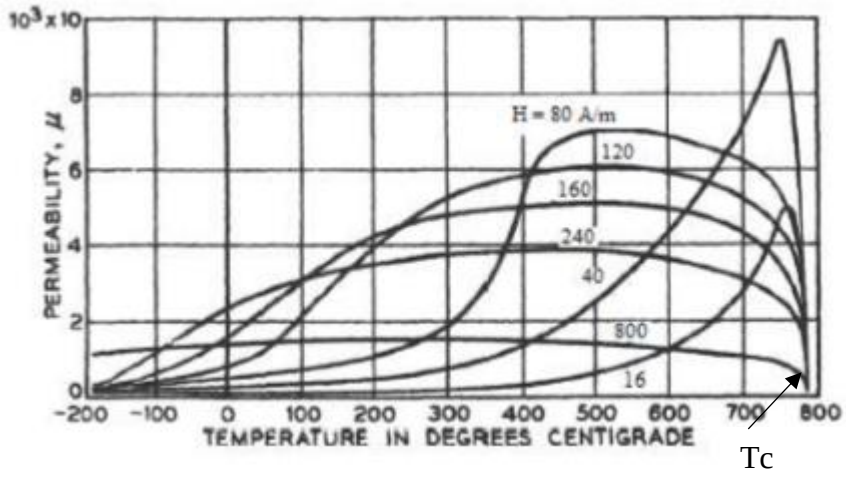

Figure 12. The effects of temperature on permeability for iron at varying constant field strengths. The Curie temperature is labelled and is shown as Tc [11].

Steel shows similar permeability temperature relationships to iron [40, 41]. A study by Zhou et al [40]. used a high temperature cylindrical EM sensor was used to measure the same set of samples mentioned in [4]. Inferred relative permeability values (predicted using a model of the EM sensor) were plotted against temperature for pure iron and 0.8 wt% C steel samples. The results are shown in figure 13. The data shows that for both samples, permeability increases non-linearly with temperature up until above 700℃. It expected that the permeability will decrease to 1 due to either phase transformation to

paramagnetic austenite or passing through the Curie temperature for steel although it is not shown in the graph. The plot for iron agrees well with the low field permeability (16 and 40 A/m) seen for iron in figure 12 which is expected as the applied field for the sensor used was approximately 50 A/m [40].

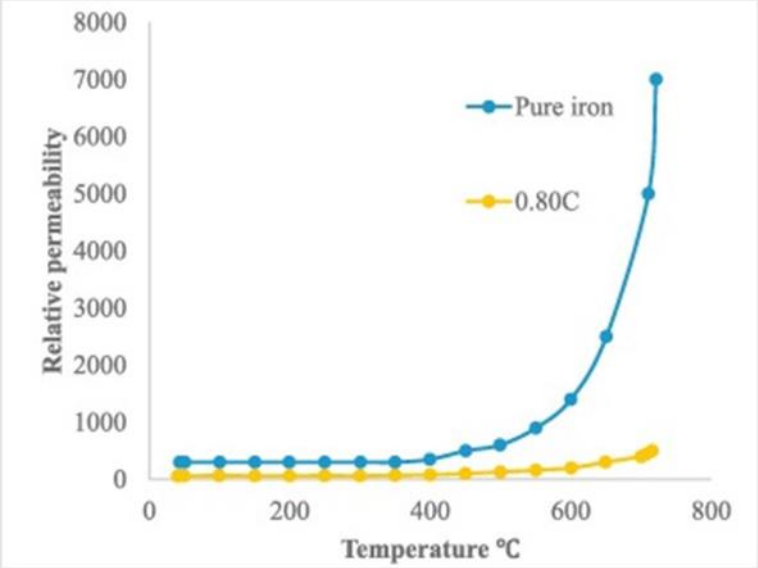

Figure 13. Permeability with temperature for pure iron and 0.80C carbon steel inferred from high temperature cylindrical EM sensor measurements [40].

As previously discussed, ferromagnetic materials are all characterized by a critical temperature known as the Curie temperature (Tc), which varies for different ferromagnetic materials; for example, iron has a Curie temperature of around 770^{o}C, whereas cobalt's is around 1110^{o}C. This is the point where thermal expansion causes the distance between the atomic centers to change, such that the material loses its ferromagnetic properties and becomes paramagnetic [11]. The Curie temperature can also be affected by a steel's chemical composition [11]. When a ferromagnetic element is alloyed with a paramagnetic element, the Curie temperature of the alloy is generally less than that of the pure ferromagnetic element. This is shown in figure 14. Elements such as chromium and manganese tend to decrease the Curie temperature of iron with increasing percentage of these elements. This is important in terms of steels as these are common alloying elements used in steel. Particularly for stainless steels where the chromium content can exceed 20% [11].

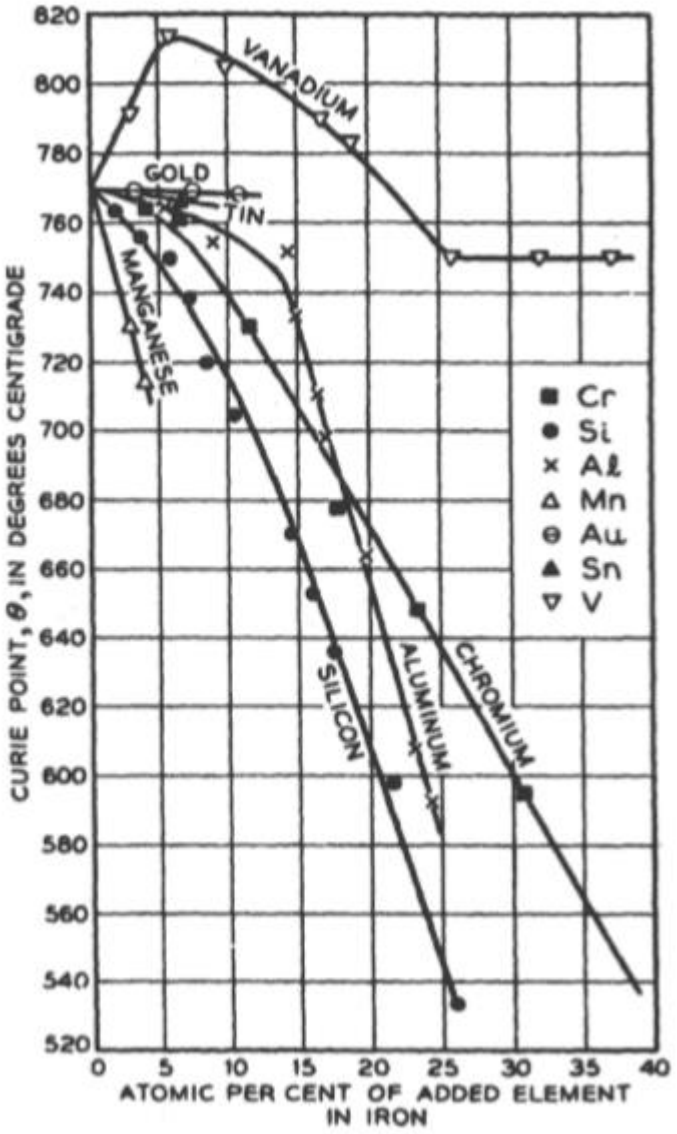

Figure 14. Effect of alloying elements on the Curie temperature of iron. The alloying elements plotted are chromium (Cr), silicon (Si), aluminium (Al), manganese (Mn), gold (Au), tin (Sn) and vanadium (v). [11]

2.9 Electrical Resistivity and Relationship with Temperature

In the microstructures of steel there are many factors that can affect electrical resistivity. These factors include dislocations, grain boundaries, and precipitates, alloying elements in solid solution (both substitutional and interstitial) and different phases. Temperature also has large effect. During electrical conduction there is a flow of electrons through the

crystal structure, and the different microstructural factors cause the electrons to scatter. This effect is known as electrical resistivity and can be described by Matthiessen's rule in equations 2 and 3 [13]:

$$\rho_{total} = \rho_T + \rho_i + \rho_d \qquad \text{Equation 2}$$

$$\rho_T = \rho_0 + aT \qquad \text{Equation 3}$$

Where ρ_{total} is the resistivity of the material and $\rho_T + \rho_i + \rho_d$ is the sum of the 'defects' that contribute to the total resistivity from temperature, impurities and deformation (dislocations) respectively. ρ_0 denotes residual resistivity, a is a constant and T is the temperature [13].

The electrical resistivity of a metal, such as steel, is affected by its composition. Figure 15 shows the relationship between electrical resistivity in iron and increasing percentages of different alloying elements [11]. It can be seen from figure 15 that the electrical resistivity of iron increases as the percentage of alloying elements increases. It can also be seen that the rate of increase changes for different alloying elements.

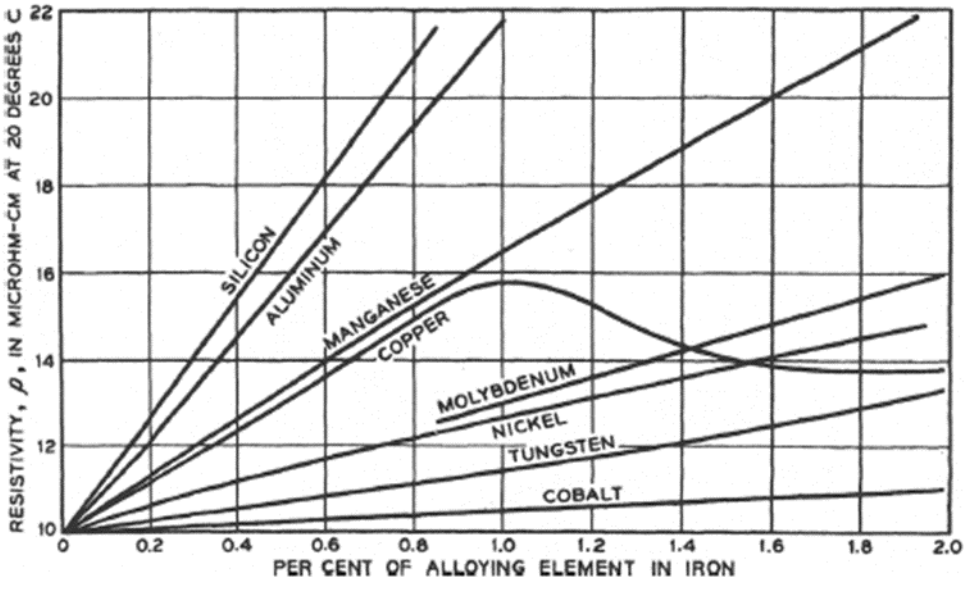

Figure 15. Relationship between electrical resistivity and addition of alloying elements in iron at 20°C [11]

A study by Ludwigson et al. [41] explored the effect of alloying elements on the resistivity of low carbon steel. It was found that with the addition of alloying elements, electrical resistivity increased with the addition of phosphorus, manganese, copper, nickel, chromium and silicon while decreasing with the addition of sulphur. This is represented in figure 16. It was also reported that the resistivity can be estimated by the sum of the alloys in solid solution, shown in equation 4 [41]:

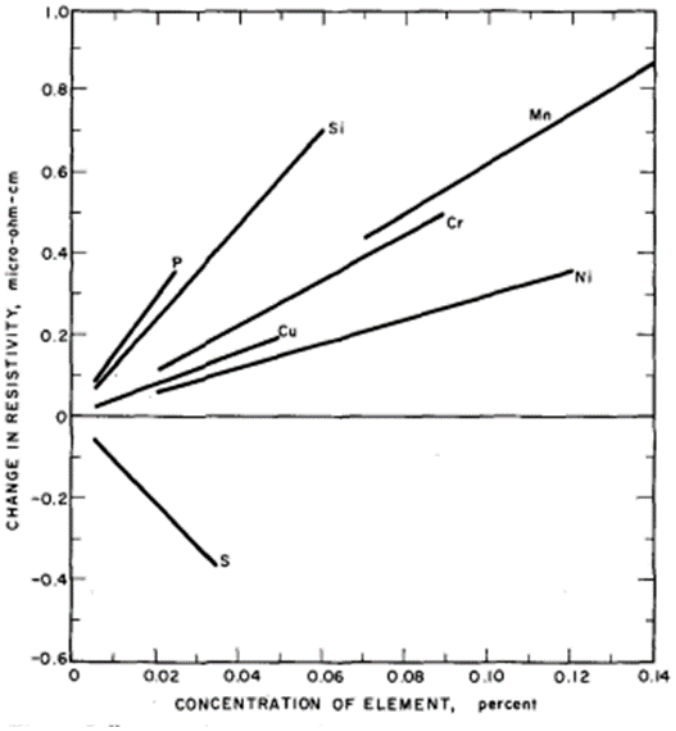

Figure 16. Dependence of change in resistivity on alloying elements in a low carbon steel. The alloying elements plotted are sulphur (S), nickel (Ni), copper (Cu), chromium (Cr), Manganese (Mn), silicon (Si) and phosphorus (P) [41].

$$\rho_{steel\ in\ \mu\Omega cm=}\ 10.1 + 6.2Mn + 14.3P + 11.7Si + 3.9Cu + 3.0Ni + 5.6Cr - 10.4S$$

Equation 4

The electrical resistivity of a metal is also affected by temperature. For pure metals and all copper-nickel alloys, electrical resistivity increases linearly with temperature above approximately -200°C. This is caused by increasing thermal vibrations at higher temperatures which in turn increases the chance of electrons in a flowing current being scattered [13].

Figure 17 shows that of the electrical resistivity of an iron sample increases with temperature. The graph shows a non-linear increase in electrical resistivity with temperature. This is because the sample was not a pure iron. Iron increases non-linearly until approximately 800°C, where the slope of the graph decreases, and then the resistivity continues to increase with a lower gradient until 1450°C [11]. The gradient change at 800°C is caused by a microstructural phase change from body centered cubic ferrite to face centered cubic austenite [13].

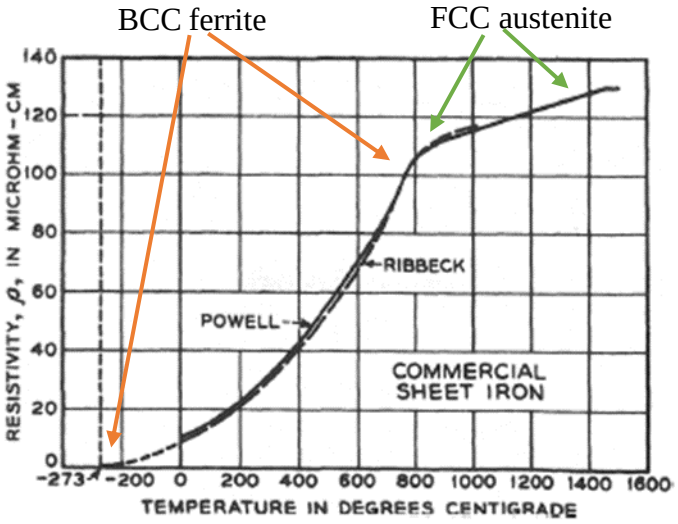

Figure 17. Resistivity with temperature for commercial sheet iron. The points on the plot where BCC ferrite and FCC austenite microstructures are expected have been labelled [11].

Steel shows a similar relationship for resistivity with increasing temperature. This is shown in figure 18, which shows the resistivity for different steels with varying temperature, where resistivity data from the ASM Handbook has been plotted against temperature. The compositions for the steels in figure 18 are given in table 1. The room temperature resistivity values vary due to the different compositions and microstructures of the steels. It can be seen from figure 18, that the resistivities for the steels increase non-linearly with increasing temperature. The gradient of the slopes increases up to around

800°C, when phase transformation from predominantly ferrite (depending on steel composition) to austenite occurs. After 800°C the slope gradient decreases but the resistivity is still increasing [42].

Table 1. Chemical composition and previous heat treatment for steels reported in the ASM handbook [42].

Nearest AISI-SAE Grade	C (%)	Mn (%)	Si (%)	Cr (%)	Ni (%)	Mo (%)	Other (%)	Treatment or Condition
1008	0.06	0.38	. . .	. . .	. . .	. . .	. . .	Annealed
1008	0.08	0.31	. . .	. . .	. . .	. . .	. . .	Annealed
1025	0.23	0.64	. . .	. . .	. . .	. . .	. . .	Annealed
1078	0.8	0.32	. . .	. . .	. . .	. . .	. . .	Annealed
(a)	1.22	0.35	. . .	. . .	. . .	. . .	. . .	Annealed
1524	0.23	1.51	. . .	. . .	. . .	. . .	0.11 Cu	Not known
5132	0.32	0.69	. . .	1.09	0.073	. . .	. . .	Annealed
(a)	0.35	0.59	. . .	0.88	0.26	0.2	. . .	Annealed
(a)	0.33	0.55	. . .	0.17	3.47	. . .	. . .	Not Known
(a)	0.34	0.55	. . .	0.78	3.53	0.39	. . .	Hardened and tempered
(a)	0.49	0.9	1.98	. . .	. . .	. . .	0.64 Cu	Not known

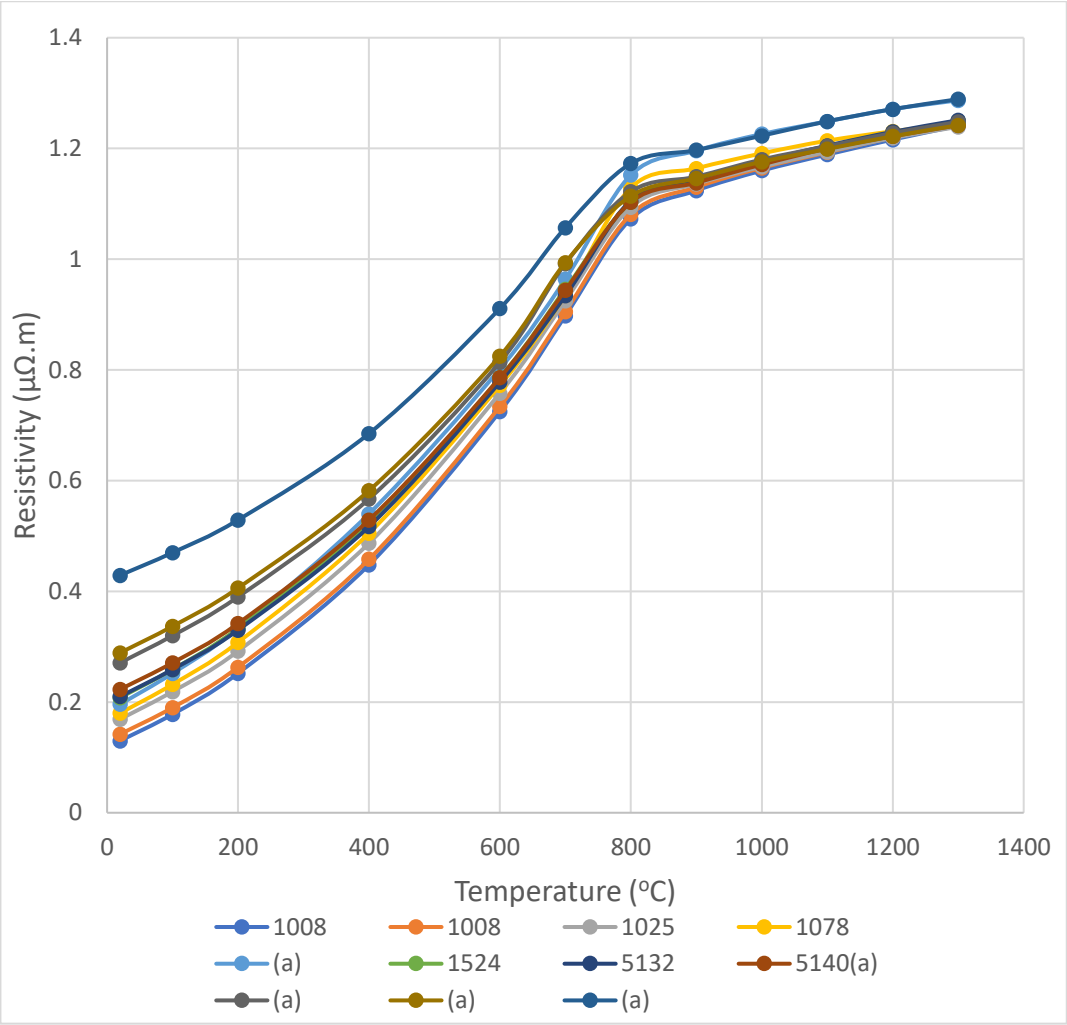

Figure 18. Resistivity with temperature for a range of steels reproduced from the ASM handbook [42]

2.9 Chapter Summary

The fundamental theories of electromagnetism have been discussed in this chapter. This was followed by discussing the effect of various factors on magnetic permeability and resistivity. It was shown that microstructure and composition have a large effect on permeability and resistivity in steel. Temperature was shown to have the largest impact on permeability and resistivity and understanding how the combination of microstructure, composition and temperature affects EM properties is important in terms of interpreting the EM signal for steel at high temperature and relating the signal to phase fraction transformed.

3. EM Fundamentals and EM sensors

EM sensors, how they work, and how they affect ferromagnetic materials are governed by the fundamental laws of electromagnetism. This section focuses on the relevant laws of electromagnetism, EM sensors and their signals. This section will also cover how EM sensor modelling and its importance. It is very important to understand the signals of the EM sensor is when considering them for the use of microstructural characterisation in steel.

3.1 EM Sensor Design

EM sensors, sometimes also called eddy current sensors, are sensitive to changes in magnetic permeability and resistivity of steel that are caused by changes in composition and microstructure. EM sensors consist of exciting coils and sensing coils and have many different designs and operating frequencies depending on their use. All EM sensors have an excitation coil, which generates a magnetic field, and a receiving coil, which is used to sense changes in the steel's magnetic and electrical properties. Sensor designs change depending on the application, for example, for testing relatively large strip or plate type samples, a ferrite cored H (or U) shaped sensor has been used [43]. Smaller cylindrical or strip samples have been measured using an air cored cylindrical sensor [35]. A diagram of an H (double U) shaped probe is given in figure 19[43].

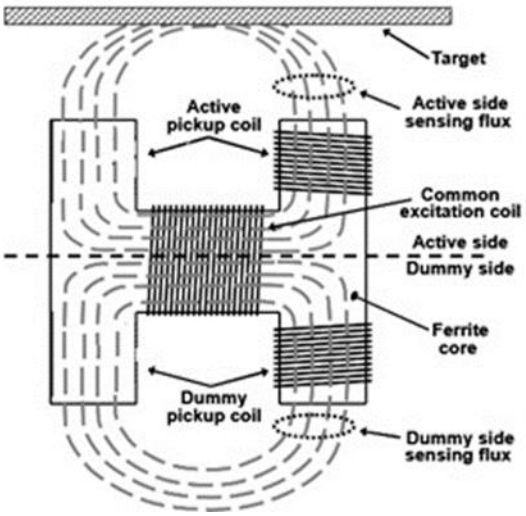

Figure 19. Schematic of an H shaped EM sensor measuring a ferromagnetic target [43].

3.2 Inductance

A current carrying coil generates a magnetic field, the direction of the current passing through the coil designates the direction of the magnetic field. Coils powered by an alternating current (AC) generate magnetic fields that change polarity in association with the change in current direction. AC circuits produce an EMF as a reaction to the changing magnetic field direction within the coil. By Lenz's law, the self-induced EMF opposes the change in magnetic field that created it. This occurrence is known as self-inductance and is defined in equation 5:

$$L = \frac{N\,\Phi_B}{I} \qquad \text{Equation 5}$$

L is the self-inductance in Henry (H), N is the number of turns of the coil, Φ_B is the magnetic flux (Wb) and I is the current in Amps (A). A change in the coil current (I), causes the magnetic flux to change. By re-arranging equation 5 and taking the derivative with respect to time, the relationship between the rates of change can be seen in equation 6:

$$N\frac{d\Phi_B}{dt} = L\frac{dI}{dt} \qquad \text{Equation 6}$$

From Faraday's law for a coil with N amount of turns, the self-induced EMF is given by:

$$\varepsilon = -N\frac{d\Phi_B}{dt} \qquad \text{Equation 7}$$

Where ε is the self-induced EMF in Volts. From equation 6, it follows that the self-induced EMF is given by:

$$\varepsilon = -L\frac{dI}{dt} \qquad \text{Equation 8}$$

The negative sign is due to Lenz's Law [12].

Suppose there are two coils that are neighbours or concentric to each other. Coil 1 is carrying an AC current and therefore has a magnetic field and flux as a result. The flux lines produced by coil 1 will also pass through coil 2. If the current in coil 1 changes, then the flux through coil 2 will change also. These events cause an EMF to be induced in coil 2 according to Faraday's law of induction. This phenomenon is known as mutual inductance (M) and is defined by equation 9 [12]:

$$M = \frac{N_2\Phi_{B2}}{I_1} = \frac{N_1\Phi_{B1}}{I_2} \qquad \text{Equation 9}$$

Where M is measured in Henry (H), N_2 is the number of turns in coil 2, Φ_{B2} is the magnetic flux in coil 2 in Wb and I_1 is the current in coil 1 in Amps (A) and vice versa for the second part of the equation. If there is a ferromagnetic material in the proximity of the magnetic field produced by coil 1, the mutual inductance is also related to the relative permeability of the material. This is shown in equation 10 and is the basis for how EM sensors work when being applied for detecting changes in steel microstructure [12]:

$$M = \frac{N_2\Phi_{B2}}{I_1} = \frac{N_2BA}{I_1} = \frac{N_1N_2\mu A}{l} \qquad \text{Equation 10}$$

Like the self-induced EMF, the mutually induced EMFs are given by:

$$\varepsilon_2 = -M\frac{dI_1}{dt} \quad And \quad \varepsilon_1 = -M\frac{dI_2}{dt} \qquad \text{Equation 11}$$

ε_1 and ε_2 are the induced EMFs in coils 1 and 2 respectively. The negative signs again are due to Lenz's law [12].

3.3 Eddy Current Theory

When a coil probe or EM sensor's generated AC magnetic field interacts with a conductive target, eddy currents are induced within the target due to Faraday's law of induction. The intensity of these eddy currents is affected by the permeability and resistivity of the target, the geometry of the target and the excitation frequency [44]. These eddy currents in turn have their own magnetic field which opposes the primary magnetic field of the interacting coil or EM sensor. A schematic of eddy current flow within a target as a result of interaction of the primary magnetic field from coil probe is given in figure 20 [44].

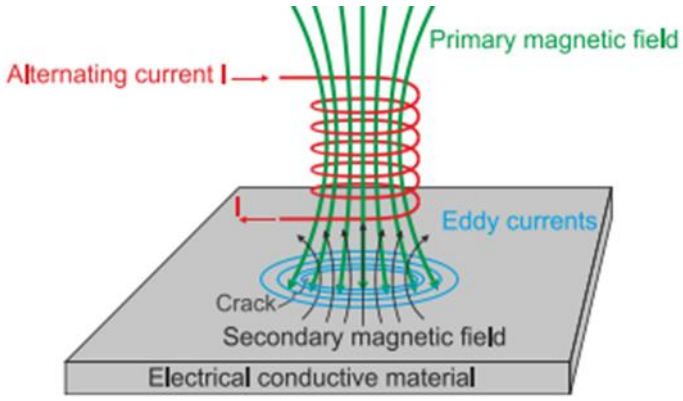

Figure 20. Interaction of a coil probe with a conductive material showing the primary and secondary magnetic fields and eddy currents [44].

As the frequency increases, the depth at which the magnetic field of the probe or EM sensor can penetrate the conductive target decreases (skin depth). This is due to the magnitude of the eddy currents increasing due to the increasing frequency, and the magnetic field of the eddy current further opposes the primary field of the probe. The skin depth equation is given in equation 12 [44]:

$$\Delta_s = \sqrt{\frac{\rho}{\pi f \mu_0 \mu_r}} \qquad \text{Equation 12}$$

Where ρ is the resistivity of the conductor in Ohm meters (Ω.m), f is the excitation frequency of the probe in Hz, and $\mu_o\mu_r$ is the relative permeability of the conductor. How the concept of eddy currents and skin depth relate to EM sensor function and signals will be explained later in this chapter [44].

3.4 Impedance

Impedance in a current carrying coil is similar to resistance in a DC circuit. The impedance (Z) of a coil with an alternating current is measured in Ohms and is represented as a complex number. It is defined as the ratio of the voltage amplitude across the circuit to the current amplitude in the circuit. Impedance is calculated by:

$$Z = \frac{V}{I} \qquad \text{Equation 13}$$

Where Z is the impedance in Ohms (Ω); V is the voltage in volts(V), and I is the current in Amps (A).

Impedance is very important in terms of EM sensors. When a conductive material is placed near an EM sensor eddy currents are induced within the sample due to Faradays law of induction. These eddy currents produce a secondary magnetic field that opposes the magnetic field from the coil. Consequently, an impedance parameter Z_c is established for the sensing coils of the sensor:

$$Z_c = R_C + jX_C \qquad \text{Equation 14}$$

R_c and jX_c represent the real and imaginary part of the impedance respectively and are both measured in Ohms (Ω). R_c is related to losses in the EM sensor [44]. The imaginary part, X_c is known as inductive reactance and is related to the induced EMF coefficient L_c (also known as real mutual inductance) in the sensing coils of the EM sensor and the frequency f [44]. The equation for X_C is given by:

$$X_c = 2\pi f L_c$$ Equation 15

The impedance magnitude |*Z*| can be calculated by:

$$|Z| = \sqrt{R_c^2 + X_C^2}$$ Equation 16

While the impedance phase angle φ (degrees) is given by:

$$\varphi = atan2\ \frac{X_c}{R_C}$$ Equation 17

The phase response of the impedance spectra is very important to this study as it is one of the main outputs of the EMspec® sensor used for this study. How the phase response links to the EM sensor response to different materials will be explained later in this chapter.

3.5 EM Sensor Function

This section will describe the effects of inductance, impedance and eddy current theory on EM sensor signals and how EM sensors are able to non-destructively characterise steel microstructure.

3.5.1 Real Mutual Inductance

The real mutual inductance as previously shown is related to the imaginary impedance and the induced EMF in the sensing coils of the EM sensor. At low frequencies, the exciting coil magnetic field penetrates the target sample and the mutual inductance of the sensing coil increases. At this point, the magnitude of the eddy currents is weak, thus relative permeability dominates the signal.

As the frequency increases, induced eddy currents increase in magnitude. These eddy currents generate a separate magnetic field which opposes the sensor generated magnetic field. With increasing frequency, the depth of magnetic field penetration into the sample surface decreases, until it can no longer penetrate due to the opposing magnetic field of

the eddy currents (skin effect). The frequency at which the magnetic field stops being able to penetrate the surface of the sample is called the zero-crossing frequency (ZCF). The ZCF is related by the electrical resistivity and the relative permeability of the sample being measured. ZCF has a linear relationship with permeability [5]. ZCF is determined by equation 18:

$$\omega_0 = \frac{\mu\alpha_0^2}{\mu_0\sigma} \qquad \text{Equation 18}$$

Where ω_0 is the ZCF in Hz, μ is the relative permeability, α_0 is defined to be 1 over the smallest dimension of the coil, and σ is the electrical conductivity in S/m.

The EMspec® sensor's primary output is the ZCF and was used in this project for high temperature measurements of steel plates during cooling. ZCF is relatively insensitive to changes in lift off, which is useful for a sensor in an industrial setting where the lift off between the sample and the sensor may change during the process. An example of the real inductance response with frequency for a steel (not specified) at different lift offs is shown in figure 21. From 35mm to 70mm lift off, the low frequency real inductance is significantly affected by changes in lift off while the ZCF (highlighted) is relatively insensitive to the lift off [45].

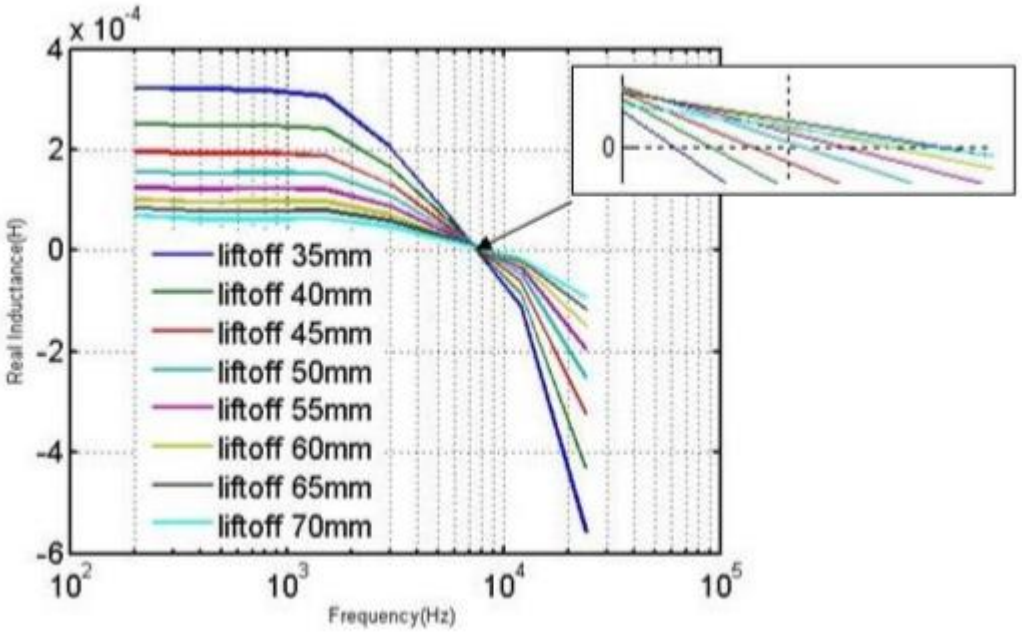

Figure 21. Real inductance with frequency for a steel being measured at different lift offs [45].

3.5.2 Phase Angle of Impedance Spectra

The phase angle of the impedance spectra and ZCF are important as they are the main outputs of the EMspec® sensor. Phase angle, like ZCF, is relatively insensitive to changes in lift off. The phase response to different targets is shown in figure 22 (background shown in grey, phasor shown as black) [7].

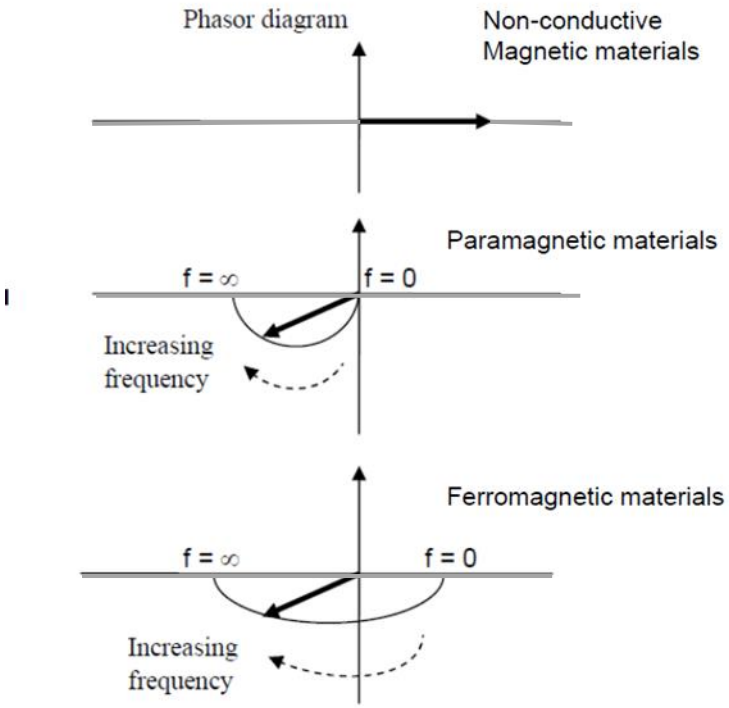

Figure 22. Schematic of phase response to a non-conductive magnetic material (top), a paramagnetic material (middle) and a ferromagnetic material (bottom). The grey x-axis represents the background signal [7].

In figure 22, the top diagram shows the phase response for a purely magnetic material with zero conductivity, in which the phase response is in phase with the background signal. For a paramagnetic material (middle), the phasor only rotates in the lower left-hand quadrant from -90º to -180º, and this is a consequence of eddy currents being induced within the material, that oppose the applied magnetic field. At very high frequencies, the magnetic field can no longer penetrate the target and the phase response

is -180º out of phase with the background. The bottom diagram shows a phase response for a ferromagnetic material which combines the previous two scenarios. The phasor rotates over the lower two quadrants from in phase with the background at zero frequency (0º) to -180º out of phase at very high frequencies [7]. The point where the phasor crosses -90º is also the ZCF for a ferromagnetic material when the magnetic field can no longer penetrate the material.

3.6 Summary

This section has gone over the fundamental laws of electromagnetism that relate to EM sensors, EM sensor functions and the different signals they output. It has been shown that the sensing coil inductance is affected by both permeability and resistivity which is very important to this study but also to all work involving EM sensors. As eddy currents are affected by permeability and resistivity which vary in steels, the sensing coils of an EM sensor will measure different signals with frequency. The phase angle of the impedance spectra and ZCF are the main output signals for the industrial sensor used in this study as both signals boasts being relatively insensitive to changes in lift off which may be experienced in an industrial setting.

4. Non-Destructive Testing Methods of Measuring the Phase Transformation in Steels

There are several methods of non-destructive testing methods of steel characterization that currently exist. This chapter will focus on reviewing the various techniques and discuss their strength and weaknesses when it comes to characterizing steel microstructural after hot rolling in an industrial setting.

4.1 X-ray Diffraction

X-Rays are high energy EM waves with wavelengths between 10^{-3} and 10^{1} nm. When an incident x-ray beam interacts with a solid, part of this beam will be diffracted by the electrons associated with atoms within the crystal lattice that is in the beam's path. The pattern and spacing of the diffracted X-rays can be measured to determine atomic or molecular structure of the target material, as the assemblage of the electrons causing the diffraction within the target will provide a distinctive signature. The mean atomic spacing and disorder within a single crystal or polycrystalline structure can be determined via analysis of this signature. The interaction and diffraction of an X-ray beam on a cubic crystal lattice structure (similar to a steel sample) is shown in figure 23 [46].

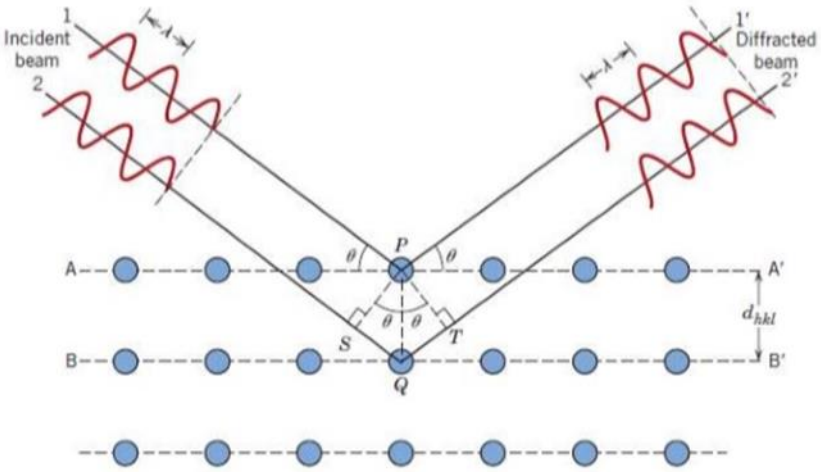

Figure 23. Schematic of x-ray diffraction technique [13].

X-ray diffraction measures 3 parameters and each give their own information about the target sample. The peak intensity provides information about crystal structure, texture and phase analysis. Crystallite size can be examined by interpreting the shape of the peak. Lastly, the position of the peak gives information about chemical composition [46, 47]. X-ray diffraction methods have been used to measure microstructural phase balance as well as crystallographic texture [46-49]. Phase balance has been monitored during the tempering of a martensitic stainless-steel using x-ray diffraction [50]. Figure 24 shows the respective peak intensities and positions with temperature for this sample. The as received microstructure consisted of martensite and retained austenite. During heating of the steel, the martensite and retained austenite was expected to transform to ferrite [11]. It can be seen during heating that there is a peak for the retained austenite (111) and martensite (101) and (110). A martensite to ferrite transformation can be seen from the ferrite peak at higher temperatures which backs up what was expected of the specimen's microstructure [50].

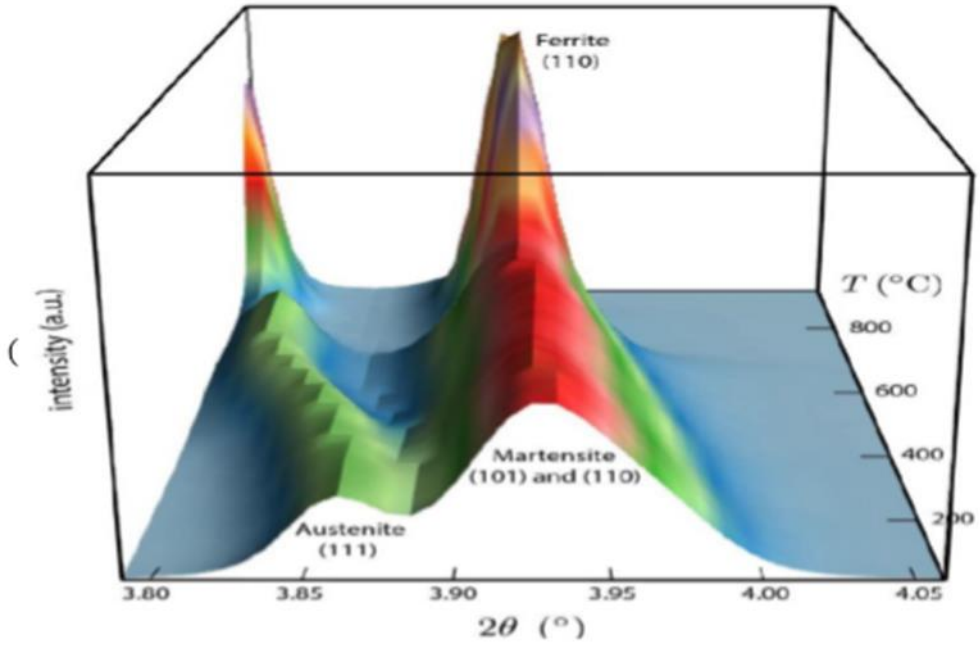

Figure 24. X-ray diffraction showing peaks and positions for microstructural phases in a martensitic stainless-steel during tempering. Martensite (101) and (110) has 2 peaks, ferrite (110) has 1 peak, the presence of retained austenite (111) is also detected [50].

Nucleation and grain growth in a structural steel during phase transformation has been monitored using x-ray diffraction. The specimen was annealed at 900℃ and fully transformed to austenite. It was then cooled to 600ºC over the period of one hour. The ferrite and pearlite grains were counted using the quantity of related reflections for ferrite and pearlite, the results are shown in figure 25. It is shown that ferrite nucleation starts at around 825℃ and continues as the sample cooled, and that pearlite grains were formed as the temperature dropped below 690ºC [51].

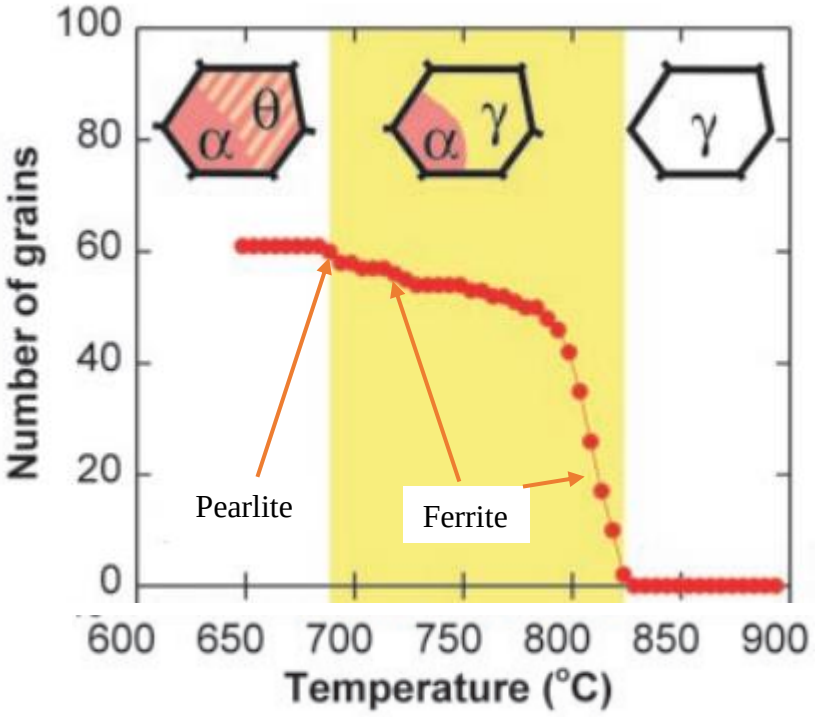

Figure 25. Number of ferrite and pearlite grains transformed as a function of temperature derived from x-ray reflections on a structural steel specimen. The increases in grain size to due to ferrite and pearlite transformations are labelled [51].

An industrial x-ray diffraction system has been developed at Hoersch-Stahl AG (Germany) which is aimed at performing texture measurements on low carbon steels at room temperature [52]. While it has been reported that x-ray diffraction techniques are largely unaffected by environmental factors such as dust, the beam does require a clear path for the beam to interact with the target. This makes it difficult when considering the use of the technique for monitoring the phase transformation of steel in an industrial setting as oxide layers would prevent the beam from interacting with the main body of the measurement sample. In addition, x-ray systems are at a disadvantage for industrial deployment due to associated health and safety risks. X-rays generated during a test can cause radiation burns to workers, therefore it needs to be housed and shielded to prevent exposure to workers during measurements [53].

4.2 Ultrasonic Techniques

Ultrasonic measurement uses high frequency sound waves, greater than 20Hz, to determine physical properties of materials. Ultrasonic testing can be used to characterise materials as well as assessing materials properties and looking for flaws such as cracks and inclusions. Typical equipment set up and measurement technique outputs are shown in figure 26. During an ultrasonic measurement, ultrasonic sound waves are transmitted into and through the material to be measured. The sound waves will be reflected from physical factors of the measured material such as its back wall, defects, inclusions and porosity. In the case of steel, the amplitude of the reflection and the time taken to receive the reflected pulse will vary with steel microstructure. If any defects (cracks or inclusions) occur in the steel, this will cause a secondary reflection to be received [54, 55].

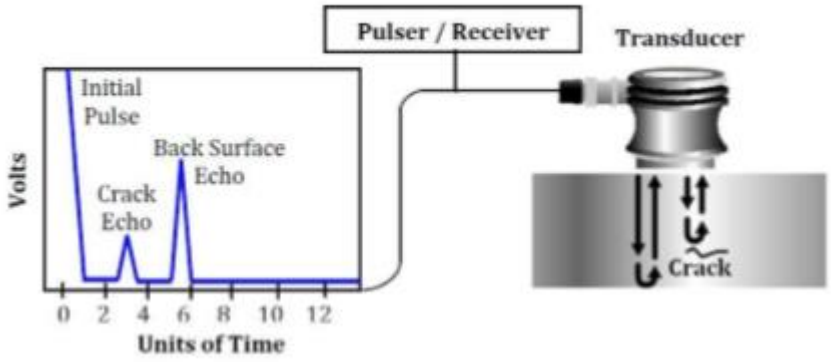

Figure 26. Basic principles of an ultrasonic measuring system [56]

Techniques such as basic ultrasonic testing, EM acoustic resonance (EMAR), EM acoustic transducers (EMAT) and laser ultrasonics exist for generation and detection.

Ultrasonic techniques have been used to characterise different amounts of cold rolling in steel. Cold rolling causes plastic deformation and increases dislocation density in steel, which in turn affects ultrasound velocity [57].

Hardened surface layer thickness has also been measured using ultrasonic measurement techniques. It was found that the reflected ultrasound waves could distinguish between the hardened layer and the transition zone, with noticeable scattering occurring in the transition zone as opposed to the hardened layer [58].

Grain size has been quantified using ultrasonic testing [58-60]. Figure 27 shows measurement of grain size by ultrasonic testing plotted against traditional ASTM grain size measurement. Velocity of ultrasonic waves were reported to decrease with decreasing grain size in maraging steels. Figure 27 shows that there is a linear relationship between the two grain size measurement techniques [60].

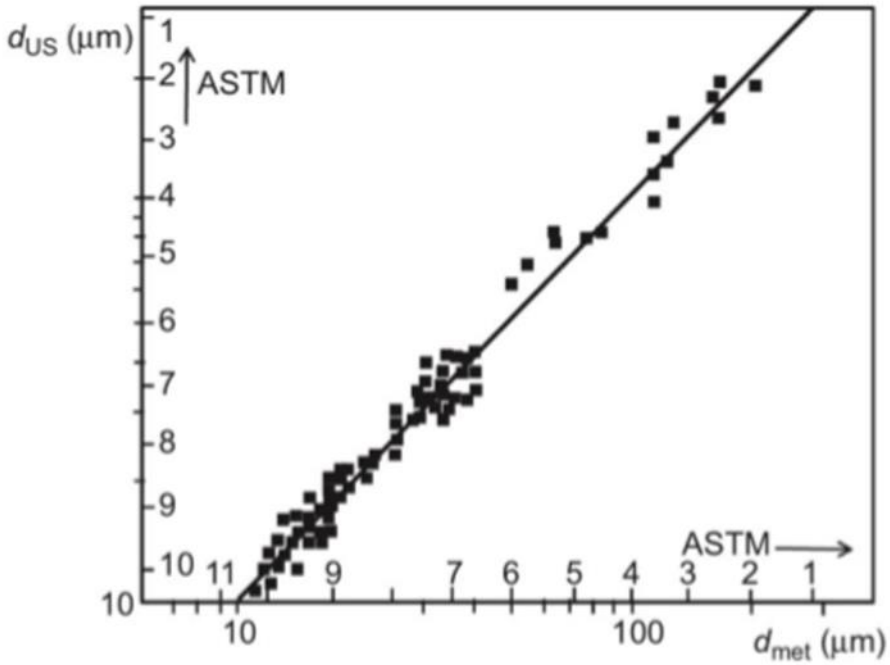

Figure 27. Comparison of grain size analysis between metallographic (dmet) and ultrasonic (dus) method [60]

Laser ultrasonics have been used to monitor recover and recrystallisation both online and offline [61, 62]. A study by Smith et al. [61] used laser ultrasonics to monitor recovery and recrystallisation of ferritic ultra-low carbon steels at 3 different constant temperatures (550℃, 730℃ and 800℃). Figure 28 shows fractional velocity change with time at temperature. The ultrasound velocity decreases with time at temperature for all the temperatures as recovery occurred. Recovery in the samples was confirmed by measurement of stress relaxation in the sample [61].

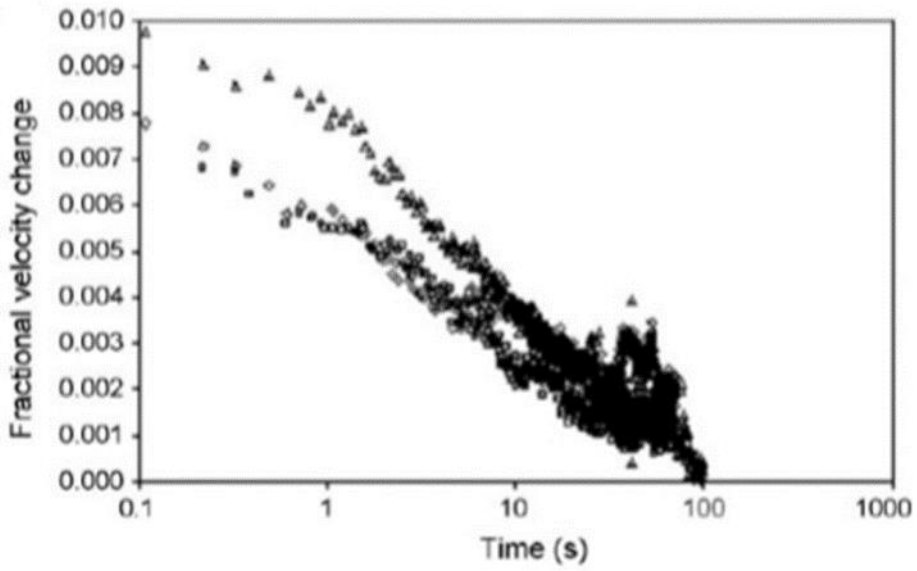

Figure 28. Fractional velocity change with time at temperature. Open triangles =500℃, Open diamonds = 730℃, Open squares = 800℃ [61]

Multiple studies have investigated the application of laser ultrasonics for detecting phase transformation in steels [63-65]. A study by Kruger et al. [63] looked at quantifying phase fraction transformed from ultrasonic measurements. Figure 29a shows ultrasound velocities dependence with temperature for ferrite, austenite and measured data for a low alloy steel. This is then compared with austenite fraction obtained from dilatometry measurements for the same sample, shown in figure 29b. The results show that austenite fraction calculated from laser ultrasonics agrees relatively well with dilatometry results with both sets of data almost overlapping each other. This shows that laser ultrasonics can not only monitor the phase transformation, but it can also quantify transformation fraction for laboratory samples [63, 65].

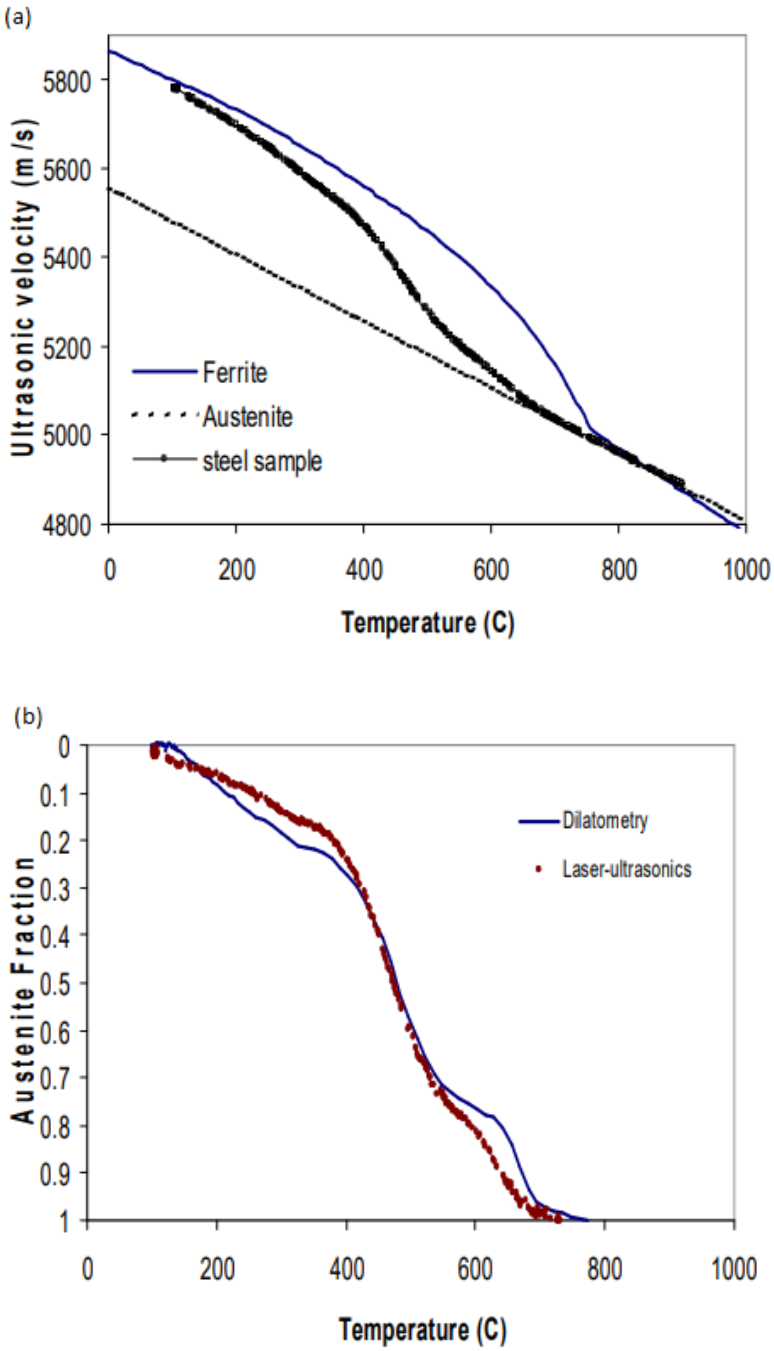

Figure 29. (a) Ultrasonic velocities with temperature for ferrite (solid line), austenite (dotted line) and measured data low alloy steel (line and symbol) and (b) austenite fraction with temperature from the ultrasonic velocities shown in (a) [63].

Laser ultrasonics have been used for steel characterisation in a hot strip mill environment in a study by Hutchinson et al. [66]. It was recognised the importance of being able to monitor the microstructural state of steel during critical points in processing such as on the ROT of a hot strip mill after hot rolling and before coiling for product quality control. This is similar to the aims of this thesis which is similarly looking at strip steel during

cooling but using an industrial EM sensor to relate the signal to microstructural state and transformation fraction. It was found from this research that laser ultrasonics technique is sensitive to different steel grades and was able to detect and monitor the transformation state of the steel during processing [66].

Ultrasonic techniques have been shown to be sensitive to different microstructural parameters such are plastic deformation, recovery, recrystallisation and phase transformation in laboratory and industrial environments.

The benefits to using ultrasonic techniques for online phase transformation measurement are that they can be used at large stand-off distances and can measure samples that are above the Curie temperature. However, there are significant weaknesses to using ultrasonic measurement techniques in industrial settings. The application of laser ultrasonics in industrial conditions are limited by the need of a clear site to the target material. Factors such as scale, dust, and water can affect the results of laser ultrasonics, making it very hard to effectively deploy in hot mill environments. The study by Hutchinson et al. [66] showed this limitation with the positioning of the laser ultrasonic sensor [66]. The sensor was only able to be positioned on the ROT after water cooling and before the coiling. The positioning meant that most of the scale had been washed away. This meant that the transformation state can only be monitored at one point after water cooling has already finished. Even at this point, the standing water on top of the steel could still affect the measurements. Another detriment to the deployment of laser ultrasonics is that the lasers pose a risk to workers in the immediate area, the lasers used are powerful and can cause damage to eyes and skin, and therefore need to be housed in a closed environment.

4.3 EM Techniques

As most steels are ferromagnetic, EM NDT techniques can be used to measure factors that are sensitive to changes in steel microstructure. Several EM techniques exist for assessing steel microstructure. This section discusses the different techniques and commercial systems that are used to assess microstructural properties in steel.

4.3.1 Magnetic Barkhausen Noise (MBN)

When an external magnetic field is applied to a ferromagnetic material, the magnetic domain walls within the material move in association with the applied field. As the magnetic domain walls move, they come across pinning points where they become pinned and then break free of the pinning points. MBN is caused by the energy release of a magnetic domain wall breaking free of a pinning point and can be measured using a microphone. When magnetisation is measured using this technique it can be seen as a series of small steps caused by the Barkhausen effect, as shown in figure 30. The more pinning points there are in a material, the greater the MBN will be and the harder it will be to magnetise or demagnetise [67].

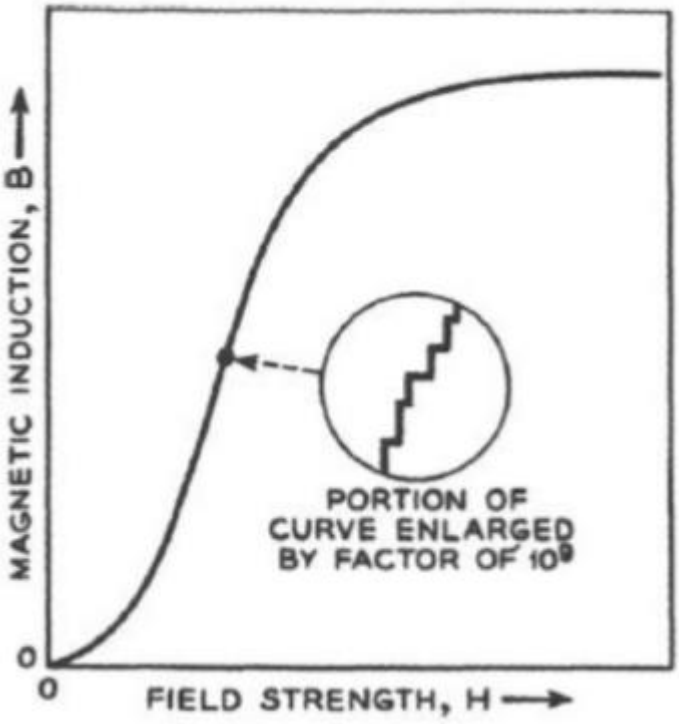

Figure 30. Steps associated with increased magnetisation responsible for MBN [11].

MBN measurement has been shown to be sensitive to numerous microstructural parameters at room temperature such as grain boundaries, dislocation structures and precipitates. These features are known to pin domain walls and so have a large effect on the MBN signal [68-70]. Dual phase steels with varying martensite-ferrite phase balances were assessed using MBN in a study by Ghanei et al. [70]. The MBN peak height

increased with increasing martensite fraction and the peaks shifted to higher magnetic fields with higher martensite fractions (figure 31). The change in peak height and position is caused by the increasing dislocation density associated with higher martensite fractions, as dislocation densities increase so do the number of pinning points, resulting in higher MBN [70].

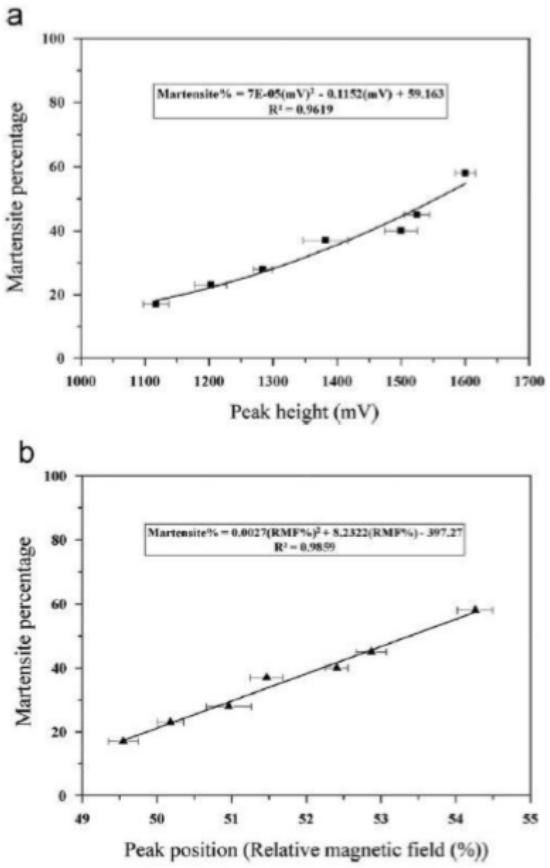

Figure 31. Relationship between MBN peak height (a) and MBN peak position (b) and martensite percentage (%) [70].

MBN has been shown to be sensitive to recovery and recrystallisation in steels [71-73]. A study by Gurruchaga et al. [73] investigated the effect of recovery and recrystallisation on the MBN signal. The results for MBN peak amplitude for different annealing temperatures with time is given in figure 32. From 300℃ - 500℃, MBN increases with annealing time which signals the steel being in recovery. At 575℃ annealing temperature, the MBN decreases with annealing time after 100 seconds as the steel is recrystalising and has a lower dislocation density. Optical microscopy was used to verify that recrystallisation had taken place within the steel [73].

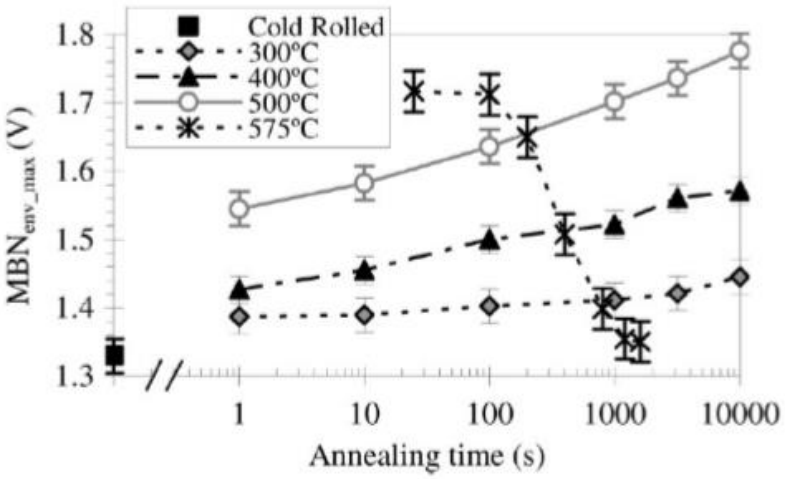

Figure 32. MBN peak amplitude response to annealing times at various temperatures in an extra low carbon steel [73].

MBN has been used to monitor stress phase transformation to martensite induced by plastic deformation in an austenitic 304 grade stainless steel. The steel was subjected to uniaxial tensile strength with different load schedules up to rupture. Figure 33 shows MBN voltage output (mV) for different loads on a 304 specimen. The graphs show that as the load increases the MBN peak becomes more distinguished and increases. This is due to the presence of ferromagnetic martensite as a result of transformation due to plastic deformation with increased load. This shows that MBN is sensitive to martensitic transformations due to plastic deformation in 304 stainless steel [74].

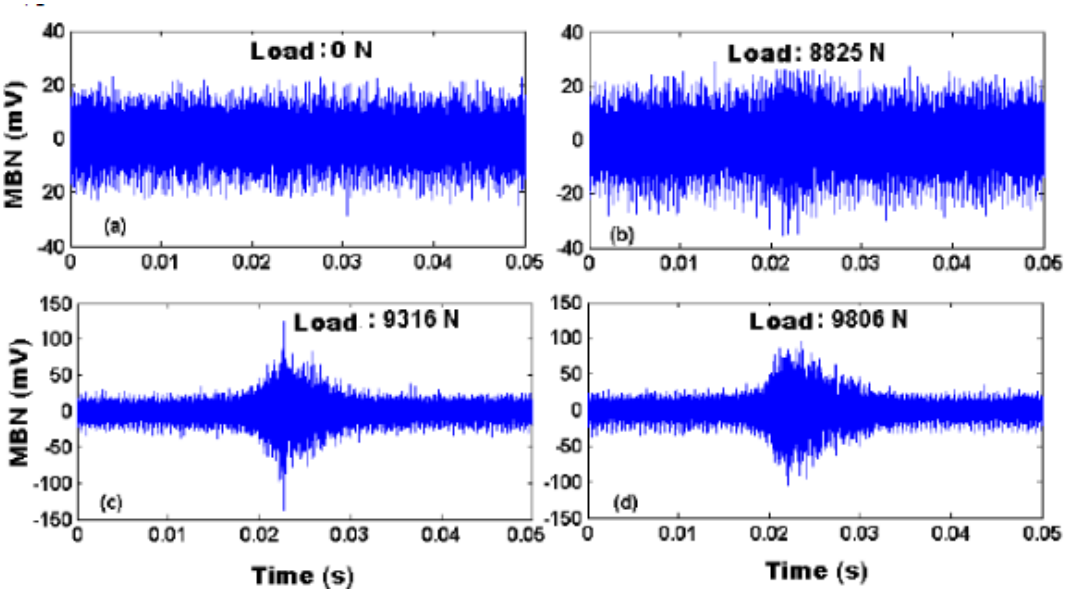

Figure 33. MBN voltage output (mV) for 4 tensile loads (0N, 8825N, 9316N and 9806N) on a 304 austenitic stainless steel [74].

In a study by Huallpa et al. [75], a martensitic transformation of an AISI D2 steel during a quench from 1200°C following annealing, was monitored using MBN. Figure 34 shows the MBN voltage outputs for measurements taken at 4 different temperatures. The increase in MBN at 200K and 77K are caused by the presence of ferromagnetic martensite due to transformation. This study shows that MBN can monitor austenite to martensite transformation during a quench to cryogenic temperatures [75].

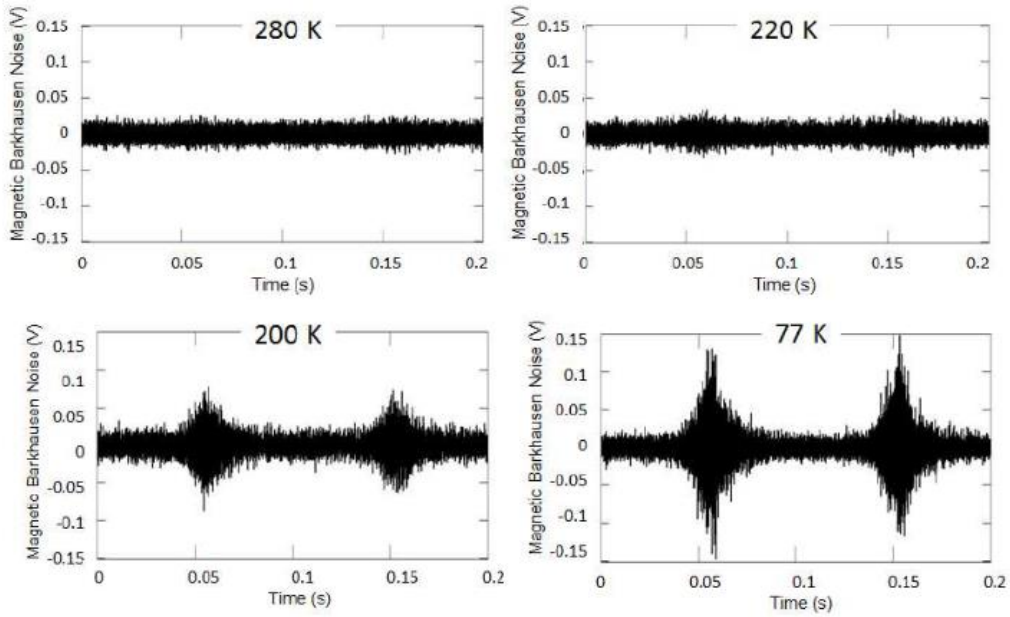

Figure 34. MBN voltage outputs measured at 4 different temperatures during quench of AISI D2 steel [75].

The literature presented has shown that MBN is sensitive to changes in different microstructural parameters, such as recovery and recrystallisation and austenite to martensite transformation.

MBN has some practical disadvantages which make it unsuitable for monitoring phase transformation in a hot strip mill environment. While MBN can be used with a lift off, this needs to be accounted for and best results are generally achieved with contact between the sample and sensor. This means that it cannot be used on a moving surface like that of a steel strip on the ROT of a hot strip mill. MBN measurements are sensitive to changes in lift off. The steel strip passing along a ROT in a hot strip mill does not maintain constant contact with the rollers of the table. Lift off distance between the strip and the sensor would change making MBN measurements inaccurate. Finally, surface preparation is required for measurements so scale would be a big problem for MBN measurements in an industrial setting.

4.3.2 Magnetic Hysteresis Loop Measurement

Magnetic hysteresis (or B-H) loop measurements can be used as a method of characterization of ferromagnetic steel microstructures. Magnetic parameters such as permeability, coercivity, remanence and saturation magnetisation can be used to determine how magnetically hard a ferromagnetic material is. B-H loops parameters can be related to microstructural parameters such as grain size [76], carbon content [27], and dislocation density [77].

Habermehl et al. [78] considered how magnetic hysteresis loops are affected by carbon content in steel. B-H loops for 0.2 wt% and 0.45 wt% carbon steels are shown in figure 35. Carbon content affects the shape of the B-H loops. Magnetic parameters such as remanence and coercivity both change with carbon content. With increasing carbon content, steels are generally harder to magnetise and demagnetise and this is clear from figure 35 [78].

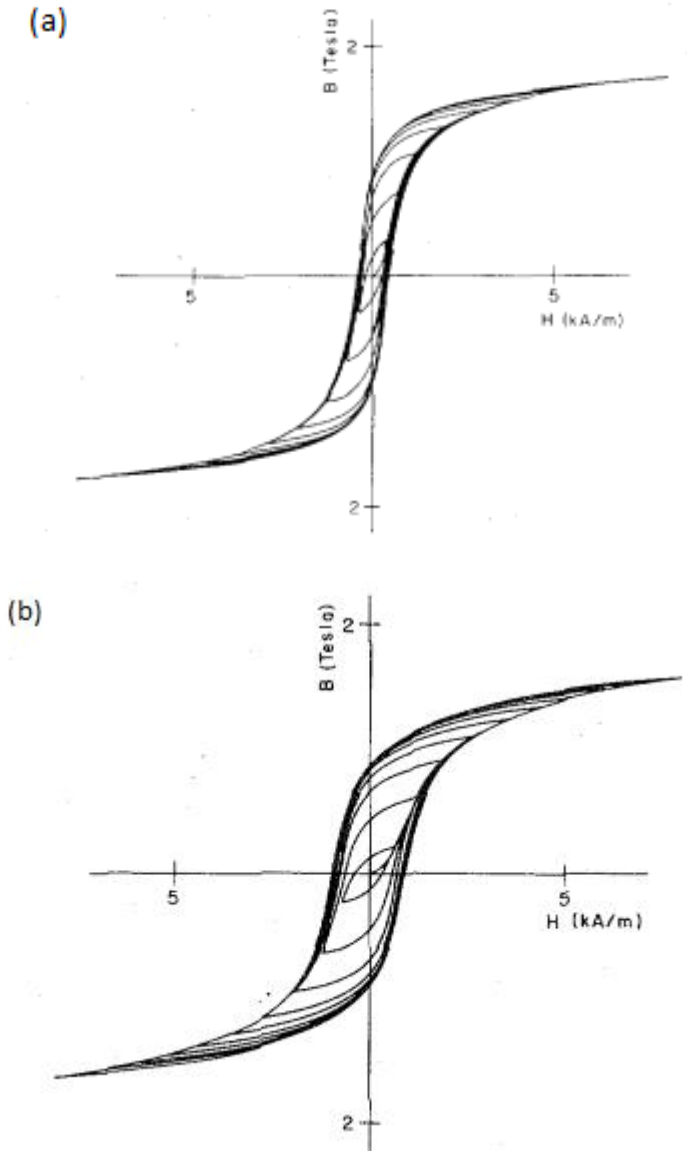

Figure 35. Magnetic hysteresis loops for a 0.2 wt% carbon steel (a) and a 0.45 wt% carbon steel (b) [78].

A study by Gurrachaga et al. [79] investigated the effect of recovery and recrystallisation on coercivity in a low carbon steel. Figure 36 shows coercivity plotted with respect to annealing time for different discreet isothermal annealing temperatures. The results show that coercivity measurements are sensitive to changes in recovery and recrystallisation. At each temperature, coercivity decreases with annealing time, and the rate at which coercivity decreases with time increases with annealing temperature. This is due to recrystallisation happening at a higher temperature than recovery, so the effect on reduction in coercivity is greater [79]. Further studies have also shown the sensitivity of B-H loops to recovery and recrystallisation [80].

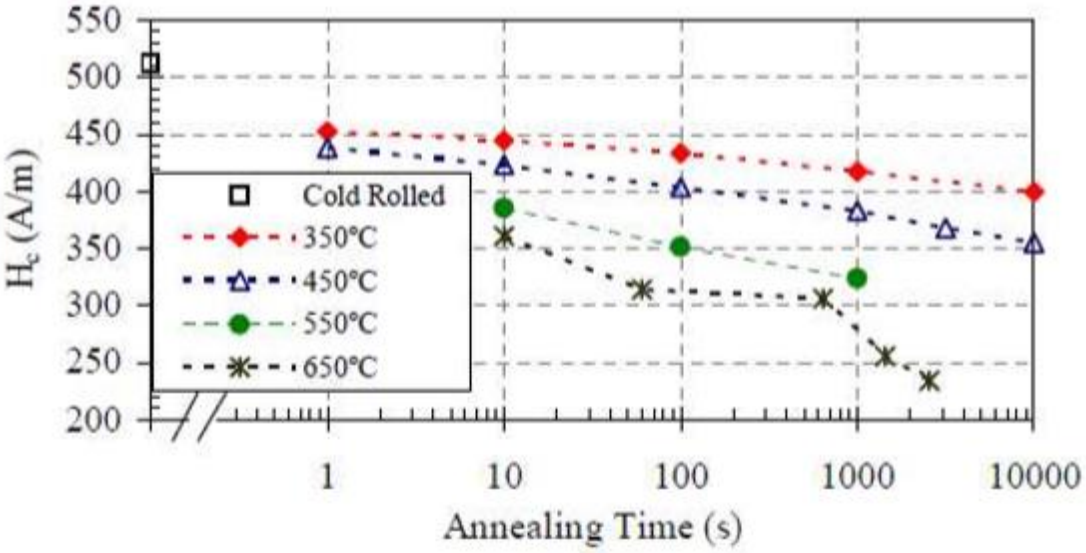

Figure 36. Coercivity (Hc) plotted with respect to annealing time at different annealing temperatures for an IF steel [79].

Numerous studies have been performed to show sensitivity of magnetic hysteresis loops to transformation of metastable austenite to martensite transformations induced by plastic deformation [81-85]. A study by Sort et al. [81] researched the effect of local ferromagnetism on austenitic (paramagnetic) stainless steels using nano-indentation. The B-H loops were obtained for the steel sample after cutting and polishing, annealing at 1127℃ and then cooled to room temperature, after making an array of nano-indentations and finally after dragging the indenter tip with a constant load (figure 37). Ferromagnetic behaviour is observed for the steel after cutting and polishing. This is due to martensite transformation as a result of this. After annealing the sample to transform the martensite back to austenite and then cooling to room temperature, the resulting B-H loop (also in figure 37) shows a linear relationship which is expected for a fully paramagnetic material. The B-H loops in figures 37b and 37c both show ferromagnetic behaviour which is due to the presence of ferromagnetic martensite following plastic deformation by the nano-indenter. The coercivity for the steel sample after nano-indenter array was 150 Oe. This is lower than for figure 37c where the nano-indenter was dragged along the sample at a constant force. This is due to the higher martensite fraction for figure 37c as a larger volume of the steel sample was plastically deformed inducing martensite transformation [81].

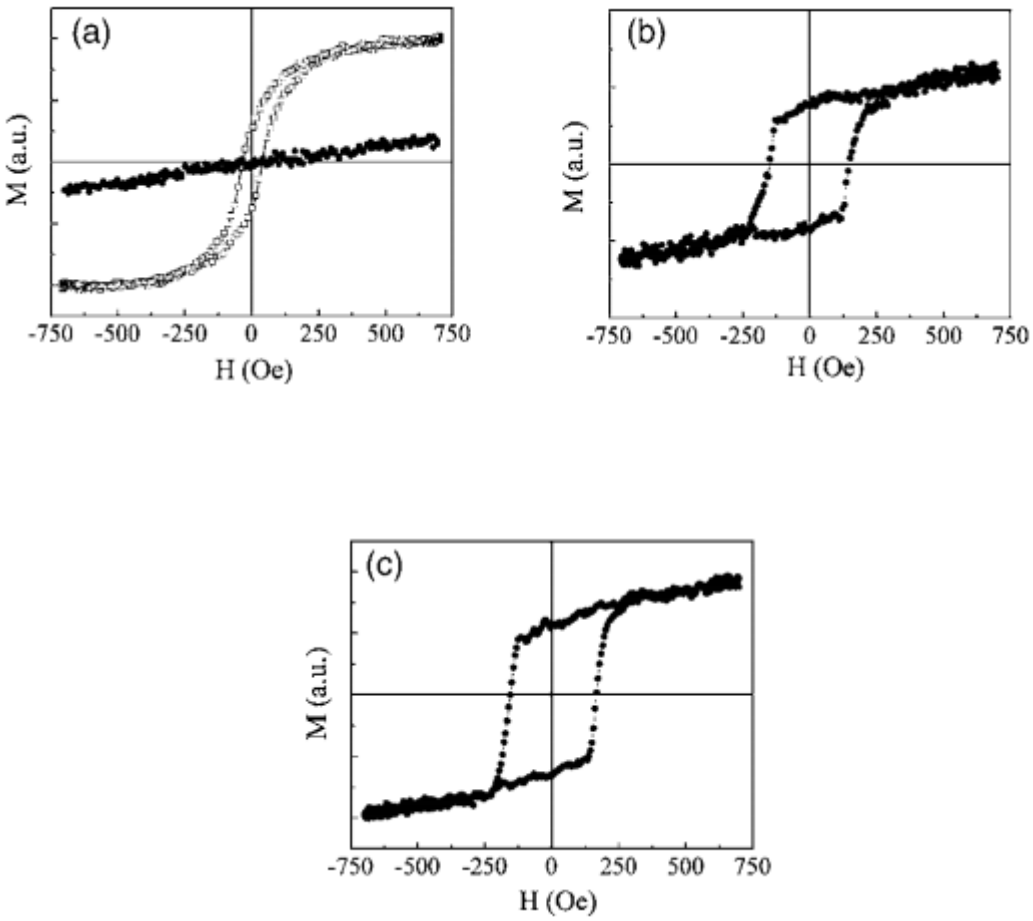

Figure 37. B-H curves for austenitic stainless steel after (a) polishing and cutting (hollow squares) and after annealing at 1127°C for 30 minutes and cooling to room temperature (solid circles) (b) after performing an array of nano indentations with a lateral size of 1µm and (c) after dragging nano-indenter along the steel with a line width of 1.8µm [81].

Magnetic hysteresis loop measurements have been shown to be sensitive to different microstructural parameters such as recrystallisation and phase transformations induced by plastic deformation in metastable austenitic stainless steels. While there is no data in the literature for measuring the phase transformation of steel during annealing processes using B-H loops, there is initial work currently being done by the university of Manchester electromagnetics group to develop a high temperature rig for measuring up to the Curie temperature. For B-H measurements, the sample and pick up coils generally need to be surrounded by the magnetisation coil as well as requiring good surface contact. This provides limitations of the technique when applying this to hot strip mill conditions as the steel will be moving quickly, will also be subject to changes in lift off and is too hot to place coils onto the surface.

4.3.3 Laboratory EM Sensors

EM sensors can be used as a method of non-destructive evaluation of steel microstructure as they are sensitive to changes in relative permeability and resistivity. The relative permeability of a steel is affected by microstructure, composition, temperature and stress. Numerous studies at room temperature have shown that EM sensors are sensitive to microstructural parameters such as grain size [35], pearlite interlamellar spacing [3, 35], phase balance [4, 37, 86-89] and phase type [4, 32, 90]. Sensitivity of EM sensors to decarburization in steels has also been shown in numerous studies both at room temperature and elevated temperatures [91-96].

Laboratory based studies have been performed at high temperatures to monitor recovery and recrystallisation in IF steels [10, 14]. A study by Hall et al. [14] used a cylindrical sensor specially constructed for high temperature measurements to monitor recovery and recrystallisation in an IF steel. IF steel samples were heated to different temperatures below the critical point and held to allow for recovery and recrystallisation to occur. The results for low frequency inductance with time are shown in figure 38. The responses for the two lower temperatures show similar trends and are different to the responses for the higher temperatures. At the lower annealing temperatures, no recrystallisation took place, only recovery. This was verified by microstructural examination. The two higher temperatures again followed a similar trend to each other but different from the lower annealing temperatures because the samples had both recovered and either partially or fully recrystallised and again this was confirmed by further quenched test microstructures [10].

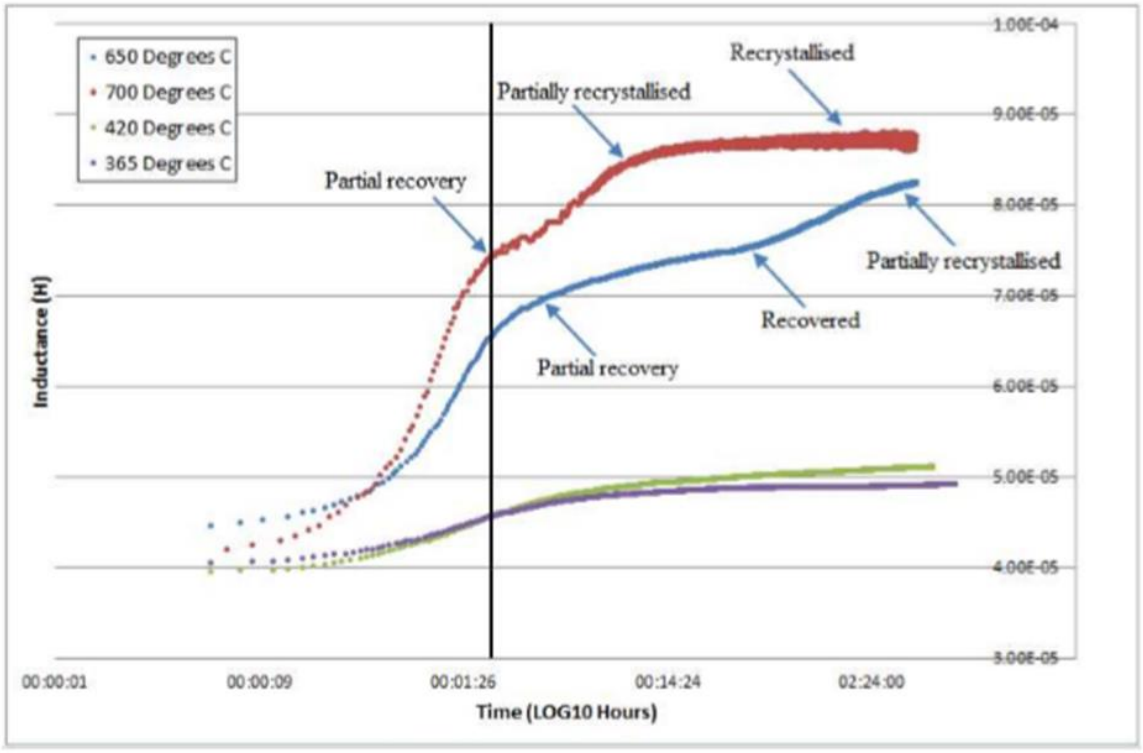

Figure 38. Inductance (H) plotted against time for IF steels at different annealing temperatures (365°C, 420°C, 650°C and 700°C). The arrows mark critical points of recovery and recrystallisation. The black vertical line indicates the end of the heating process, data shown before this shows inductance changes related to changes in temperature [10].

Laboratory based EM sensors have also been used in multiple studies to monitor the phase transformation of steel during cooling from high temperatures [91, 93, 97]. A study by Dickinson et al. [97] developed a multifrequency EM sensor purposed for monitoring the phase transformation of hot strip steel. The system developed contained impedance measuring circuitry and a sensing head which consisted of an H shaped ferrite core. The ferrite core had dimensions of 115mm high, 100mm wide, a 25mm square cross section and had 5 coils; 1 exciting coil and 4 sensing coils. The geometry of the sensing head allowed it to work with a lift off ranging from 10mm-100mm. The sensor was used to monitor strip samples (measuring 137mm×87mm×2mm) of varying carbon content as they cooled from 1000°C. The samples were heated to 1000°C to fully transform the samples to austenite followed by slow cooling. During cooling it was expected that the low, medium and high carbon contents of the samples would drive different phase transformations. This is the initial stages of the work that led to the development of the EMspec® sensor. Figure 39 shows imaginary impedance data from these trials for a low,

medium and high carbon steel [97].

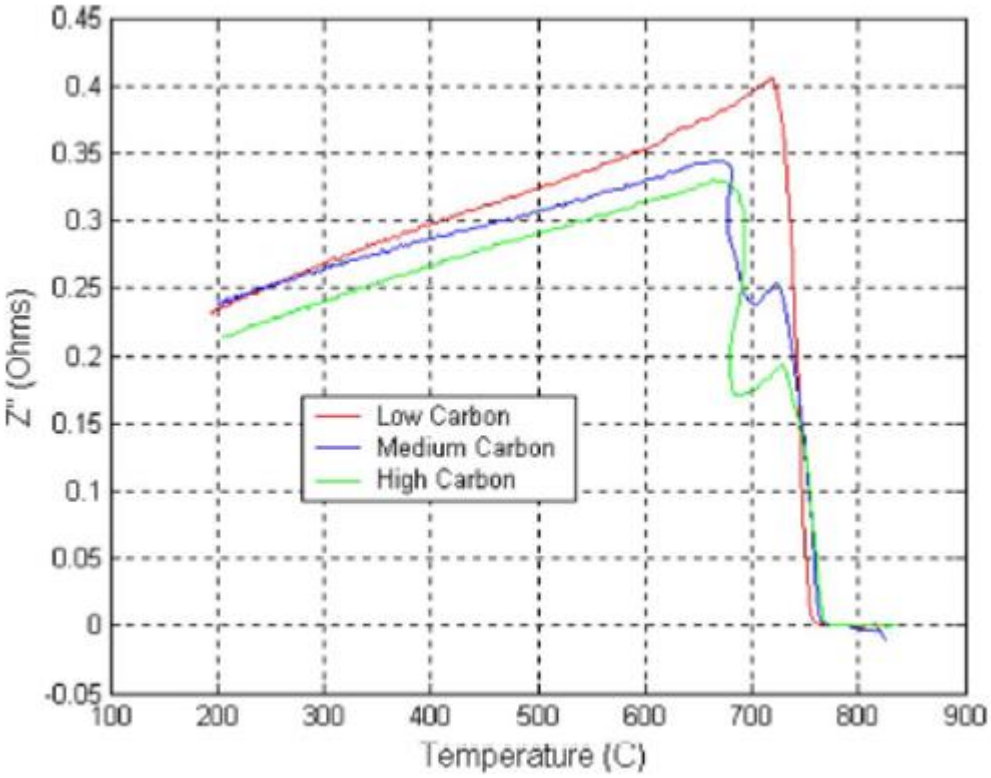

Figure 39. Imaginary impedance at 12.5Hz for a low, medium and high carbon steel during cooling from 1000°C [97].

The Curie temperature (T_c) for these steels is around 770°C (assuming they don't start transforming at a lower temperature. For all samples, the imaginary impedance is zero above approximately 770°C, this is consistent with a paramagnetic austenitic material. At 770°C the imaginary impedance starts to increase rapidly for each sample. For the low carbon steel, the imaginary impedance increases rapidly at approximately 770°C during cooling and reaches a peak value of 0.4 Ω at approximately 720°C, after that the imaginary impedance decreases at a constant rate until measurements stop at 200°C. The response shown for the low carbon steel is consistent with a response for a single-phase ferritic steel.

For the low carbon sample, the graph shows a sharp increase in signal at 770°C (Curie temperature) and this is because with a low carbon content, the sample fully transforms to ferrite above the Curie temperature, then the sensor is just detecting paramagnetic to ferromagnetic transformation at the Curie temperature. The graph shows two transformations for the medium and high carbon steel samples. The first increase in imaginary impedance at 770°C in both samples is due to the ferrite formed above the

Curie temperature becoming ferromagnetic. The second transformation is due to the remaining austenite transforming to pro-eutectoid pearlite due to the samples having a higher carbon content. The high carbon steel was expected to have a lower ferrite and higher pearlite content than the medium steel, and this is shown in their respective changes in impedance; the high carbon steel has a lower change in imaginary impedance at the Curie temperature (lower ferrite content) and a larger change in imaginary impedance at approximately 680ºC (higher pearlite content due to higher carbon content) [97].

4.3.4 Commercially Available Systems

There are several commercially available EM systems that are being used to measure microstructural parameters in industrial or laboratory environments. Each system has benefits and disadvantages, this section provides a summary of the different systems.

4.3.4.1 IMPOC

The Impulse Magnetic Online Controller (IMPOC) has been developed to monitor cold steel strip online. IMPOC relates changes in magnetic properties to mechanical properties such as tensile strength [98]. The IMPOC system is being used in steel plants in various locations such as pickling lines, continuous annealing lines and hot dip galvanising lines. IMPOC systems work by magnetising the steel strip using a pulsed magnetic field and measuring the amount of remanence. The measured residual magnetisation is then correlated to mechanical properties using a mathematical model. IMPOC systems are capable of measuring moving strips up to a speed of 900 m/s. The IMPOC system is sensitive to changes in lift off between the material surface and sensor, this is accounted for by a sensor head on both the top and bottom sides of the strip. A schematic diagram of the IMPOC system measuring a steel strip is shown in figure 40. The system has not been adapted for monitoring the phase transformation of a moving hot strip in a hot strip mill environment. It would be difficult to implement this sensor system in a hot strip mill environment, as the system requires a sensor head both below and above the sensor. Practically it would be difficult due to the changes in lift off that can be experienced by the head and tail of the steel strip, which could cause the steel to impact the part of the

system that sits above the hot strip. Also, the upper sensor could interrupt the cooling of the top surface of the hot strip [98].

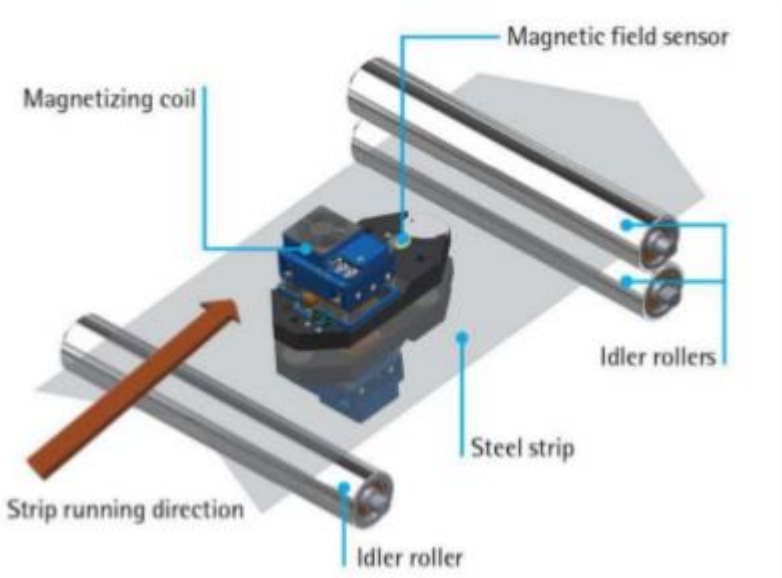

Figure 40. Diagram of IMPOC system measuring a steel strip [98].

4.3.4.2 HACOM

Harmonic Analysis Coil Online Measurement (HACOM) is a type of hysteresis measurement system that has been developed to measure changes in microstructural parameters [98]. HACOM uses sinusoidal magnetisation at relatively low fields at four different frequencies between 20Hz and 5kHz to make measurements. The magnetisation of the sample runs through hysteresis loops; the magnetic hysteresis induces field changes into receiving coils which is analysed using fast a Fourier transform. HACOM provides non-destructive determination of mechanical material properties such as tensile strength and yield strength. The system has been used to monitor cold rolling in three different steels: interstitial free (IF), micro-alloyed (MA) and dual phase (DP). Figure 41 shows that the HACOM signal decreases monotonically with increasing elongation for DP and IF steels [98].

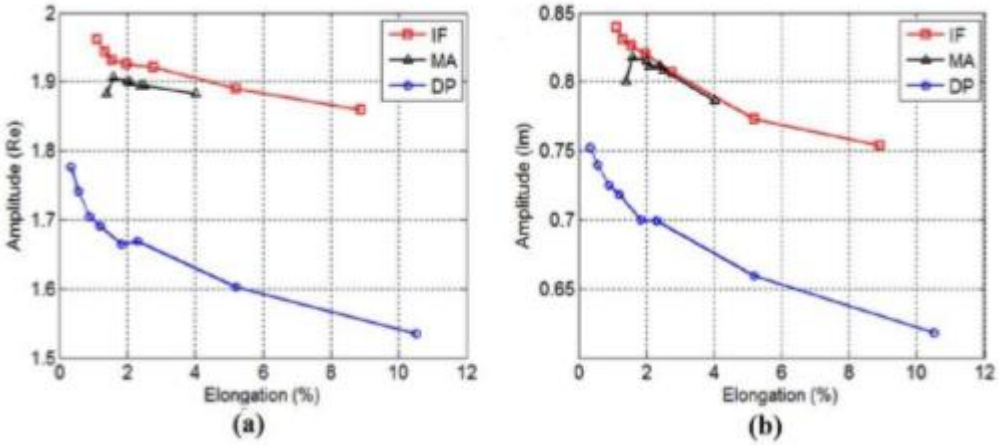

Figure 41. Plots of real (a) and imaginary (b) HACOM system signal with increasing percentage elongation [98].

HACOM is extremely sensitive to external EM noise; in a hot strip mill there are many sources of external EM noise which could lead to errors in HACOM readings. Thus, the HACOM system requires magnetic shielding when deployed online. The system is very sensitive to the residual stress state of the material and lift off. Lift off effects are accounted for by using two sensor heads, one on either side of the steel strip, with the mean value of both sensors used as the measurement value. This would make it very difficult to install in an industrial environment such as a hot strip mill ROT due to the disruption of other equipment required for this. It could be installed at the end of the ROT where there is more room, however, in practice, the changes in lift off experienced by the head and tail of the steel strip could cause the hot steel to impact the upper part of the system [98].

4.3.4.3 EMspec® Sensor System

EMspec® sensor technology has been installed on the ROT of the TATA hot strip mill in IJmuiden. Three EMspec® sensors have been installed between the rollers at different points of the ROT. Having multiple sensors in the ROT allows phase transformation to be monitored as the strip cools along the line [6, 8, 43]. The EMspec® sensors measures

phase angle and ZCF, which is less sensitive to lift off and allows the sensors to operate at a 40mm lift off [45]. EMspec® sensor measurements are unaffected by environmental factors such as water, steam and dust.

EMspec® sensors are not limited in position on the ROT unlike the laser ultrasonics system in the study by Hutchinson et al. [66], where the laser ultrasonic equipment had to be positioned after the water cooling banks so most of the scale had been cleaned from the steel and the laser had a clear line of sight to the target [66]. A previous iteration was trialled at a rod and bar mill and was able to successfully measure the phase transformation [7]. An external and similar in-house EM system has been developed by Arcelor Mittal and was able to detect and monitor the phase transformation of steel in a hot strip mill. Here, the sensor measurements were successfully used to detect the phase transformation of the hot strip moving along the ROT. They were also able to use the system to optimize the cooling process and improve microstructural uniformity along the length of the strip [9, 99]. There have been no further developments on this sensor system in the literature.

The EMspec® sensors installed in the IJmuiden hot strip mill have been used to measure austenite to ferrite transformation and phase balance [43]. The next stage in development is to have a robust full quantitative and predictive approach to relate the signals to transformed fraction, with validation. An EMspec® sensor of identical design to the sensor heads used on the ROT of the hot strip mill in IJmuiden, has been installed into Warwick Manufacturing Group's bespoke laboratory furnace and ROT (described in chapter 5). The laboratory furnace and ROT was built to simulate the conditions of an industrial hot strip mill ROT on a laboratory scale. It enables continuous EMspec® sensor measurement of reheated steel plates as they cool from up to 1100^{o}C. The laboratory furnace and ROT is capable of different cooling rates such as cooling in ambient air, forced air or water jet cooling.

4.4 EM Modelling

Measured EM signals are affected by the physical, magnetic and electrical properties of the samples being measured. To fully understand the measured signals in relation to the magnetic properties of the measured sample, modelling is used to consider the effects of

the different parameters and their significance. FEMs have been developed for different EM sensors, including the EMspec® sensor. This section will review the modelling work that has been completed.

A study by Zhou et al [4, 35]. investigated the effect of phase fraction and second phase distribution on the low field relative permeability. A 3D FEM of the magnetic flux distribution through ferrite-austenite and ferrite-pearlite microstructures was developed and is shown in figure 42. It is shown in the modelled results that 30% ferrite in a pearlite matrix had a higher permeability than for 30% ferrite in an austenite matrix. This is because the flux lines can pass through the ferromagnetic pearlitic regions when the ferrite grains are isolated. However, for the 30% ferrite in austenite, the flux lines cannot pass through the austenite regions when the ferrite grains are isolated, as they are paramagnetic. This results in a lower permeability at low ferrite fractions for ferrite austenite microstructures compared to ferrite pearlite [4, 35]. This is important in context to the work in this thesis, as this give an idea of how the magnetic flux will behave when the steel is transforming and has a low ferrite fraction.

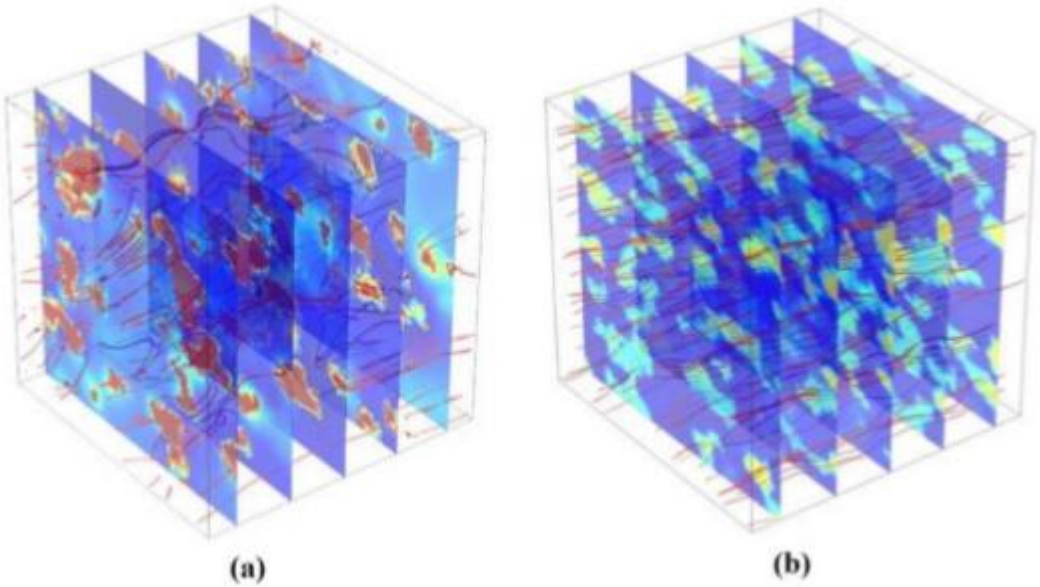

Figure 42. Modelled flux distribution though a ferrite-austenite microstructure with 30 % ferrite (a) and a ferrite-pearlite microstructure with 30 % ferrite (b) [4, 35].

A study by Jolfaei et al. [100, 101] used an EM sensor and 3D FE model of the sensor (shown in figure 43) to explore the relationship between relative permeability and

microstructure to predict tensile strength in dual phase steels of different thicknesses. It was found that the measured relative permeability was strongly related to the ferrite-martensite phase balance, with permeability increasing with greater ferrite fractions. Figure 44 shows calibration curves developed as part of the study for different strength dual phase steel samples and thicknesses. The calibration curves relate the modelled real inductance (mH) to low field relative permeability, the data points show physical EM sensor measurement values taken to validate the modelled curves. With this validated calibration curve, the measured EM signal of a given dual phase steel sheet at any thickness ranging from 1-4mm is related to permeability, and therefore the tensile strength can be estimated [100. 101].

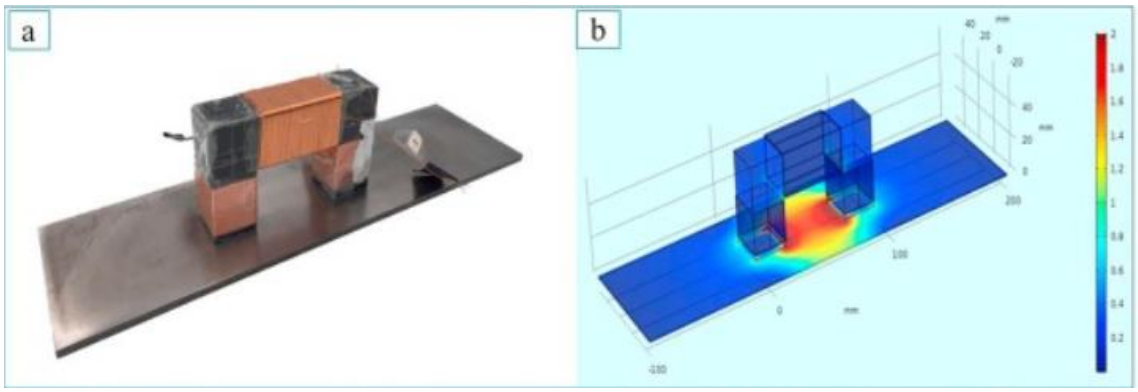

Figure 43. U-shaped EM sensor on a steel sample (a) and the 3D FE model of the same sensor and steel strip (b) The colours represent the modelled magnetic flux intensity [100].

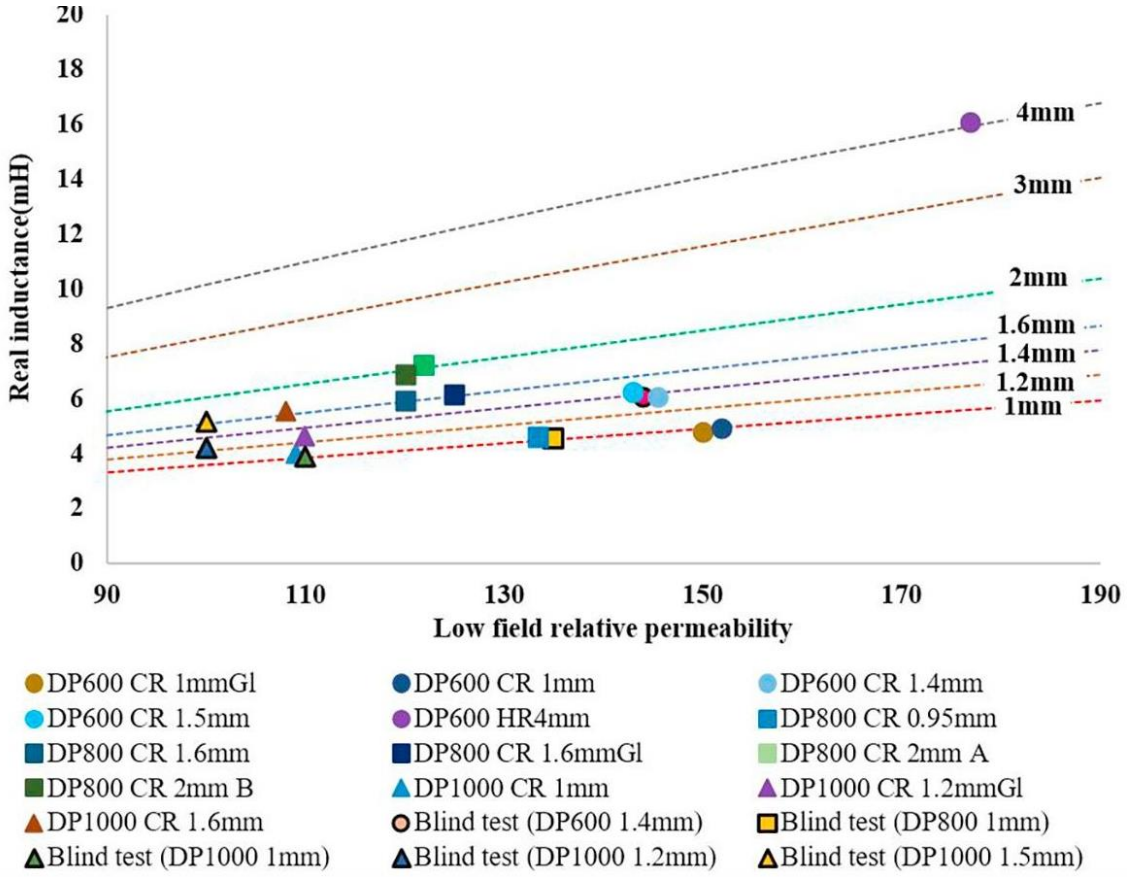

Figure 44. Calibration curves relating low frequency (10 Hz) real inductance with permeability for different thickness samples. The dashed lines represent modelling results (for 1 mm–4 mm strip thickness) and experimental data for commercial DP samples of different thicknesses are indicated by different points [100].

An EM sensor system for detecting the phase transformation during cooling on the ROT of a hot strip mill was modelled using Maxwell 3D and is shown in figure 45. Parameters including signal amplitude, phase angle and the effect of surrounding structures such as the rollers (shown in figure 45) were studied to optimise the real life set up and procedure. Figure 46 shows modelled ZCF as a function of relative permeability. It can be clearly seen that ZCF is directly proportional to relative permeability [45].

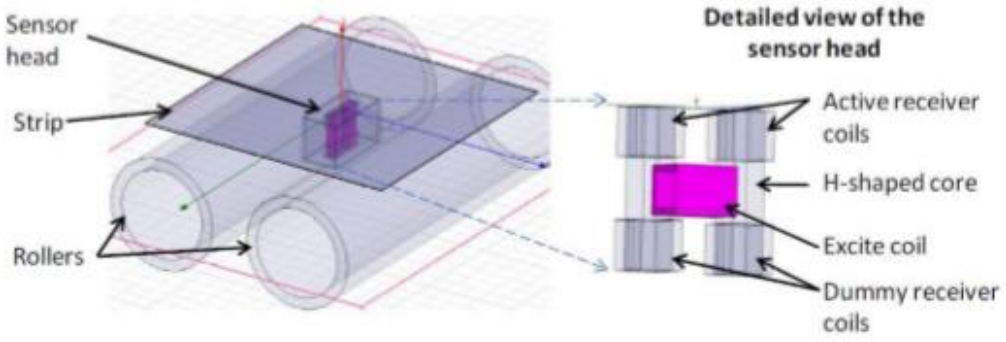

Figure 45. Model of an H shaped EM sensor between rollers with a steel strip sample above the sensor. The model was built to show effect of rollers on the EM signal while measuring a steel [45].

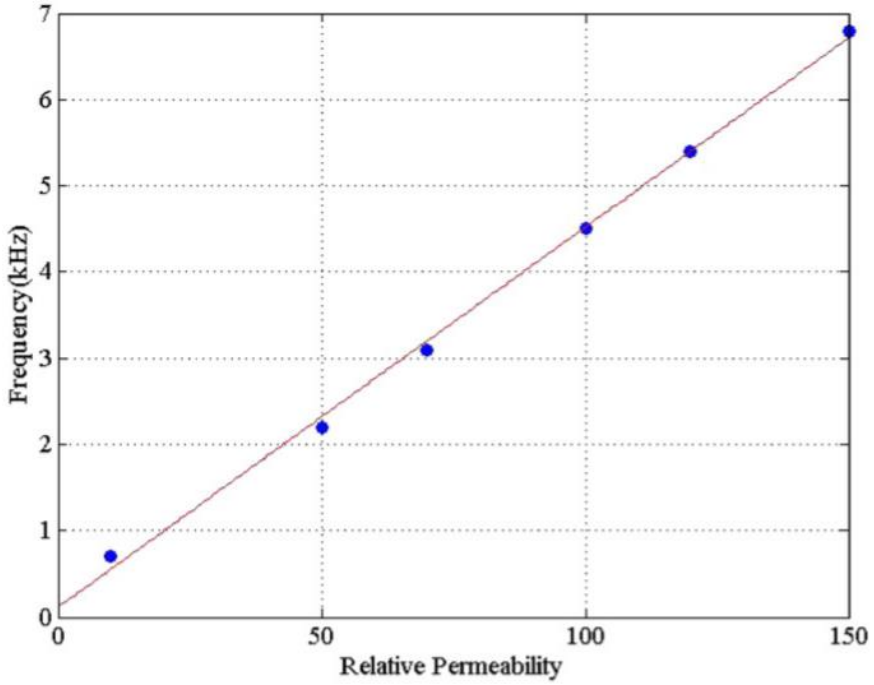

Figure 46. Modelled ZCF as a function of relative permeability [45].

4.5 Summary

This chapter has discussed different non-destructive techniques and their associated signals that can be related to the microstructure of steel. The different strengths and weaknesses of each technique have been considered.

It has been shown that X-Ray diffraction measurements can be related to changes in microstructural parameters. However, the need for a direct line of sight to the measurement target makes it difficult to apply this technique in an industrial environment due to environmental and processing factors such as dust, steam and water and oxides. Further to this, the associated health and safety risks associated with X-Rays makes it an expensive and impractical solution.

Ultrasonic techniques have been shown to be sensitive to changes in microstructural factors such as grain size, dislocation density and phase change. The laser ultrasonic technique can operate at a significant standoff distance, however the need for a clear line of sight to the target material for reliable measurements is limiting for this technique when it comes hot strip mill conditions. This was shown in the study by Hutchinson et al. [66], where the ultrasonic sensor was only able to be placed at the end of the ROT after cooling, so the water had washed away most of or all the scale.

There is very little in the literature that shows the ability of MBN to monitor the phase transformation. MBN is unsuitable for monitoring the phase transformation in hot strip mill conditions because it is difficult to be used on a moving surface. MBN is very sensitive to changes in lift off; strips of steel are not completely flat as they pass along the ROT causing changing amounts of lift-off. Accurate measurements with MBN require a smooth surface finish and surface contact further increasing its impracticality as a measurement technique in a hot strip mill environment.

Whilst there is currently initial development of a high temperature B-H loop measurement rig designed to go above the Curie temperature at the university of Manchester, this type of set up would not be able to be applied to measuring the phase transformation of strip steel online in a hot strip mill. While HACOM and IMPOC are techniques that measure B-H curves, they have not been adapted to measuring in a hot strip mill environment and are currently only used for cold strip. IMPOC and HACOM have been used in cold strip mills for correlation of measurements to mechanical properties. Neither technique has been adapted monitoring of phase transformation in hot strip mill environments. While they could be adapted, it would be difficult in practice as the upper sensor head of both systems could be impacted by the hot steel due to changes in lift off experienced by the head and tail of the strip.

EM sensors have been shown to be sensitive to microstructural parameters such as pearlite interlamellar spacing, grain size and phase balance at room temperature. They have also been able to detect the phase transformation (from austenite to ferrite) of strip online in a hot strip mill.

The EMspec® sensor system has been used to measure magnetic parameters related to austenite-ferrite phase transformation at different points on a hot strip mill ROT. EMspec® sensor measurements have been shown to be unaffected by environmental factors such as water, dust and steam. This project develops that work to investigate the relationship between the EMspec sensor signal (ZCF) and phase fraction transformed. This study aims to monitor the full transformation of a range of steels during dynamic cooling and to quantitatively relate the ZCF to phase fraction transformed.

5. Materials and Experimental Procedure

5.1 Materials

5.1.1 Materials for Edge Effect and Lift off Testing

A range of dual phase (DP) and interstitial free (IF) strip steel sheets, supplied by Tata Steel Europe in a hot rolled condition, were used for testing the effect of non-microstructural parameters (edge effect and lift off) on the signal of the EMspec® sensor. The DP samples all had dimensions of 500 mm × 500 mm and had a thickness of 3.64 mm whereas the IF samples used had dimensions of 500 mm × 470 mm and had a thickness of 3 mm. Although multiple DP and IF samples were used in this section of experiments, they were all cut from the same coil and therefore have the same chemical composition. The compositions of the IF and the DP steels are given in table 2 and table 3 respectively.

Table 2. IF steel chemical composition in wt%.

C	Mn	Al	Cu	Ti	N
0.002	0.219	0.035	0.023	0.067	0.0088

Table 3. DP steel chemical composition in wt%.

C	Mn	P	S	Si	Al	Cu	Cr	Ni	N
0.078	1.35	0.044	0.002	0.045	0.044	0.012	0.458	0.018	0.004

5.1.2 Materials for EMspec® Sensor Testing on ROT and Furnace System

A range of carbon steels, a duplex steel and a 2.25Cr-1Mo steel were sourced for testing on the ROT and furnace system using the EMspec® industrial sensor. The thicknesses of the samples ranged from 3 to 10mm. Chemical compositions for these samples were either obtained using a combination of omission electron spectroscopy (OES) and carbon sulphur analyser or provided by the supplier. The chemical compositions for the steels in wt%, are shown in table 4.

Table 4. Dimensions and chemical compositions of steels used for ROT and furnace system in wt%.

Steel Type	**Dimensions (mm)**	**Thickness (mm)**	**C**	**Si**	**Mn**	**P**	**S**	**Cr**	**Mo**	**Ni**
Mild	500 × 500	3	0.16	0.01	0.81	0.007	0.003	0.018	0.0025	0.007
Mild	500 × 500	6	0.17	0.035	0.83	0.015	0.009	0.033	0.0018	0.013
Mild	500 × 500	10	0.18	0.009	0.87	0.015	0.012	0.015	0.001	0.003
Medium Carbon	500 × 500	10	0.5	0.04	0.9	0.03	0.035	0.4	0.001	0.4
High Carbon	415 × 460	3	0.76	0.197	0.72	0.007	0.0005	0.166	0.016	0.067
Duplex Stainless	500 × 500	6	0.03	0.33	1.63	0.022	0.0005	23.2	2.89	5.54
Cr-Mo	500 × 500	3	0.11	0.29	0.58	0.013	0.002	2.12	0.94	0.06
Cr-Mo	500 × 500	6	0.11	0.29	0.58	0.013	0.002	2.12	0.94	0.06

5.2 Sample Preparation, Microscopy and Image Analysis

In preparation for optical microscopy, sectioned samples were cut and mounted in non-conductive phenocure, such that the exposed surface for polishing was through thickness with the rolling direction. The sample was then ground and polished to an OPS finish and etched with 2% nital. A Nikon Eclipse LV150N optical microscope was then used to obtain optical micrographs for each sample for microstructural characterization. Micrographs were used in Image J image analysis software to measure second phase fraction and ferrite grain size. 5 micrographs per sample were measured and an average and standard deviation calculated for second phase fraction.

5.3 Resistivity Measurements

5.3.1 Room Temperature

To obtain the electrical resistivity of a sample, a Cropico DO5000 microhommeter was used to measure the resistance of a small strip sample (100 mm × 10 mm × the sample thickness) using the 4-point probe method. 5 measurements of resistance were carried out per sample and then the resistivity for each of these was calculated (equation 19) from the equation for the relationship between resistance and resistivity [13].

$$R = \frac{\rho L}{A} \qquad \text{Equation 19}$$

Where R is the resistance, ρ is the resistivity, L is the length between the voltage sensing terminals, and A is the cross-sectional area of the sample. The 5 values for resistivity were used to calculate an average and standard deviation.

5.3.2 High Temperature

A gleeble 3500 system with a resistance module at the university of Birmingham was used for high temperature resistivity measurements. The resistance module also uses the 4-point probe method. A strip sample with dimensions of (150mm × 10mm × 3mm) was secured using the gleeble grips. Temperature was measured using a K-type thermocouple. The sample was then heated up in 50℃ steps which each took 100 seconds. At each 50℃ intervals, the temperature was held for 40 seconds while the resistance measurements were performed, and an average taken. This was repeated until 800℃. Resistance measurements at each temperature interval were converted to resistivity using equation 19 and a standard deviation was taken.

5.4 Dilatometry

A DIL805A/D dilatometer was used for measuring the transformation behaviour of the samples in table 4. The sample sizes used were 5mm × sample thickness × 10mm. The cooling thermal cycle in the dilatometer was programmed to reproduce the cooling trajectory measured for the 500 x 500 mm samples on the ROT in order to determine the phase fraction with temperature during transformation. This information was then used to see how EMspec® sensor ZCF value varied with phase fraction during transformation. Samples were heated to 980℃ in 5 minutes. Samples were then held at temperature for 5 minutes. For sample cooling, the cooling rate for that specific steel type when a larger sample had been measured on the ROT was used. Linear steps at 50℃ intervals were programmed to mimic the ROT cooling rates as closely as possible. Once the sample had passed transformation, the dilatometer was programmed to cool linearly as at this point the cooling rate would have no effect on transformation. Analysis of the length change data was then performed. An example of sample length change with temperature during the cooling cycle is shown in figure 47. The data analysis method used to obtain transformation fraction is also shown in the figure 47.

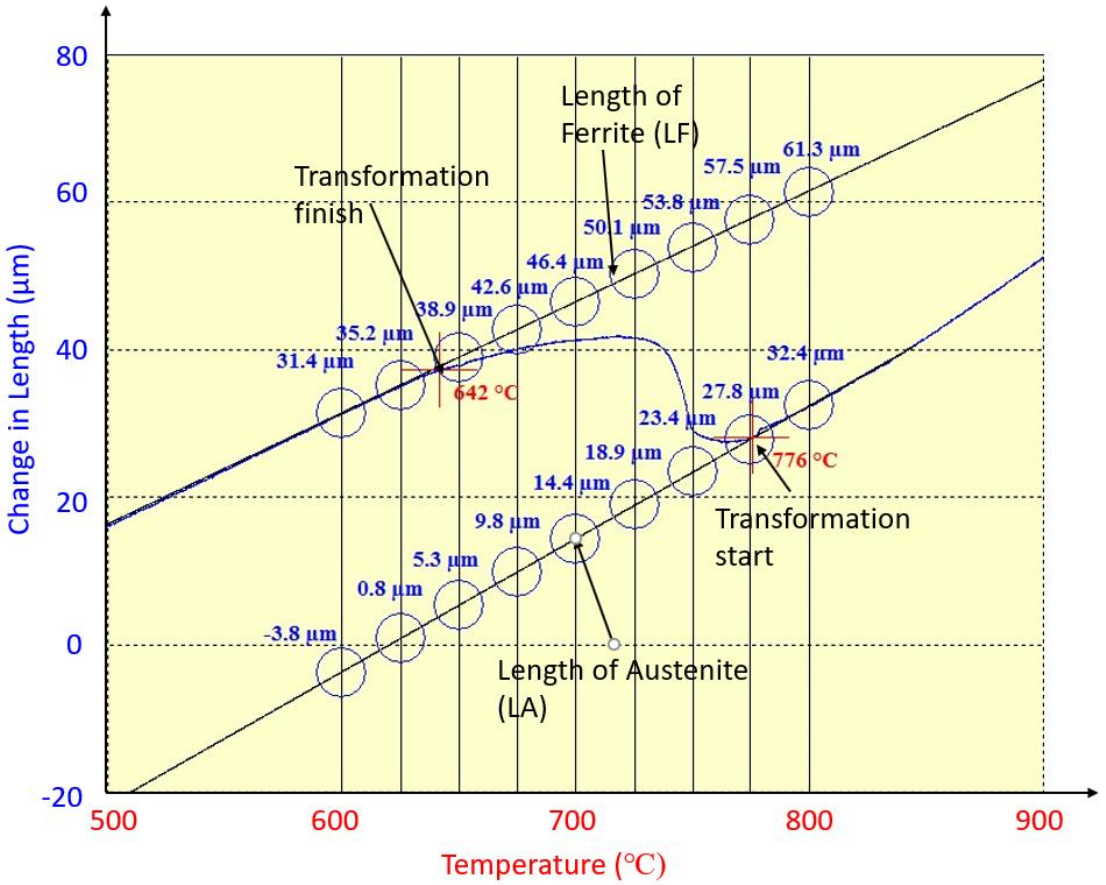

Figure 47. Change in length with temperature during cooling cycle for 6mm mild steel. Transformation start and finish temperatures are marked and shown in red. Tangent lines (black straight lines) drawn against the measured data (blue line) for transformed fraction calculation. Values on the tangent lines are change in length values (from initial room temperature value).

The measured data in figure 47 shows that the change in length decreases with decreasing temperature between 900°C and 776°C. At this point the steel is fully austenitic (FCC) and the gradient relates to the thermal expansivity of austenite. At 776°C, the gradient for change in length alters due to the austenite starting to transform to ferrite. As ferrite is BCC it has a higher volume than FCC, the sample increases in length as transformation progresses. The transformation start temperature was obtained by drawing a tangent line (LA) to the measured data before the gradient change. The point at which the measured data deviates from the tangent line is marked as the transformation start temperature and this is shown in figure 47. Towards the end of transformation, the change in length data starts to decrease with temperature, and once the steel has fully transformed, the sample decreases in length with decreasing temperature with a linear gradient, related to the thermal expansivity of ferrite. The transformation finish temperature was obtained in the same way it was for transformation start. A tangent line (LF) was drawn against the

measured data after transformation. The point at which the measured data deviates from the final gradient and tangent line is the transformation finish temperature and this is marked in figure 47. Figure 47 shows the length change values determined at 25°C intervals along the LA and LF tangent lines. These values were used as part of a Lever rule calculation (equation 20) along with the measured length change values (LAM) to calculate transformed phase fraction at 25°C intervals during transformation.

$$\boldsymbol{Phase\ Fraction} = \frac{(\boldsymbol{LAM - LA})}{(\boldsymbol{LF - LA})} \qquad \text{Equation 20}$$

Three dilatometry tests were performed per steel and standard deviation values determined for phase fraction with temperature.

5.5 EM Sensor Measurement

5.5.1 Lab Based U-Shaped Sensor

A ferrite cored, U-shaped sensor that was developed in a parallel project has been used, along with a COMSOL model for the sensor – sample geometry [100], to determine the as received permeability for the set of steel samples used in this project (table 4). The U-shaped sensor consists of a U-shaped ferrite core and has a generating coil with 100 turns of 0.20mm copper wire, and 2 sensing coils with 86 turns each of 0.16mm insulated copper wire. The core consists of a bridge of 100mm, leg lengths of 56mm and leg thickness of 25mm. A photo of the sensor is shown in figure 48.

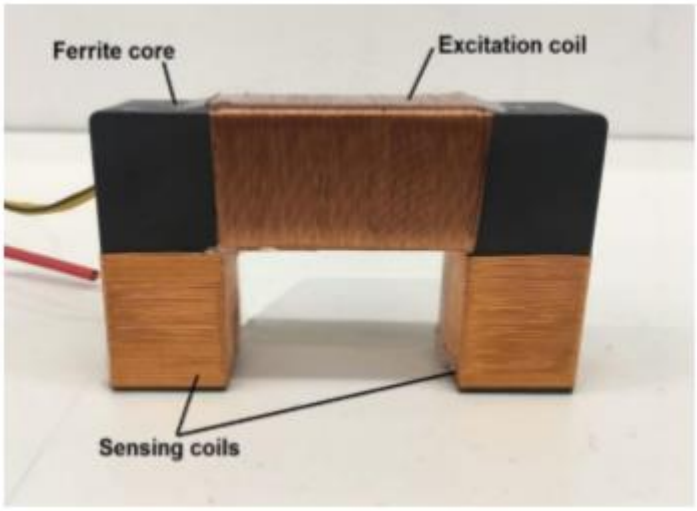

Figure 48. U shaped sensor with bridge =100mm, legs= 56mm and thickness of 25mm. The sensor consists of an exciting coil with 100 turns, and 2 sensing coils each with 86 turns [100].

The U-shaped EM sensor's exciting coil was driven using a Solartron 1260 impedance analyser with a voltage of 3V and swept from 1-65000 Hz. The exciting coil magnetises the target sample while the sensing coils detect changes in EMF as a result of the alternating magnetic field being in the presence of a steel sample. Room temperature measurements were performed on the steels in table 4 for prediction of room temperature permeability. 8 measurements were performed per sample (4 transverse and 4 with rolling direction). The real inductance with frequency for each measurement was obtained and a standard deviation taken. Low frequency (approx. 10 Hz) real inductance was used in a model developed for the sensor (described in [101]) to predict room temperature permeability for the samples measured. It should be noted that the sensor and model had been validated (from independent measurements) for samples of known permeability. The low frequency inductance values are dominated by the permeability of the steel as the eddy current effect is minimal at low frequencies, so the effect of resistivity is not seen here. This is observed as the plateau region at low frequency and can be seen in figure 21 in chapter 3. The errors in these measurements are a combination of the errors on the solartron 1260 (± 0.1%) and repeatability error.

5.5.2 EMspec® Sensor Measurements

The EMspec® industrial sensor used for this project was provided by Primetals Technologies Ltd. The sensor consists of an H shaped ferrite core with an exciting coil and two sensing coils (one dummy and one active). A schematic of the sensor is shown in figure 49.

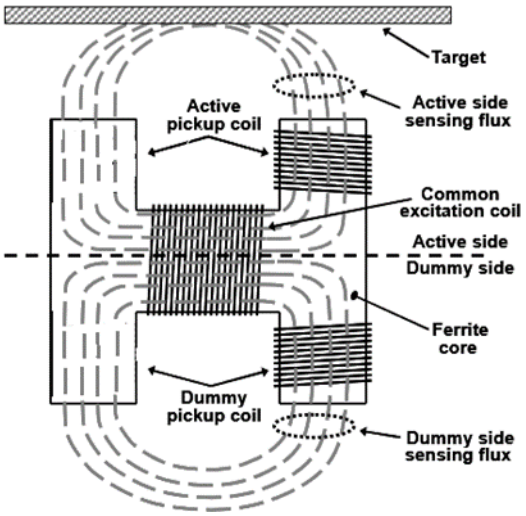

Figure 49. Schematic of EMspec® industrial H shaped sensor measuring a steel target [7].

The sensor has dimensions of 103mm (height) × 153mm (distance between outer edges of both sensor feet) × 25mm (depth) and is the same as the sensors currently used online on the ROT in the hot strip mill in IJmuiden steel works [8, 43]. The sensor is mounted in a martensitic stainless-steel container, which provides magnetic shielding from sources of external magnetic noise factors such as moving rollers or electric motors. The sensor and container are further mounted in an environmental housing enabling it to survive harsh ROT conditions (high temperatures, steam and water). While the sensor is running, water flows through the environmental housing, keeping the sensor at ambient temperatures regardless of the temperature of the surrounding environment.

The sensor operates at 40mm lift off (distance between the ferrite core and steel strip). The sensor and housing are designed to be mounted between the rollers on a ROT to monitor the steel moving along the ROT. The sensor head is connected to a multi-frequency impedance analyser and requires three programs to run simultaneously whilst in use:

- Multi-Frequency Impedance Analysis (MFIA) or Head Controller EMspec® - This program controls the sensor configuration parameters such as calibration and power settings. The sensor requires calibration before each use, described later in this section.
- Data Server DJX – This is a server application which interprets and processes the impedance data from the sensor. ZCF is calculated in this application.
- Sprite Data Logger – This programme logs and saves the data recorded by the sensor.

The sensor runs simultaneously at 8 frequencies ranging from 0.375 kHz to 48 kHz. The voltages at these frequencies are set up automatically by the MFIA software to optimize the sensor output at each frequency without exceeding the capabilities of the system.

The sensor must be calibrated before it can be used in laboratory applications, to ensure that measurements are consistent. The calibration process is as follows:

1. The voltages of the active and dummy coils are subtracted from one another with no target material present. The voltage difference will not be zero due to the influence of the canister.

2. A matching opposite voltage value is applied to the sensor to cancel out the effects of the canister.

3. A digital signal processor is used to calculate impedance, if there is any residual impedance then the calibration process (to this point in the process) has not worked sufficiently and must be repeated.

4. A ceramic ferrite (high permeability, low conductivity) calibration sample is placed over the sensor and measured. The impedance values for the ceramic ferrite are used to set the upper impedance and zero phase angle values.

When testing the sensor for edge effect, a 500 mm square, 3.64mm thick DP sample was placed over the sensor such that it was in the middle of the sample. The sample was then moved at 10 mm intervals in both the X and Y direction until the sensor was close to the sample edge. An EM measurement was taken for 6-8 seconds 3 times at each interval and the ZCF and standard deviation was calculated. Guidelines were drawn on the sample to aid with moving. The point at which the ZCF increased significantly (>50Hz) was defined to be when the edge effect was affecting the signal significantly. This value of 50 Hz was

deemed to be significant as this is approximately the deviation in signal seen when measuring multiple DP samples cut from the same. The X and Y direction for edge effect testing is shown later in this chapter in figure 51. The distance between the sensor and the sample edge is defined as the distance between the outer edges of the sensor foot and the sample edge. Edge effect tests were performed at 40mm lift off

When testing the sensor for dependence on lift off, the sample was placed over the sensor so that the sensor feet were situated in the middle. Increasing lift off was provided by approximately 8 mm thick plywood blocks, being placed over the sensor. A measurement at each lift off was carried out 3 times each for 6-8 seconds and an average ZCF and standard deviation was calculated.

5.5.2.1 Effect of ROT Surrounding Structure on the EMspec® Signal

The laboratory furnace and ROT is primarily made of steel parts. It was anticipated that the ROT structure could have influenced the EMspec® measurements. It was important to make sure that any effects of the ROT structure were understood.

Experiments were completed with the EMspec® out of the ROT, in free space. The samples presented in table 4, except for the 10mm mild steel samples, were all measured individually above the EMspec® sensor in free space out of the ROT. Three measurements were taken for sample over a period of 10s. The samples were measured with the same lift off (40mm) in the as received condition. The data from these tests was recorded.

The EMspec® sensor was then installed into the ROT and the tests were repeated. The data from both sets of experiments was then compared for each sample using average and standard deviation values.

5.5.2.2 High Temperature EMspec® Measurements using the ROT and Furnace System

As previously mentioned, an EMspec® industrial sensor has been integrated into a bespoke system consisting of a ROT and a furnace, purposely designed and constructed with the aim of being able to monitor steel samples at high temperatures using an

industrial EMspec® sensor. A photograph of the ROT and the sensor integrated between the rollers is shown in figure 50.

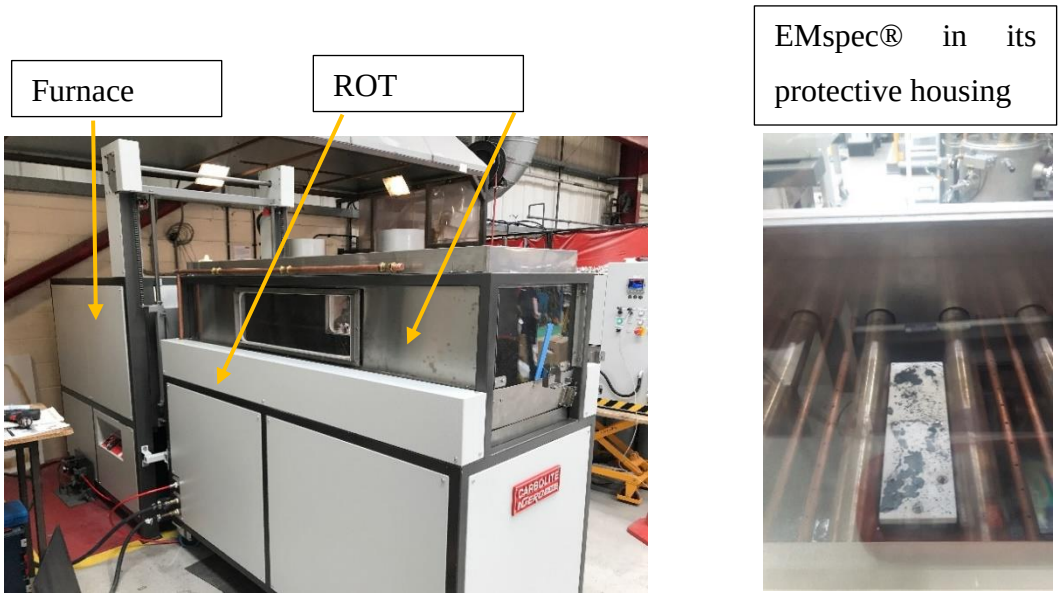

(a) (b)

Figure 50. (a) Picture of ROT and furnace system and (b) EMspec® integrated between the ROT rollers in its protective housing.

The ROT and furnace system is an automated system and consists of powered rollers both in the ROT and in the furnace to allow easy transition of the steel sample to and from the furnace and then over the sensor when cooling. The rollers in the ROT are made from 304 stainless steel while the rollers in the furnace are made from silicon carbide to be able to survive the high temperatures. The system is capable of forced air cooling and water quenching steel samples when cooling in the ROT. The system has a control panel which allows the user to perform necessary procedures when in use. The control panel has a load and unload function, which automatically rolls a steel sample to the back of the furnace and unloads back into the ROT when necessary. A spring switch exists at the back of the furnace. When loading a sample, the sample will trigger this switch when it reaches the back of the furnace. This lets the system know that the sample is loaded, and the rollers can stop, and the furnace door can shut. When the sample is unloaded the switch spring will be released which lets the system know the sample is no longer at the back of the furnace. The control panel also has an 'inch' back and forth function which allows the user to move the sample back and forth in the ROT slowly. Buttons for air cooling and water cooling are also on the control panel.

When setting up for a high temperature experiment the sample being tested first needed thermocouples attached. Temperature was monitored using 1 or 2 K-type thermocouples with a fibreglass sheath connected to a data logger. The wires were cut to 4m in length each. Holes were drilled in the steel sample, the thermocouple wires were placed in the hole, and then the hole was closed by deforming an area next to the hole. Thermocouples were placed at 150mm from the edge of the sample due to the limitations of the drill available. A schematic of the placement of the thermocouples on the sample is shown in figure 51.

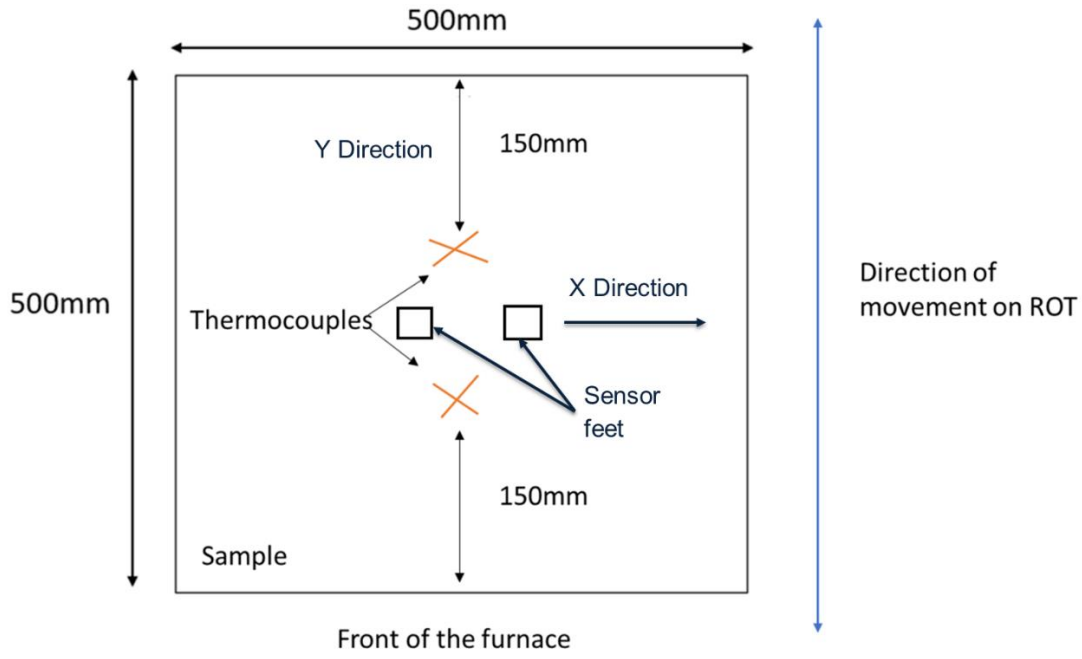

Figure 51. Position of the thermocouples on the samples used for high temperature EMspec® testing. The position of the back of the furnace and the direction of sample movement on the ROT is also shown. The position of the sensor feet and the x and y direction with respect to the sensor is also indicated.

With the sample ready for heating, the EMspec® sensor was set up using the steps mentioned previously in this chapter. The sample was then manually loaded into the ROT. With the sample in the ROT, extra time was spent making sure the sample is straight, to minimize the risk of the sample getting stuck or move in transit to and from the furnace. With the sample straightened, the sample was then positioned over the EMspec® sensor and 1 room temperature measurement before heat treatment was taken for 10 seconds. Once this measurement was finished, the sample was then loaded into the furnace which has already been preheated to 980°C. Once the loading was complete, the sample was left to heat up to 980°C. This temperature was chosen, as it gives enough time for the sample to be unloaded out of the furnace and be over the sensor, before it has cooled through the Curie temperature. When both thermocouples had passed 980°C, the sample was left in

the furnace for 2-4 minutes longer before the unloading procedure could begin to ensure uniformity. The sample was left in the furnace for as little time as possible, to minimise any decarburisation that may occur while the steel is being heated, as it is known that decarburisation effects the EM sensor signal [94-96]. With both thermocouples at and above 980°C, the sample was then unloaded from the furnace. Once the sample was above the sensor, and the sensor was positioned as close to the centre of the sample as possible, the rollers were stopped, and the sensor switched on to commence measuring while the sample cooled in air. While the sample was cooling and sensor measuring, the sample was jogged back and forth over the sensor. (approximately 4-8 cm). This was to make the cooling as uniform as possible, and to reduce the formation of cold strips due to multiple points along the sample being in contact with the rollers and therefore cooling faster than the areas not in contact. The sensor measured and obtained phase angle and ZCF values while the sample cooled to 200°C. This process was used for the steels in table 4. Two or three tests were performed per steel type depending on sample availability.

5.5.3 EMspec® Model

A 3D FEM of the EMspec® sensor installed on the lab-based ROT has been developed in a parallel project by Dr Jialong Shen using the ac/dc module in COMSOL Multiphysics. This model was produced with the aim of predicting a quantitative transformation fraction from the EMspec® measurements. The model consists of the H shaped ferrite core, a copper exciting coil, 2 copper sensing coils (1 active and 1 dummy) and the ferromagnetic canister that the sensor sits in. All the geometries used matched the EMspec® sensor head located in the ROT and were provided by Primetals Technologies Ltd. The model also considers the setting up and calibration of the real sensor to output modelled ‘processed data’. An image of the modelled sensor over a target sample is given in figure 52. The model is further described in [102]. The model can predict the ZCF for a sample if the material properties of resistivity and permeability are known.

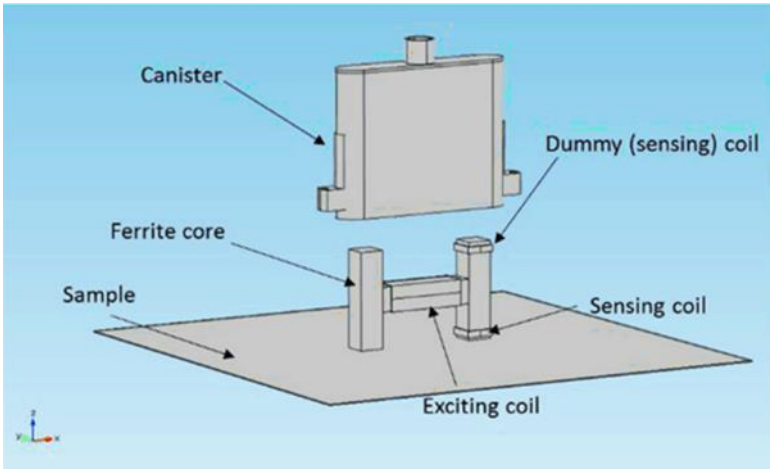

Figure 52. Modelled EMspec® sensor positioned at the centre of a 500 x 500 mm^2 sample. The canister is shown lifted above the sensor for clarity [102].

The developed model was used in this work to output predicted ZCF values with temperature for comparison to the experimental data. The transformation behaviour, obtained from dilatometry for each sample, was used to give the phase fraction with temperature from which an effective permeability and resistivity with temperature were calculated using power law calculations for austenite/ferrite, austenite/pearlite and austenite/bainite phase fractions. The power law equation used is as follows:

$$\mu_e^\beta = (1-f)\mu_1^\beta + f\mu_2^\beta \qquad \text{Equation 21}$$

μ_e, μ_1 and μ_2 are the effective permeability and the permeability of phase 1 and phase 2 respectively. F is for the phase fraction, and β is the fitting factor. The same formula can be used for resistivity. Permeability with temperature relationships for the different phases were obtained from the literature (ferrite and pearlite) [40] or by interpolated behaviour based on these known relationships for bainite. This assumed the permeability with temperature curve has the same shape as the pearlite literature data but offset. The offset was determined from measured room temperature permeability values. The resistivity values were either measured values (for the mild steel and high carbon steel, see section 7) or interpolated using the known relationship with temperature for a range of different steels [42]. Using the calculated effective permeabilities and resistivities for the various phase balances at different temperatures, the EMspec® COMSOL model was used to predict ZCF during transformation for comparison to the experimental data.

6. Measurement of EMspec® Sensor Sensitivity to Non-Microstructural Parameters

EM sensors are sensitive to changes in permeability and resistivity, which is a result of changes in microstructure as discussed in chapter 3, however, they are also sensitive to non-microstructural factors such as being close to the sample edge, lift off and thickness. In this section, the EMspec® sensor sensitivity to edge effect is presented to determine the minimum sample size required for signals to be unaffected by edge effect. The sensor was also tested for the signal dependence on lift off as well as the effect of the surrounding structure on the EMspec® sensor signal. It is important to test for these sensitivities to give confidence that any change in signal is due to changes in microstructure and not caused by a non-microstructural parameter.

6.1 EMspec® Sensor Sensitivity to Edge Effect

The EMspec® sensor was tested for edge effect in both the X and Y direction (X and Y directions shown in figure 51) so that a minimum sample geometry could be quantified. A dual phase (DP) sample (measuring 500 × 500 × 3.64 mm) was used for the measurements and the edge effect results in the X and Y directions are shown in figure 53 and figure 54 respectively. The composition for this sample is given in chapter 5. A 40 mm lift off was used in these tests, which corresponds to the lift off between the EMspec® sensor and strip during operation in the Tata Steel hot strip mill in IJmuiden [8].

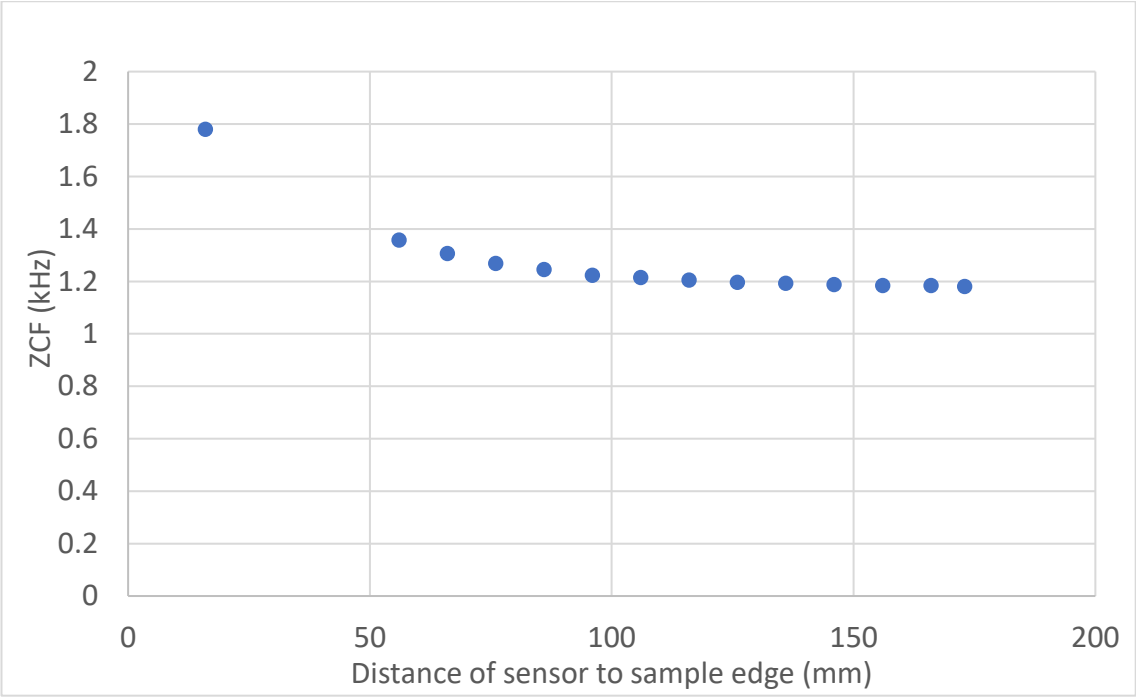

Figure 53. ZCF plotted against distance of sensor to sample edge in X direction

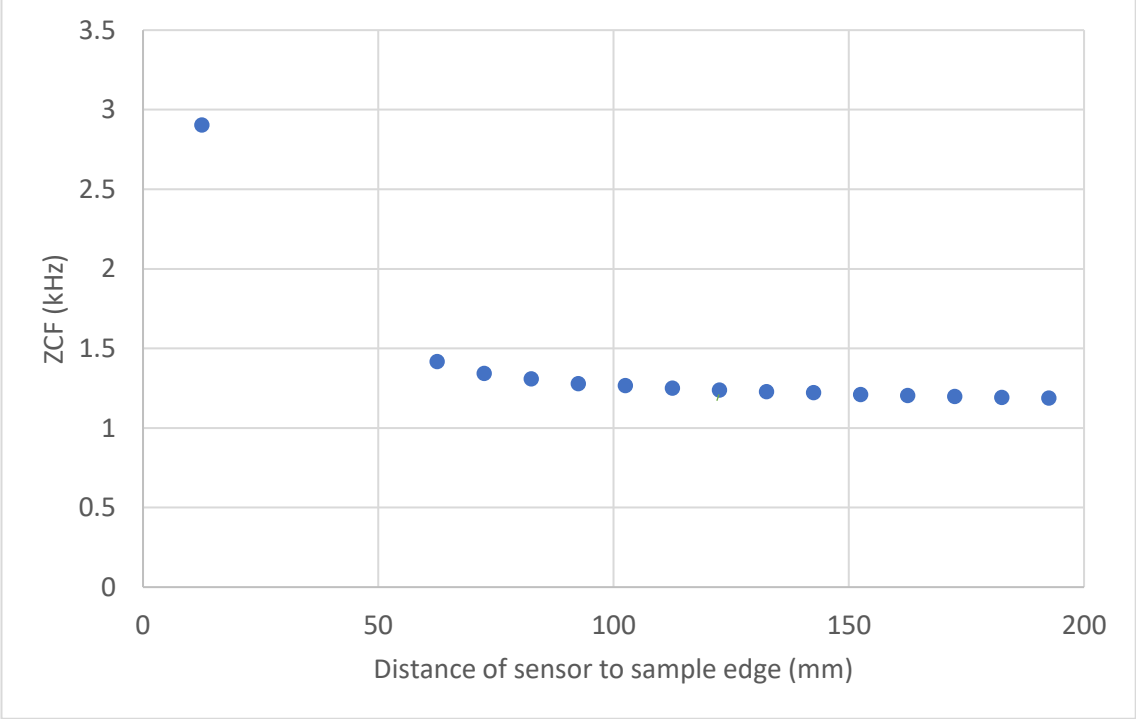

Figure 54. ZCF plotted against distance of sensor to sample edge in Y direction

The graphs in figure 53 and figure 54 show similar trends, with the ZCF showing a relatively flat response until the sensor approaches the sample edge where the ZCF noticeably increases. The ZCF is affected by the interaction of the applied magnetic field and eddy current generated magnetic field in the sample. Near the edge of the sample the eddy currents and magnetic field will be non-symmetric, which changes the ZCF. In the X direction, the results show that the signal has significantly increased (discussed in section 5) due to edge effect, at approximately 80mm from the sample edge. In the Y direction, the ZCF has significantly increased at approx. 120mm from the sample edge Therefore, when taking the sensor dimensions (103mm × 153mm × 20mm) into account, the minimum required sample size for there to be no edge effect when measuring with EMspec® sensor is 386mm × 265mm (XX × YY).

6.2 EMspec® Sensor Sensitivity to Changes in Lift Off

The EMspec® sensor was tested for sensitivity to sample lift off using a dual phase and a low carbon sample, measuring 500 × 500 × 3.64 and 465 × 500 × 3 mm respectively (compositions given in section 5). The data for both samples is given in figure 55. It can be seen from the graph that the data for dual phase and low carbon samples follow similar trends with ZCF decreasing with increasing lift off. At approximately 65 mm lift off there is a plateau in the data and the sensor is virtually lift off independent. Both data sets were analyzed to see how much of a deviation in lift off would be required for the samples ZCF s' to overlap (which would mean the grades would not be distinguished from each other) and this is shown by the green lines in figure 55. For the low carbon sample to be confused with the dual phase sample, the lift off when measuring the low carbon sample would need to be approximately 10-13 mm higher than the dual phase steel in the 20-65mm range. During operation in a hot strip mill, the lift off between the strip and sensor should be relatively constant when the strip is held under tension (i.e. the strip is held in the coiler and final rolling stand). However, the front and back ends of the strip will not be under tension at times and the lift off can vary. On the ROT as part of the ROT and furnace system, when the sample comes out of the furnace it can become bowed as a result of

heat treatment. Therefore, depending on which way, the sample is bowed, this can potentially influence lift off as the sample moves over the rollers.

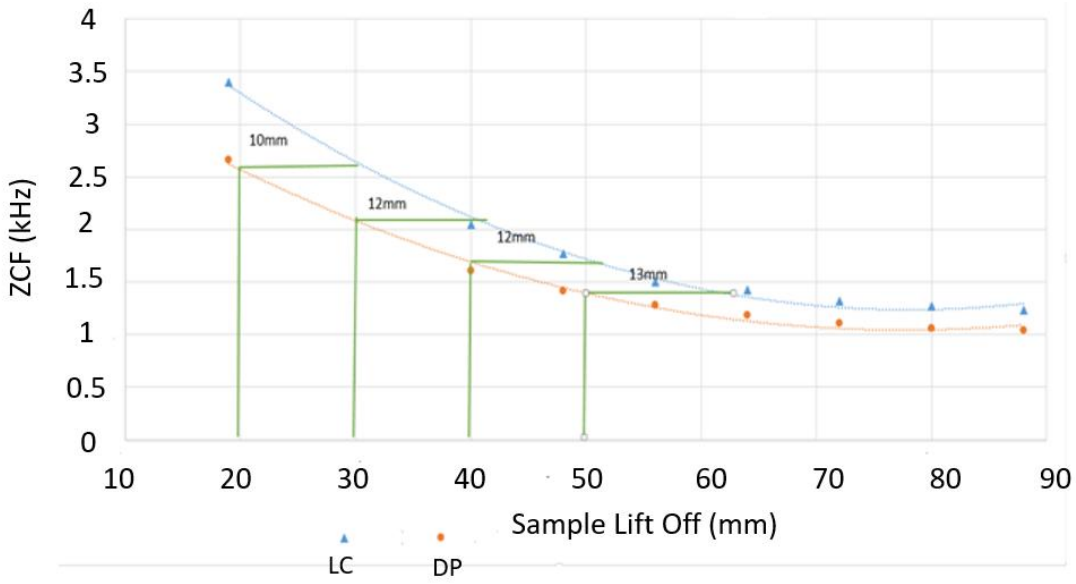

Figure 55. ZCF plotted with varying sample lift offs. Blue triangles represent low carbon (LC) data while orange circle represents dual phase (DP)

6.3 Modelled Effect of Sample Thickness on the EMspec® Sensor Signal

An initial study on the influence of sample thickness on the ZCF has been carried out using the EMspec® model in parallel project by Dr. Jialong Shen. Low and high ferrite transformed fractions (20%, 50% and 90% ferrite) at 500, 651 and 721 °C for thicknesses of 1.5, 3 and 6 mm have been investigated. It was found that higher ZCF values were seen for thinner samples. This is due to the limited flow of the eddy currents which in turn means that it takes a higher frequency before the real inductance decreases, which leads to higher ZCF values. Percentage change in ZCF for 1.5 and 3mm thickness when compared with a 6mm sample has been plotted in figure 56 (6mm sample ZCF taken as reference values). The influence of thickness is particularly seen for low ferrite fractions at low temperatures (lower permeability) because the effective skin depth is larger. Generally, there is very little effect of thickness at high ferrite fractions (90%) in this temperature range [103].

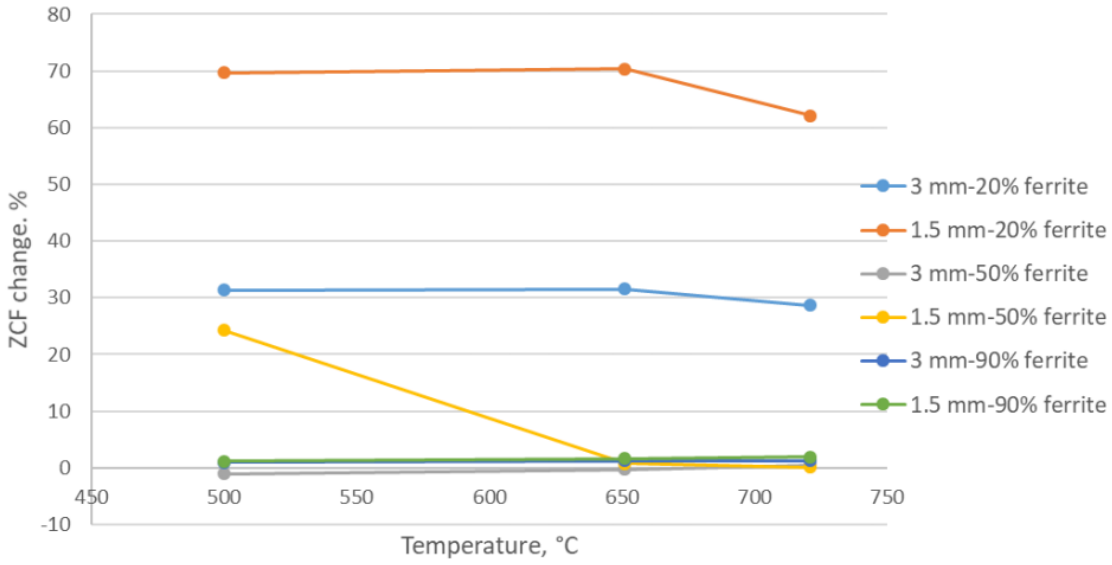

Figure 56. Percentage change in ZCF for 1.5mm and 3mm thickness samples when compared with 6mm thickness [103].

6.4 Sensitivity of the EMspec® Sensor to the ROT Surrounding Structures

As the EMspec® sensor was to be installed in between the rollers in the ROT, it was important to carry out measurements both out of the ROT and when installed to see if there is an effect of the surrounding structures on the EMspec® signal. Figure 57 shows the plots of samples measured in the lab (no ROT) compared to measurements of the same samples on the ROT. If there was no effect of the ROT, the data should follow a trajectory of Y = X. However, it can be seen from figure 57 that this is not the case. The ROT ZCF values are consistently higher than the results from the lab, and the trend shown is not linear as ZCF increases. This is likely caused by the surrounding structures in the ROT such as the rollers. While measuring a sample, the austenitic stainless-steel rollers are also being measured. This will cause an increase in resistivity for any measurement, as the austenitic stainless steel has higher resistivity than most of the steels measured on the ROT.

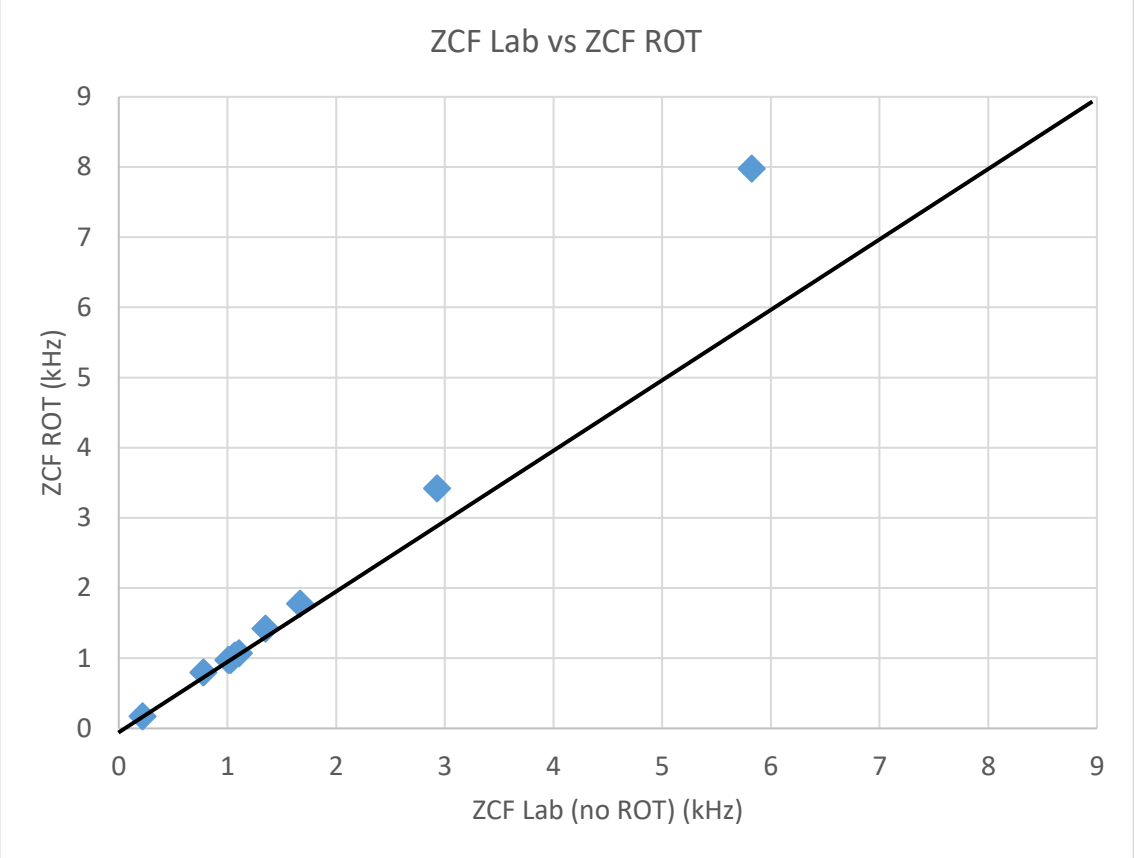

Figure 57. Comparison of EMspec® measurements from the lab (no ROT) and when installed on the ROT.

6.5 Summary

In this section the EMspec® sensor has been measured for edge effects, change in lift off and effect of the surrounding structure (ROT). The EMspec® sensor was also modelled to look at the effect of change in thickness of sample [103]. From the edge effect measurements, it was found that the ZCF increased significantly when 80mm away from the sample edge in the X direction and 120mm away from the sample edge in the Y direction. Therefore, when considering the dimensions of the EMspec® sensor, the minimum sample size required for there to be no edge effect was calculated to be 386mm × 265mm (XX × YY). Obviously, it is difficult to guarantee the sample position is the same every test, so a general sample size of 500 × 500mm (unless stated otherwise) has been used in this thesis to minimise the chance of any edge effects.

The sensor was also tested for its sensitivity to sample lift off, in which, it was found that for both a dual phase and a low carbon sample, the ZCF decreases up to 65mm lift off where there on, the sensor is virtually lift off independent. It was also found that to confuse the low carbon sample with the dual phase sample, the low carbon steel would have to have a 10-13mm higher lift off than the dual phase steel in the 20-65mm lift off range.

The EMspec® sensor has been modelled for the effect of thickness at different ferrite austenite phase balance at different temperatures. It was shown that thinner samples at at low ferrite fractions at lower temperatures was found to affect the ZCF the most. This is due to the restricted flow of eddie currents in thinner sample and because of the higher skin depth at lower permeabilties. At high ferrite fractions there is very little to no effect of thickness [103].

The surrounding structures of the ROT was found to affect the EMspec® sensor signal. Samples that were measured on the ROT would increase in ZCF when compared with the measurements performed in the lab (no ROT). This is likely to be caused by the surrounding structures on the ROT such as the rollers.

7. Materials for ROT Information

To be able to understand and interpret the high temperature ZCF's that the EMspec® sensor is measuring on hot samples, it is important to first know other necessary information about the samples such as room temperature resistivity and permeability. Resistivity with temperature is also mentioned here as this is one of the inputs into the EMspec® sensor model.

7.1 Room Temperature Permeabilities and Resistivities of Materials for ROT

Room temperature permeabilities and resistivities have been measured for the samples mentioned in table 4. In order to obtain permeability of the samples, a U-shaped sensor (mentioned in chapter 5) was first used to measure the low frequency real inductance. The permeabilities were then predicted by fitting the model to the experimental data. Room temperature permeabilities and resistivities are shown in figure 58. The order of permeability is as follows: Low carbon > Mild 6mm ≥ 3mm Mild > High Carbon > Cr-Mo > Duplex. This order of permeabilities is to be expected as a low carbon steel is mostly ferritic. The duplex stainless steel is very highly alloyed and has a significant amount of paramagnetic austenite phase, so it makes sense that this would exhibit the lowest permeability. For resistivity the order is reversed from permeability and is as follows: Duplex > Cr-Mo > High Carbon > Mild 6mm > 3mm Mild > Low Carbon. This order is to be expected as a duplex stainless steel is very highly alloyed and has austenitic phase which has a higher resistivity than ferrite, pearlite and bainite at room temperature. Room temperature resistivities have not been provided for the 10mm mild and medium carbon steels as these samples were sourced and bought later and there was not enough time to obtain this data for those.

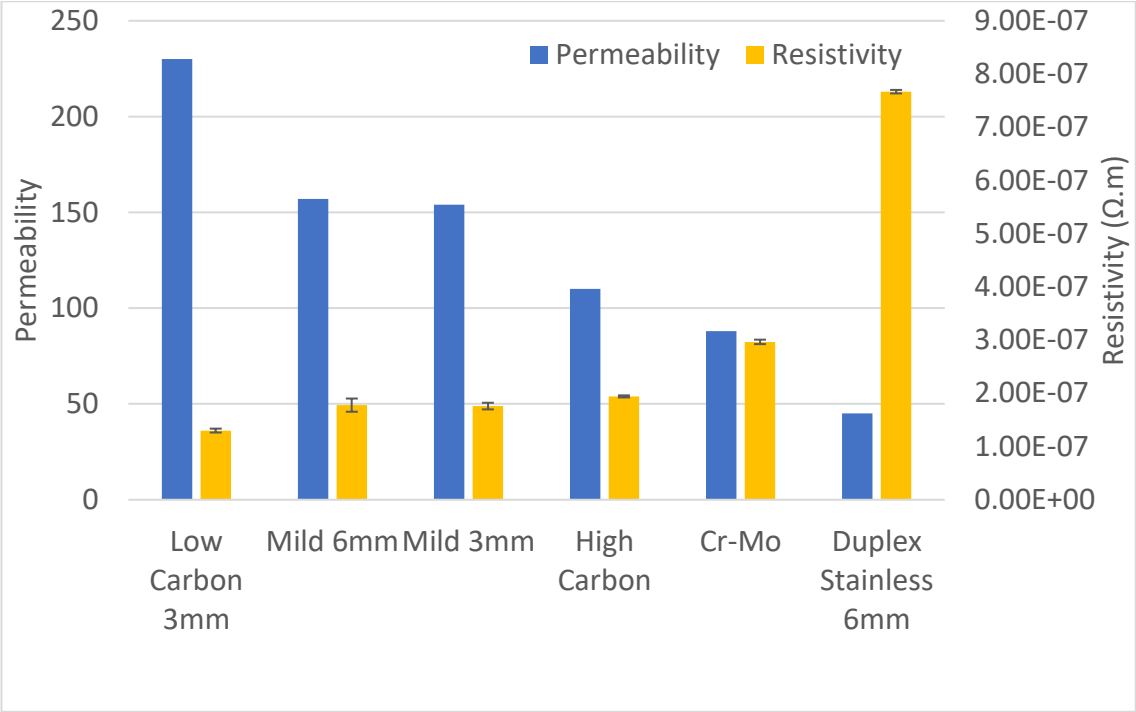

Figure 58. Room temperature permeabilities and resistivities for steels to be tested using EMspec® sensor.

7.2 Resistivity with Temperature

Figure 59 shows resistivity with temperature for low carbon, high carbon, duplex stainless steel and extrapolated resistivities for Cr-Mo steel using the ASM handbook [2]. These are to be used as inputs for the EMspec® model when predicting ZCF. The austenite values were extrapolated by taking the values for a low carbon steel when above 900°C and extrapolating down to room temperature using the known relationship of an austenitic steel resistivity with temperature. The high carbon steel has a higher resistivity with temperature which is due to the higher carbon content, and therefore more carbide precipitates in the form of pearlite. The Cr-Mo steel extrapolated has a higher resistivity than the carbon steels which is expected as it is more highly alloyed with elements such as chromium and niobium, which increases the resistivity of a steel [41]. The austenitic extrapolation has a higher resistivity below 800°C which is expected as austenite exhibits an FCC crystal structure which is more tightly packed than BCC [13]. The duplex stainless steel has the highest resistivity as it is the most highly alloyed of the steels with over 20% chromium and has austenitic phase which as previously stated which would also increase the resistivity.

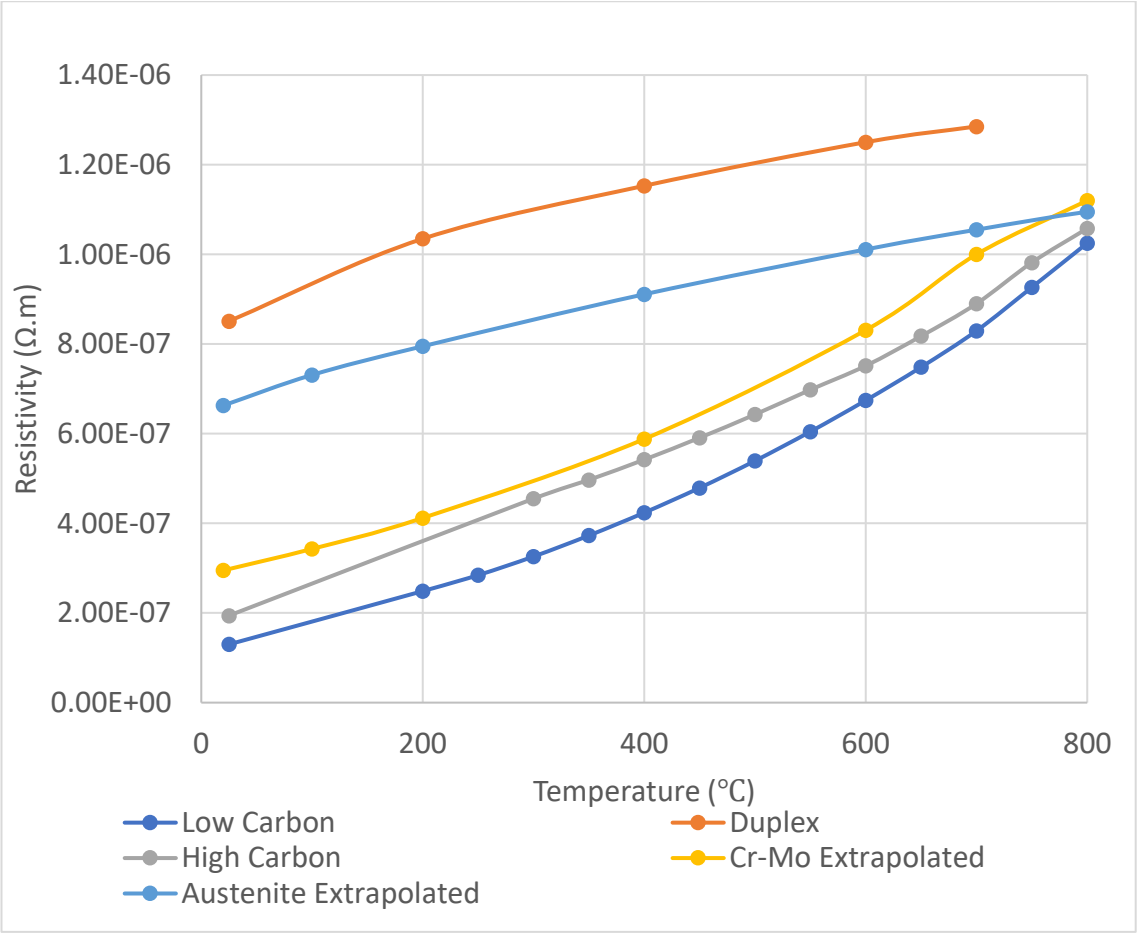

Figure 59. Resistivity with temperature for low carbon steel, high carbon steel, austenite (extrapolated), duplex stainless steel, and Cr-Mo steel (extrapolated).

7.3 Summary

This chapter has summarised the relevant information for the materials used for high temperature testing using the EMspec® sensor. The room temperature permeabilities and resistivities and the resistivity of relevant microstructural phases with temperature have been reported.

8. Measurement and Modelling of the EMspec® Sensor Response to the Phase Transformation in Dynamically Cooled Steels

As the temperature of a ferromagnetic material increases up towards the Curie temperature, so does its permeability; above the Curie point the permeability rapidly decreases towards 1 (i.e. paramagnetic). EM sensors are sensitive to changes in permeability and can be used to monitor the phase transformation from paramagnetic austenite to ferromagnetic (if below the Curie temperature) phases, however as the permeability is also affected by temperature this needs to be determined before a quantitative relationship between EM sensor signal and fraction transformed can be established. High temperature EMspec® sensor responses for multiple carbon steels, a 2.25 Cr-Mo steel and a duplex stainless steel have been measured, modelled and related to the microstructural state (phase fraction transformed) in this section.

8.1 Carbon Steels

8.1.1 3mm Mild Steel

8.1.1.1 Microstructure Characterisation

Microstructures for the 3mm mild steel in the as received condition and after heat treatment following high temperature EMspec® measurements are shown in figures 60-63. Heat treated samples were heated to 980°C in the furnace and allowed to cool in air while being monitored by the EMspec® sensor. Figure 60 shows the as received sample, which has a microstructure consisting of a ferrite matrix with a random distribution of pearlite and bainite. The heat-treated samples shown in figures 61-63 show a ferrite matrix with randomly distributed pearlite and small amount of bainite. The samples treated on the ROT also appear to have a larger ferrite grain size than the as received

sample, which is likely caused by the relatively high austenitising temperature and slow cooling rate. Micrographs have also been taken to determine whether any decarburization occurred at the surface for the 3 tests and these are shown in figures 64-66. Decarburisation is important as the formation of a low carbon ferrite region at the surface of a sample is known to affect the EM signal on cooling as low carbon ferrite transforms at a higher temperature than the bulk and also has a higher permeability than a ferrite + pearlite structure [91-93]. For test 1, the micrographs of the top and bottom surfaces show no evidence that any decarburisation has taken place. There is evidence of decarburisation on the top surface for test 2. The micrographs for test 3 however clearly show evidence of decarburisation with high ferrite fraction regions existing particularly on the bottom surface of this sample. The resultant microstructure for the 3mm mild steel following dilatometry heat treatment is shown in figure 67. This microstructure has a ferrite pearlite microstructure with a small amount of bainite, which is similar the microstructures following heat treatment on the ROT in figures 61-63 which is expected. It also has a visibly coarser grain structure than for the as received sample in figure 60. The as received sample has a ferrite fraction of around 70% while the after-heat treatment (both ROT and dilatometry) bulk ferrite fractions are very similar with values of around 80% (table 5).

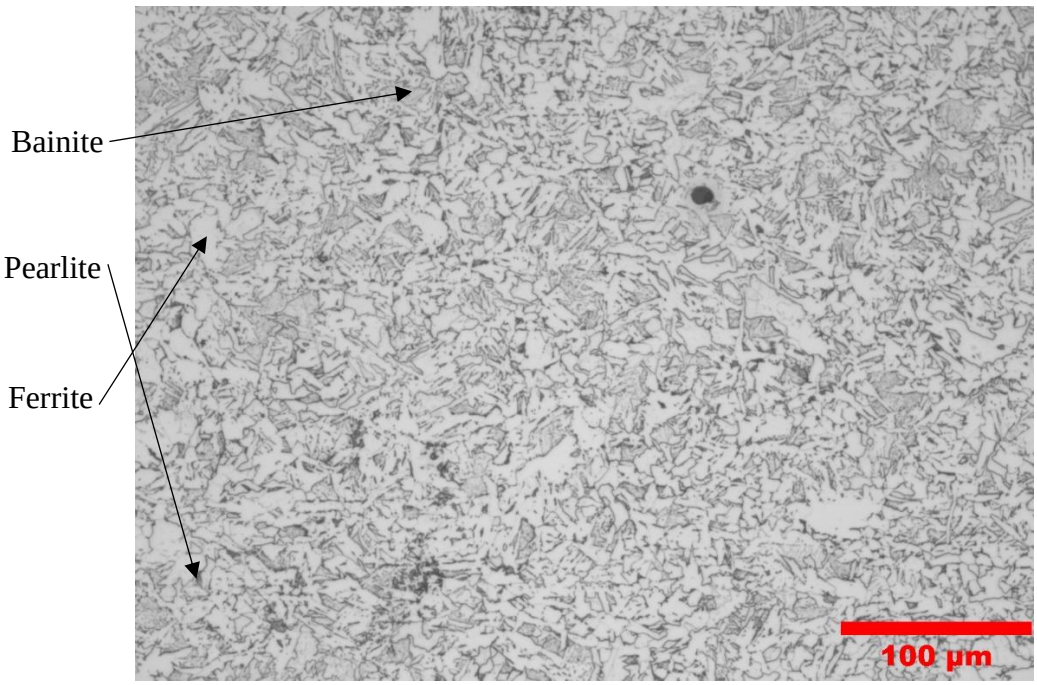

Figure 60. Optical microstructure at 20× magnification of 3mm mild steel in as received condition. Areas of ferrite, bainite and pearlite have been labelled.

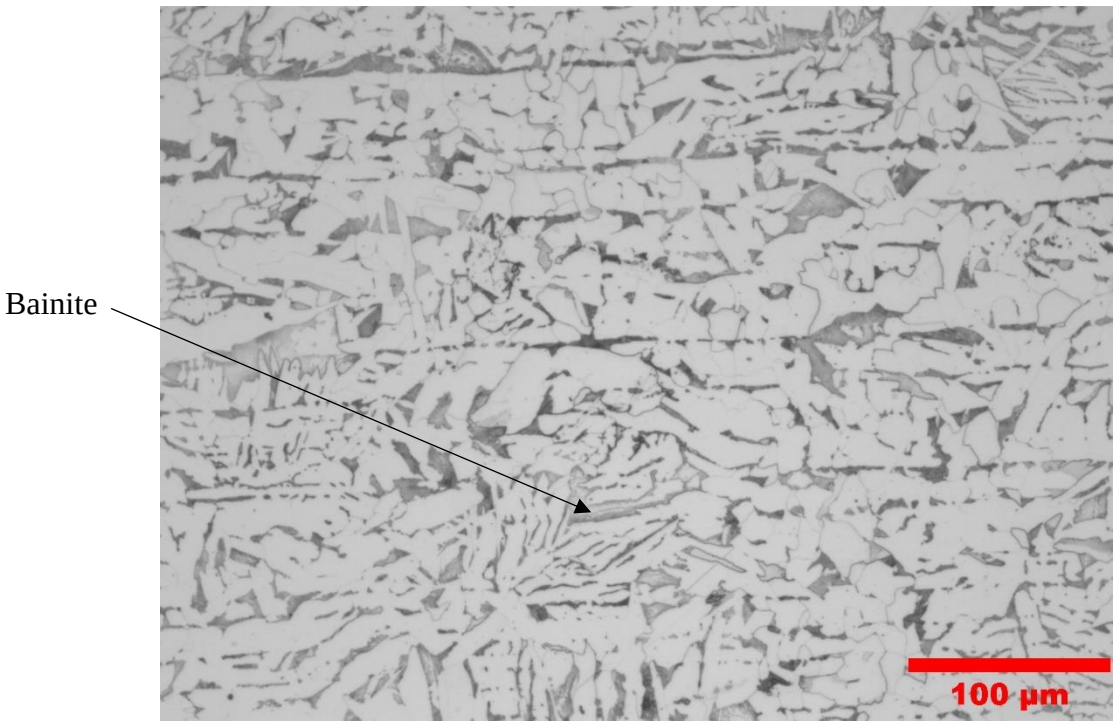

Figure 61. Optical microstructure at 20× magnification of 3mm mild steel following heat treatment for test 1. An area of bainite has been labelled.

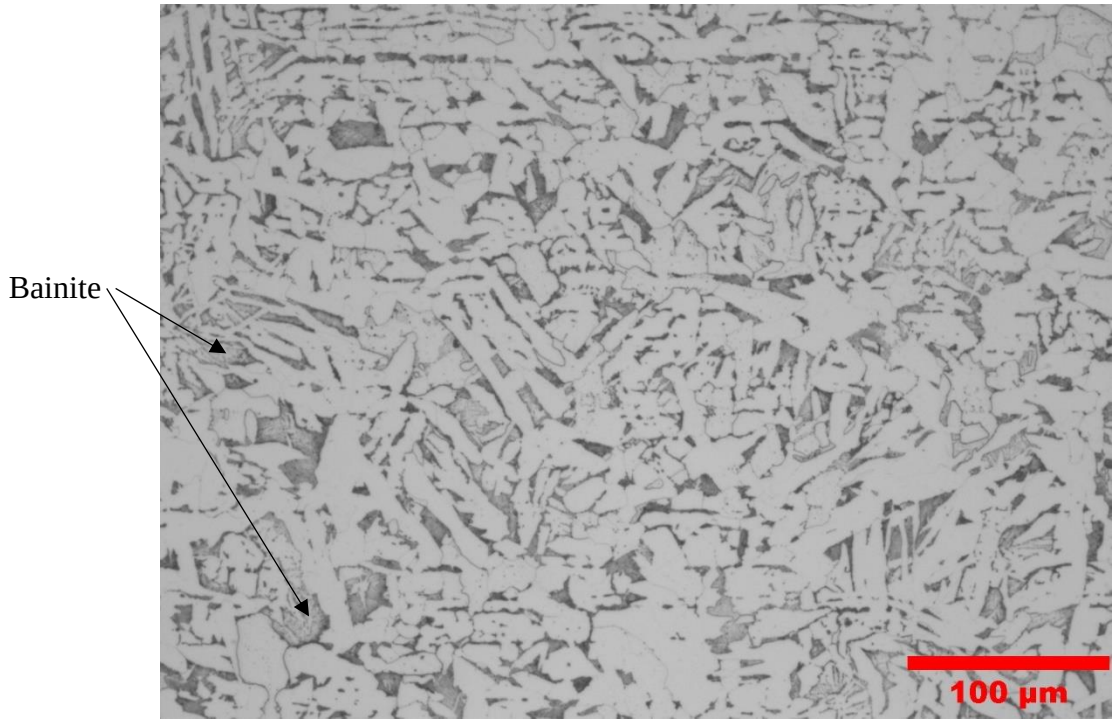

Figure 62. Optical microstructure at 20× magnification of 3mm mild steel following heat treatment for test 2. Some areas of bainite have been labelled.

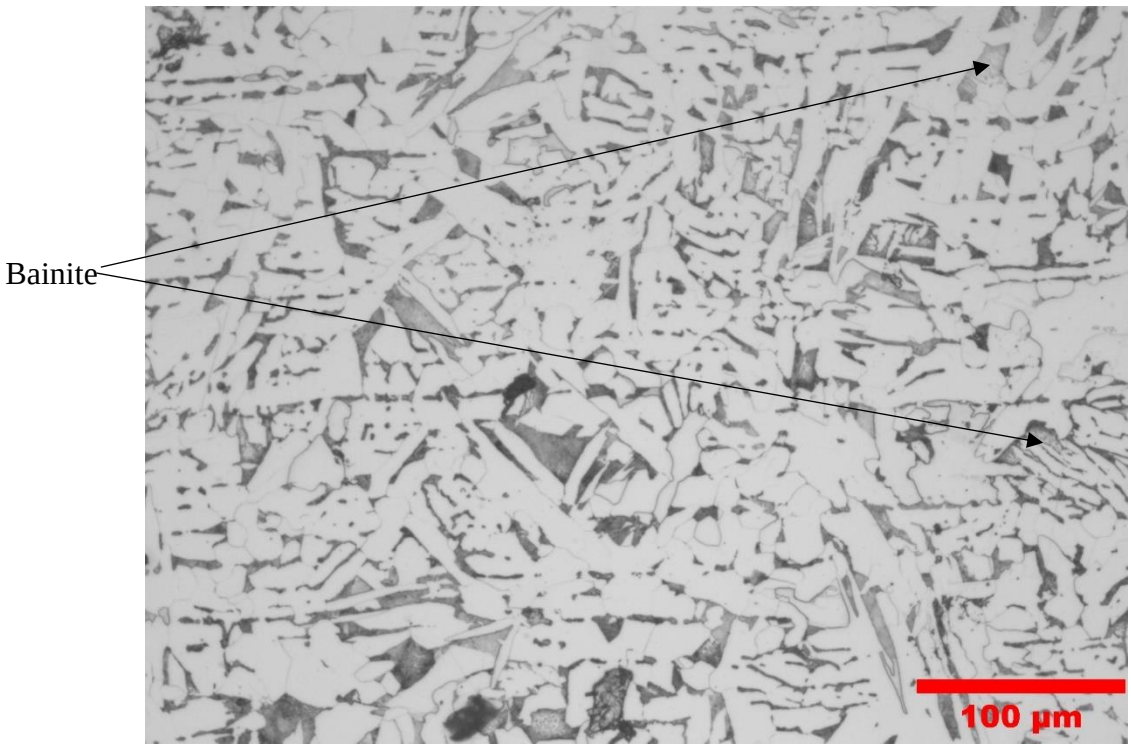

Figure 63. Optical microstructure at 20× magnification of 3mm mild steel following heat treatment for test 3. An area of bainite has been labelled.

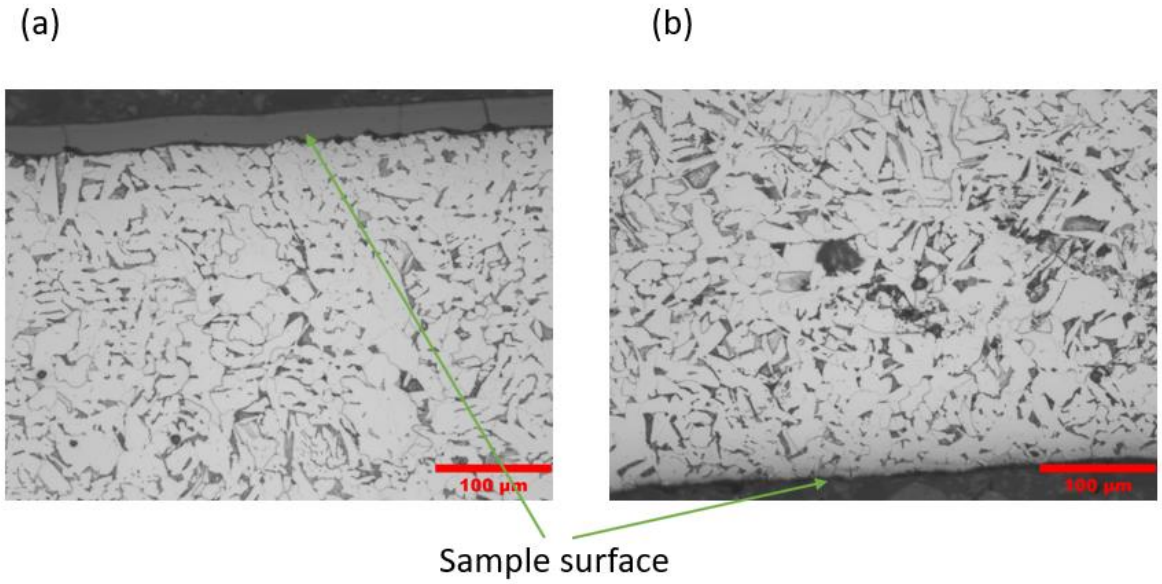

Figure 64. Optical microstructures at 20× magnification looking at top surface (a) and bottom surface (b) of the 3mm mild steel used in test 1.

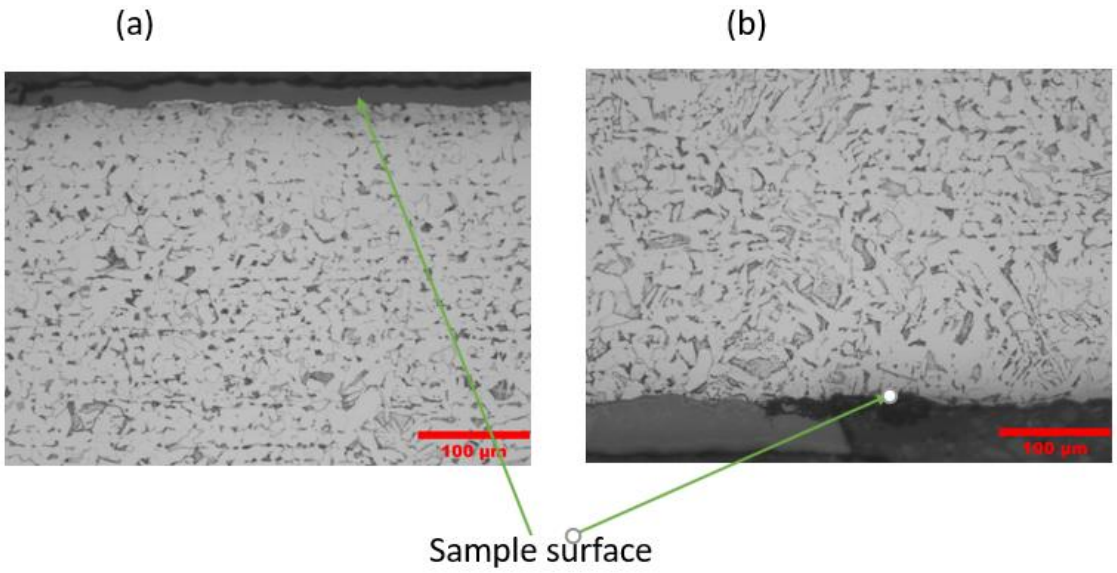

Figure 65. Optical microstructures at 20× magnification looking at top surface (a) and bottom surface (b) of the 3mm mild steel used in test 2.

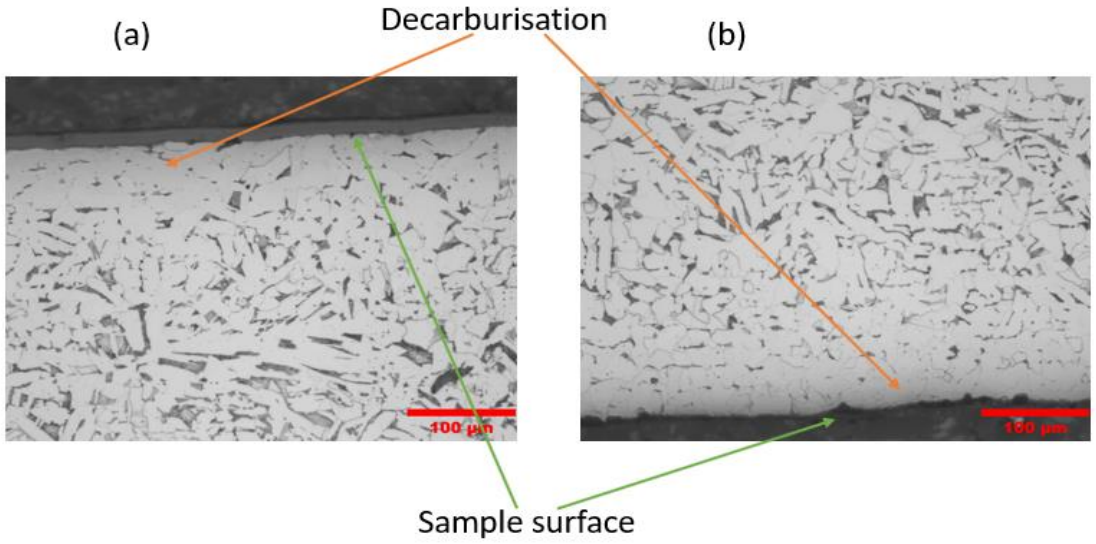

Figure 66. Optical microstructures at 20× magnification showing evidence of decarburisation at top surface (a) and bottom surface (b) of the 3mm mild steel used in test 3.

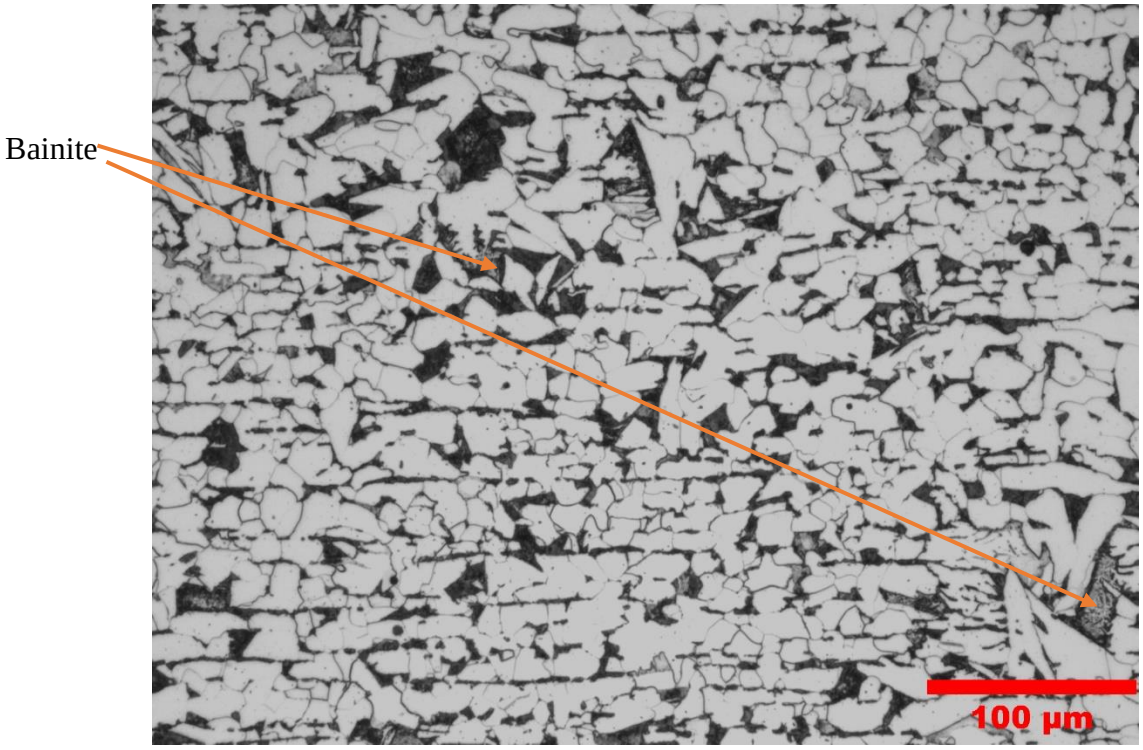

Figure 67. Optical microstructure at 20× magnification of 3mm mild steel following dilatometry heat treatment. Areas of bainite have been indicated using label and arrows.

Table 5. Ferrite fractions in % for 3mm mild steel in as received condition, after 3 heat treatments following EMspec® sensor measurements and following dilatometry heat treatment.

As Received	Test 1	Test 2	Test 3	Dilatometry
71.73 ± 0.59	79.75 ± 0.63	80.80 ± 3.03	81.13 ± 0.74	81.57 ± 0.45

8.1.1.2 Cooling Trajectories

The cooling trajectories for tests 1-3 and the temperature discrepancy between the two thermocouples (T1-T2) used on the samples is shown in figures 68-70. For all 3 tests upon cooling start, there is an initial spike in temperature difference between thermocouples 1 and 2. This is because thermocouple 2 is closer to the back of the furnace, while thermocouple 1 is closer to the furnace door. Therefore thermocouple 1 is always the first out of the furnace door which causes this initial spike in temperature difference as the part of the sample around thermocouple 1 is exposed to the atmosphere outside of the furnace first. As thermocouple 2 leaves the furnace and is exposed to the atmosphere

outside of the door, its cooling rate increase quickly and the temperature discrepancy between thermocouples 1 and 2 decreases. Test 1 shows good temperature uniformity throughout cooling with the two thermocouples staying within 10℃ of each other throughout cooling. Test 2 shows a temperature discrepancy throughout cooling mostly staying between 20 and 30℃ between thermocouples 1 and 2 until closer to room temperature where the temperature discrepancy decreases. The difference between thermocouples 1 and 2 stays around 30℃ for test 3. After latent heating has occurred at approximately 700℃ then the temperature uniformity improves as the sample cools towards room temperature.

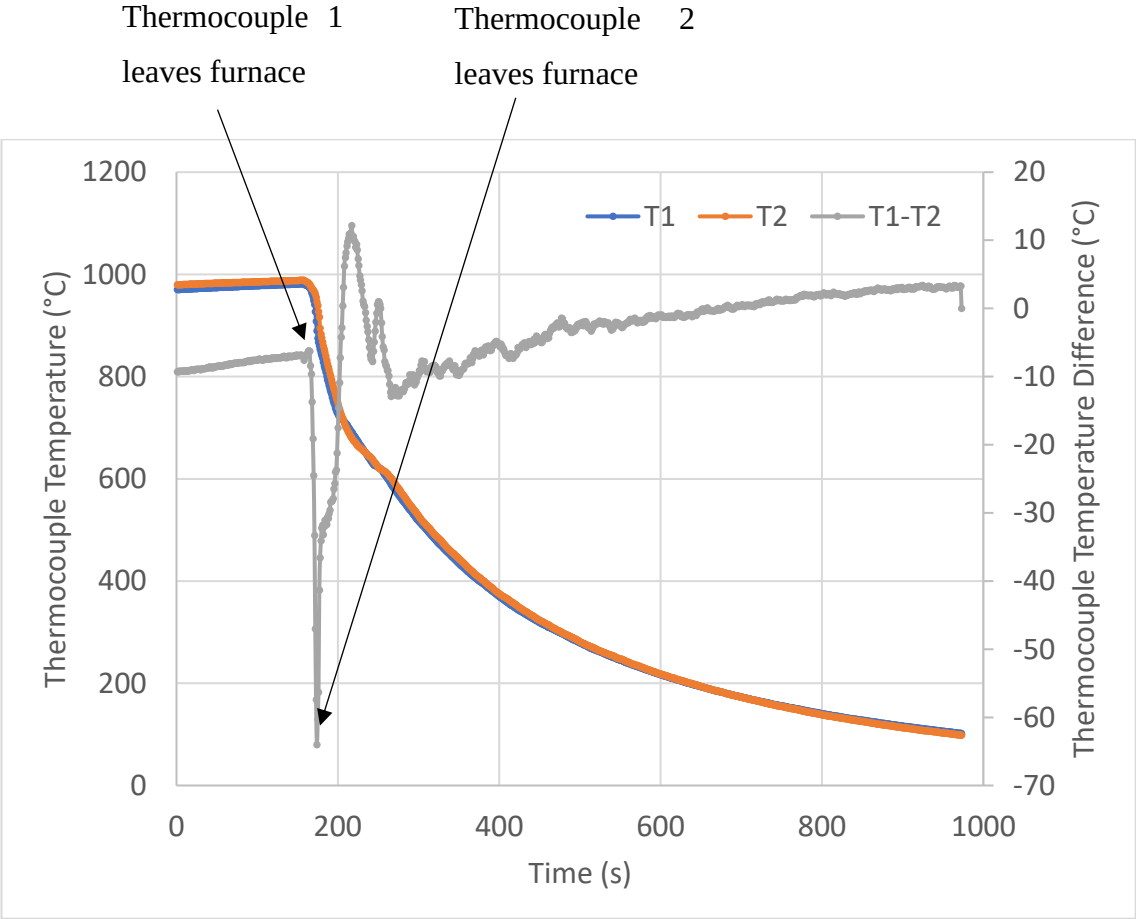

Figure 68. Cooling trajectory for 3mm steel during test 1. Thermocouple 1 (T1) and thermocouple 2 (T2) are plotted along with temperature difference between the two thermocouples (T1-T2). The points at which thermocouples 1 and 2 leave the furnace are indicated on the T1-T2 graph.

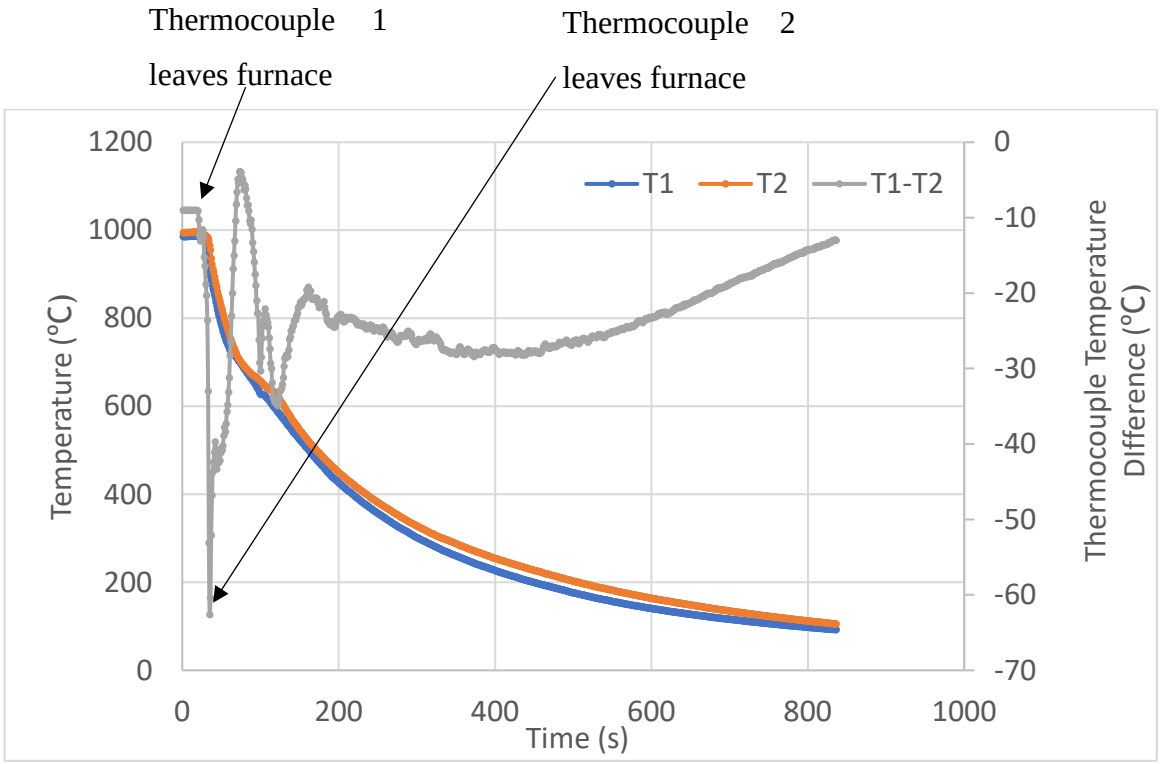

Figure 69. Cooling trajectory for 3mm steel during test 2. Thermocouple 1 (T1) and thermocouple 2 (T2) are plotted along with temperature difference between the two thermocouples (T1-T2). The points at which thermocouples 1 and 2 leave the furnace are indicated on the T1-T2 graph.

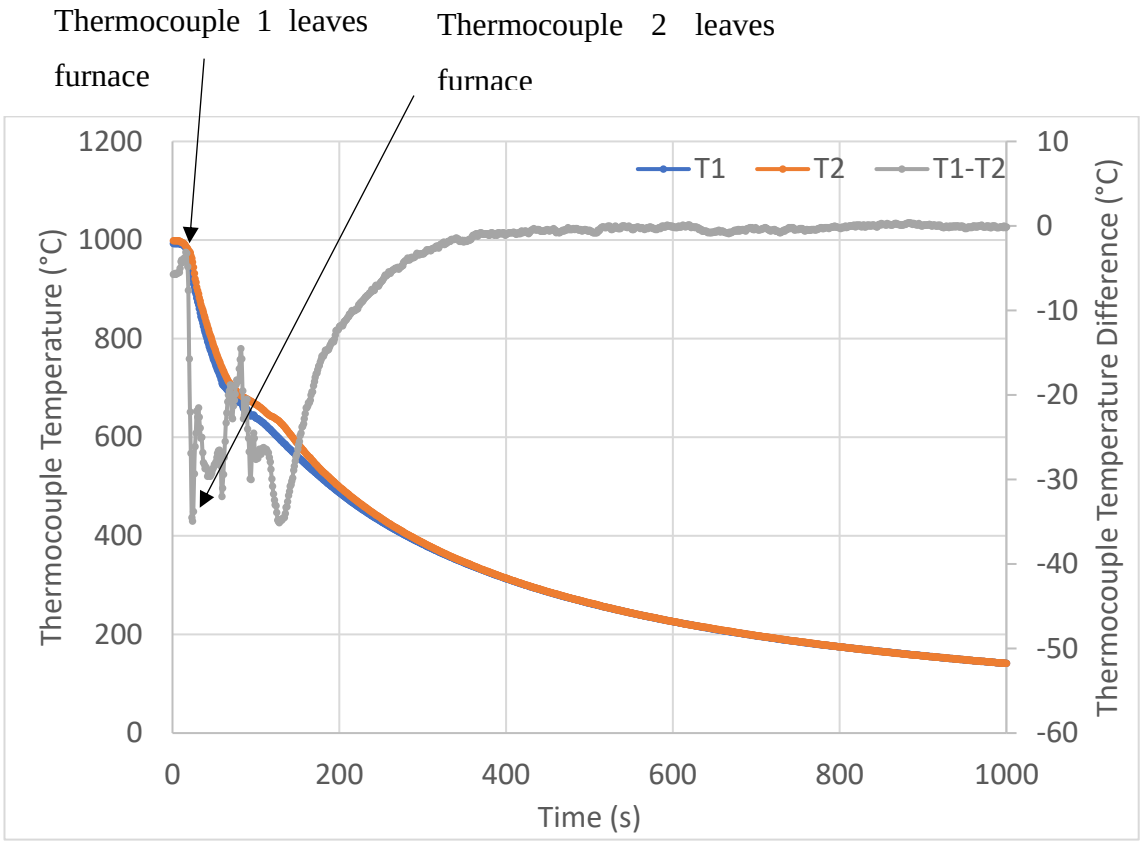

Figure 70. Cooling trajectory for 3mm steel during test 3. Thermocouple 1 (T1) and thermocouple 2 (T2) are plotted along with temperature difference between the two thermocouples (T1-T2). The points at which thermocouples 1 and 2 leave the furnace are indicated on the T1-T2 graph.

The average cooling trajectory for the 3mm mild steel from EMspec® sensor tests 1-3 is shown in figure 71. Figure 71 shows that the cooling rates of the three tests are not the same. Cooling trajectories for tests 1 and 2 mostly overlap which is expected as the procedure was the same. The difference in cooling rate for test 3 is caused by the sample getting stuck on the way out of the furnace during an initial attempt to unload the sample for EMspec® sensor testing. The sample was reloaded into the furnace and reheated and then the procedure was performed again successfully. Due to the longer exposure to the high temperatures for this sample, more oxide was formed and caused the lower cooling rate of this sample compared to tests 1 and 2. This is also consistent with more decarburisation being shown in the test 3 microstructure compared to tests 1 and 2.

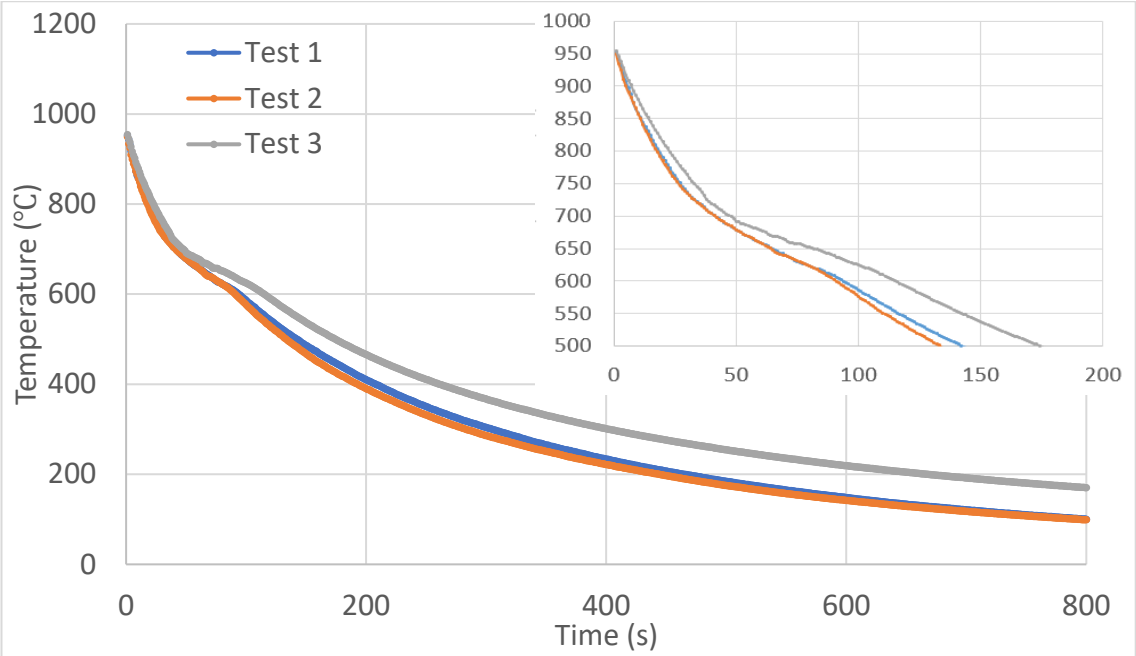

Figure 71. Average temperature of 3mm mild steel (tests 1-3) with time during cooling in air. An expanded view is also shown.

8.1.1.3 EMspec® Sensor Results and Relation of ZCF to Phase Percentage Transformed and EMspec® Sensor Model

Figure 72 shows the measured and modelled ZCF with temperature for the 500mm ×500mm × 3mm mild steel plates cooling in air. Transformed percentage is also plotted with temperature on the second Y axis. At approx. 800°C the ZCF is very low which is due to the steel being austenitic at this point and therefore paramagnetic. As the steels cool, the ZCF for all the tests begins to increase at approximately 730°C, which is below the Curie temperature for this steel (expected to be approximately 760°C). This is consistent with ferromagnetic phase being present, which means transformation has begun. The increases in ZCF is due to the increase in low field magnetic permeability of the material. For tests 1 and 2, the signal increases sharply with the gradient starting to decrease at approximately 680°C. The ZCF for tests 1 and 2 continue to increase with a lower gradient until approximately 650°C. At this point, the ZCF for tests 1 and 2 peak with a ZCF of approximately 31kHz. Following the peak in signal for both tests, the ZCF decreases with temperature due to the associated decrease in resistivity and permeability due to decreasing temperature. For test 3, the ZCF begins to increase at approximately

730°C like tests 1 and 2. This is consistent with transformation to ferrite occurring. However, unlike tests 1 and 2, the ZCF for test 3 continues to increase sharply until it peaks at approximately 680°C with a signal of around 50 kHz, nearly 20 kHz higher than for tests 1 and 2. This is consistent with the higher amounts of decarburisation formed due to longer exposure to high temperatures during heating causing a higher permeability. This would be consistent with previous literature that has shown decarburisation to influence the EM signal during the phase transformation [91-93].

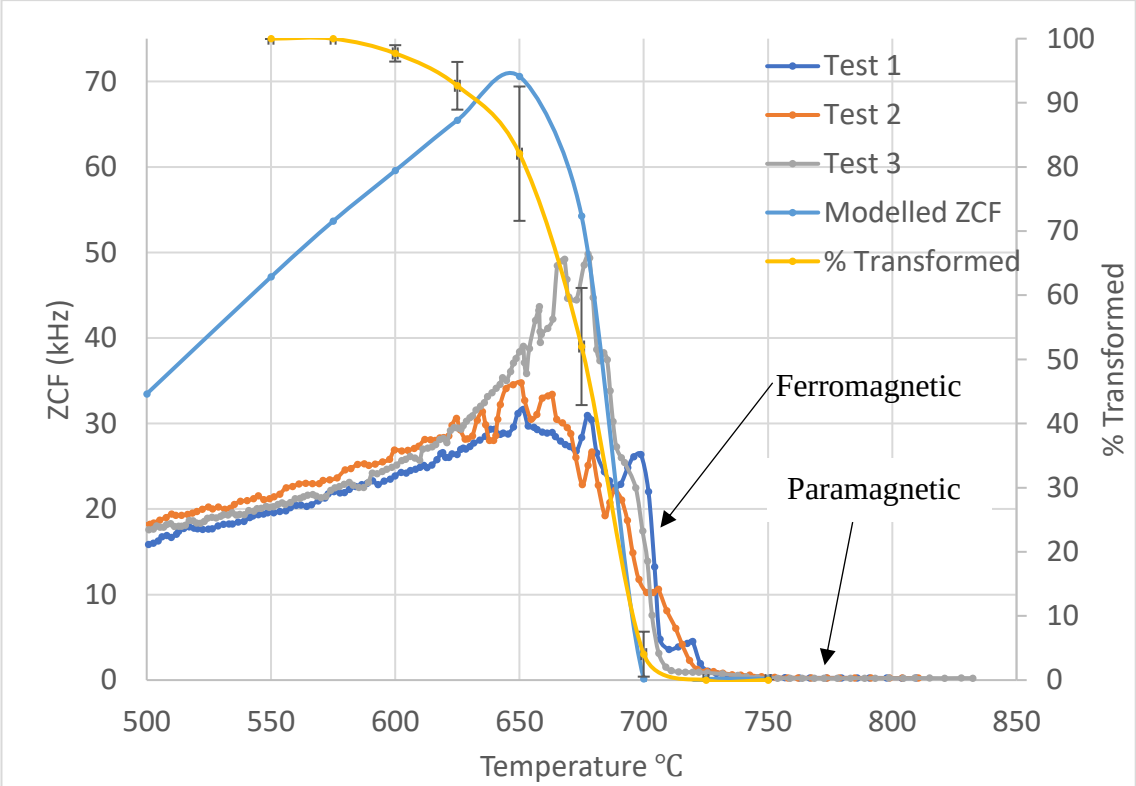

Figure 72. Measured and modelled ZCF with temperature. Transformed percentage also plotted with temperature on the second Y axis. The points at which the steel is paramagnetic and ferromagnetic are indicated on the ZCF graph.

Phase percentage transformed obtained from dilatometry has been plotted with temperature with ZCF on a secondary Y axis to explore how ZCF varies while the sample is transforming for the 3mm mild steel. The phase fraction during transformation will be for the bulk microstructure as decarburisation is not considered. Figure 72 shows that the increase in ZCF occurs at around the same temperature that the steel begins to transform. This does not agree with the study by Hao et al. [88], however it should be noted that temperature inhomogeneity in the experimental samples can be seen in figures 68-70 and errors in temperature measurement will exist between the non-uniform 500mm^2 sample

and the much smaller dilatometry sample. There is room for variability in the temperature and phase fraction where the ZCF begins to increase. The ZCF for tests 1 and 2 peak when the steel is expected to be around 80% transformed. At this point, the remaining austenite to pearlite/bainite transformation does not appear to have a significant effect on the sample permeability to cause a further increase in ZCF. The decrease in permeability and resistivity with the decrease in temperature in this instance appears to be more significant, so the ZCF decreases despite the steel probably not being fully transformed. For test 3 it is not easy to relate the ZCF directly to the fraction transformed because the cooling rate was different to that used for the dilatometry test and the possible influence of decarburisation was not considered.

Figure 72 shows the modelled ZCF agrees with the experimental data initially with the increases in ZCF for both increasing at around the same temperature. However due to the error in temperature measurement between the dilatometry and ROT sample, there is room for variability in the temperature at which the experimental ZCF increases due to phase transformation. The peak ZCF from the model does not agree with the experimental data. This is due the modelled data not being correct as the phase angles with frequency do not follow the expected trend. Figure 73 shows the modelled phase angle at peak permeability during phase transformation for the 3mm mild and for the 3mm high carbon steel. The predicted permeability for the 3mm mild steel is significantly higher than for the high carbon steel which is expected as the 3mm mild consists of a predominantly ferrite with some pearlite while the high carbon steel is fully pearlitic [26]. It is expected that the phase angles would become more negative rotating between 0 and -180 degrees [6] which is shown for the modelled high carbon data. However, for the 3mm mild the phase angle initially decreases but then there is an increase in phase angle between 1500 and 3000 Hz. This is followed by the phase angle decreasing with frequency. This trend in phase angle for the 3mm mild modelled data may be due to a higher mesh being required to solve for the higher permeabilities exhibited by mild steels at high temperatures, but the modelling station used did not have the capability to do this.

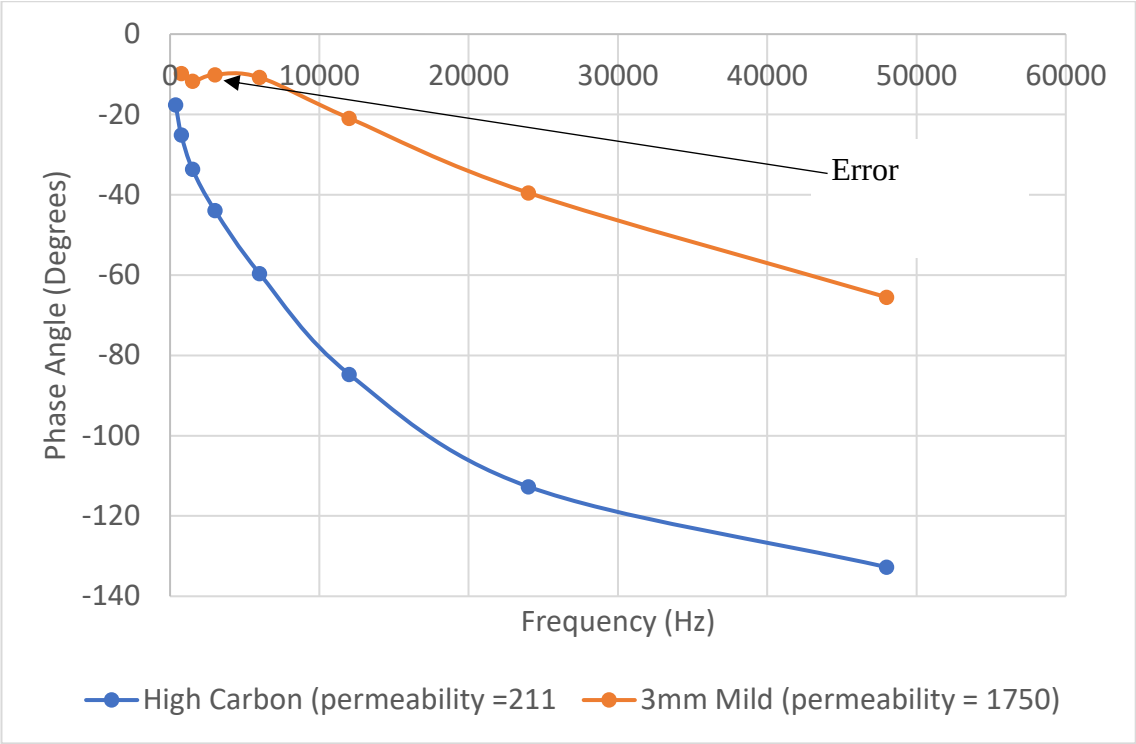

Figure 73. Modelled phase angle with frequency for 3mm mild and 3mm high carbon at their peak effective permeability during transformation (calculated by power law). Error in 3mm mild steel data is indicated.

8.1.2 6mm Mild Steel

8.1.2.1 Microstructural Characterisation

The microstructural state of the 6mm mild steel in the as received condition and after heat treatment on the ROT has been evaluated and is shown in figures 74-77. 500 × 500 mm plate samples were heated to 980°C in the furnace and allowed to cool in air while being measured by the EMspec® sensor. The microstructure for the 6mm mild steel in the as received condition consists of ferrite with a random distribution of bainite. Figures 75-77 show that the microstructures following heat treatments for tests 1, 2 and 3 consist a ferrite matrix with banded pearlite (with possible small amount of bainite); areas with higher bainite fraction are shown in figure 78 for tests 1 and 3. The grain structure also appears to be coarser in the after heat treatment microstructures compared to the as received microstructure. The after-heat treatment microstructure from the ROT agrees with the microstructure after dilatometry heat treatment (figure 79). As discussed in section 8.1.1, the formation of ferrite at the surface of a steel can occur during heat treatment due to

decarburisation and this can affect the resultant EM sensor signals measured for the steel [91-93]. Therefore, optical micrographs of the top and bottom surfaces of the plates are shown in figures 80-82. All three heat treated samples show evidence of decarburisation with regions of ferrite (little to no pearlite) located at both the top and bottom surfaces of the samples. The ferrite fractions in the 6mm mild steel in the as received condition, after heat treatments for tests 1-3 and dilatometry is shown in table 6. The phase fractions for the as received sample and after heat treatments (ROT and dilatometry) for tests 1 and 3 are very similar all ranging from 79-82%.

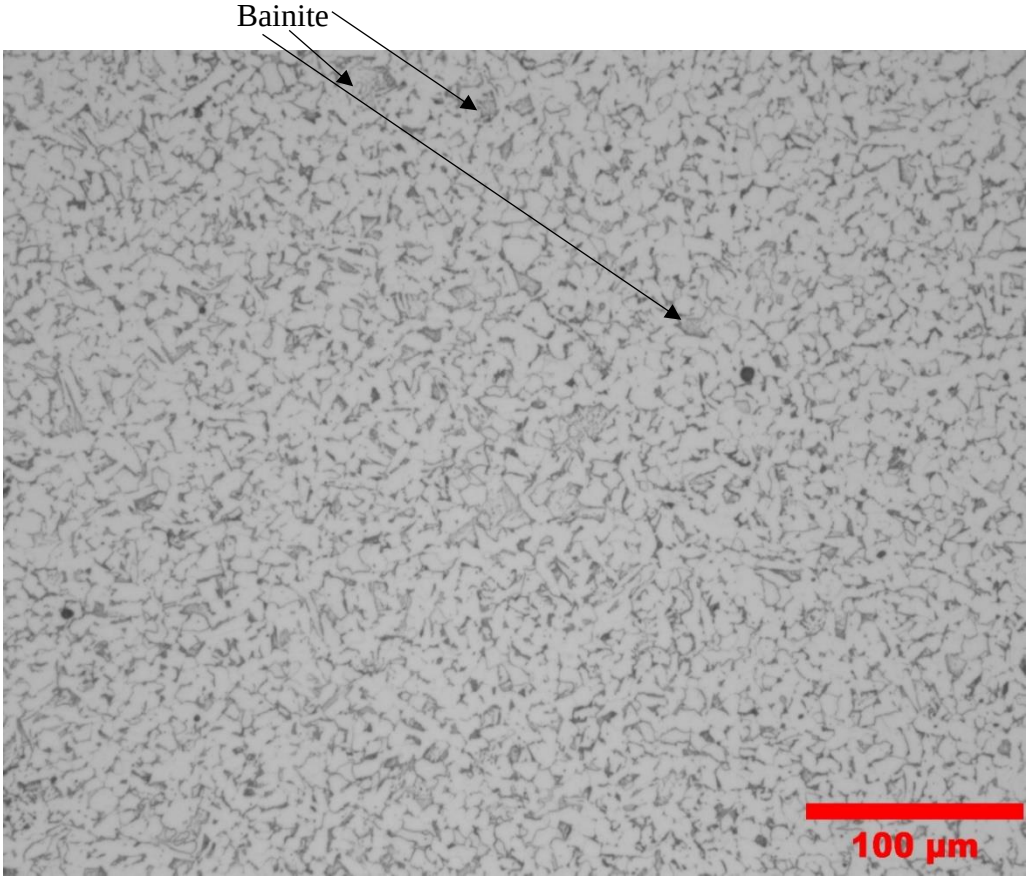

Figure 74. Optical microstructure at 20× magnification of 6mm mild steel in the as received condition. Bainitic regions have been indicated using arrows.

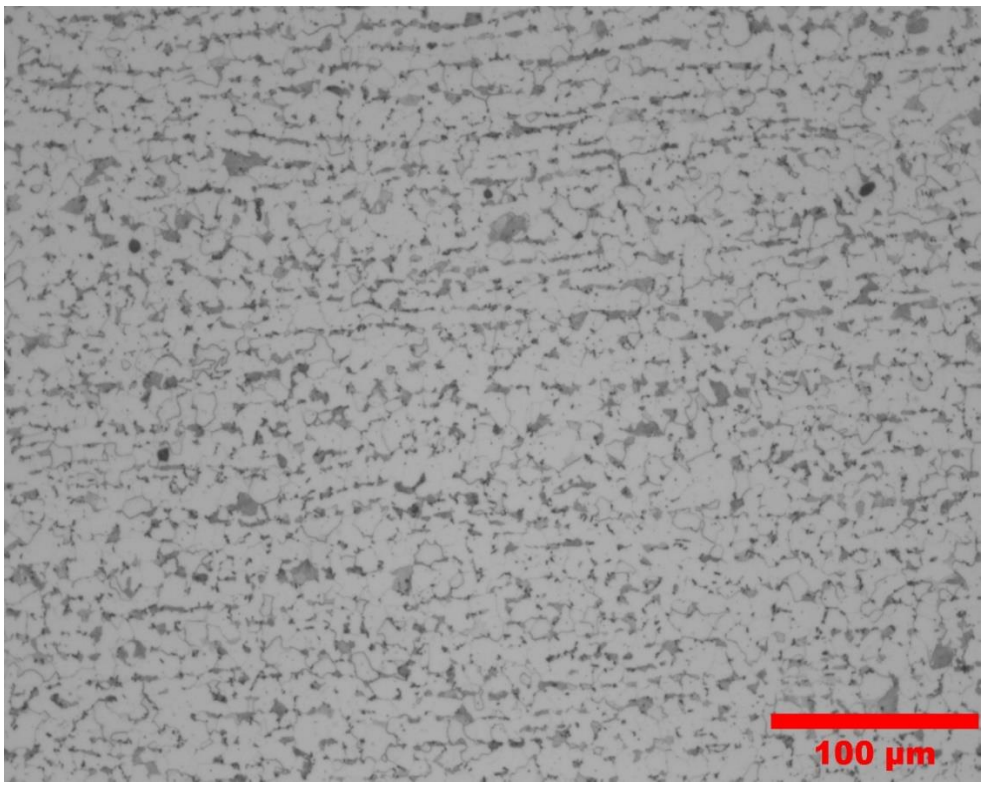

Figure 75. Optical microstructure at 20× magnification of the 6mm mild steel after heat treatment for test 1.

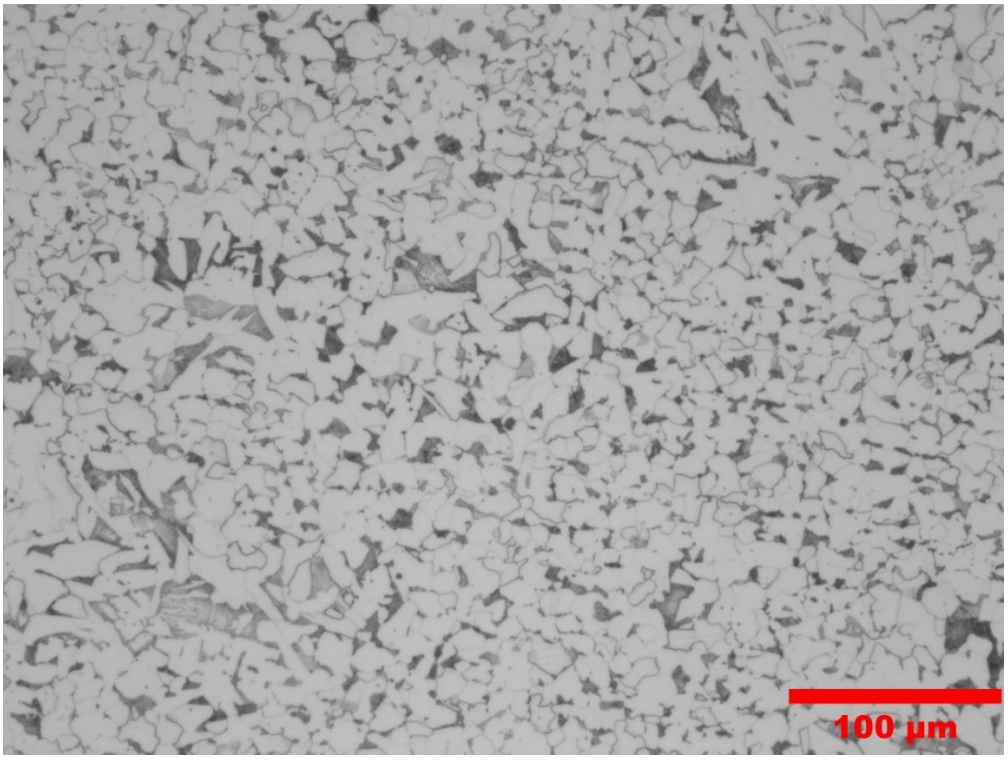

Figure 76. Optical microstructure at 20× magnification of a 6mm mild steel after heat treatment for test 2.

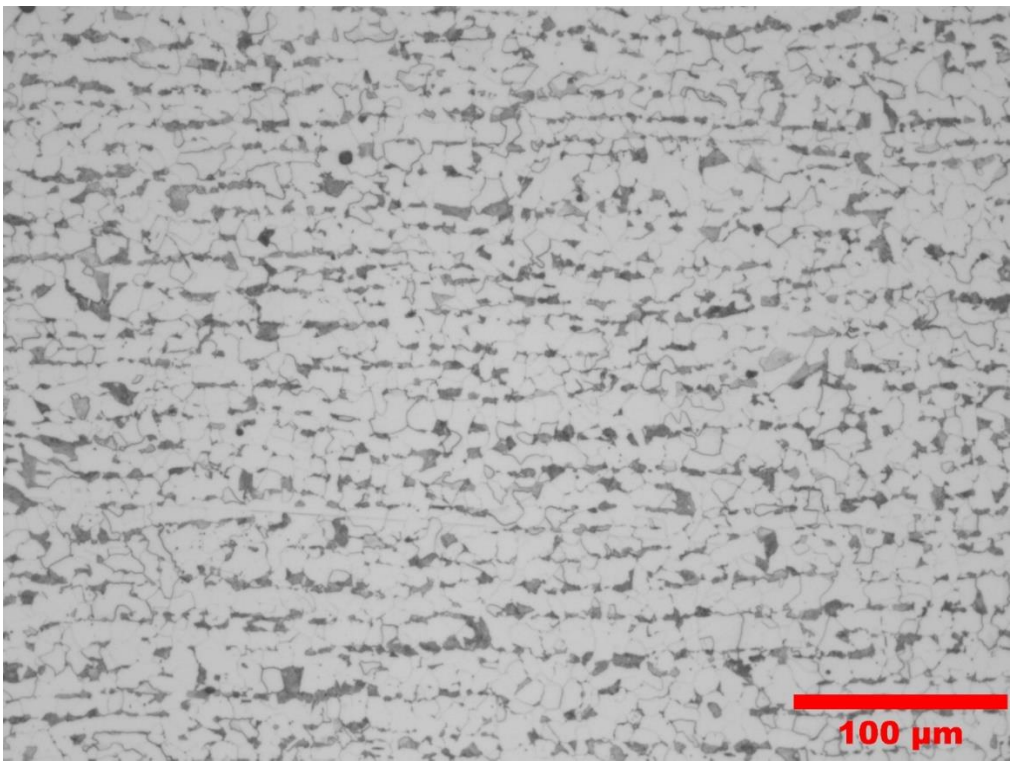

Figure 77. Optical microstructure at 20× magnification of a 6mm mild steel after heat treatment for test 3.

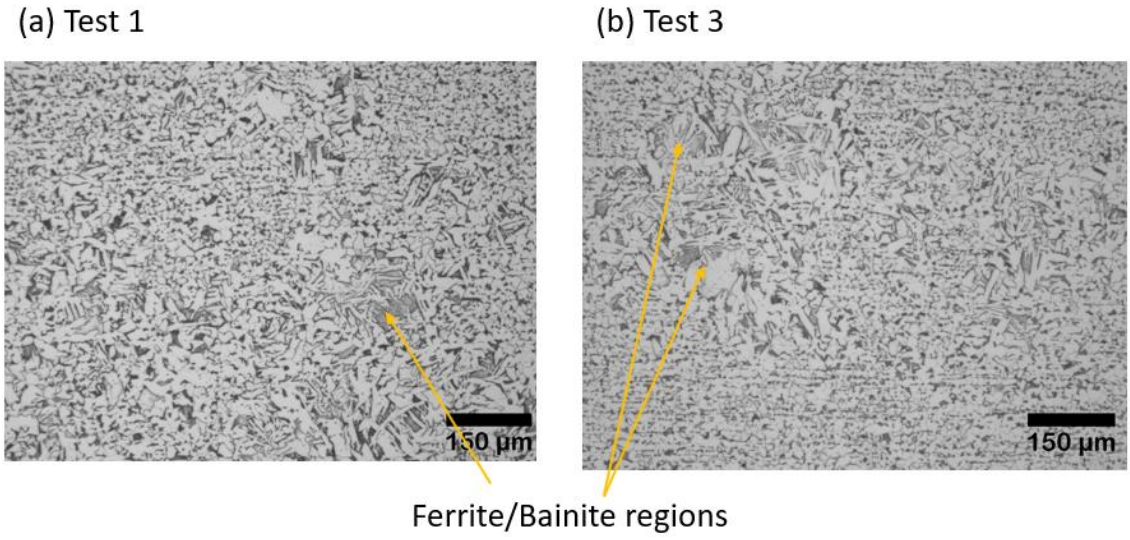

Figure 78. Optical microstructures at 10× magnification for (a) 6mm mild steel test 1 and (b) 6mm mild steel test 3. Regions with ferrite/bainite microstructure marked using yellow arrows.

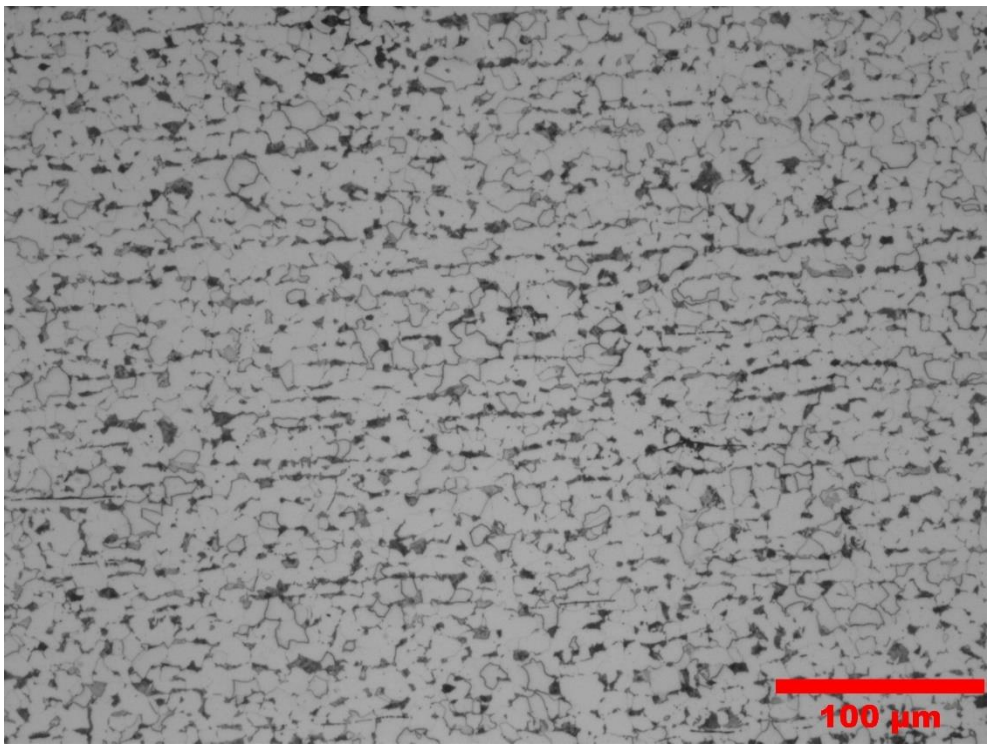

Figure 79. Optical microstructure at 20× magnification of the 6mm mild steel following dilatometry heat treatment.

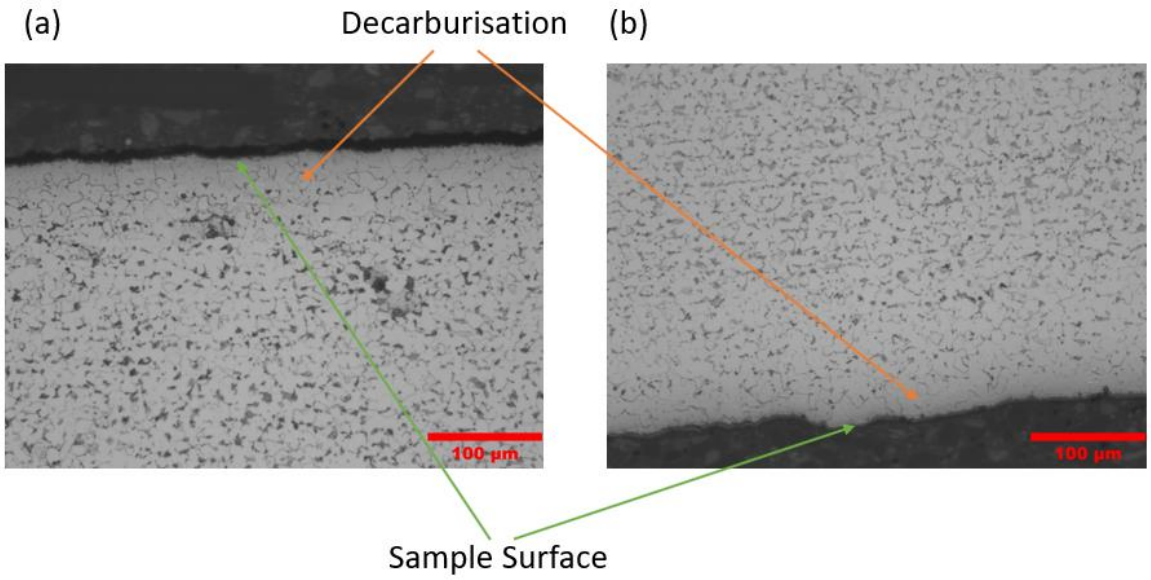

Figure 80. Optical microstructures at 20× magnification looking at top surface (a) and bottom surface (b) of the 6mm mild steel used in test 1. Decarburisation and sample surface are indicated using the coloured arrows.

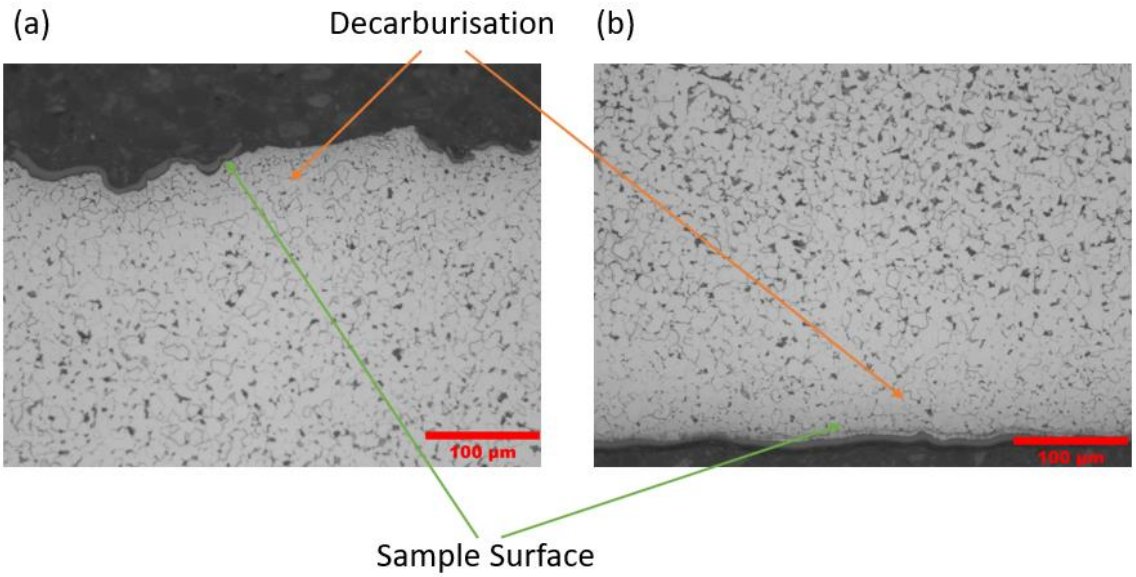

Figure 81. Optical microstructures at 20× magnification looking at top surface (a) and bottom surface (b) of the 6mm mild steel used in test 2. Decarburisation and the sample surface are indicated using the coloured arrows.

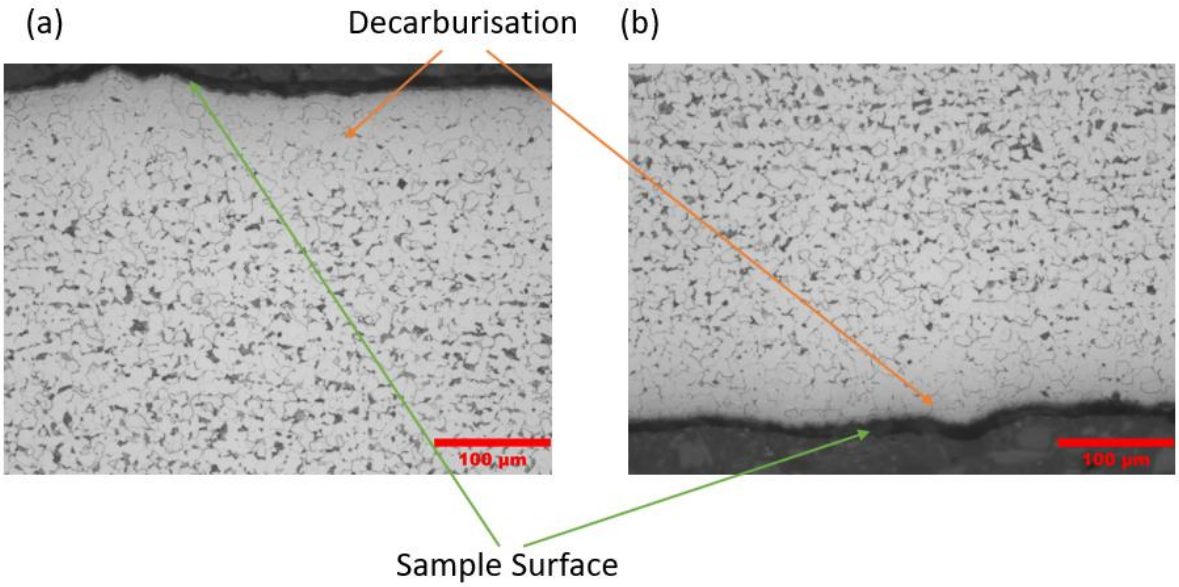

Figure 82. Optical microstructures at 20× magnification looking at top surface (a) and bottom surface (b) of the 6mm mild steel used in test 3. Decarburisation and sample surface are indicated.

Table 6. Ferrite fractions in % for 6mm mild steel in as received condition, after 3 heat treatments following EMspec® sensor measurements and dilatometry heat treatment.

As Received	Test 1	Test 2	Test 3	Dilatometry
79.61 ± 1.72	81.26 ± 0.45	80.37 ± 1.84	81.70 ± 0.36	81.45 ± 0.71

8.1.2.2 Cooling Trajectories

The cooling trajectories for 6mm mild steel from tests 1-3 are shown in figures 83-85. There is an initial spike in temperature difference for tests 1-3 which is caused by thermocouple 1 leaving the furnace before thermocouple 2, therefore thermocouple 1 will start cooling faster than thermocouple two initially until thermocouple 2 leaves the furnace also. All 3 tests show evidence of latent heating firstly at approximately 740°C which is consistent with a ferritic transformation. The 2nd latent heating that occurs for tests 1-3 occurs at approximately 640°C which would be consistent with transformation to pearlite. When latent heating occurs at both 740°C and 640°C this causes the temperature difference between the two thermocouples for tests 1-3 to become closer together (appears as 2 spikes). This is due to thermocouple 1 going through latent heating before thermocouple 2. This causes thermocouple 1 temperature to become closer to thermocouple 2 as its cooling rate has decreased due to latent heating. However, as thermocouple 2 goes through latent heating, then the temperature difference restores as at this point thermocouple 1 will be cooling faster than thermocouple 2 as its latent heating has ended and cooling rate has increased again. This suggests that the area of the samples around thermocouple 1 is transforming at a slightly different time to thermocouple 2. The temperature discrepancy between thermocouples 1 and 2 for the 3 tests generally sits between 10 and 20°C and decreases as the overall temperature of the sample decreases with cooling time.

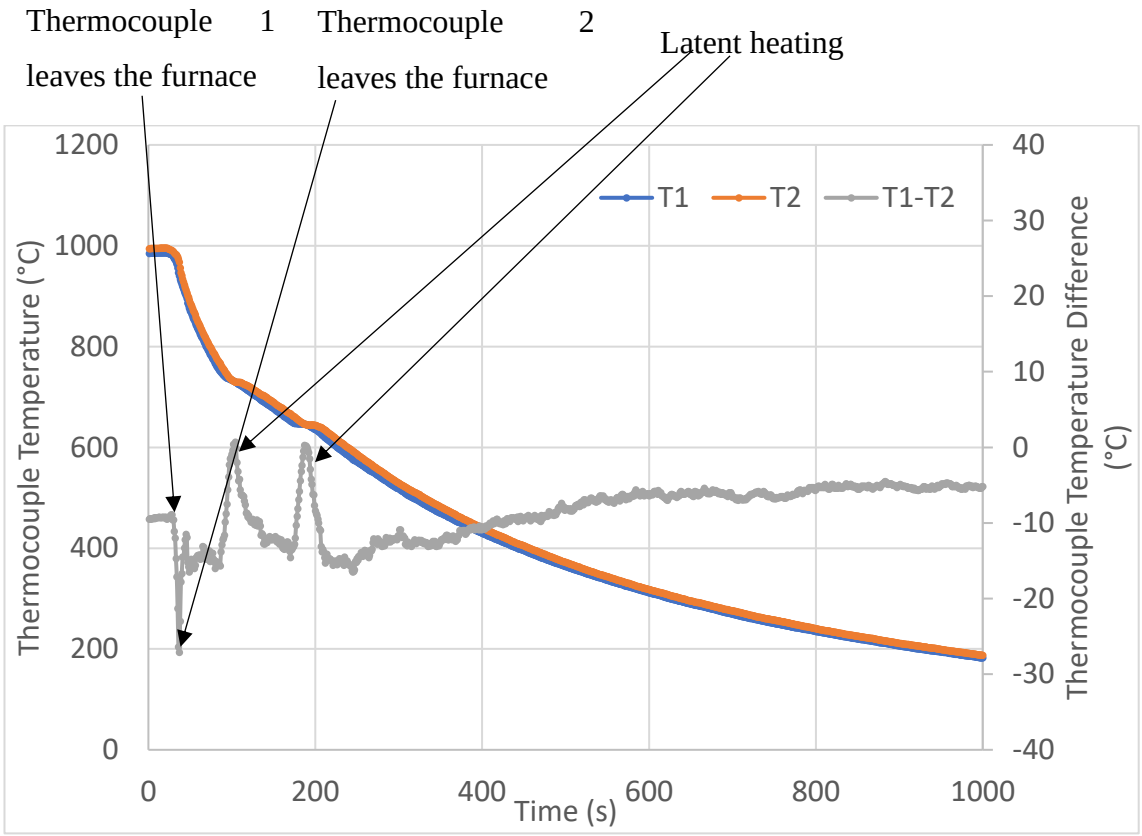

Figure 83. Cooling trajectory for 6mm steel during test 1. Thermocouple 1 (T1) and thermocouple 2 (T2) are plotted along with temperature difference between the two thermocouples (T1-T2). The points at which thermocouples 1 and 2 leave the furnace, and latent heating occurs are indicated on the T1-T2 graph.

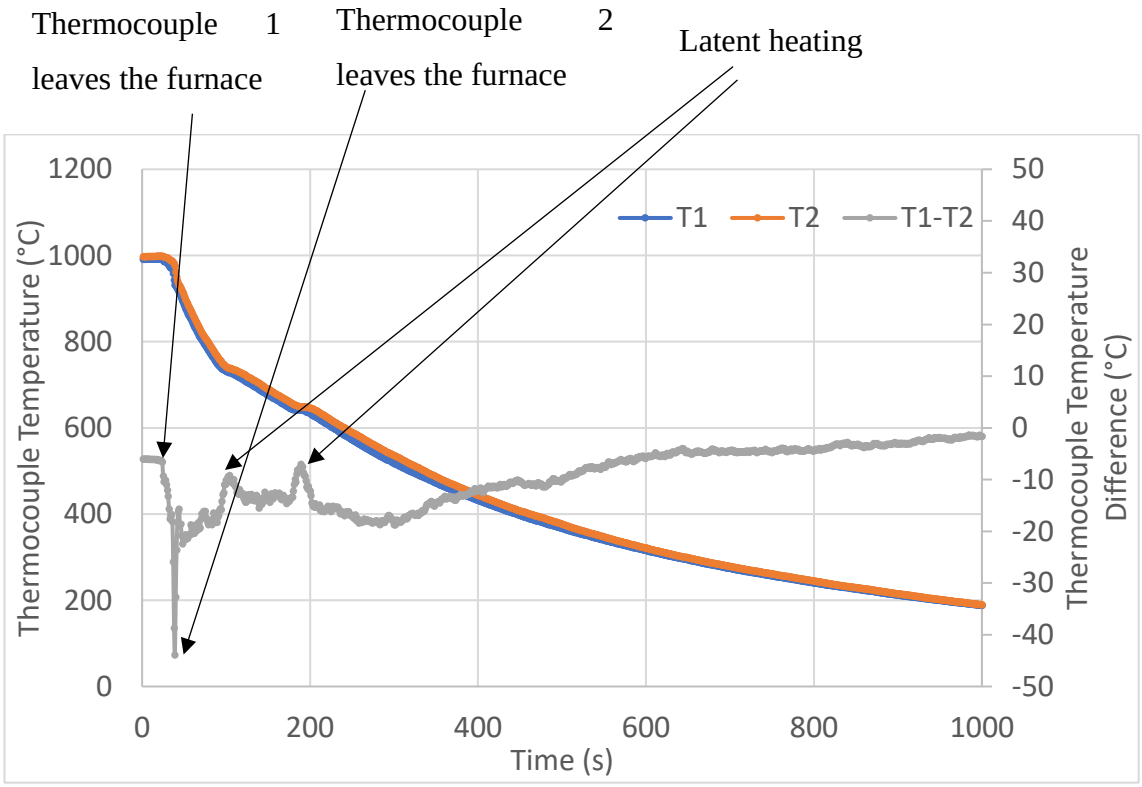

Figure 84. Cooling trajectory for 6mm steel during test 2. Thermocouple 1 (T1) and thermocouple 2 (T2) are plotted along with temperature difference between the two thermocouples (T1-T2). The point where thermocouples 1 and 2 leave the furnace and latent heating occurs is indicated on the T1-T2 graph.

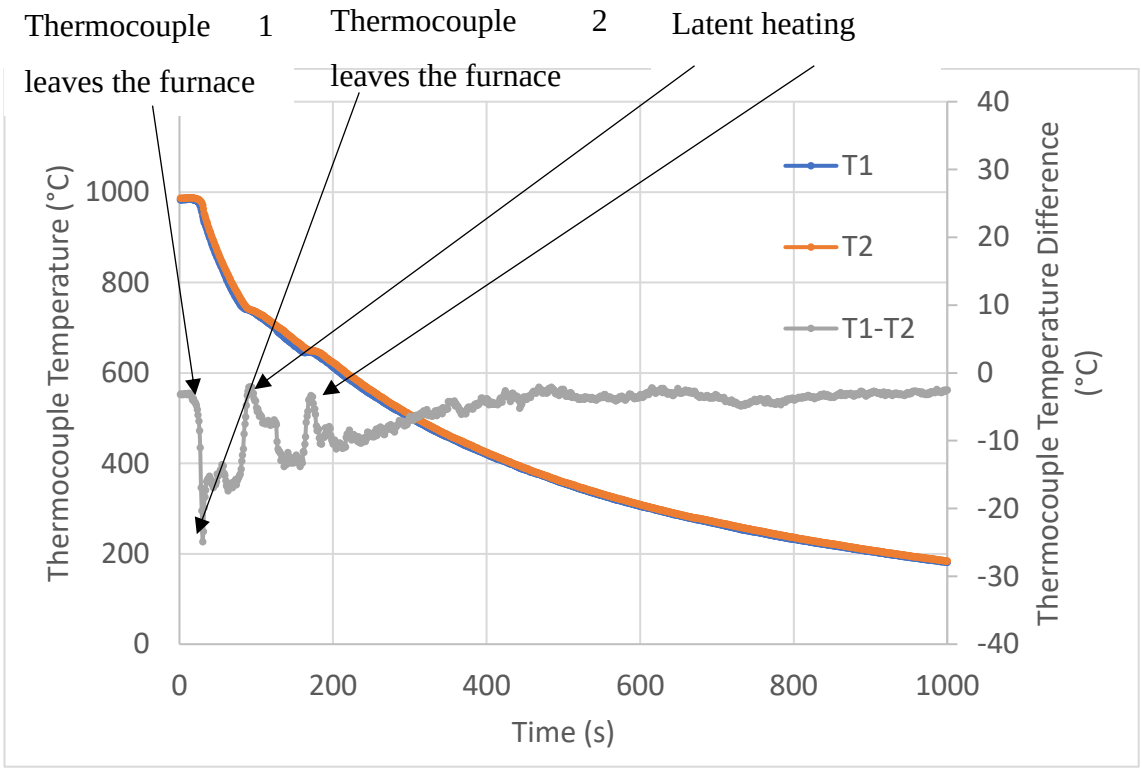

Figure 85. Cooling trajectory for 6mm steel during test 3. Thermocouple 1 (T1) and thermocouple 2 (T2) are plotted along with temperature difference between the two thermocouples (T1-T2). The point at which thermocouples 1 and 2 leave the furnace and latent heating occurs is indicated on the T1-T2 graph.

Figure 86 shows the average cooling trajectories for the 3 EMspec® sensor tests on the 6mm mild steel while cooling in air. The graph shows that the cooling rates are very repeatable with tests 1 and 2 overlapping each other. Test 3 does appear to have a slightly faster cooling rate below 700°C. The cause of this is unknown as the procedure was the same for all 3 tests. Figure 86 shows two points during cooling where the temperature trajectory changes. This occurs at approximately 740°C and again at approximately 640°C and this is consistent for all three data sets. These changes in temperature trajectory are consistent with latent heating due to transformation to ferrite at the higher temperature and transformation to pearlite at the lower temperature.

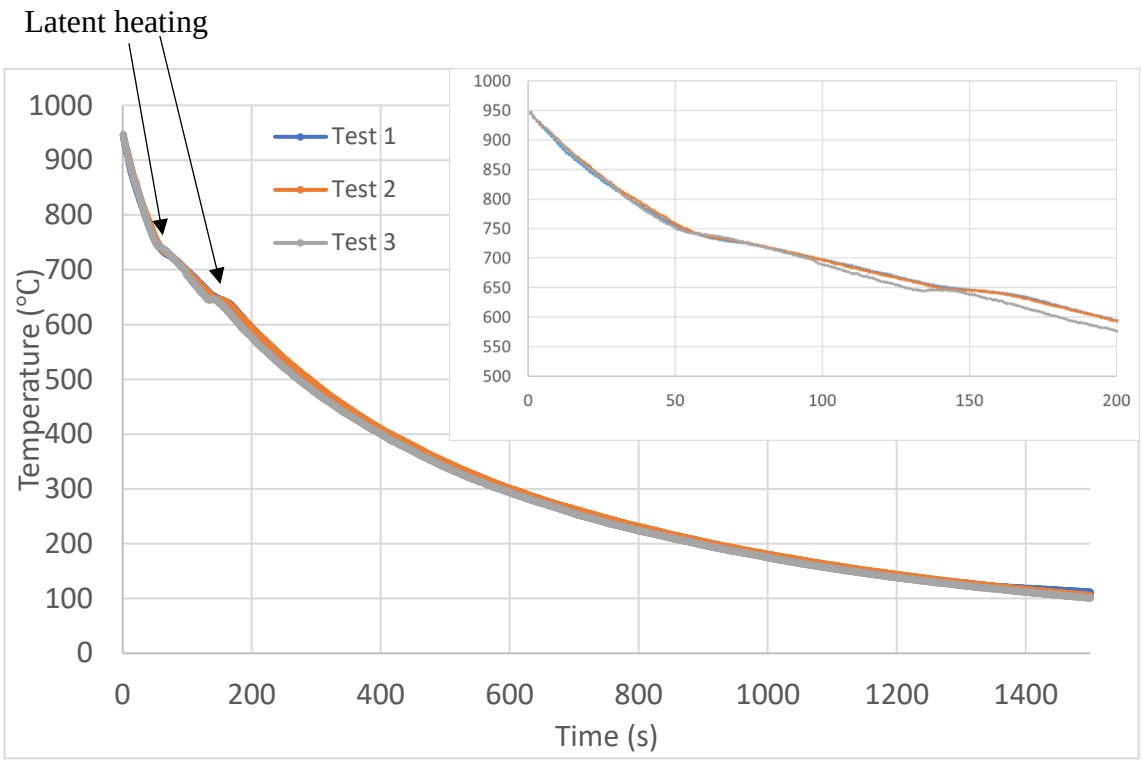

Figure 86. Average temperature of 6mm mild steel with time during cooling in air for EMspec® tests 1, 2 and 3. Expanded view is also shown at higher temperatures. The latent heating is indicated with the arrows.

8.1.2.3 EMspec® Sensor Results and Relation of ZCF to Phase Percentage Transformed and EMspec® Sensor Model

Figure 87 shows the measured and modelled ZCF with temperature for 6mm mild steel. Transformed percentage obtained from dilatometry is also plotted with temperature on the second Y axis. There is very good repeatability in measurement. At 800°C, the ZCF for all three tests is very low and this is due to the sample being austenitic at this temperature and therefore paramagnetic. The ZCF stays consistently low until approximately 750°C where the ZCF begins to increase very sharply. This signals that transformation has begun, and the sensor is detecting bulk ferromagnetic phase. This would be consistent with a ferrite transformation for this steel. The signal for the three tests continues to increase until a peak at around 710°C with ZCFs of approximately 78kHz for test 1 and 71 kHz for tests 2 and 3. Following the ZCF peaks, the ZCF begins to decrease with temperature until approximately 650°C where the trajectory of ZCF

decrease with temperature becomes steeper. This is likely because in the temperature 710 – 650°C range, the steel has not fully transformed. The remaining austenite is likely transforming to pearlite here. In this instance, the increase in permeability due to ferromagnetic pearlite forming is not as significant as the decrease in permeability due to decrease in temperature. Therefore, the effective permeability decreases and therefore so does the ZCF. This results in there being a less steep decrease in ZCF between 710°C and 650°C. After 650°C, the ZCF continues to decrease with temperature due to decrease in permeability and resistivity.

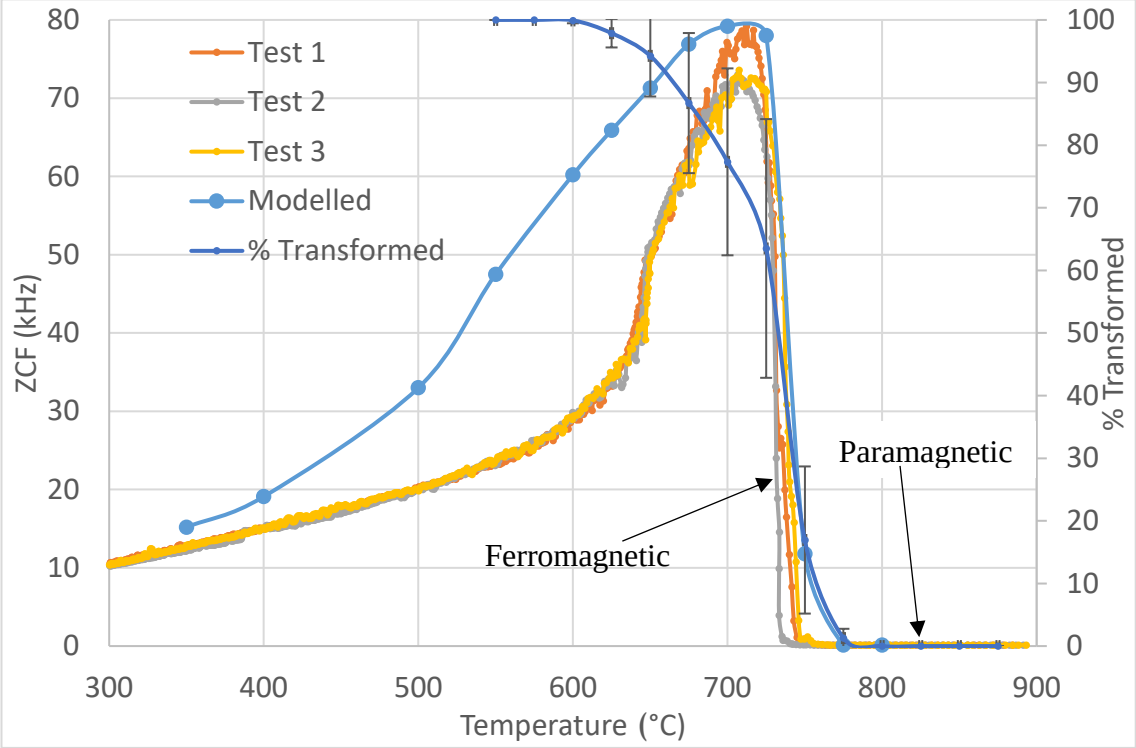

Figure 87. Measured and modelled ZCF with temperature for 6mm mild steel. Transformed percentage obtained from dilatometry also plotted with temperature on the second Y axis. The points at which the steel is paramagnetic and ferromagnetic are indicated.

Phase percentage transformed has been obtained from dilatometry measurements and plotted on the secondary Y axis against temperature in figure 87. The phase percentage transformed only considers ferrite pearlite transformations as transformation to bainite appears to have little effect on the ZCF as the bainite fraction, qualitatively, is very low. The ZCF has been plotted on the primary Y axis for relation to phase percentage transformed with temperature. It can be seen from figure 87 that the ZCF for all three tests begins to increase signalling the presence of ferromagnetic ferrite phase when the

phase percentage transformed is approximately 35%. This agrees with Hao et al. [37] where it was showed that the permeability of room temperature austenite-ferrite fractions does not show a significant change in permeability until the ferrite percentage reaches 35% due to the need for ferrite connectivity in the microstructure – this is when considering random distribution of ferrite fraction [37]. However, there is some temperature inhomogeneity in the samples during cooling, as shown from figures 83-85 as opposed to a small dilatometry sample where the temperature will be uniform. When taking this into account there could be some variability in the temperature where the ZCF begins to increase due to the presence of ferromagnetic phase. For figure 87, it appears that the ZCF peaks at approximately 75% transformed ferrite fraction. This is consistent with most of the ferrite transformation being completed, as the after-heat treatment microstructures on the ROT show an approximately 81% ferrite fraction in table 6. Following the ZCF peak, the ZCF decreases with temperature as the remaining 20% austenite transforms to pearlite. The decreasing ZCF trajectory becomes steeper at 650°C. This coincides with the phase transformed percentage being around 94% transformed, however the repeatability errors on the phase fraction obtained from dilatometry show variability of transformed percentage up to 6%. This means that at this temperature the steel could be fully transformed or approximately 88% transformed.

Figure 87 shows that the point at which the modelled ZCF increases due to transformation occurs earlier than for the experimental data. This is due to the nature of the calculation of effective permeability for input into the EMspec® model. The power law with a fitting factor of 1/3 (discussed in section 5.5.3.) was used to calculate effective permeability. It has been shown a study by Yin et al. [87, 88] that there is an offset between power law permeability and permeability predicted using microstructure model and EM sensor model. This is due to the power law not considering the need for connective ferrite to be present before there is a significant change in permeability. The study by Yin et al. [87, 88] showed that the effective permeability for austenite ferrite phase balances did not show a significant increase until the ferrite percentage reached 35% for the FEM and microstructure models. This offset could be larger at higher temperatures due to the higher permeability of ferrite at higher temperatures. The modelled ZCF peak agrees well with the experimental data however below 700°C there exists an offset between the modelled data and experimental data which decreases as the temperature decreases. This offset is because the modelled data is likely incorrect. Like for the 3mm mild steel discussed in 8.1.1.4, there is an unexpected trend in phase angle with frequency for the very high

permeability simulations. Figure 88 plots the modelled phase angle with temperature for the 6mm mild steel at its highest permeability during transformation. This has been compared with the peak permeability for the high carbon steel. For the high carbon steel, the phase angle become more negative with frequency which is expected [6]. However, like the 3mm mild steel simulation, the phase angle becomes more negative, then becomes more positive before becoming more negative again. This again may be due to the modelling station used to run these simulations not having the necessary specification to run a fine enough mesh for the higher permeabilities to be solved.

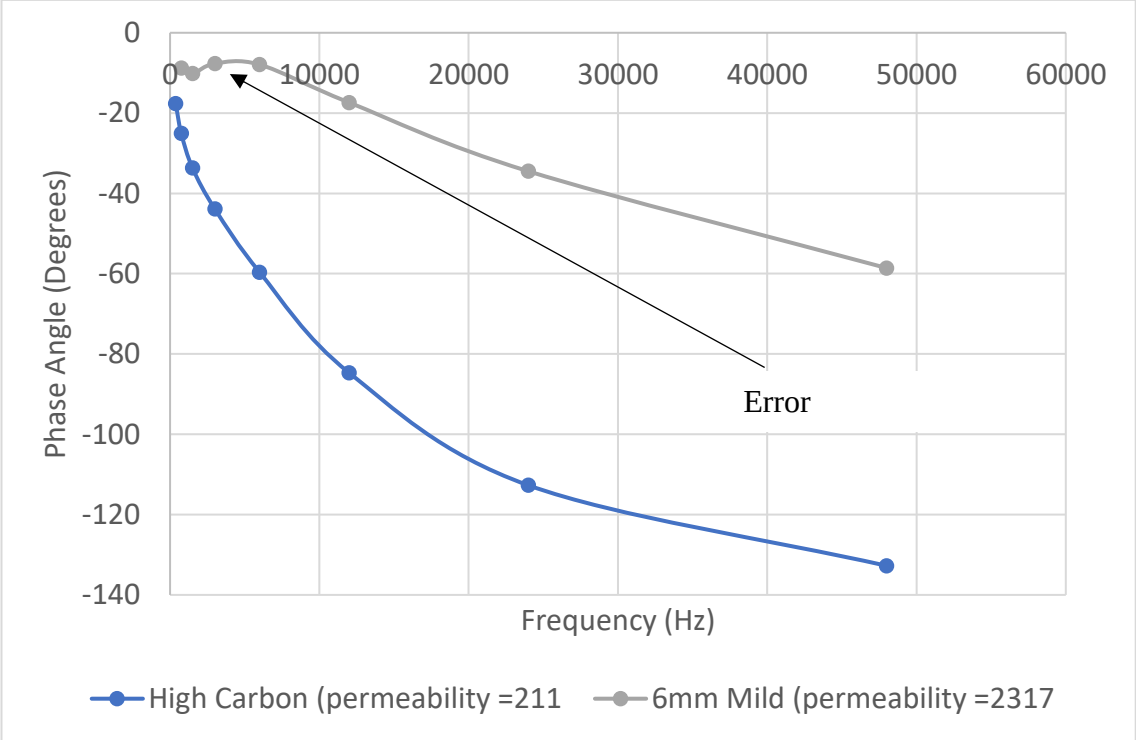

Figure 88. Modelled phase angle with frequency for 6mm mild and 3mm high carbon at their peak effective permeability during transformation (calculated by power law). The error in the data in indicated.

8.1.3 10mm Mild Steel

8.1.3.1 Microstructural Characterisation

Figures 89-92 show the microstructural state of the 10mm mild steel in the as received condition and after heat treatment on the ROT. 500 × 500mm plate samples were cooled in air while being measured using the EMspec® sensor following furnace heating to 980°C. The as received microstructure has a microstructure consisting of a ferrite matrix with a random distribution of pearlite and bainite. After heat treatment for tests 1, 2 and 3 the resulting room temperature microstructures consist of a ferrite matrix with banded pearlite. The three heat treated samples have a coarser grain structure than in the as received condition. The presence of ferrite at the surface can occur after high temperature heat treatments due to decarburisation, as discussed section 8.1.1.1 [91-93]. As this can affect EM sensor signals, micrographs of top and bottom surfaces have been taken and are shown in figures 93-95. Evidence of decarburisation (regions of ferrite with little or no pearlite) is shown in the microstructures for all three tests on the top and bottom surfaces. The microstructure following dilatometry heat treatment (figure 96) is like figures 90-92, and visibly has a coarser grain structure than the as received microstructure. Table 7 shows the ferrite fractions of the as received sample, after the three heat treatments on the ROT and after dilatometry heat treatment. The as received sample has a ferrite fraction of approximately 81% while the heat-treated samples (ROT and dilatometry) have slightly higher ferrite fractions at 85-86%. The slightly higher ferrite fractions are due to there being no bainite in the heat-treated microstructures.

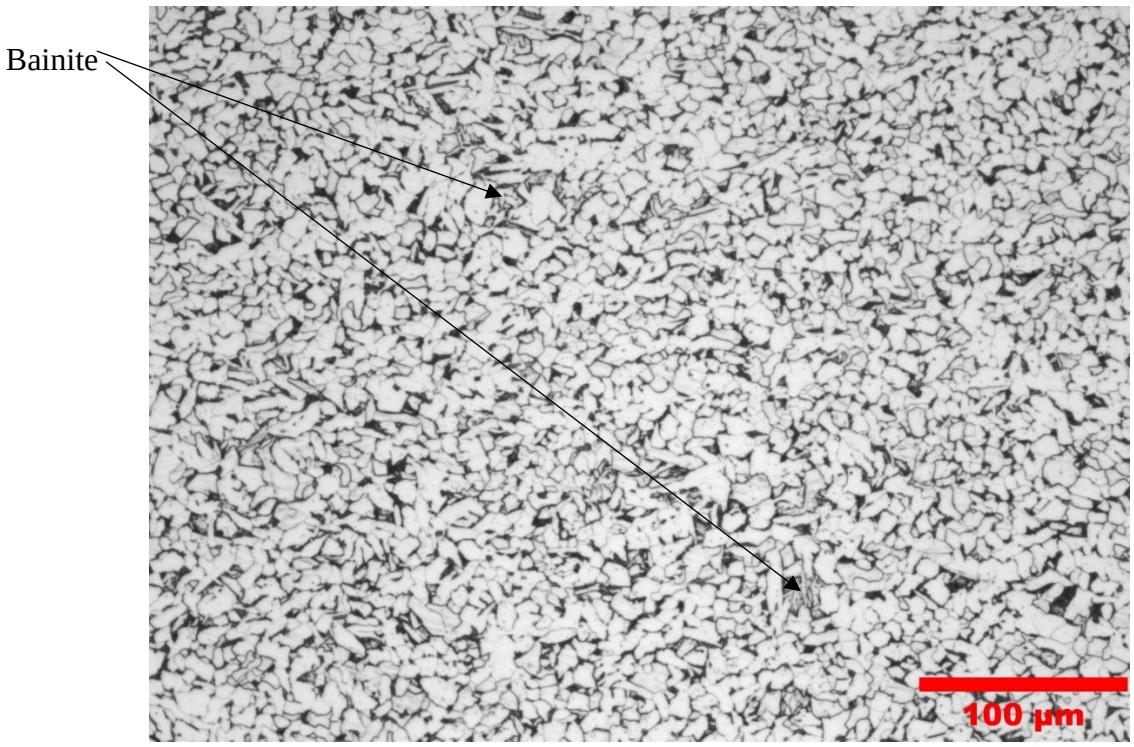

Figure 89. Optical microstructure at 20× magnification of a 10mm mild steel in the as received condition. Areas of bainite are indicated.

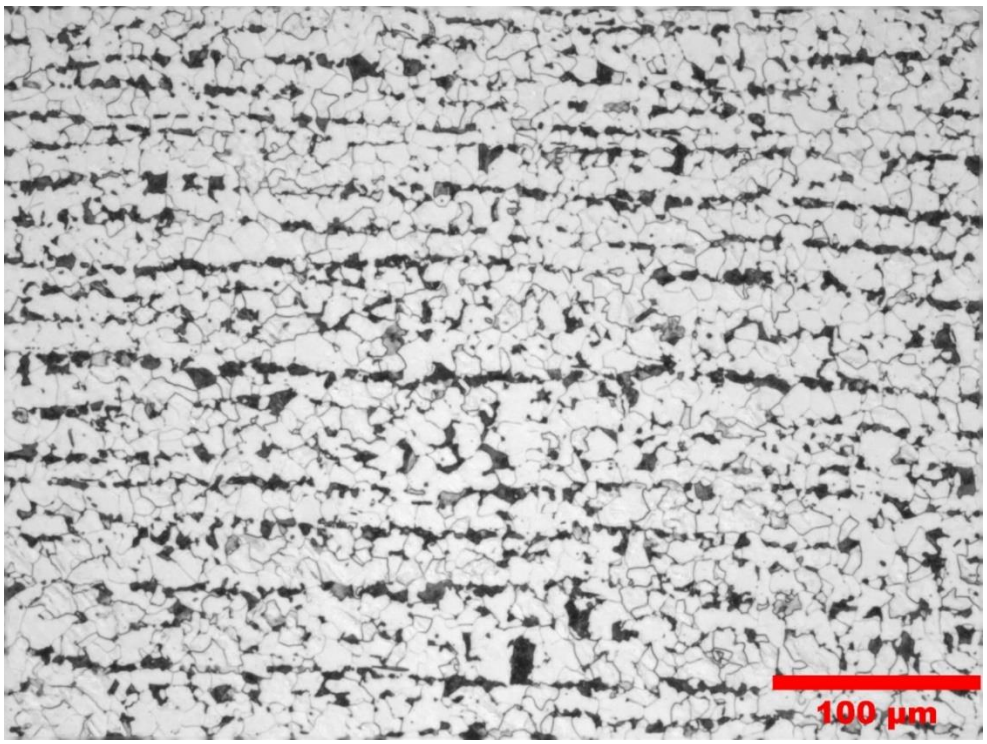

Figure 90. Optical microstructure at 20× magnification of a 10mm mild steel after heat treatment for test 1.

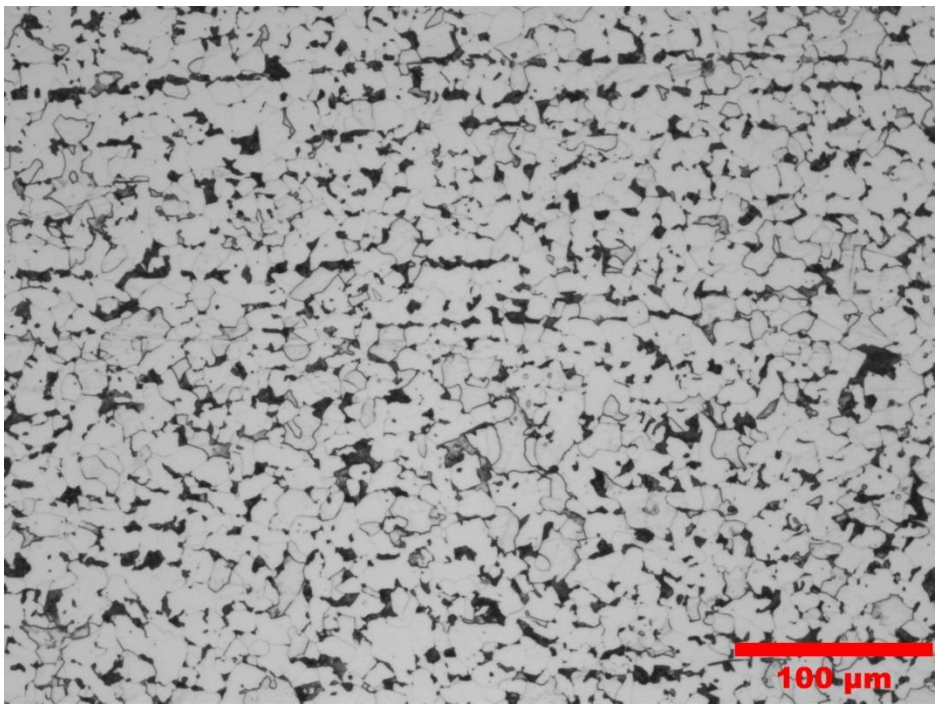

Figure 91.Optical microstructure at 20× magnification of a 10mm mild steel after heat treatment for test 2.

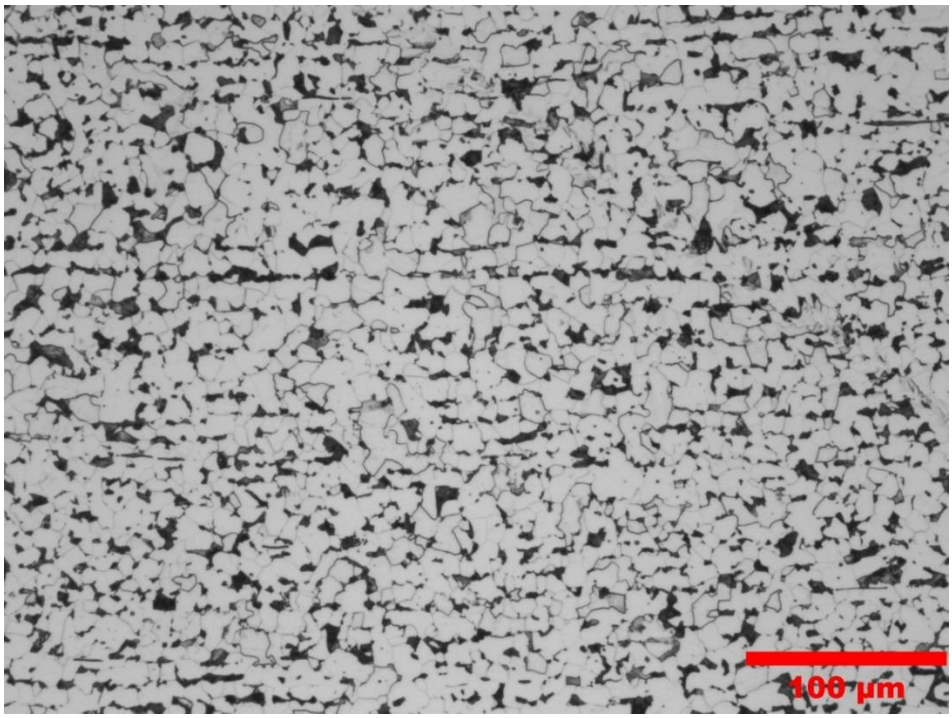

Figure 92. Optical microstructure at 20× magnification of a 10mm mild steel after heat treatment for test 3.

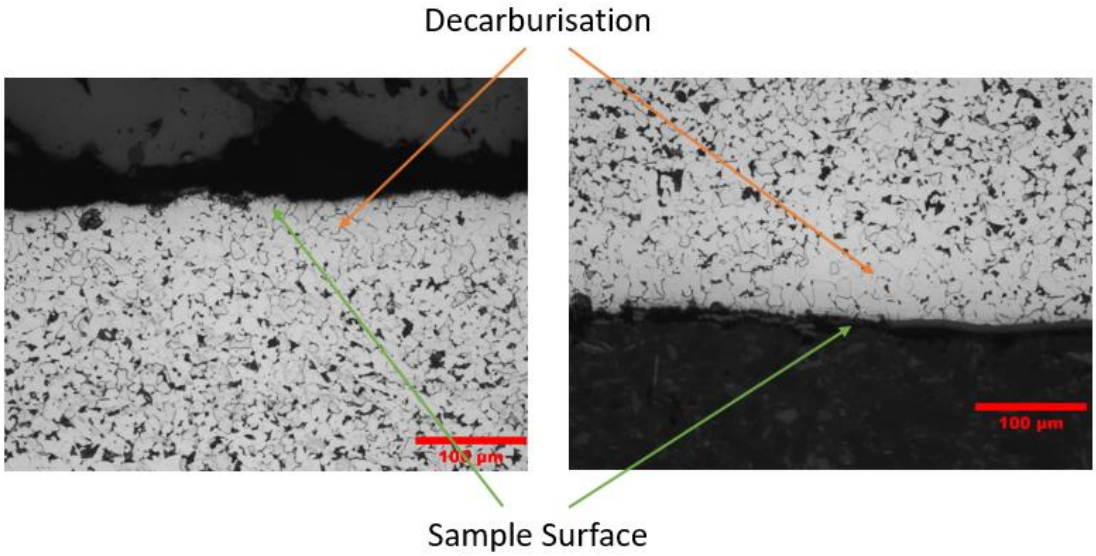

Figure 93. Optical microstructures at 20× magnification looking at top surface (a) and bottom surface (b) of the 10mm mild steel used in test 1. Sample surface and decarburisation regions are indicated using coloured arrows.

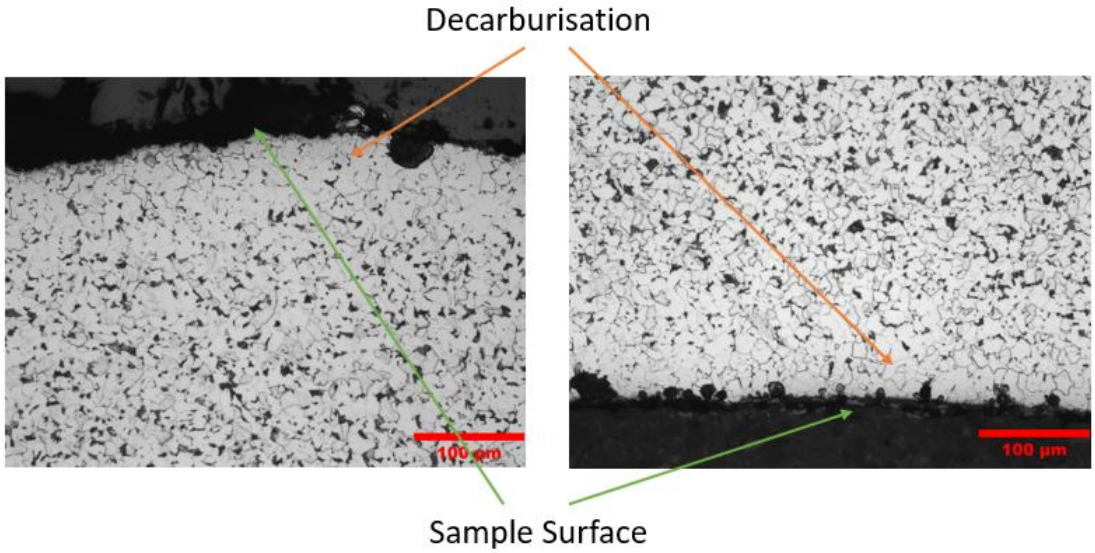

Figure 94. Optical microstructures at 20× magnification looking at top surface (a) and bottom surface (b) of the 10mm mild steel used in test 2. Sample surface and decarburisation regions are indicated using coloured arrows.

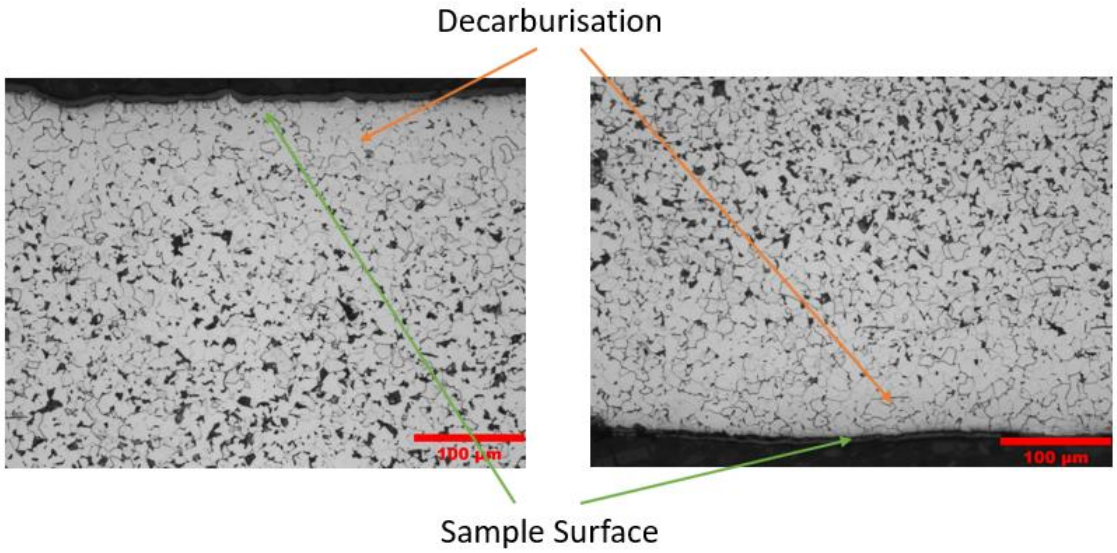

Figure 95. Optical microstructures at 20× magnification looking at top surface (a) and bottom surface (b) of the 10mm mild steel used in test 3. Sample surface and decarburisation regions are indicated using coloured arrows.

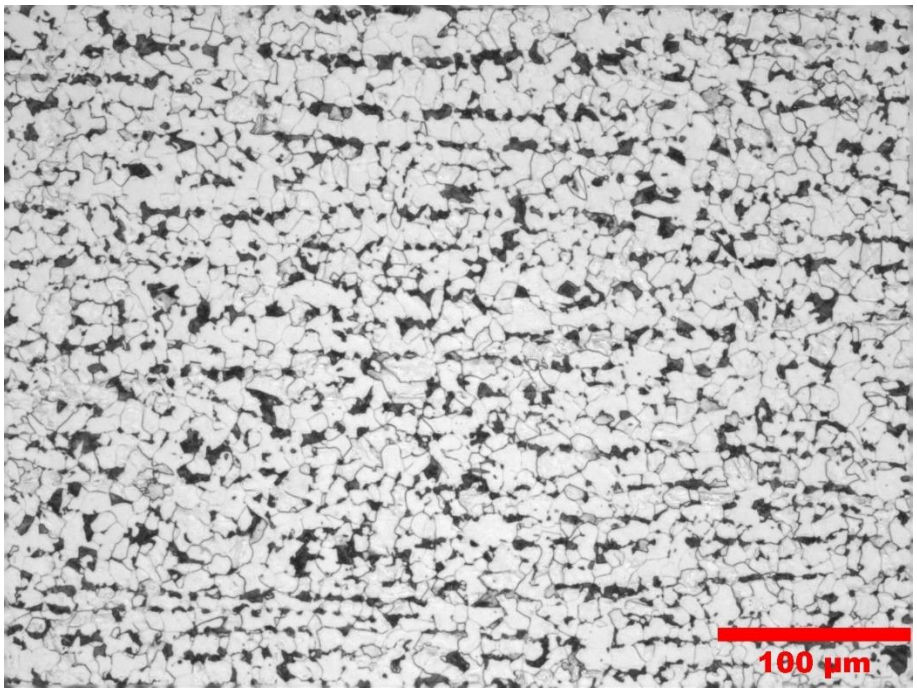

Figure 96. Optical microstructures at 20× magnification of a 10mm mild steel following dilatometry heat treatment.

Table 7. Ferrite fractions in % for the 10mm mild steel in the as received condition and after heat treatments (Tests 1 – 3) following EMspec® sensor measurements.

As Received	Test 1	Test 2	Test 3	Test 4
81.47 ± 0.52	85.41 ± 0.35	85.96 ± 0.94	86.19 ± 1.00	85.96 ± 0.90

8.1.3.2 Cooling Trajectories

The cooling trajectories for tests 1-3 and the temperature discrepancy between the two thermocouples (T1-T2) used on the samples is shown in figures 97-99. For all three tests at the start of the recorded cooling phase there is an initial spike in temperature difference between thermocouples 1 and 2. This is because thermocouple 2 is closer to the back of the furnace, while thermocouple 1 is closer to the furnace door. Therefore thermocouple 1 is always the first out of the furnace door which causes this initial spike in temperature difference as the part of the sample around thermocouple 1 is exposed to the atmosphere outside of the furnace first. As thermocouple 2 leaves the furnace and the area of the sample surrounding thermocouple 2 is exposed to the atmosphere outside of the door, its cooling rate increases quickly and the temperature discrepancy between thermocouples 1 and 2 decreases. Tests 1 and 3 show good temperature uniformity between the two thermocouples with the temperature difference measuring between 0 and 10℃ throughout cooling. Test 2 shows a larger temperature discrepancy when cooling between 980℃ and approximately 780℃. The experimental procedure for the tests were same so there is no obvious reason for the difference. Following this the temperature difference is between 10 and 20℃ when the sample is cooling between 780 and 600℃. From 600℃, the temperature difference between thermocouples 1 and 2 sits between 0 and 10℃ gradually decreasing towards 0 as the temperature of the sample decreases.

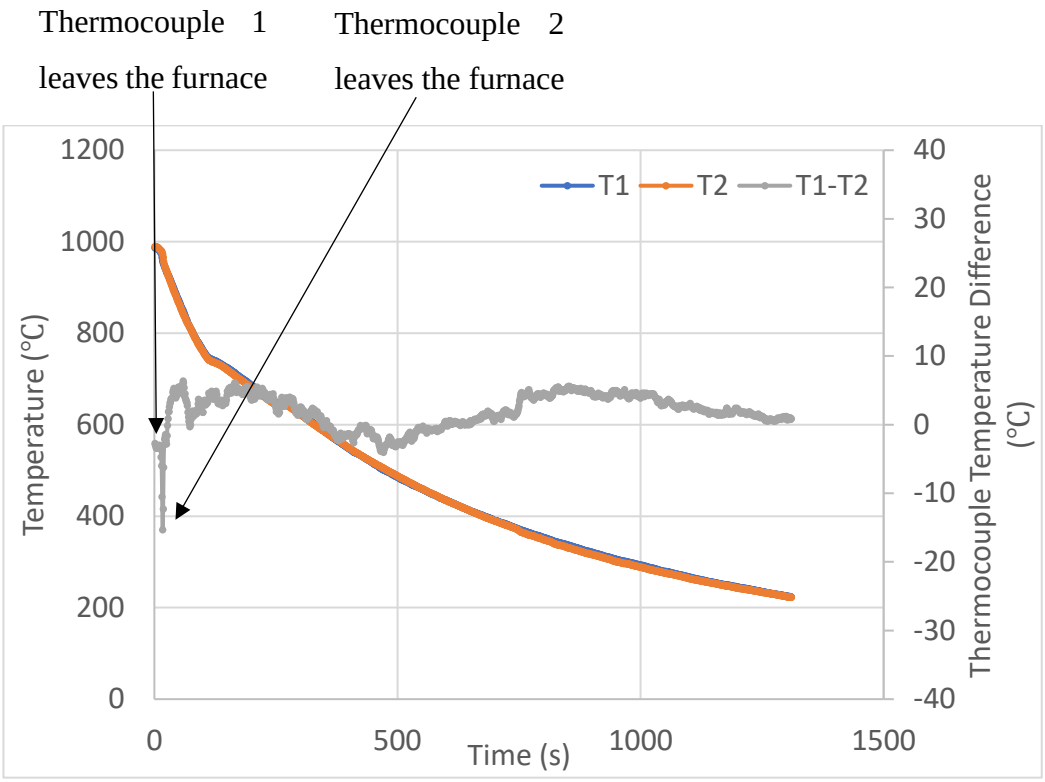

Figure 97. Cooling trajectory for 10mm steel during test 1. Thermocouple 1 (T1) and thermocouple 2 (T2) are plotted along with temperature difference between the two thermocouples (T1-T2). The points at which thermocouples 1 and 2 leave the furnace is indicated.

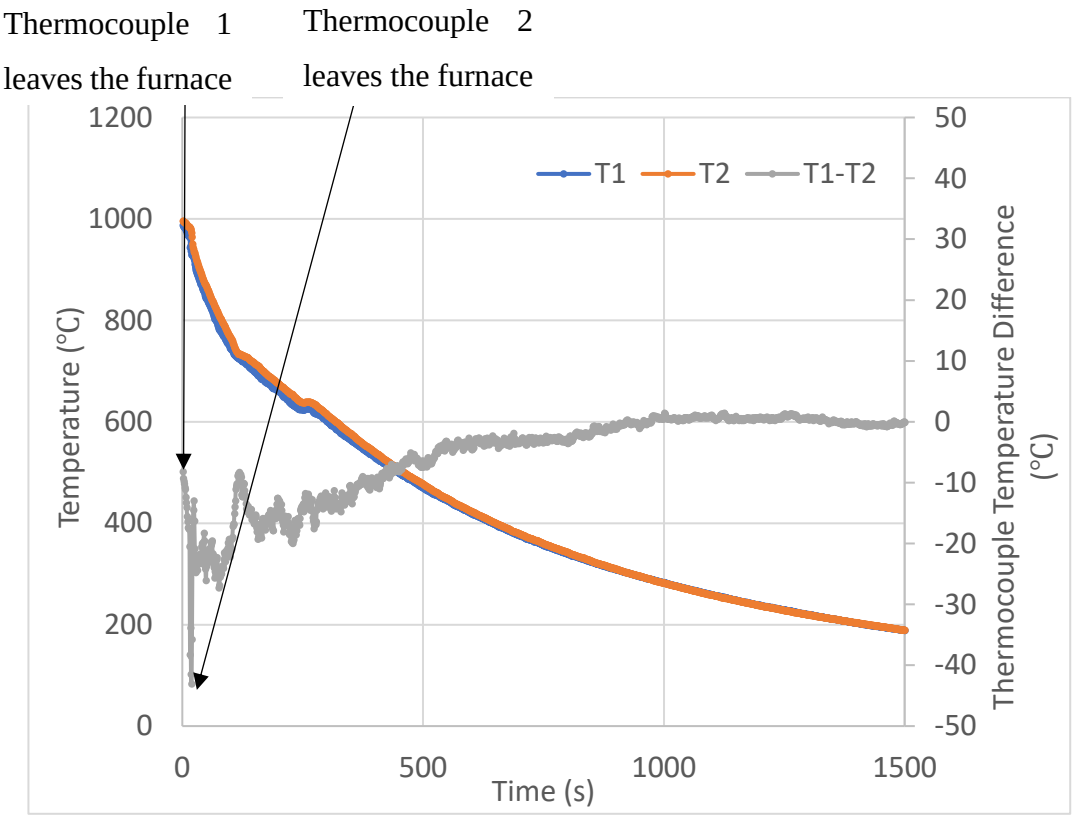

Figure 98. Cooling trajectory for 10mm steel during test 2. Thermocouple 1 (T1) and thermocouple 2 (T2) are plotted along with temperature difference between the two thermocouples (T1-T2). The points at which thermocouples 1 and 2 leave the furnace are indicated.

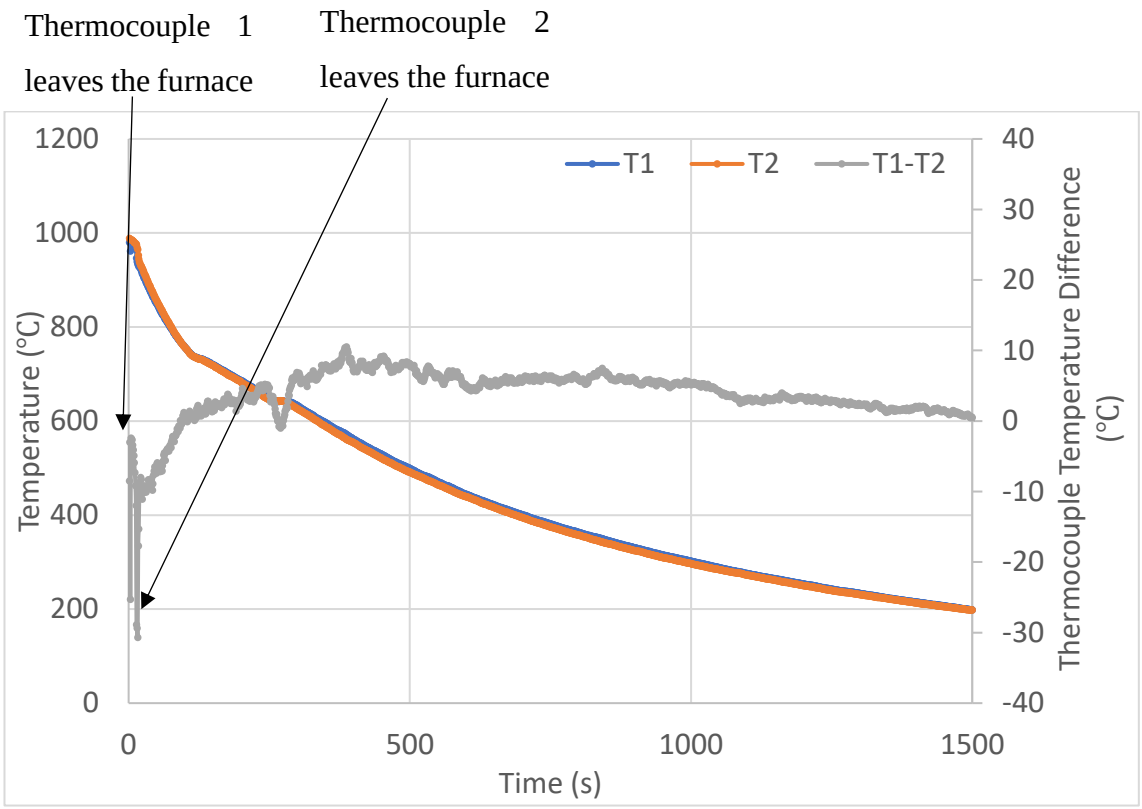

Figure 99. Cooling trajectory for 10mm steel during test 3. Thermocouple 1 (T1) and thermocouple 2 (T2) are plotted along with temperature difference between the two thermocouples (T1-T2). The point at which thermocouples 1 and 2 leave the furnace are indicated.

The average cooling trajectories for the three EMspec® sensor tests on the 10mm mild steel plate while cooling in air is shown in figure 100. The cooling trajectories for the 10mm mild steel are generally repeatable, with results for tests 1 and 3 overlapping each-other. Test 2 cools at a similar rate to tests 1 and 3 until approximately 750°C when latent heating begins. From 750°C test 2 appears to have a faster cooling rate than tests 1 and 3, however when looking at the temperature difference from figure 98, and this is also the test where the thermocouple difference was greatest perhaps suggesting non-uniformity for the plate, possibly due to differences in oxide cover. Figure 100 shows for all three tests that latent heating occurs and changes the cooling rate at approximately 750°C and again at approximately 650°C and this is consistent with a ferrite and pearlite transformations respectively.

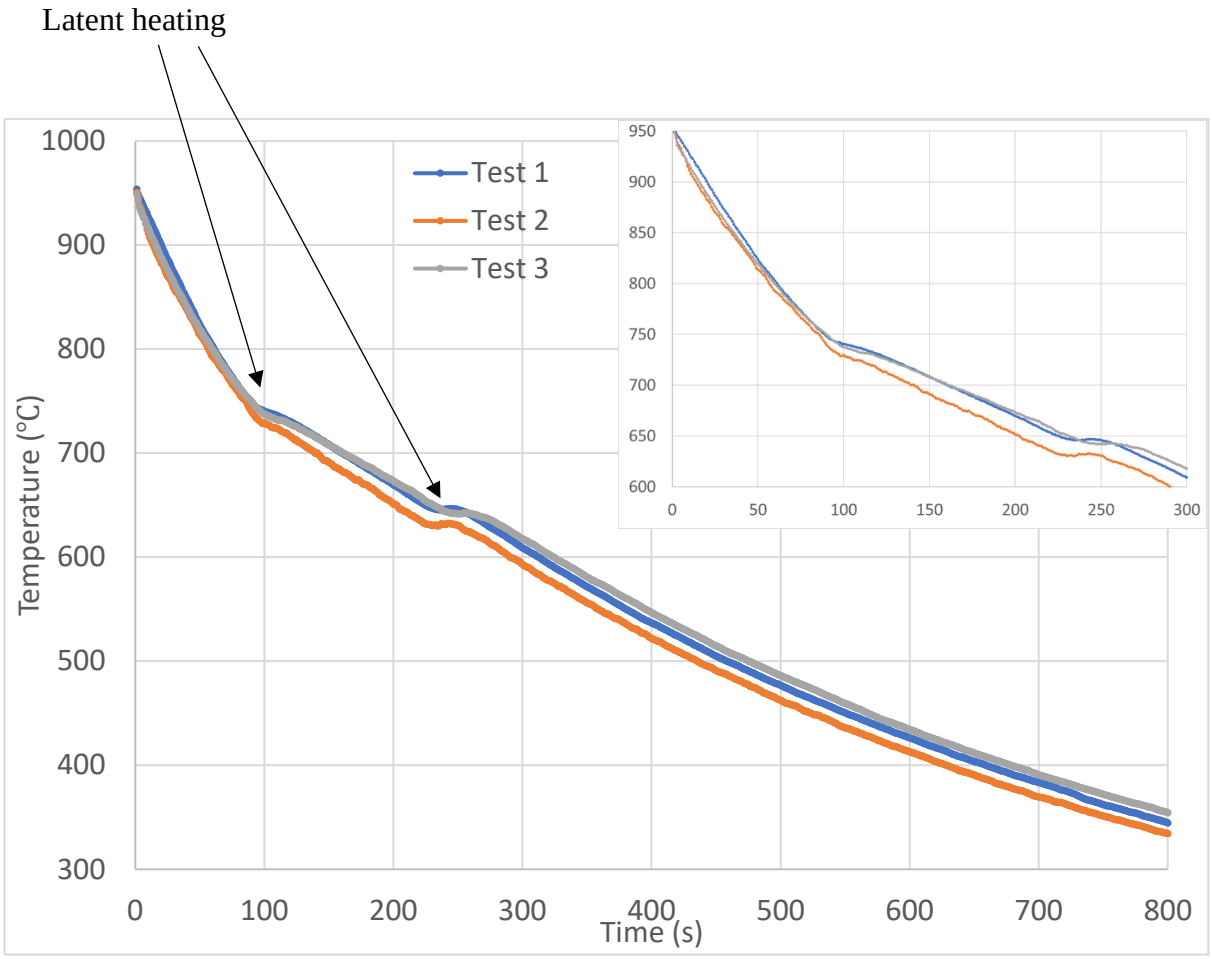

Figure 100. Average temperature of 10mm mild steel with time during cooling in air for EMspec® tests 1, 2 and 3. Expanded view is also shown at higher temperatures. The points at which latent heating occur are indicated.

8.1.3.3 EMspec® Sensor Results and Relation to Phase Fraction Transformed and EMspec® Sensor Model

The measured and modelled ZCF with temperature for 10mm mild steel are shown in figure 101. Transformed percentage obtained from dilatometry also plotted with temperature on the second Y axis. The results indicate very good repeatability in ZCF measurement. The ZCF at 800°C, where the sample is fully austenitic and therefore paramagnetic, is very low. The ZCF stays consistently low until approximately 750°C where the ZCF begins to increase very sharply. This signals that transformation has begun, and the sensor is detecting bulk ferromagnetic phase. This would be consistent with a ferrite transformation for this steel. The signal for the three tests continues to increase until a peak at approximately 725°C with ZCFs of approximately 125kHz for all

three tests. The ZCF decreases with temperature following the ZCF peak due to the decrease in permeability and resistivity.

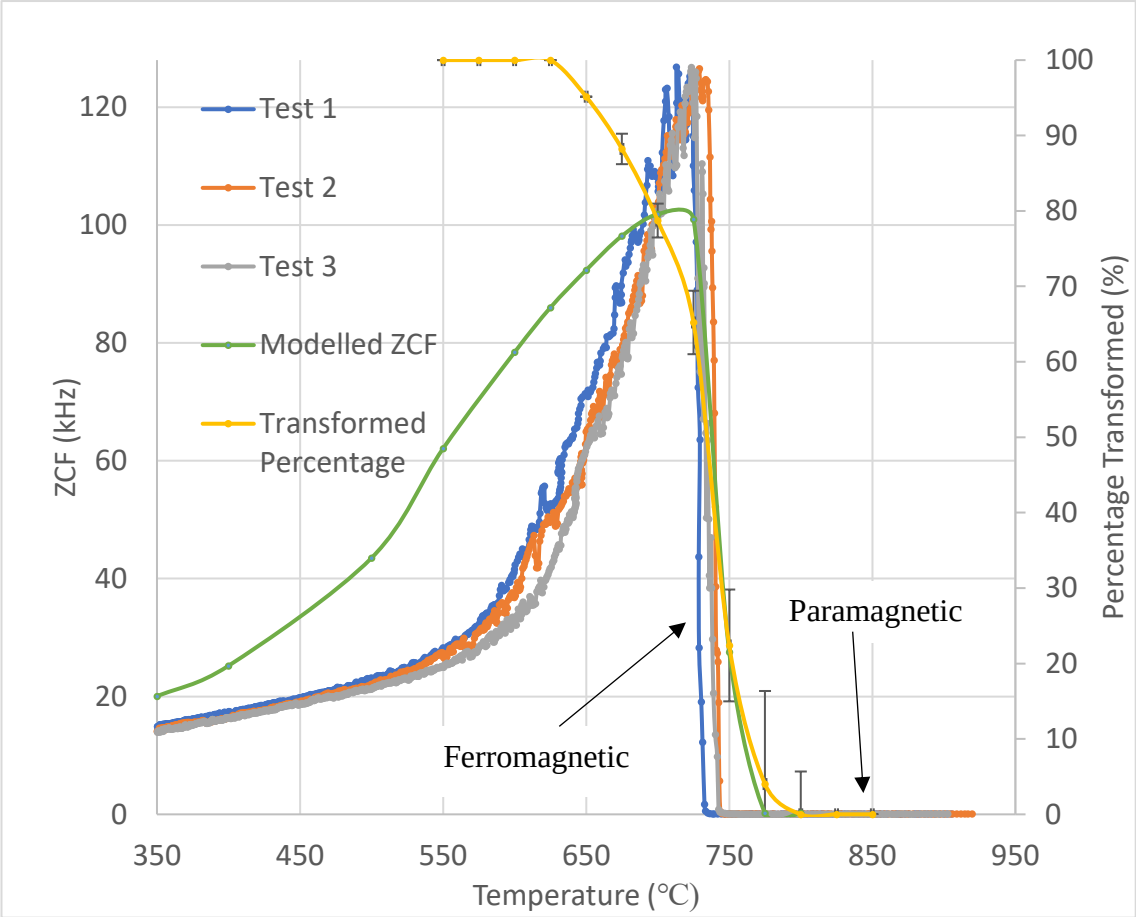

Figure 101. Measured and modelled ZCF with temperature for 10mm mild steel. Transformed percentage obtained from dilatometry also plotted with temperature on the second Y axis. Points where the steel is paramagnetic and ferromagnetic are indicated on the ZCF graph.

Figure 101 shows that for all EMspec® sensor tests, the ZCF's all start to increase at approximately 35-40% ferrite fraction which agrees with Hao et al. [37] where a significant change in permeability occurs when a connected ferrite phase forms at around 35-40% ferrite. This is discussed in chapter 2 and shown in figure 11. It should also be noted that errors may arise relating the ZCF, measured from a large plate where temperature non-uniformity can occur, to phase fraction calculated from measurements on a small dilatometry sample. However, the data is consistent with reported trends from the literature on magnetic permeability and ferrite austenite phase balances. The ZCF peaks at approximately when the steel is expected to be about 70-75% transformed. The after-heat treatment microstructure exhibits a ferrite fraction of 85%. So, this would tend

to suggest that the final 10-15% of ferrite transformation does not increase the permeability enough to increase ZCF. This does not agree with the reported trends in ferrite fractions which reports that there is no change in the rate of increase of permeability with ferrite phase percentage between 70 and 85% ferrite in a ferrite austenite microstructure [37]. However it is not like for like as the steel is at a higher temperature which would result in a higher permeability for ferrite [11] and there is also the competing effects of decrease in permeability due to decrease in temperature and increase in permeability due to increasing ferrite phase. There is also the experimental error in temperature measurement between the small dilatometry sample and the larger ROT sample to consider. While the remaining untransformed austenite transforms to pearlite, determined to be at around 650°C, there is no increase in ZCF. This is suggested to be because the increase in permeability due to pearlite formation is less significant than the decrease in permeability and resistivity due to decreasing temperature.

Figure 101 shows that the modelled ZCF data does not agree with the experimental data. The increase in modelled ZCF due to increase in permeability due to higher amount of ferromagnetic phase occurs earlier than for the experimental ZCF, almost in accordance with the phase fraction from dilatometry. The power law with a fitting factor of 1/3 (discussed in section 5.5.3) was used to calculate effective permeability. It has been shown a study by Yin et al. [87, 88] that there is an offset between power law permeability and permeability predicted using microstructure and EM sensor models. This is due to the power law not considering the need for connective ferrite to be present before there is a significant change in permeability. The study by Yin et al. [87, 88] showed that the effective permeability for austenite ferrite phase balances had increased to approximately 30 at a ferrite percentage of 35% when the permeabilities for the FEM model and EM sensor model start to increase as previously discussed. This offset could be larger at higher temperatures due to the higher permeability of ferrite at higher temperatures. The modelled ZCF increases until it peaks at 700°C. The modelled ZCF's in figure 101 are likely not correct. Like for the 3mm and 6mm mild steels as previously discussed in this chapter, there is an unexpected trend in the modelled phase angle with frequency for the very high permeability simulations. Figure 102 plots the modelled phase angle with temperature for the 6mm mild steel at its highest permeability during transformation. This has been compared with the peak permeability for the high carbon steel. For the high carbon steel, the phase angle becomes more negative with frequency which is expected [6]. However, like the 3mm and 6mm mild steel simulations, the phase angle becomes

more negative, then becomes more positive before becoming more negative again. This is likely the cause of the constant offset in ZCF between the measured and modelled data at the ZCF peak and with decreasing temperature. This again may be due to the modelling station used to run these simulations not having the necessary specification to run a fine enough mesh for the higher permeabilities to be solved.

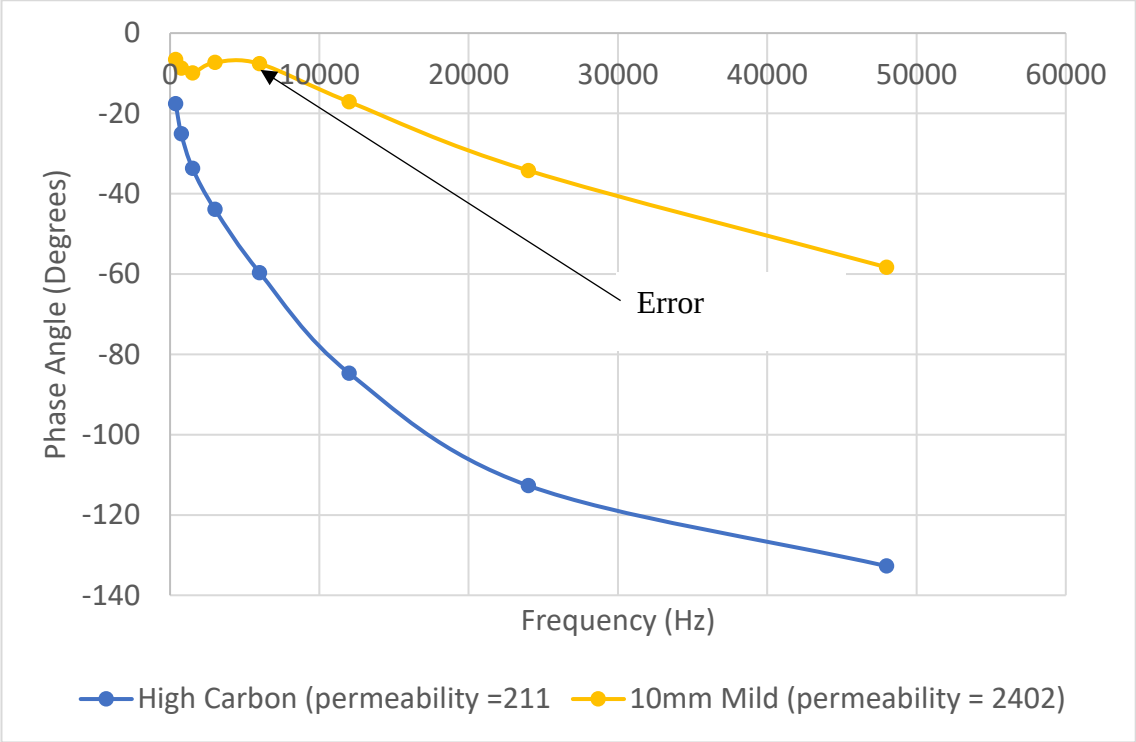

Figure 102. Modelled phase angle with frequency for 10mm mild and 3mm high carbon at their peak effective permeability during transformation (calculated by power law). The error in the data is indicated.

8.1.4 Comparison of the EMspec® Sensor Response to Phase Transformation in Mild Steel Plates of Different Thickness

Figure 103 shows the ZCF with temperature for the 3mm, 6mm and 10mm mild steel. The average cooling trajectories for the 3mm, 6mm and 10mm mild steels are plotted in figure 104. A comparison of the phase percentages transformed from dilatometry for each thickness is shown in figure 105. Figure 103 shows that the EMspec® sensor can distinguish between the same grade mild steel with different thicknesses while

dynamically cooling in air. The 3mm thick sample has the fastest cooling rate of the three thickness, which results in the transformation starting at a lower temperature than for the 10mm and 6mm mild steel. This is represented both in the phase percentage transformed in figure 105 and is also shown by the ZCF starting to increase at the lowest temperature of the three thicknesses. Tests 1 and 2 for the 3mm sample have a ZCF peak of approximately 31kHz and 34kHz respectively and test 3 has a ZCF of approximately 50 kHz. The peak ZCF is lower than for the 6mm and 10mm samples due to the transformation starting at a lower temperature due to the faster cooling rate, thus, the point at which the 3mm steel has its highest permeability value is at a temperature lower than that of the 6mm and 10mm. In addition, the 3mm sample contained some bainite as well as ferrite and pearlite compared to the predominantly ferrite and pearlite structure of the 6 and 10mm samples. This means that the ferrite fraction is less and hence the effective permeability will also be lower. The 10mm mild has the slowest average cooling rate as shown in figure 104 and this results in a slightly higher transformation start temperature during cooling. Figure 105 shows that the 10mm mild steel starts transforming at a higher temperature than the other plates however the error bars do overlap with the 6mm mild steel. The 10mm mild steel ZCF starts to increase during transformation, however there is some overlap with the 6mm mild steel when considering errors for temperature measurement and temperature inhomogeneity. Despite there not being a significant difference in percentage transformed between the 6mm and 10mm mild, the 10mm mild has its peak ZCF at approximately 725℃ with a signal of approximately 125 kHz when phase percentage transformed is approximately 65-70%. The 6mm mild steel peaks at approximately 710℃ with a phase percentage transformed of approximately 70% and ZCF of approximately 78kHz for test 1 and approximately 70kHz for tests 2 and 3. As they have similar transformed percentages at their ZCF peaks, the higher ZCF value for the 10mm mild steel samples is consistent with this occurring at a higher temperature and therefore being related to a higher permeability. There should not be an effect of thickness as discussed in section 6.3 which shows that there is not expected to be an effect of thickness on the EMspec® signal in this ferrite fraction and thickness range.

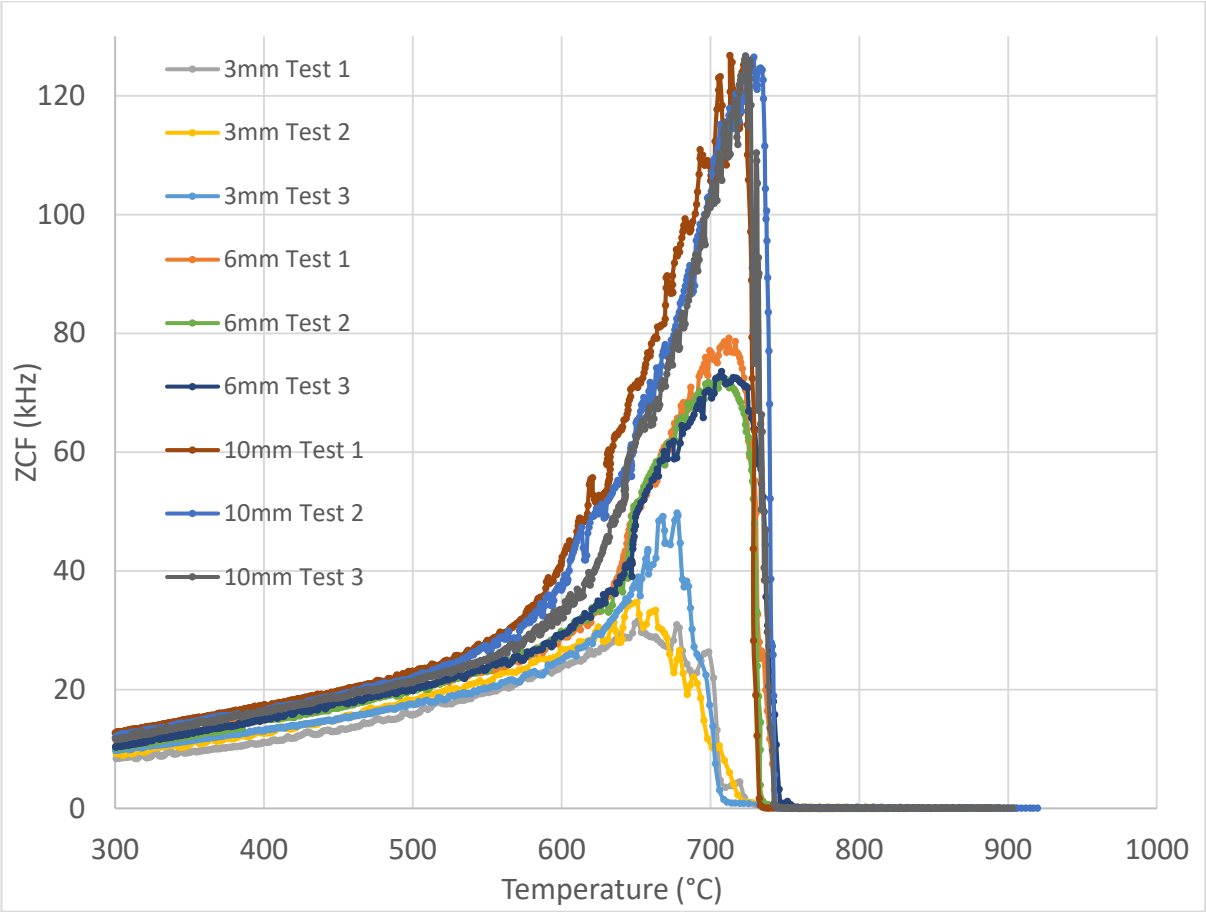

Figure 103. ZCF with temperature for 3mm mild steel tests 1-3, 6mm mild steel tests 1-3 and finally the 10mm mild steel tests 1-3.

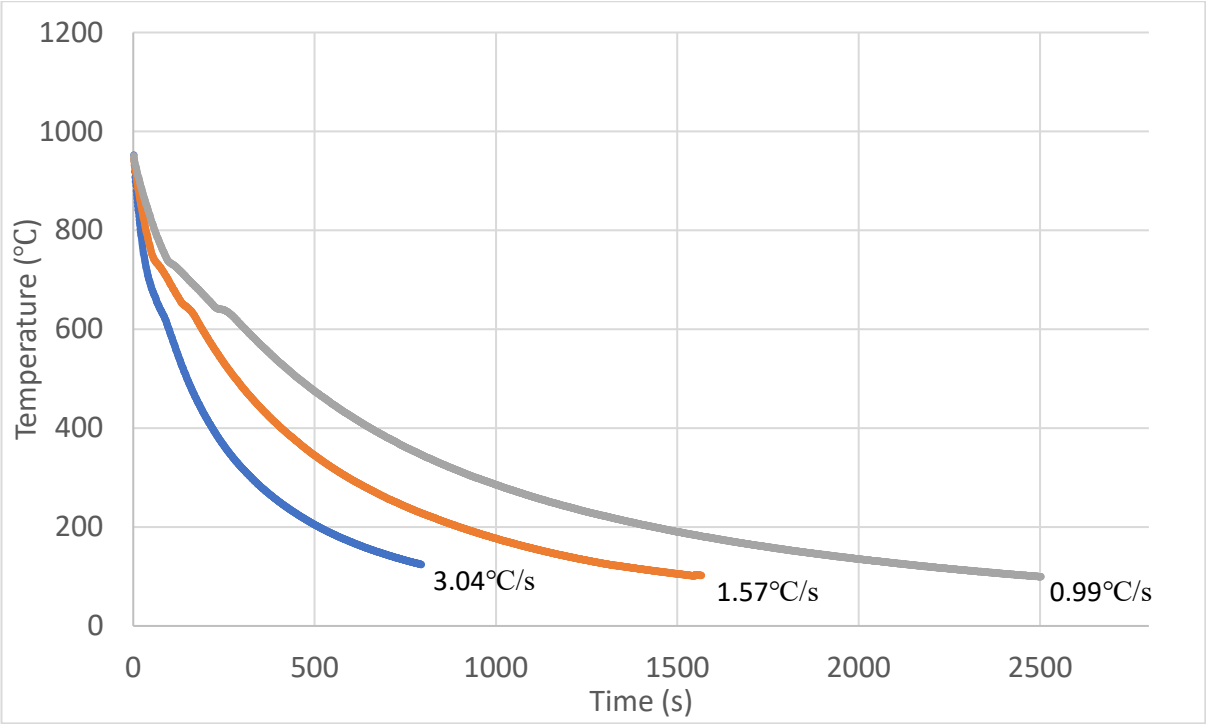

Figure 104. Average cooling trajectories for the 3mm mild steel, 6mm mild steel and the 10mm mild steel during EMspec® sensor measurements. Cooling rates between 980°C and 500°C also stated for each sample.

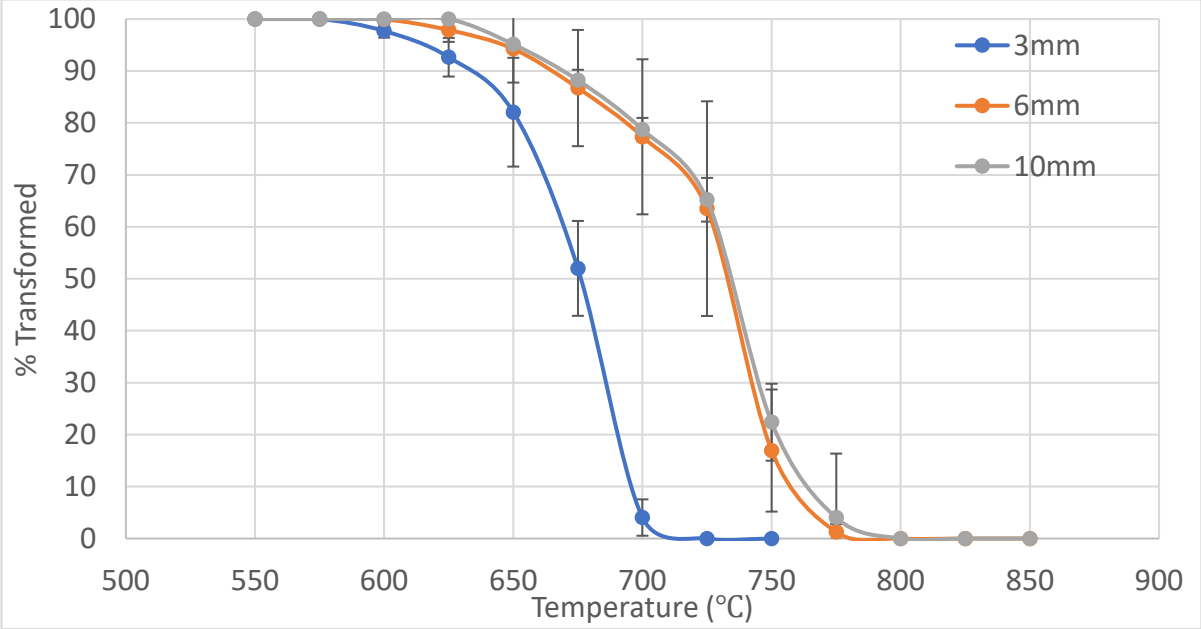

Figure 105: Phase percentage transformed for 3mm mild steel, 6mm mild steel and 10mm mild steel. Obtained from dilatometry tests.

8.1.5 High Carbon Steel

8.1.5.1 Microstructural Characterisation

The microstructural state of the 3mm high carbon steel in the as received condition and after heat treatment for tests 1-3 is shown in figures 106-109. 413×457mm plates were heated in the furnace to 980°C before cooling in air while being monitored by the EMspec® sensor. Figure 106 shows that the steel in the as received condition exhibits a coarse pearlitic microstructure and shows evidence of spherodisation. Following heat treatments for test 1-3, the microstructure remains fully pearlitic but has a fine pearlite structure. As previously discussed, formation of low carbon ferrite can occur at the surface of a steel during heat treatments due to decarburisation. This can affect EM sensor signals, so micrographs of the top and bottom surfaces of the high carbon steel following heat treatments for test 1-3 have been obtained to see if any decarburisation occurred during heat treatment (figures 110-112). The microstructures following heat treatments for tests 1-3 show evidence that decarburisation has occurred in these steels - tests 1 and 3 show evidence of discontinuous decarburisation with some ferrite/pearlite and some fully pearlitic regions at the surface. Test 2 shows no evidence of decarburisation on the top surface and a very small amount of randomly distributed ferrite occurring on the bottom surface. There is no difference in experimental procedure for these tests so there is no obvious reason why test 2 would show evidence of less decarburisation – this may indicate local variability in decarburisation for the large plate samples as only a small area was examined microstructurally. Figure 113 shows the microstructure for the 3mm high carbon steel following dilatometry heat treatment. The microstructure exhibits a fine pearlite structure, like for the microstructures in figures 107-109 which is expected.

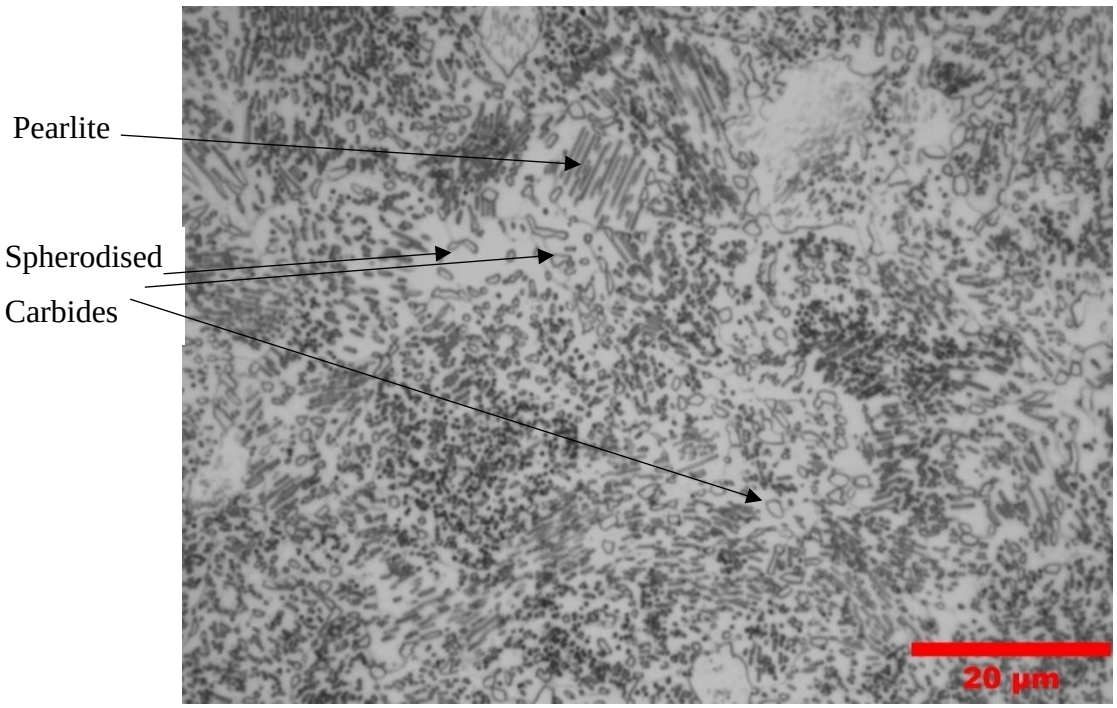

Figure 106. Optical microstructure at 100× magnification of a 3mm high carbon steel in the as received condition. Regions of pearlite and spheroidised carbides have been indicated.

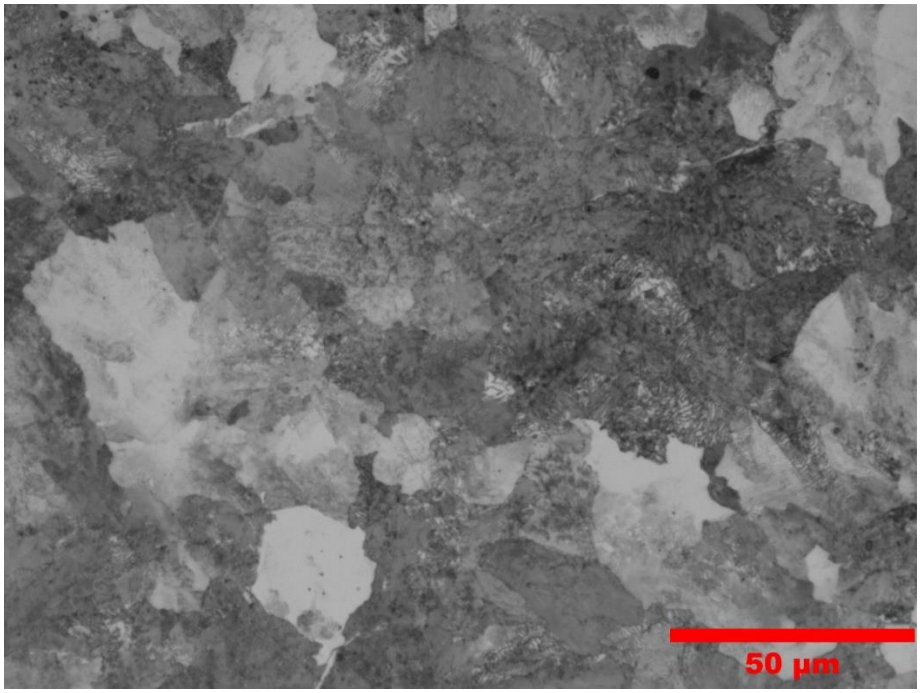

Figure 107. Optical microstructure at 50× magnification of a 3mm high carbon steel after heat treatment for test 1.

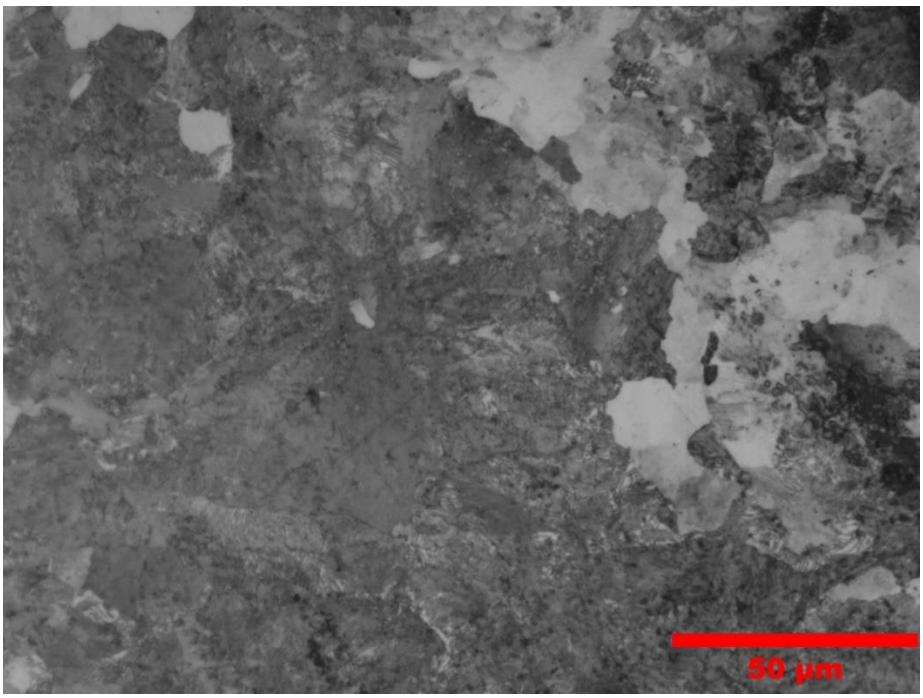

Figure 108. Optical microstructure at 50× magnification of a 3mm high carbon steel after heat treatment for test 2.

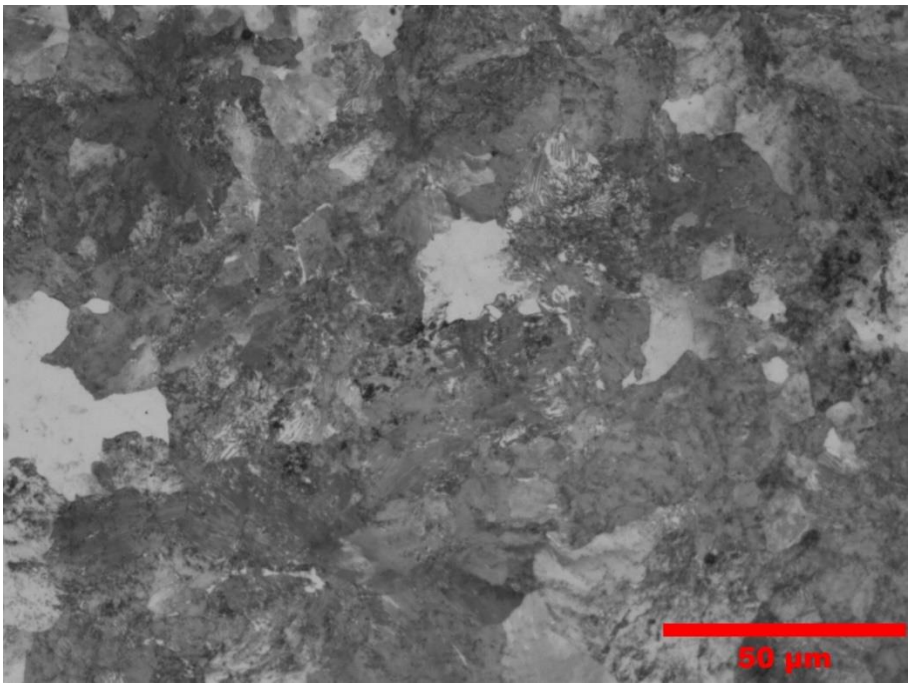

Figure 109. Optical microstructure at 50× magnification of a 3mm high carbon steel after heat treatment for test 3.

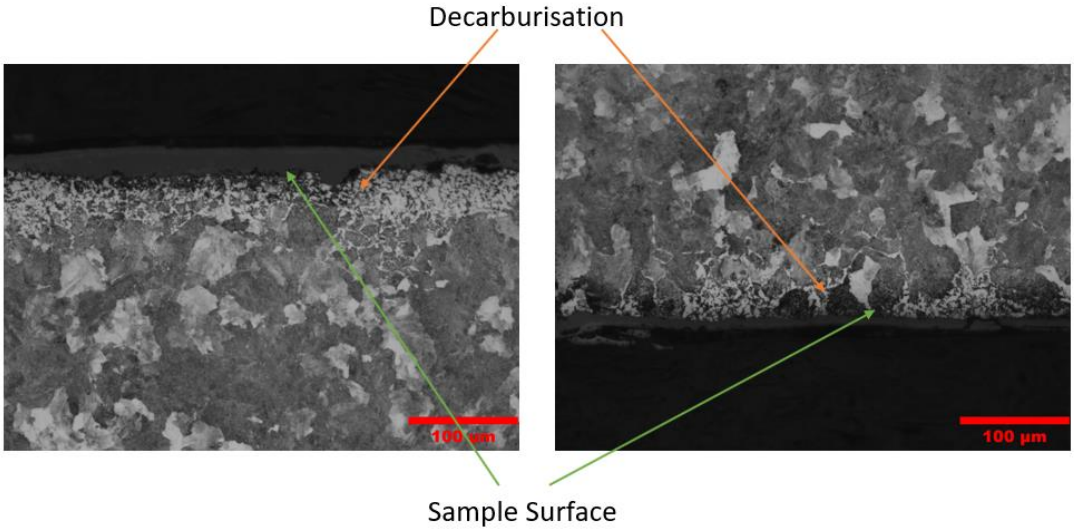

Figure 110. Optical microstructures at 20× magnification looking at top surface (a) and bottom surface (b) of the high carbon steel used in test 1.

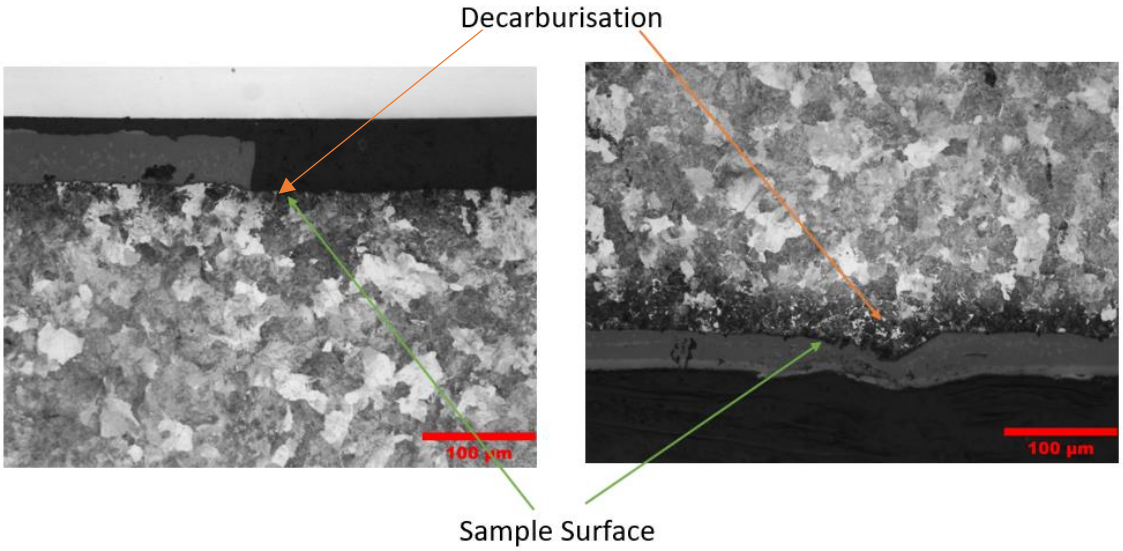

Figure 111. Optical microstructures at 20× magnification looking at top surface (a) and bottom surface (b) of the high carbon steel used in test 2.

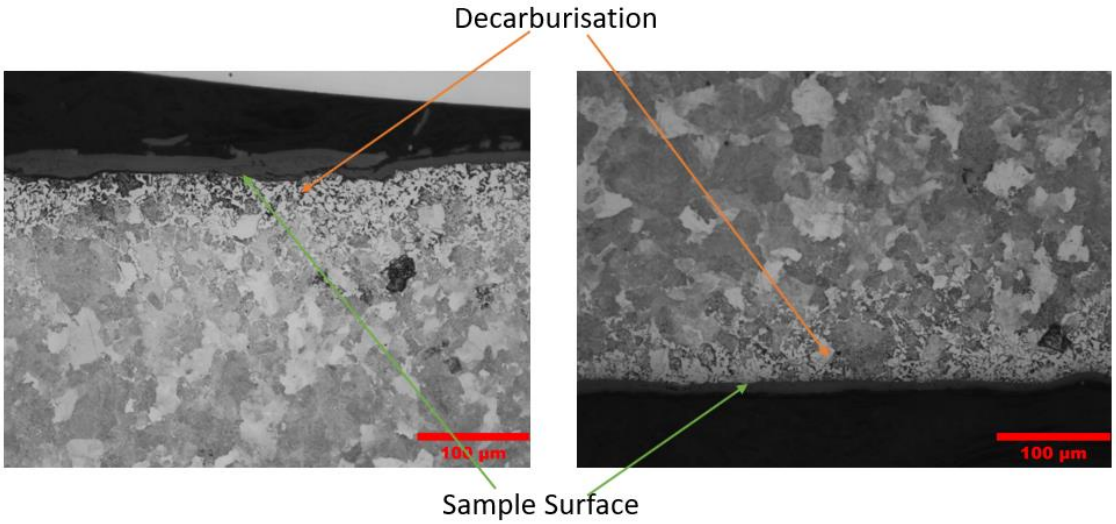

Figure 112. Optical microstructures at 20× magnification looking at top surface (a) and bottom surface (b) of the high carbon steel used in test 3.

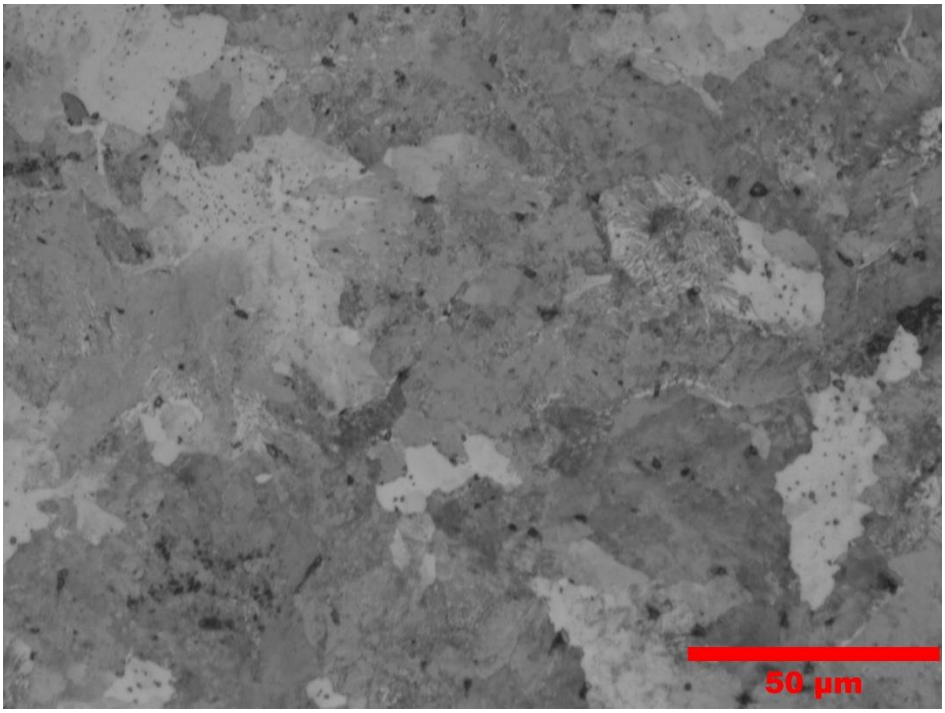

Figure 113. Optical microstructure at 50× magnification of 3mm high carbon steel following dilatometry heat treatment.

8.1.5.2 Cooling Trajectories

For tests 1 and 3, one thermocouple was used to monitor the temperature during heating and cooling. This is because for test 1, only a one channel data logger was available at the time of this test. For test 3, two thermocouples were connected to the sample however one of them became disconnected during heat treatment. For both tests, the thermocouples were closer to the furnace door when the sample was in the furnace (i.e. the front of the plate sample as it is removed from the furnace). For test 2, two thermocouples were used on the plate - one closer to the back of the furnace and one closer to the furnace door. Figure 114 shows the cooling trajectory for test 2 and the temperature difference between thermcouple 1 and 2, which indicates the sample temperature uniformity during testing of the high carbon steel plate. As the sample begins cooling, there is a large initial descrepency between thermocouples 1 and 2. This is because as the sample is rolled out of the furnace, the part of the plate where thermocouple 1 is situated is exposed to the atmosphere outside of the furnace first, and thus starts cooling more rapidly while the side of the plate where thermocouple 2 is positioned is in the furnace. After the initial spike in temperature difference, thermocouple 2 cooling rate starts to increase as it leaves the furnace. With the whole sample out of the furnace, the temperature difference between thermcouple 1 and 2 is initially between 20 and 30℃. At approximately 610℃ the temperature of thermocouple 1 increases due to this part of the sample being affected by the latent heat. This is caused austenite to pearlite transformation occuring. This causes thermocouple 1 for a short time, to have a higher temperature than thermocouple 2. Thermocouple 2 temperature then increases due this part of the sample going through austenite to pearlite transformation and thus releasing latent heat. The difference in thermocouple temperature shifts to approximately 30℃. After the plate has fully transformed to pearlite the temperature difference between the two thermocouples gradually decreases as the sample cools towards room temperature.

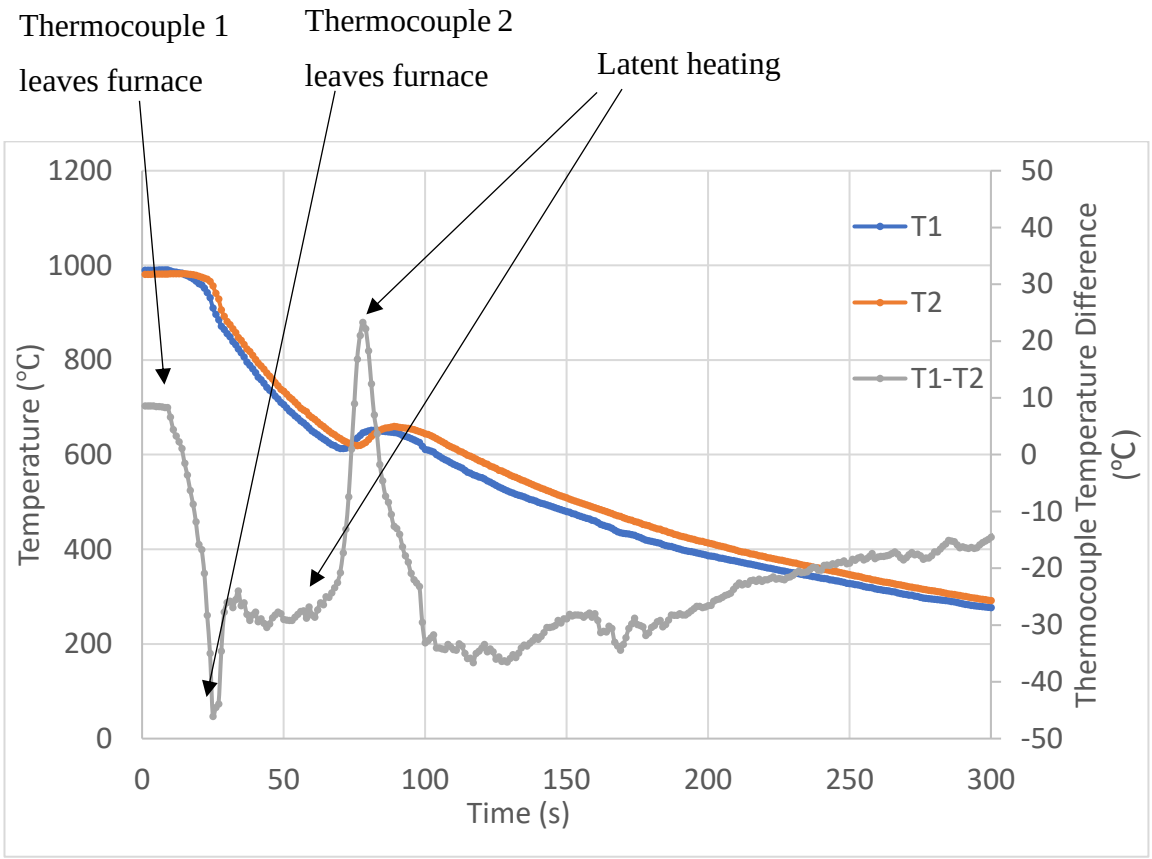

Figure 114. Cooling trajectory for 3mm high carbon steel during test 2. Thermocouple 1 (T1) and thermocouple 2 (T2) are plotted along with temperature difference between the two thermocouples (T1-T2). The points at which thermocouples 1 and 2 leave the furnace and latent heating occurs have been indicated on the T1-T2 graph.

The cooling trajectory comparison for the three tests of the high carbon steel is shown in figure 115. Only the thermocouple at the front of the furnace for each test (T1) has been plotted for this comparison. It can be seen from figure 115 that the cooling trajectories show good repeatability before the latent heat due to transformation. During latent heating, tests 1 and 2 temperatures are close however it appears there is some noise in the test 3 data. This could be due to poor thermocouple contact. Following latent heating, the three data sets overlap each other while cooling towards room temperature.

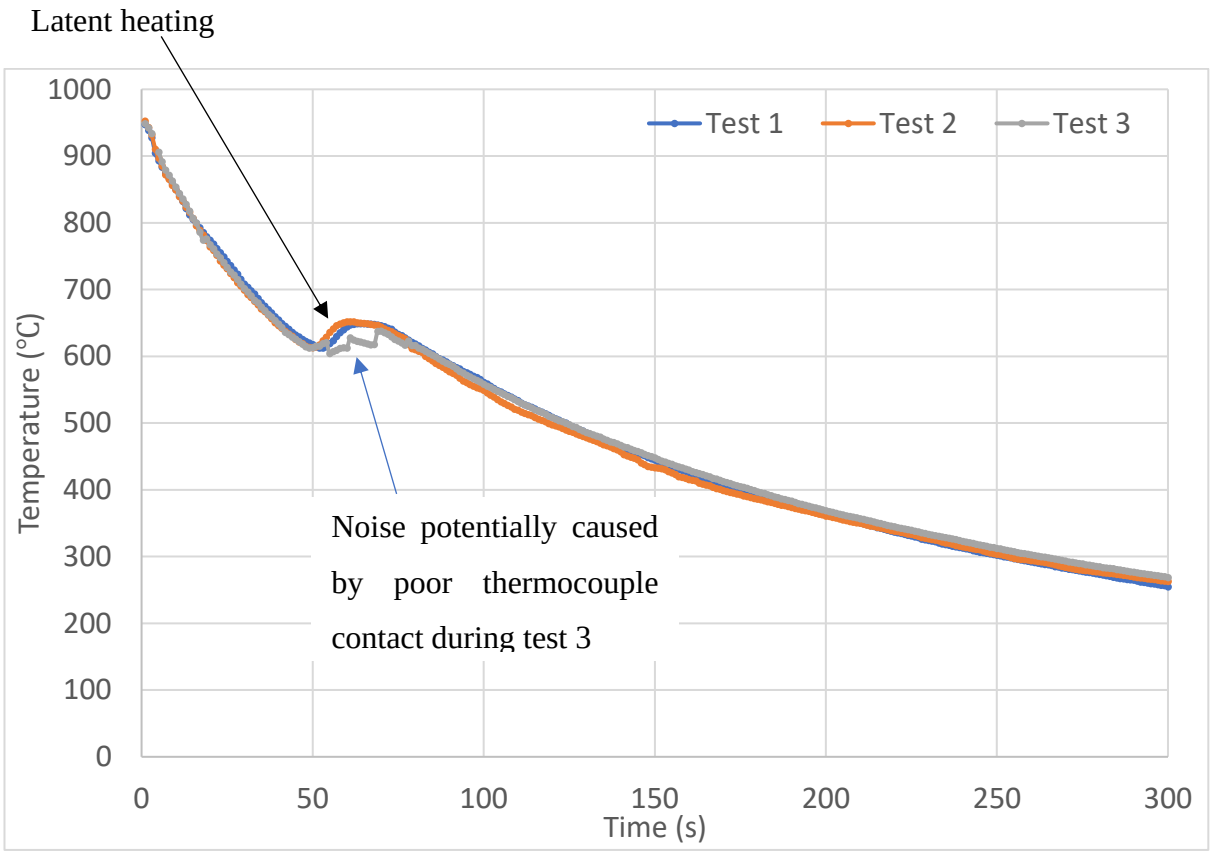

Figure 115. Temperature of thermocouple 1 (closer to furnace entrance) for 3mm high carbon steel with time during cooling in air for EMspec® tests 1, 2 and 3. The point where latent heating occurs is indicated. The noise in test 3 potentially caused by poor thermocouple contact in test 3 is also indicated.

8.1.5.3 EMspec® Sensor Results and Relation to Phase Fraction Transformed and EMspec® Sensor Model

Figure 116 shows the ZCF with temperature for EMspec® tests 1-3 on the 3mm high carbon steel. For all tests, the ZCF is very low from 800°C to about 615°C. At approximately 615°C the plate temperature increases for all tests due to latent heating and the ZCF begins to increase at the start of latent heating and that transformation has begun. The change in temperature due to latent heating appears to be less continuous for test 3 and this is due to the noise in the thermocouple data, discussed in figure 115. During transformation the ZCF increases sharply. For tests 1 and 3, the ZCF peaks at about 11 and 12 kHz respectively at a temperature of approximately 620°C. Test 2 peaks at approximately 9kHz at a temperature of about 640°C. This is because the temperatures in test 2 are the average values for the two thermocouples and therefore considers the

temperature profile along the sample. Following the ZCF peaks for tests 1 and 3, there is very good repeatability in the ZCF values decreasing with temperature with the data sets perfectly overlapping each other. Test 2 follows a slightly different trajectory and had a lower ZCF peak than tests 1 and 3. This may because the sample for test 2 showed very little decarburisation compared to tests 1 and 3 (figures 110-112) which would explain the discrepancy in signal. This is also backed up by the fact that the ZCF's appear to be moving towards overlapping each at lower temperatures when the permeability of ferrite decreases significantly [11]. This data shows that the EMspec® can monitor the full pearlitic transformation of a high carbon steel.

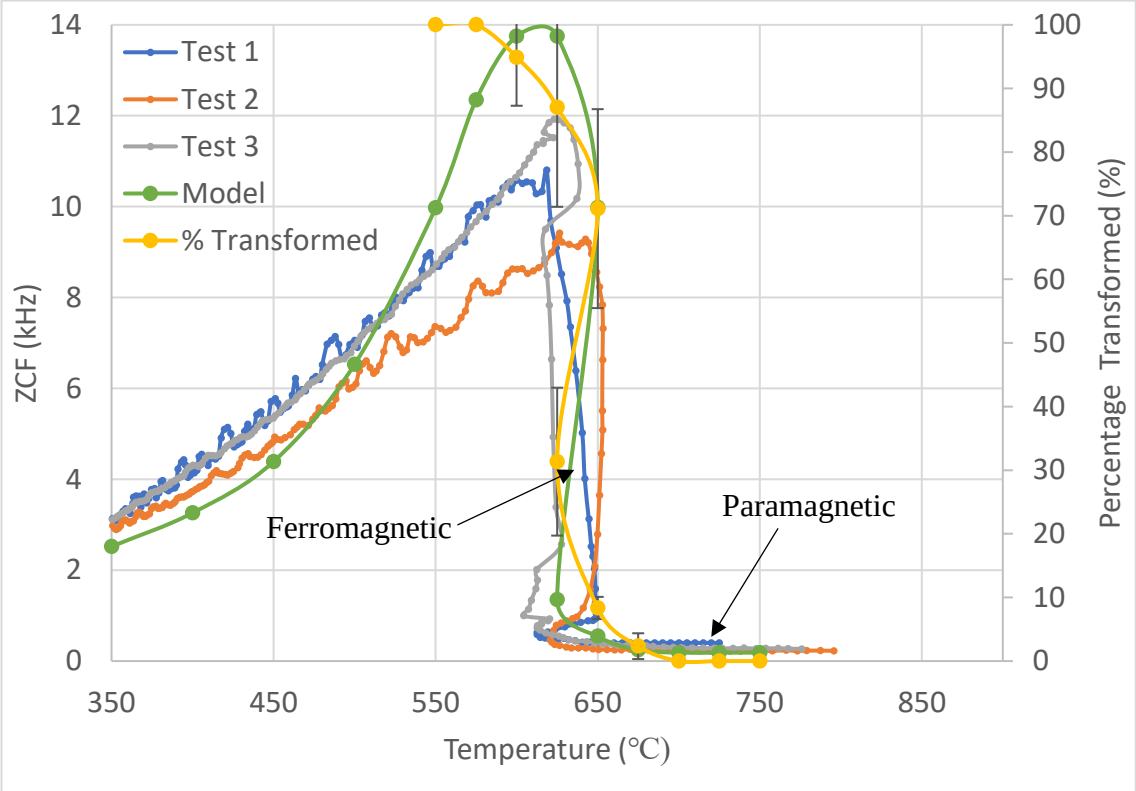

Figure 116. Measured and modelled ZCF with temperature for 10mm mild steel. Transformed percentage obtained from dilatometry also plotted with temperature on the second Y axis. The points at which the steel is paramagnetic and ferromagnetic are indicated on the ZCF graph.

The dilatometer was programmed to consider the latent heat that the high carbon steel experiences during transformation. Figure 116 shows that the experimental ZCF for tests 1-3 begins to increase signalling that austenite to pearlite transformation has begun when the phase percentage transformed obtained from dilatometry is between 30 and 40% for all three tests. Hao et al. [37] predicts permeability of ferrite austenite phase fractions at room temperature to increase significantly when the ferrite fraction reaches 35%. The fact

that the ZCF does not increase until the steel is between 30 and 40% transformed tends to suggest that a fully pearlitic steel also needs to have connectivity before the permeability increases enough to increase the ZCF. It should be noted that there is temperature inhomogeneity across the plate sample and therefore the plate does not transform uniformly, which will make the direct quantitative comparison between phase fraction and ZCF indicative only. The ZCF for all three tests peaks when the phase percentage data expects the steel to be approximately 85% transformed. This tends to suggest that the remaining 15% pearlite to transform does not increase the permeability enough to overcome the decrease in permeability due to decreasing temperature, again noting the point about temperature inhomogeneity for the plate. In addition, there will be some error in the interpretation of the dilatometry data to obtain the phase percentages quoted. This is because the latent heating was included in the dilatometry program to mimic the plate temperature profile as closely as possible on the ROT. However, this made the relative length change data difficult to interpret. The pearlite transformation also occurs over a very narrow temperature range, which will increase uncertainty in the relationship with ZCF.

Despite the potential errors in the dilatometry data, the modelled ZCF appears to agree relatively well with the experimental data, as shown in figure 116. The point at which the signal starts to increase is earlier than for experimental ZCF, and this is likely due to the power law equation (described in chapter 5) used to calculate the effective permeability of the pearlite austenite phase balances at temperature does not take into account the connectivity of the ferromagnetic phase (in this case pearlite) in the microstructure. However, it is not well known what the effect of connectivity of pearlite in pearlite austenite phase balances has on permeability as this has only been investigated for ferrite austenite and ferrite pearlite phase balances [4, 37]. The point at which the ZCF peaks agrees well with the experimental data, with the modelled ZCF peaking when the dilatometry data expects the transformed percentage to be approximately 87%.

8.1.6 Medium Carbon Steel

A medium carbon steel has been monitored during transformation using the EMspec® sensor to investigate if the sensor can distinguish between the two transformations expected to occur (ferrite and pearlite). No microstructural analysis of this steel has been performed as time did not permit. However, a micrograph of the same steel grade (C45) has been sourced from the internet to give an idea of what the microstructure should look like in the as received condition and is shown in figure 117. It can be seen from figure 117 that a C45 steel consists of ferrite pearlite phase balance expected in the range of 40-60% ferrite depending on composition. The ferrite and pearlite phases are randomly distributed, and some regions of connected ferrite exist in this microstructure. It is expected that this steel will experience noticeable decarburisation following heat treatment assuming the procedure is the same as the 10mm mild steel which also showed evidence of decarburisation following heat treatment.

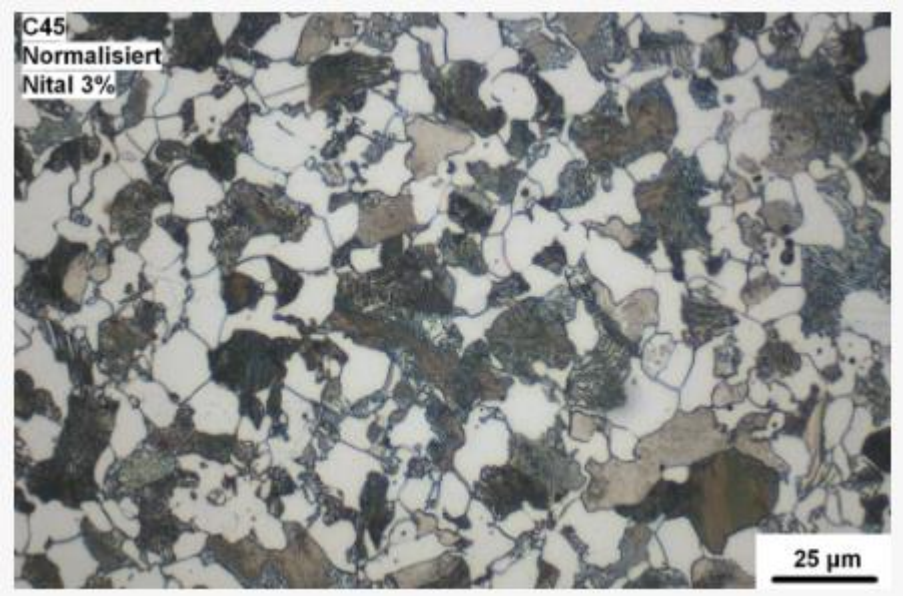

Figure 117. Optical microstructure of a C45 steel sourced from [104].

8.1.6.1 Cooling Trajectories

The cooling trajectories for tests 1-3 on the medium carbon steel is shown in figures 118-120. The temperature difference between the two thermocouples (T1-T2) is also plotted on the 2nd Y axis. For all 3 tests, there is an initial spike in temperature difference between thermocouples 1 and 2. This is because thermocouple 1 is closer to the furnace door while thermocouple 2 is closer to the back of the furnace. Therefore, thermocouple 1 be exposed to the atmosphere outside of the furnace first as the sample is rolled out. This causes the initial difference in temperature, however as thermocouple 2 leaves the furnace, the temperature difference decreases. For tests 1 and 3, the temperature of the two thermocouples appears to be relatively uniform with the temperature difference staying between 0 and 10°C throughout the entire cooling. For test 2, when latent heating occurs due to what would be consistent as a pearlite transformation, the latent heating occurs earlier for thermocouple 2 than it does for thermocouple 1. This causes the temperature difference to be between 10 and 15°C when this is occurring. Following latent heating the temperature difference decreases towards zero with decreasing temperature of the sample.

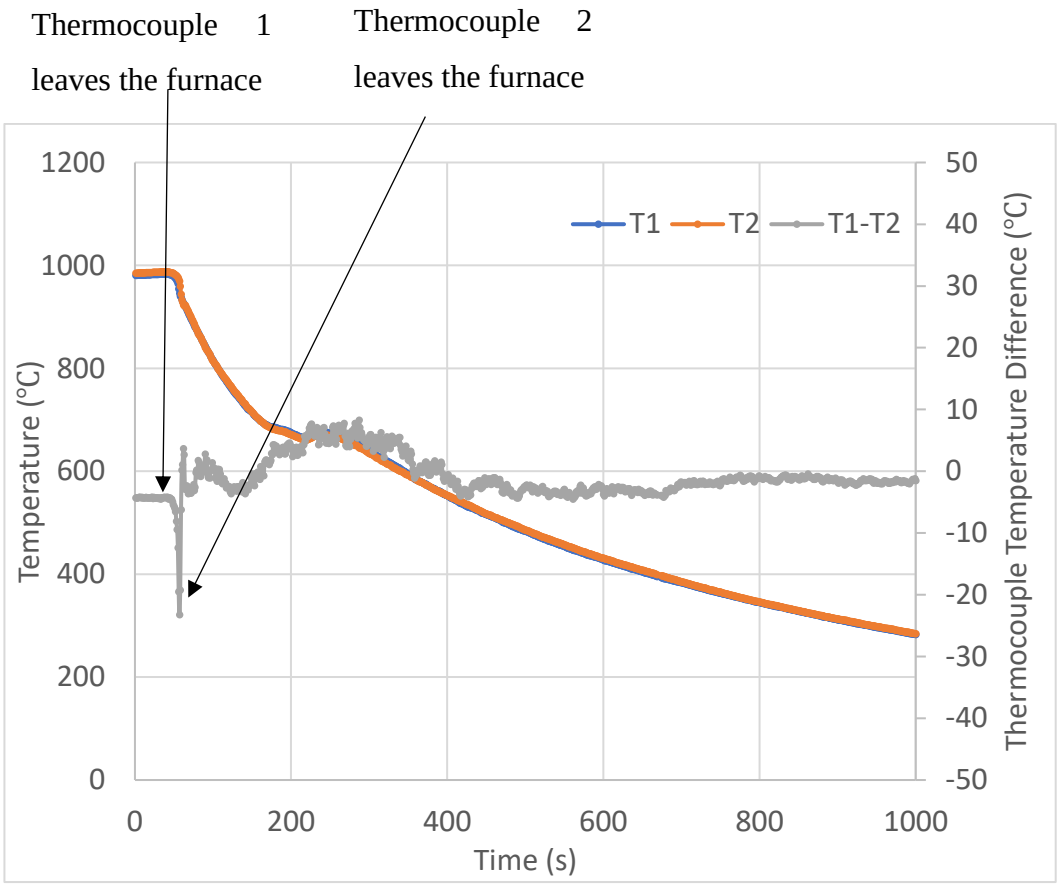

Figure 118. *Cooling trajectory for 10mm medium carbon steel during test 1. Thermocouple 1 (T1) and thermocouple 2 (T2) are plotted along with temperature difference between the two thermocouples (T1-T2). The points at which thermocouples 1 and 2 leave the furnace are indicated on the T1-T2 graph.*

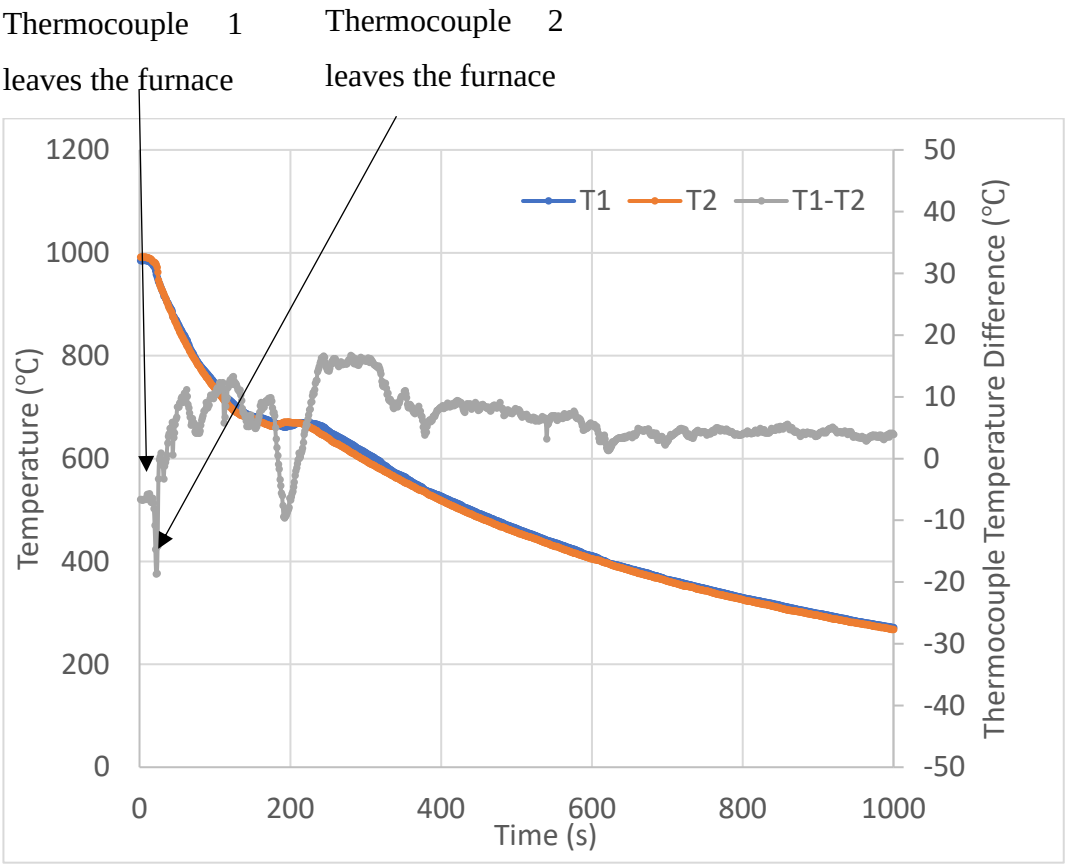

Figure 119. Cooling trajectory for 10mm medium carbon steel during test 2. Thermocouple 1 (T1) and thermocouple 2 (T2) are plotted along with temperature difference between the two thermocouples (T1-T2). The points at which thermocouples 1 and 2 leave the furnace are indicated on the T1-T2 graph.

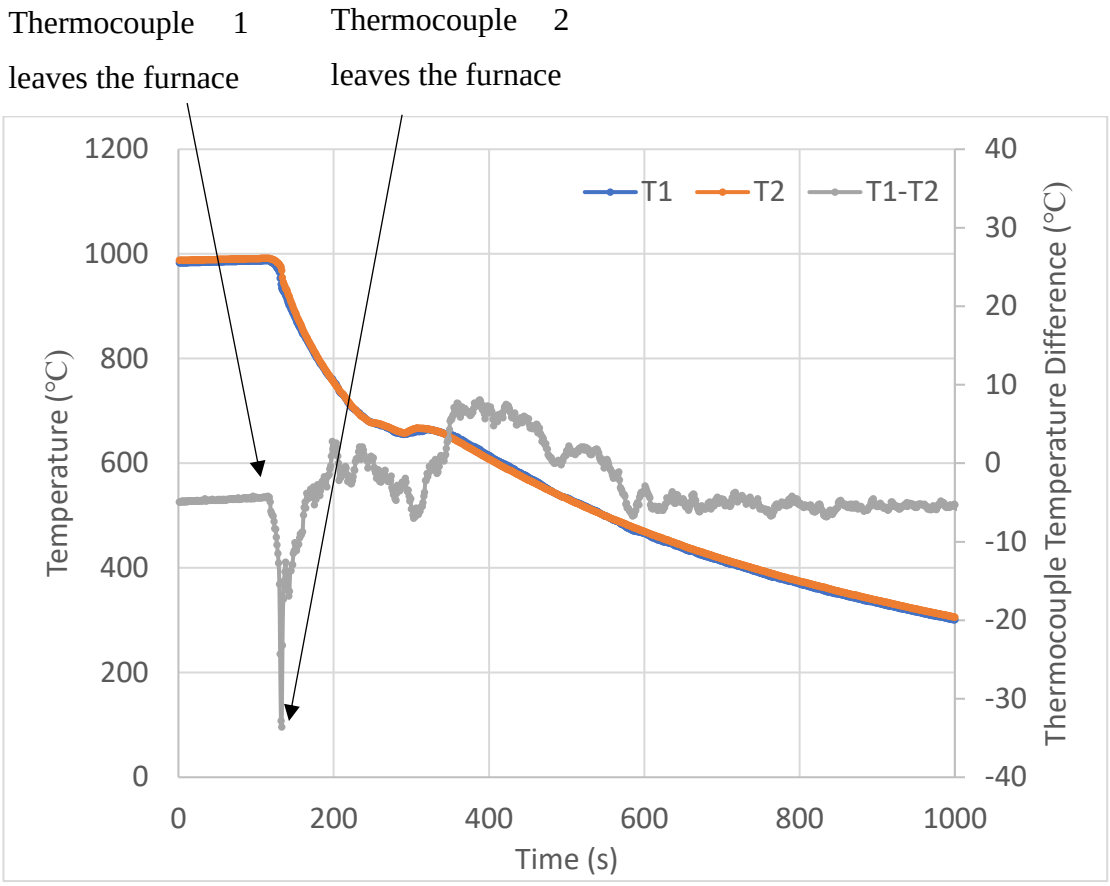

Figure 120. Cooling trajectory for 10mm medium carbon steel during test 3. Thermocouple 1 (T1) and thermocouple 2 (T2) are plotted along with temperature difference between the two thermocouples (T1-T2). The points at which thermocouples 1 and 2 leave the furnace are indicated on the T1-T2 graph.

The average cooling trajectory for 10mm medium carbon steel from EMspec® tests 1-3 is shown in figure 121. The cooling trajectories overlap each other throughout the entire cooling and show very good repeatability. At approximately 690°C, there is a slight change in cooling trajectory for the three tests. This would be consistent with start of latent heating due to ferrite transformation. As the three tests continue to cool, a more obvious change in cooling trajectory occurs at about 660°C. This is consistent with latent heating caused by a pearlitic reaction here.

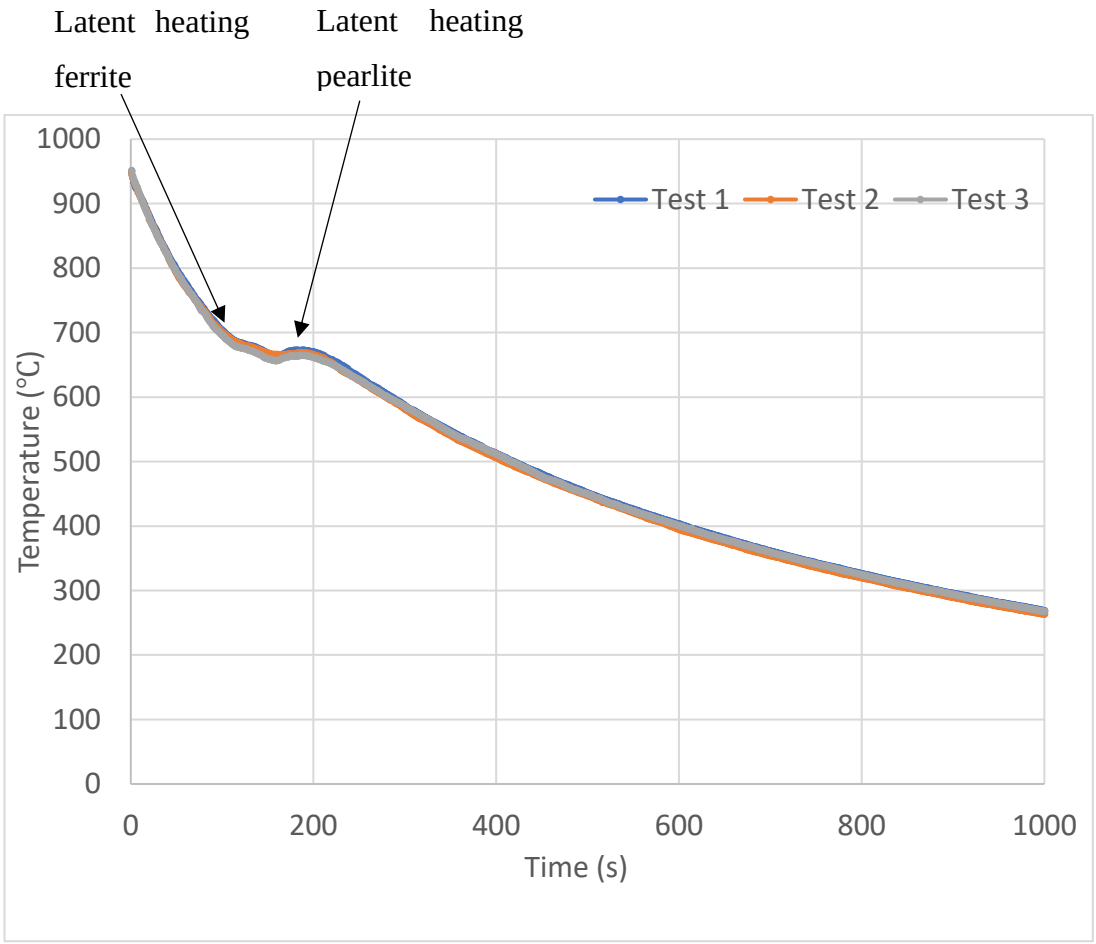

Figure 121. Average cooling trajectories for 10mm medium carbon steel test 1-3. The latent heating caused by the ferrite and pearlite transformations are indicated.

8.1.6.2 EMspec® Sensor Results

The EMspec® sensor results for the medium carbon steel for tests 1-3 is shown in figure 122. Above 800℃ the steel is fully austenitic and therefore paramagnetic which results in the ZCF being very low. The temperature cools through the Curie temperature (around 760℃) and there is still no change in ZCF which suggests that the steel is still austenitic at this point. At approximately 740℃ the ZCF for test 2 increases signalling that transformation has started. Tests 1 and 3 ZCF's start to increase at approximately 730℃. When considering the temperature discrepancy on test 2, the temperature at which the ZCF increases could be as low as for tests 1 and 2. All 3 tests exhibit two peaks in ZCF which may be caused by the two transformations that occur in a medium carbon steel to form ferrite and then pearlite. This would be consistent with a study by Dickinson et al. [97] and Papaelias et al. [91], where two transformations were detected for a medium carbon steel for ferrite followed by pearlite. The initial peak for test 2 occurs at approximately 725℃ with a ZCF of approximately 85 kHz. For test 1, the initial peak is

less obvious, and occurs at 716℃ with a ZCF of approximately 50kHz. The initial peak for test 3 peaks at 71 kHz at a temperature of about 700℃. Following the initial peaks for the 3 tests, the ZCF decreases initially before the ZCF increases for a second peak. For test 1 the second peak in ZCF occurs at 685℃ with a signal of approximately 70 kHz. Both tests 2 and 3 have ZCF peaks of approximately 80kHz with the peaks for test 2 occurring at around 680℃ while the peak for test 3 occurs at 675℃. The potential ferrite and pearlite ZCF peaks are offset from the latent heating that occurs during the cooling trajectories for these tests (figure 121). Latent heating for ferrite occurs at approximately 690℃ while pearlite latent heating occurs at approximately 660℃. This offset can be explained by temperature inhomogeneity across the sample and potentially through thickness. It should be noted that the absolute values of ZCF are not representative for a steel with this microstructure. This due to errors in the estimation of the phase angles by the EMspec® sensor software being inaccurate. This is shown in the appendix. Dilatometry and therefore modelling have not been performed for this steel.

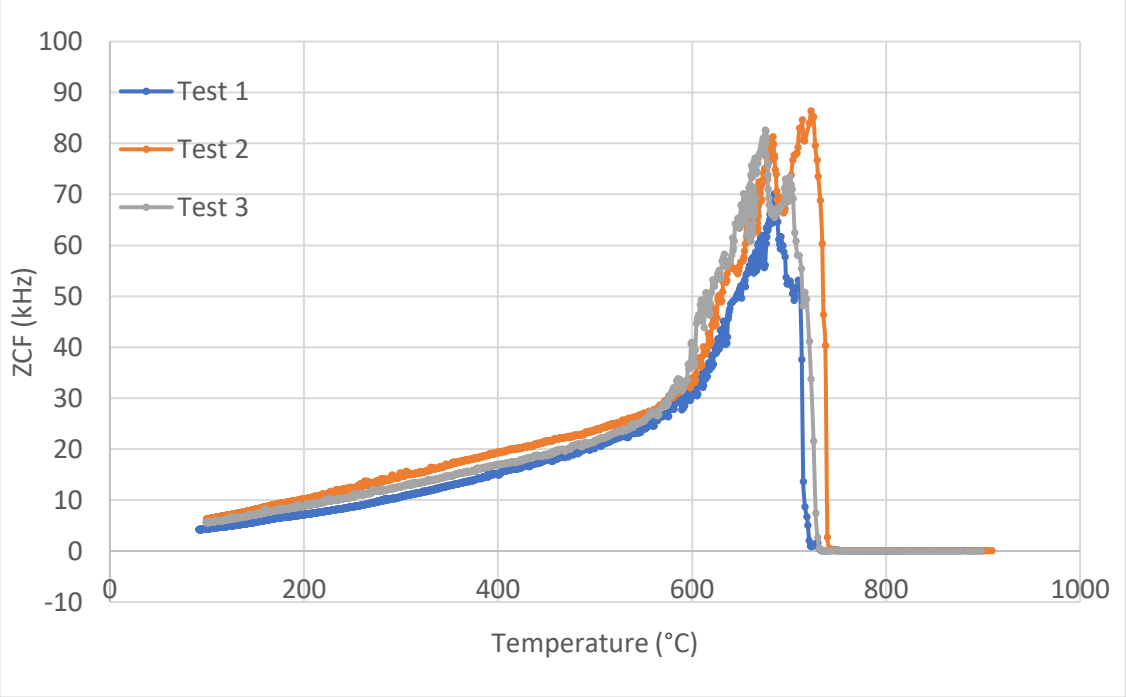

Figure 122. ZCF plotted with temperature for 10mm medium carbon steel tests 1-3.

8.1.7 Comparison of the EMspec® Sensor Response to Steels of Different Carbon Content

This section aims to inspect the difference between the EMspec® sensor measurements for steels of different carbon content, in this case for a 3mm mild steel and 3mm high carbon steel. The reason for choosing these samples is so the comparison would be like for like in terms of sample thickness, with the only difference being the chemical composition. Figure 123 shows the average cooling trajectory for the mild and high carbon steels at 3mm thickness. The cooling rate between 950℃ and 650℃ has been indicated as significant latent heating occurs after this temperature for the high carbon steel. The graph shows that the high carbon steel has a higher cooling rate than the mild steel. This is due to differing amounts of oxide forming on both samples; more oxide was formed on the 3mm mild steel which slows the cooling rate.

The phase percentage transformed with temperature obtained from dilatometry is shown in figure 124 for the 3mm mild and high carbon steel. It can be clearly seen that the mild steel transforms at a higher temperature. This is expected due to the mild steel having a lower carbon content [13]. Figure 125 shows the ZCF for mild steel and high carbon steel from tests 1-3 for both. The graph shows that the increase in ZCF signalling transformation has begun occurs at a higher temperature (approximately 730℃) than the high carbon steel (approximately 615℃) which is consistent with the phase percentage transformed obtained from dilatometry. The mild steel also has a higher ZCF peak on average than for the high carbon steel. This is due to a combination of transforming starting at a higher temperature, so any ferromagnetic phase formed would have a higher permeability purely due to temperature [11]. As well as that, mild steel microstructure has connected ferrite which has a higher permeability than the microstructure for the high carbon steel which is predominantly pearlite [4]. This agrees with the studies by Thompson et al. [26] and Zhou et al. [4]. This also agrees with the studies by Dickinson et al. [97] and Papaelias et al. [91, 92] who showed that a lower carbon steel has a higher EM signal during transformation at higher temperatures than for a high carbon steel. As the ZCF decreases with temperature following the ZCF peaks for both steels, the ZCF for the mild steel remains higher than for the high carbon steel which is consistent with the mild steel having a higher permeability. This shows that the EMspec® sensor can clearly distinguish between steels of different carbon content.

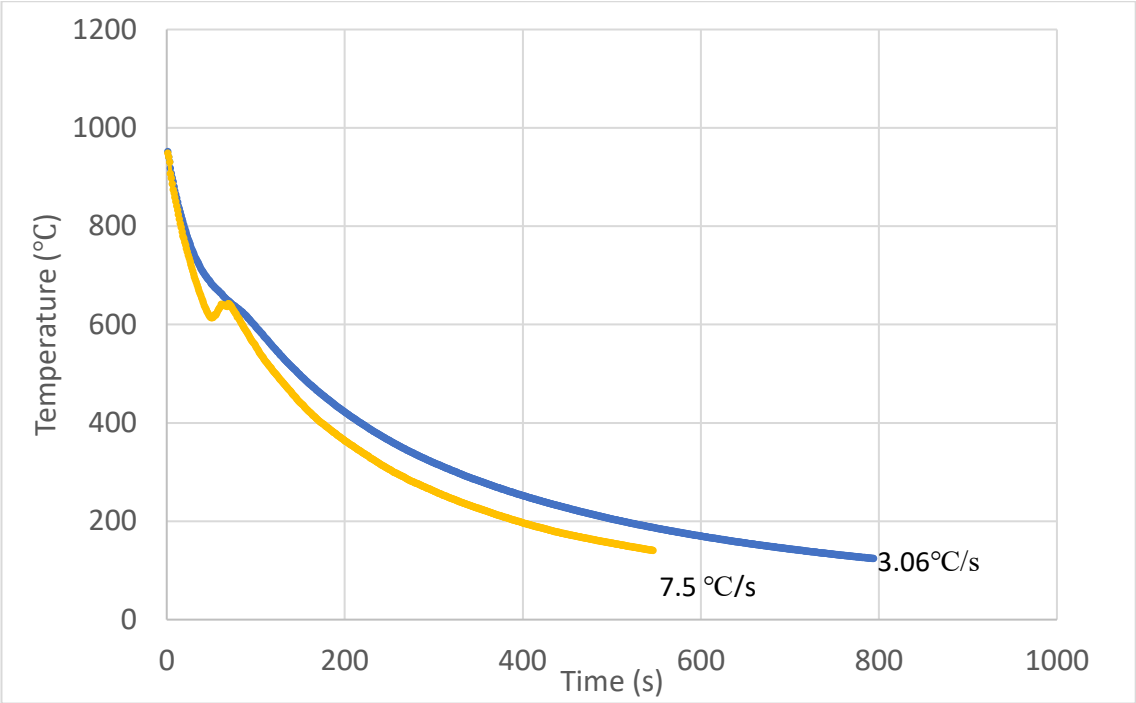

Figure 123. Average cooling trajectory of 3mm mild steel and 3mm high carbon steel. Cooling rates between 950℃ and 650℃ have been indicated.

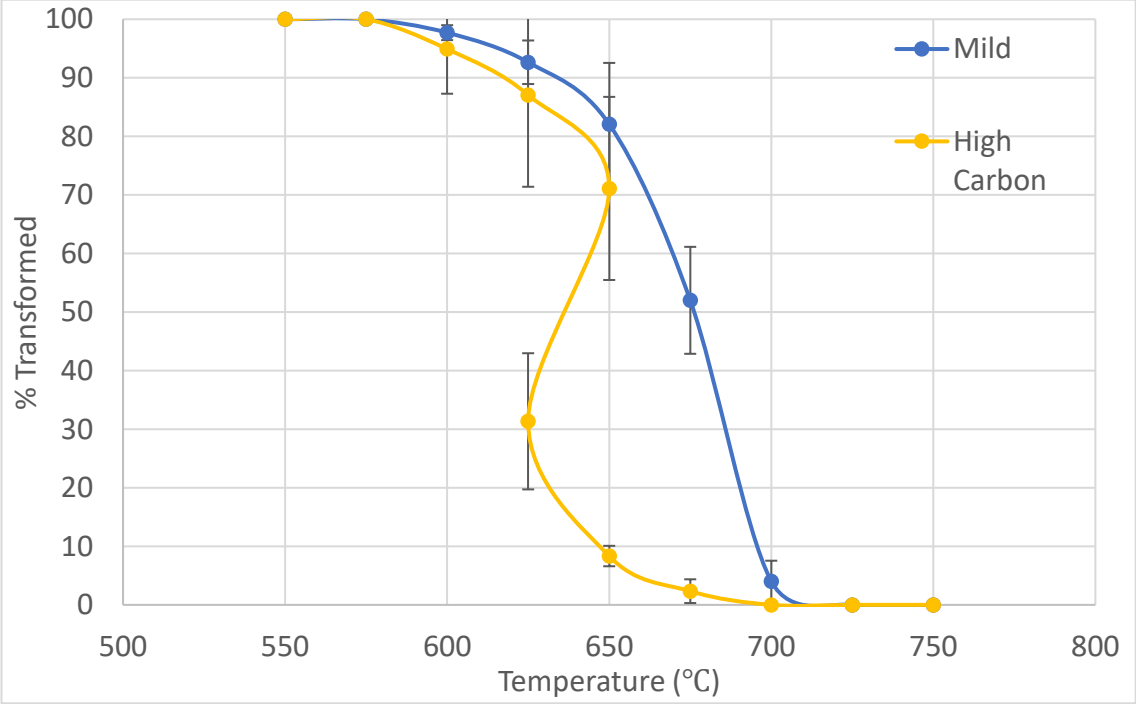

Figure 124. Phase percentage transformed with temperature for 3mm mild and 3mm high carbon steels obtained from dilatometry.

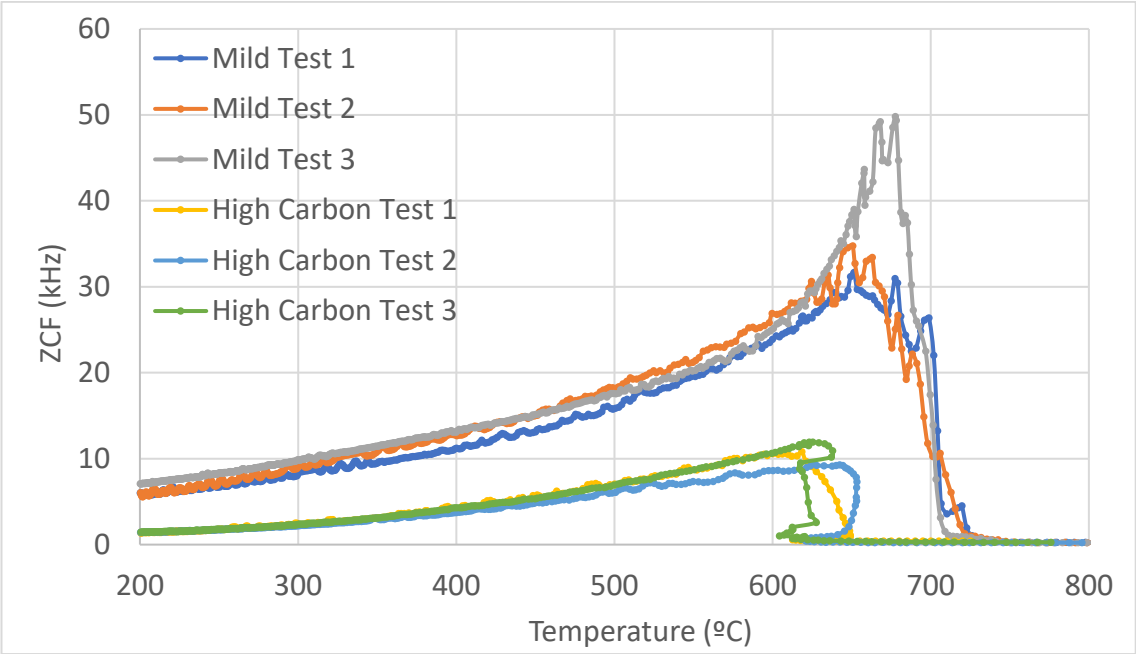

Figure 125. ZCF with temperature for 3mm mild steel tests 1-3 and 3mm high carbon steel tests 1-3.

8.2 2.25Cr - 1Mo Steel

Due to its chemical composition (shown in table 4), 2.25 Cr – 1 Mo steels have good hardenability with the two main alloying elements, chromium and molybdenum, delaying the ferritic transformation at slower cooling rates meaning bainite is expected at the cooling rates seen for the furnace-roller ROT experiments [105]. Therefore, a 2.25 Cr – 1 Mo steel grade was chosen for EMspec® sensor testing to examine the relationship between sensor signal and bainite transformation, all occurring at temperatures significantly lower than the Curie temperature for steel.

8.2.1 Microstructural Characterisation

The optical microstructures for the 3mm 2.25 Cr – 1 Mo steel in the as received condition, and following heat treatments for tests 1 and 2, are shown in figures 126-128 respectively. The as received sample has a tempered bainite microstructure consisting of a ferrite

matrix with distributed cementite in the grains and on the grain boundary. Little evidence of the bainitic lath structure remains. Following the furnace-roller ROT heat treatments for tests 1 and 2, the microstructures have a fully bainitic microstructure. The micrographs do look different however this is down to an etching effect; the sample for test two was not well etched and initially it was difficult to see the microstructural features. However, the contrast was enhanced using ImageJ software to show the microstructural features more clearly. As previously discussed in chapter 2, formation of low carbon ferrite can occur at the surface of a steel during heat treatments due to decarburisation as previously discussed. This can affect EM sensor signals, therefore micrographs of the top and bottom surfaces of the Cr-Mo steel following heat treatments for test 1 and 2 have been obtained to see if any decarburisation occurred and are shown in figures 129 and 130 respectively. For both tests, the top and bottom surface shows evidence of some non-uniform decarburisation with some scattered ferrite grains occurring near the surface. Figure 131 shows the microstructure of the 2.25Cr-1Mo steel following dilatometry heat treatment. It exhibits a fully bainitic structure. This is similar to the microstructures following heat treatment on the ROT (figures 127 and 128) which is expected.

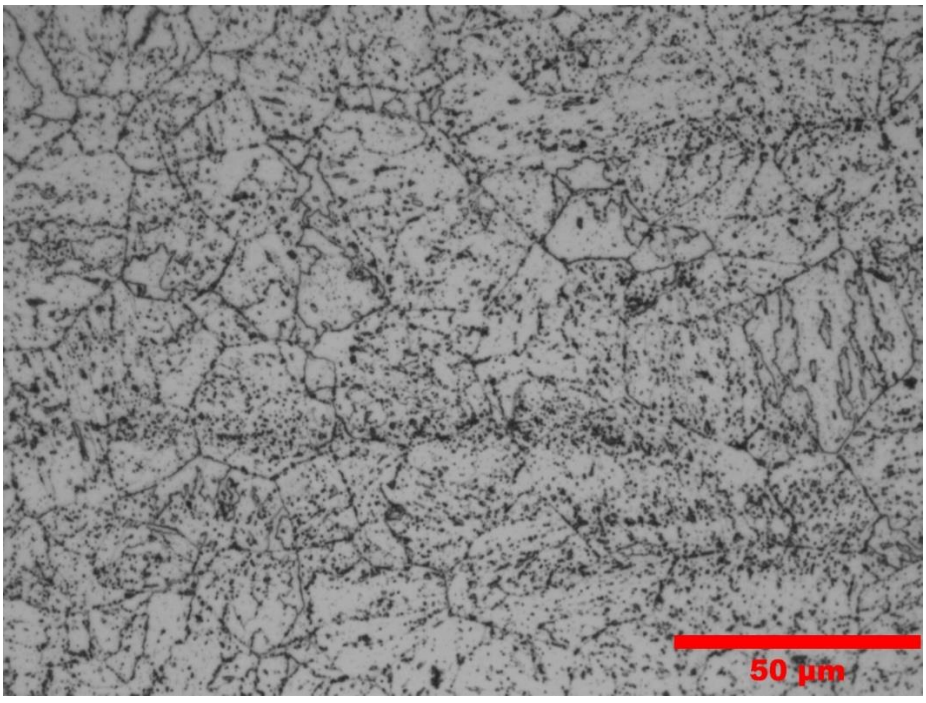

Figure 126. Optical microstructure at 50× magnification of a 3mm 2.25 Cr - 1 Mo steel in the as received condition.

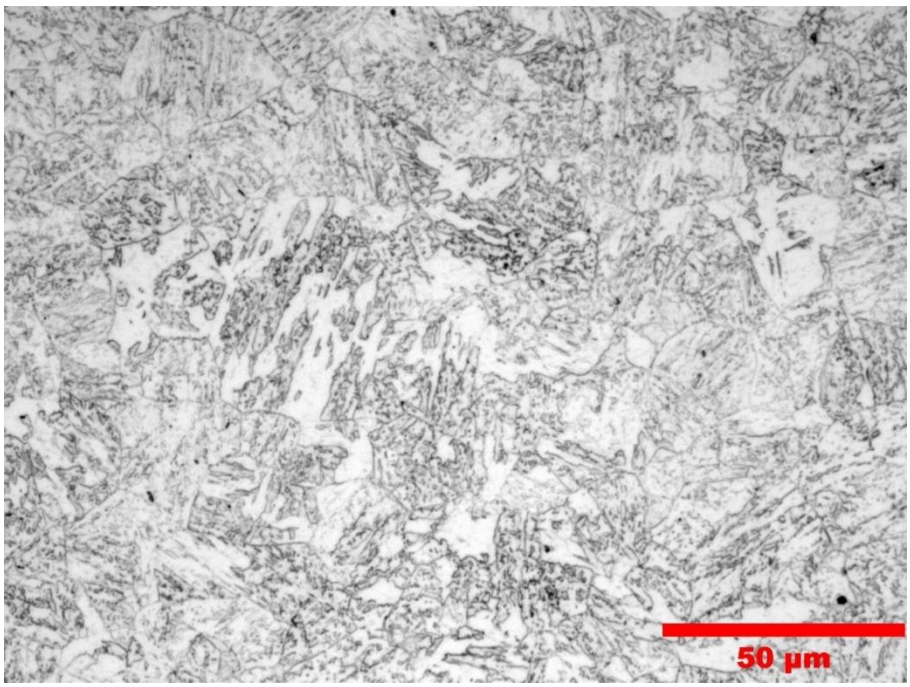

Figure 127. Optical microstructure at 50× magnification of a 3mm 2.25 Cr - 1 Mo steel following heat treatment for EMspec® test 1.

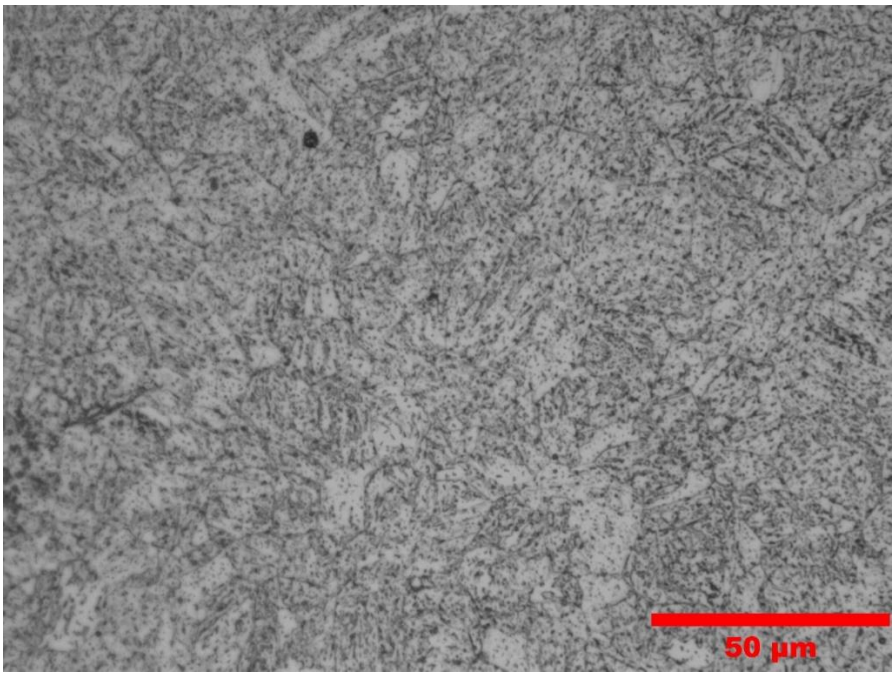

Figure 128. Optical microstructure at 50× magnification of a 3mm 2.25 Cr - 1 Mo steel following heat treatment for EMspec® test 2.

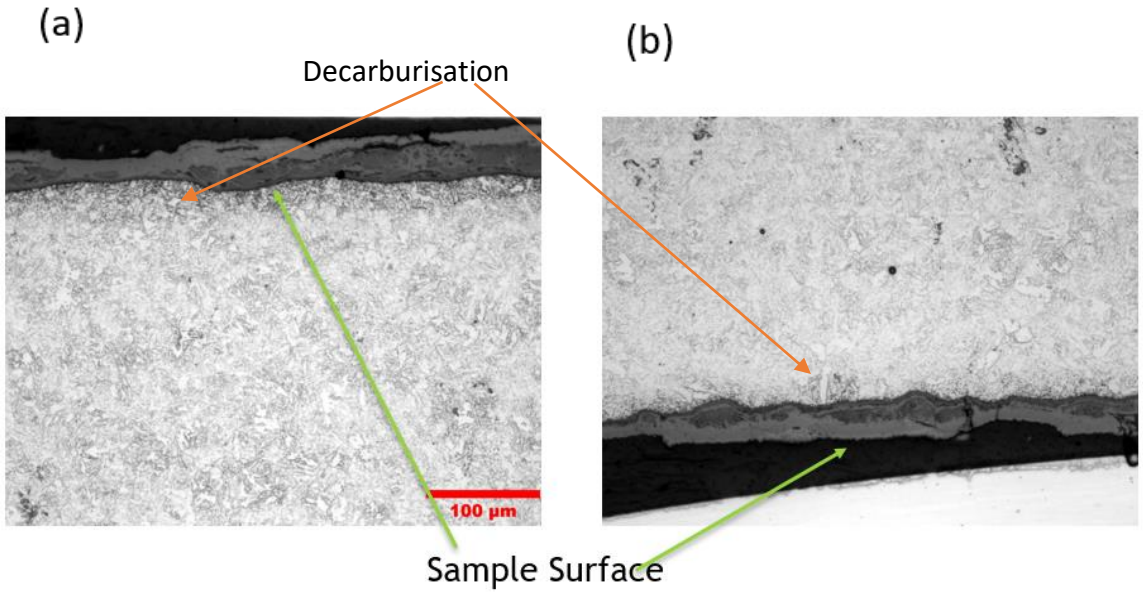

Figure 129. Optical microstructures at 20× magnification looking at top surface (a) and bottom surface (b) of the 3mm 2.25 Cr – 1 Mo steel used in test 1.

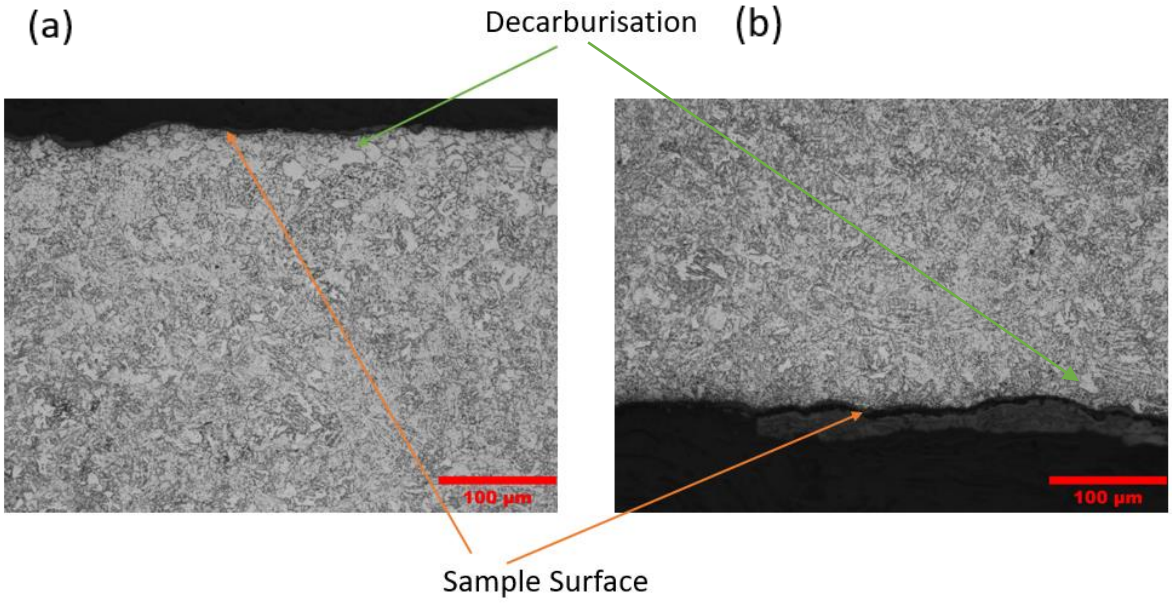

Figure 130. Optical microstructures at 20× magnification looking at to surface (a) and bottom surface (b) of the 3mm 2.25 Cr - 1 Mo steel used in test 2.

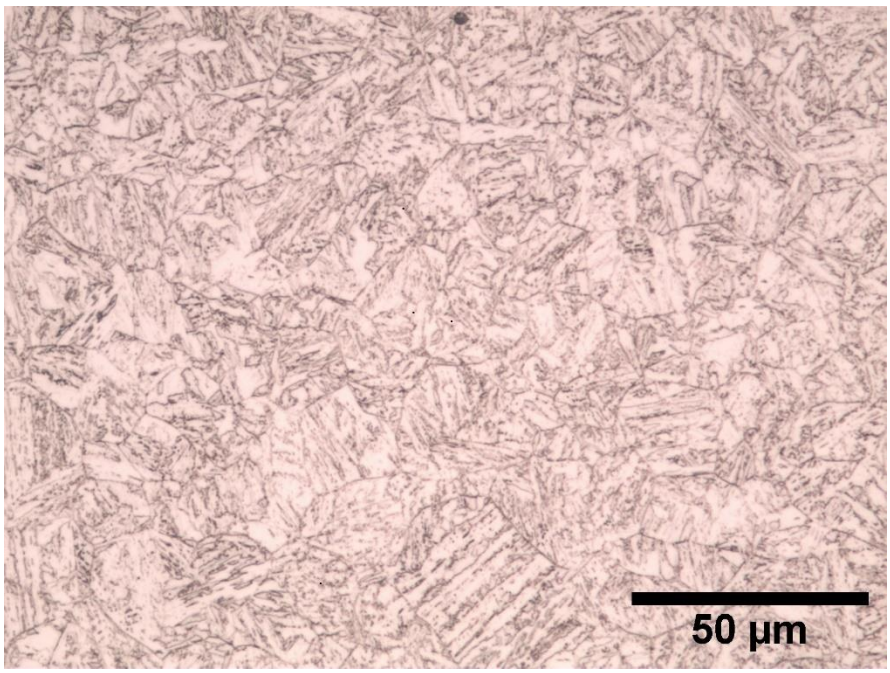

Figure 131. Optical microstructure at 50× magnification of a 3mm 2.25Cr-1Mo steel following dilatometry heat treatment.

8.2.2 Cooling Trajectories

The cooling trajectories for EMspec® tests 1 and 2 on the Cr-Mo steel are shown in figure 132. Test 2 clearly has a slower cooling rate than test 1. The reason for this is not obvious as the experimental procedure for both tests were the same. These tests were measured using only one thermocouple situated on the sample closer to the furnace door. This is because only one channel data logger was available at the time of testing. For both tests there is a change in cooling trajectory at around 500°C and this is due to the latent heating as a result of a bainitic transformation occurring at this temperature.

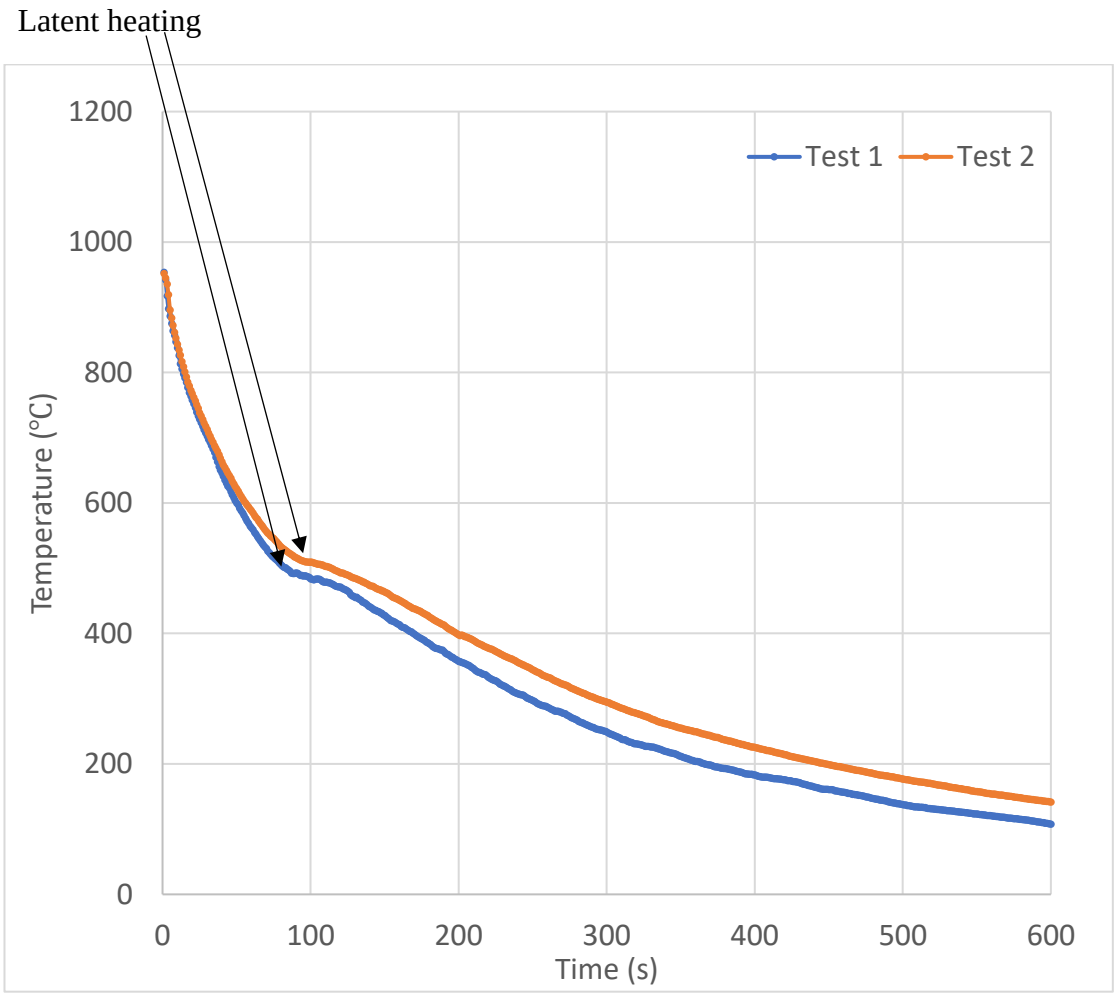

Figure 132. Cooling trajectories for 2.25Cr-1Mo steel following heat treatment for EMspec® sensor tests 1 and 2. The point where latent heating occurs for both tests is indicated.

8.2.3 EMspec® Sensor Results and Relation to Phase Fraction Transformed and EMspec® Sensor Model

The EMspec® sensor results for the 3mm 2.25 Cr – 1 Mo tests 1 and 2 are shown in figure 133. Above 500°C, the signal is relatively low, however it is higher than what is expected for a fully austenitic sample (approximately 0.8kHz). This is likely due to the non-uniform decarburisation shown in figures 129 and 130; the isolated regions of decarburisation have transformed to ferrite at a higher temperature. At around 500°C the ZCF for test 2 starts to increase. The fact that the ZCF increases earlier for test two is consistent with it transforming earlier than for test 1 due to the cooling rate for test 2 being lower. The ZCF for test 1 starts to increase at approximately 480°C which suggests that bainitic

transformation has started for this sample. The ZCF for test 2 peaks at approximately 400°C with a ZCF of around 5.5 kHz. This is higher than the temperature that the test 1 ZCF peaks at (approximately 390°C). The peak signal for test 1 is approximately 4.5 kHz. This is consistent with the sample having a lower permeability (and lower resistivity) as it is transforming later, so its ZCF peak will occur at a lower temperature. However, it should be noted that temperature inhomogeneity has been observed for the large plate samples, discussed in section 8.1.1, which means that there may be some error in the determined temperature – transformation relationship. Following the ZCF peaks for both tests, the ZCF decreases with decreasing temperature, which occurs as the sample has finished, or is close to finishing transforming so the decrease in permeability and resistivity due to decreasing temperature becomes the dominant effect on the signal.

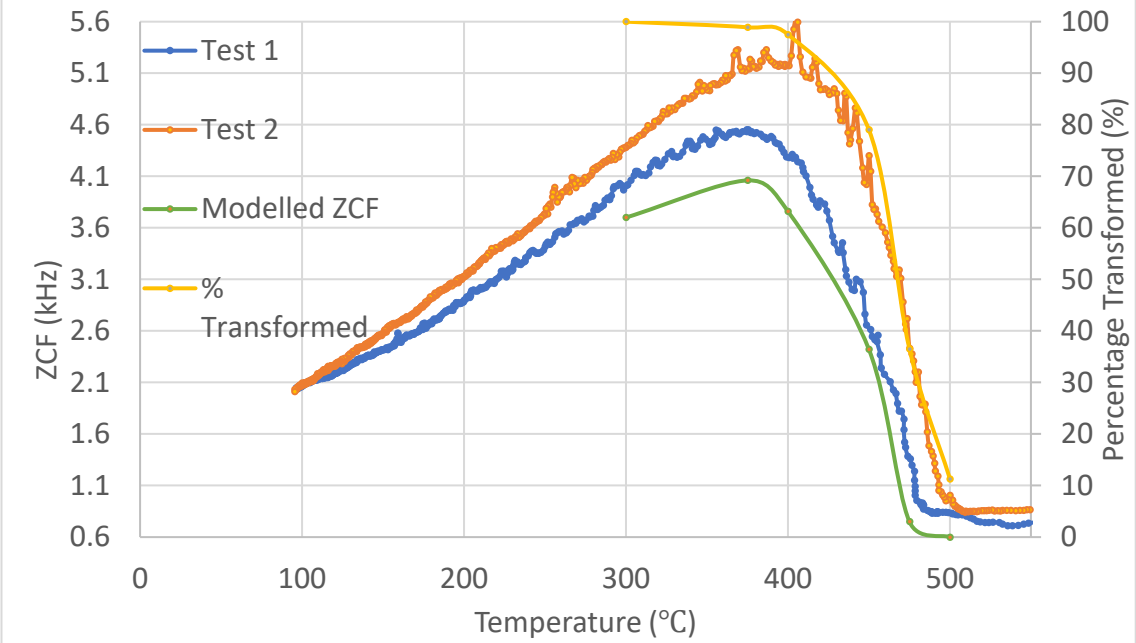

Figure 133. Measured and modelled ZCF with temperature for 3mm 2.25 Cr – 1 Mo Steel. Transformed percentage also plotted with temperature on the second Y axis.

For relation of ZCF to phase fraction transformed and the EMspec® sensor model, only test 1 will be considered as the cooling rate used in dilatometry was based on cooling rate achieved on the ROT for this measurement. Figure 133 shows that the ZCF begins to increase when the dilatometry data suggests that the sample should be around 35% transformed for test 1. This tends to suggest that there is a need for a minimum phase fraction (which may be linked to a needed for connectivity of the ferromagnetic phase) of the transformed bainite needed before there is a significant increase in permeability to increase the ZCF. This is consistent with the findings of Hao et al. [37]. The peak in ZCF

for test 1 coincides with the dilatometry data showing that the steel should be almost fully transformed at approximately 375°C. The ZCF decreases with temperature once the steel is predicted to be fully transformed due to decrease in permeability and resistivity, with no further increase in permeability due to increase in ferromagnetic phase. The difference in the temperature for the dilatometry transformation start and ZCF increase could also be affected by temperature inhomogeneity in the plate samples and differences in cooling rates between the plate cooling and dilatometry. This is because the cooling trajectory used during dilatometry did not perfectly match that of the dynamically cooled sample on the ROT, due to using a Newtonian cooling function (based on test 1 cooling rate on the ROT) for this dilatometry test. However, the model does agree well with the experimental data with both following the same trend despite these potential differences with a small difference in the predicted and experimental peak ZCF. The difference in the absolute values could be due to the model not considering the small amount of decarburisation, but also the methods of extrapolating permeability and resistivity values.

8.3 Duplex Stainless Steel

Duplex stainless steels have been chosen for testing using the EMspec® sensor, as it was expected that it would maintain a constant phase balance of austenite and ferrite at high temperatures. As it was expected to maintain a constant microstructure, this is useful for prediction and validation of the ZCF for the EMspec® sensor model.

8.3.1 Microstructural Characterisation

The as received microstructure is shown via an EBSD image in figure 134. Ferritic phase is shown as blue while the austenitic phase is shown as yellow. The as received microstructure consists of banded ferrite and austenite with elongated grains. A ferrite austenite phase balance of 57:43 was quantified. The optical microstructure for the duplex stainless steel after heat treatments for tests 1-3 is shown in figures 135-137. 500 × 500mm samples were heated in the furnace to 980°C and allowed to cool in air for tests 1 and 2 and held for 5 minutes, whilst for test 3 the sample was held in the furnace at 800°C for around 30 minutes before testing. The micrographs following heat treatments for tests 1 and 2 are shown in figures 135 and 136. Tests 1 and 2 show a ferrite (dark) and austenite (light) microstructure. There also appears to be evidence of a small amount of a

third phase which is expected to be sigma phase (indicated in the figures). For test 3 (figure 137), the micrograph shows that a more significant formation of sigma phase has occurred. Sigma phase is a paramagnetic inter metallic phase rich in iron and chromium. It is undesirable to form sigma phase in duplex stainless steels as it can have a negative effect on mechanical properties and corrosion resistance [106]. Sigma phase forms at high temperatures, ranging from 600℃ – 1000℃, with the fastest precipitation of the phase occurring between 800℃ and 850℃ (figure 138). The observation of sigma phase in the test 3 sample is consistent with the plate having been held at 800℃ for around 30 minutes [106], whilst for tests 1 and 2 the higher temperature hold appears to have been sufficient to form a small amount of sigma phase.

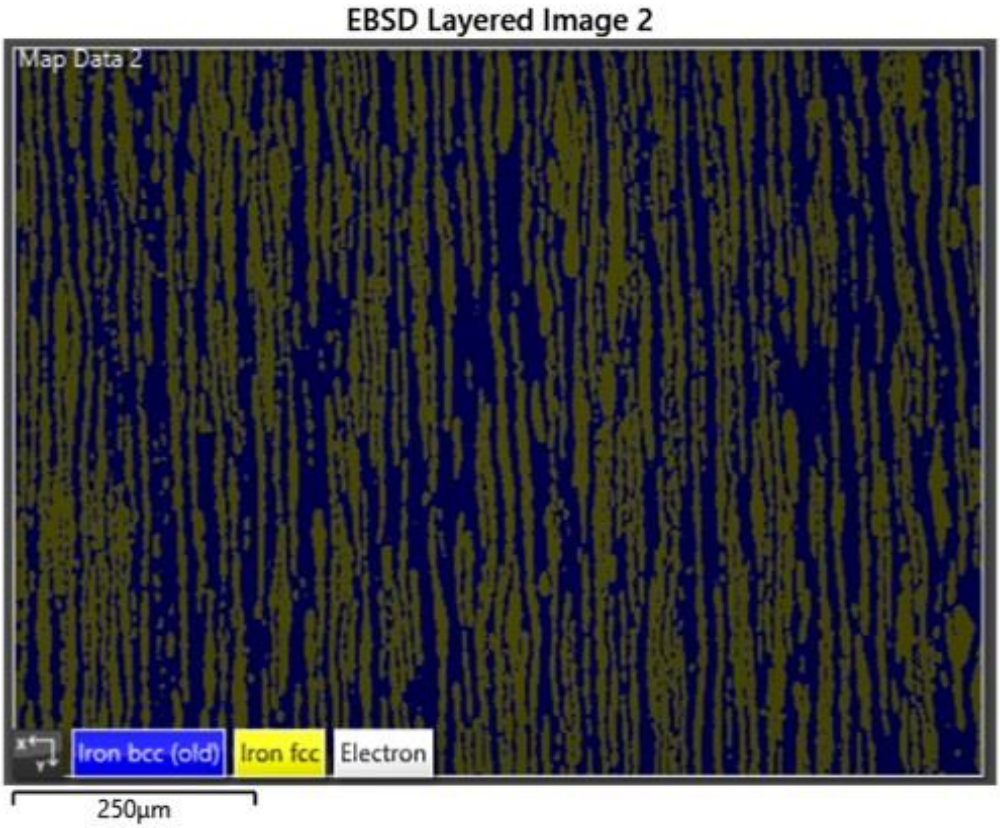

Figure 134. EBSD image of the duplex stainless steel in the as received condition.

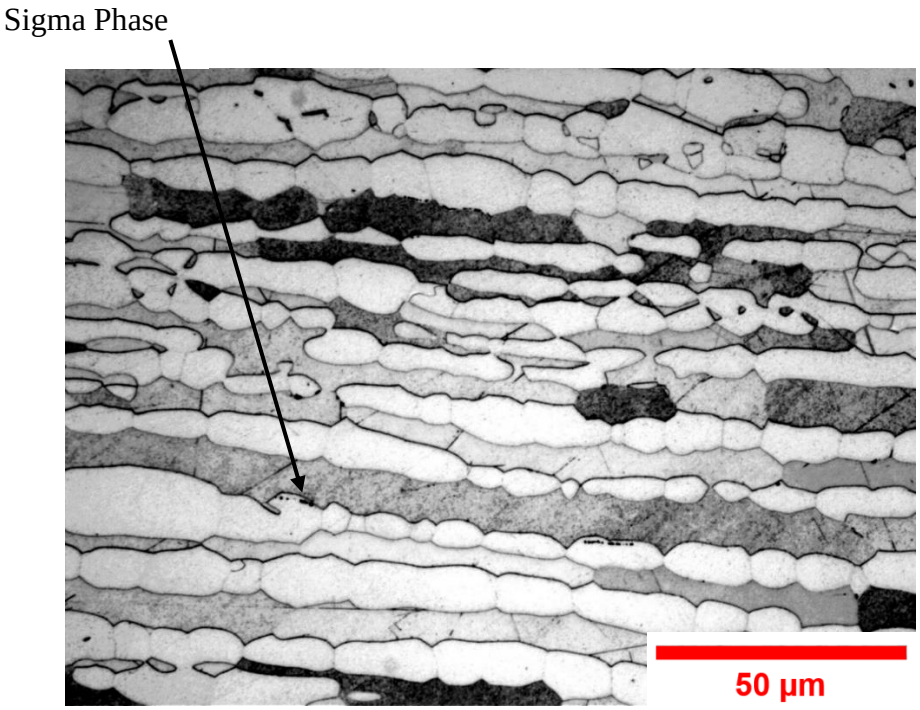

Figure 135. Optical microstructure at 50× magnification of a duplex stainless-steel following heat treatment for EMspec® test 1. Regions of sigma phase are indicated.

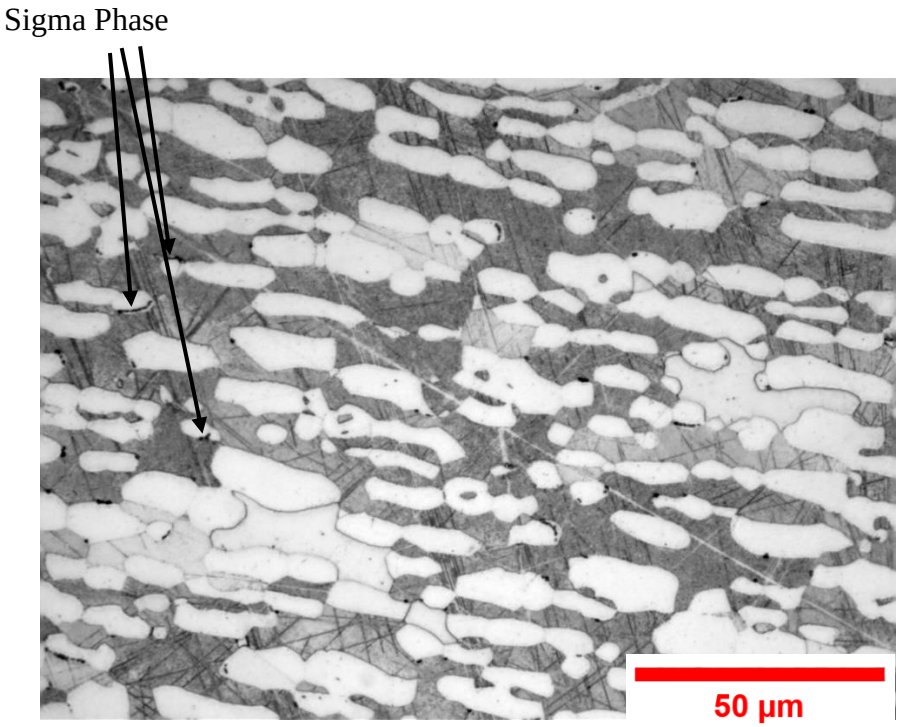

Figure 136. Optical microstructure at 50× magnification of a duplex stainless-steel following heat treatment for EMspec® test 2. Regions of sigma phase are indicated.

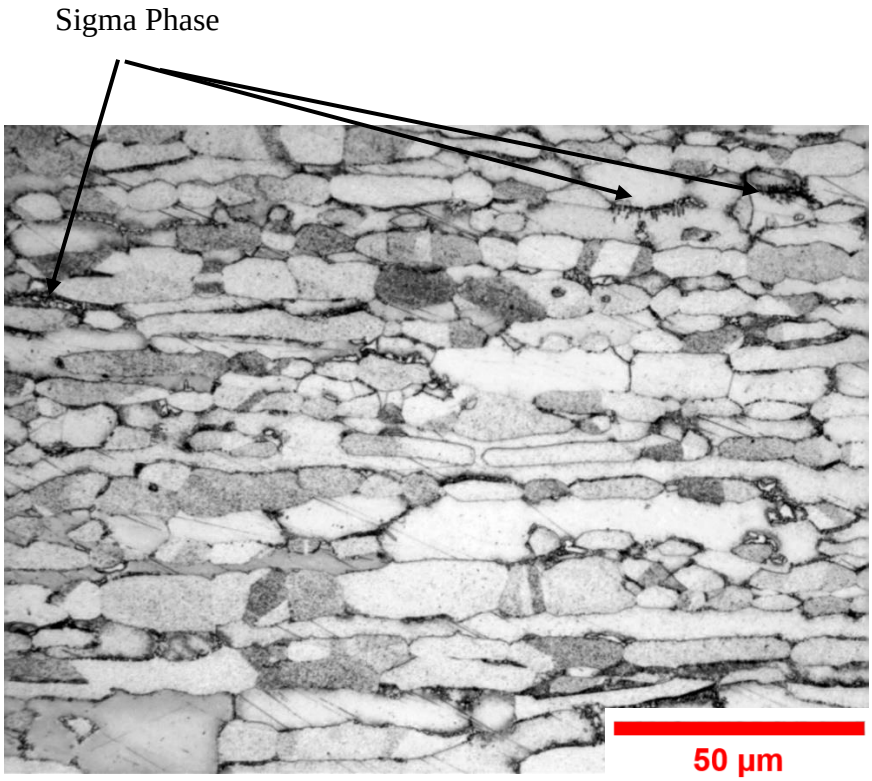

Figure 137. Optical microstructure at 50× magnification of a duplex stainless-steel following heat treatment for EMspec® test 3. Regions of sigma phase are indicated.

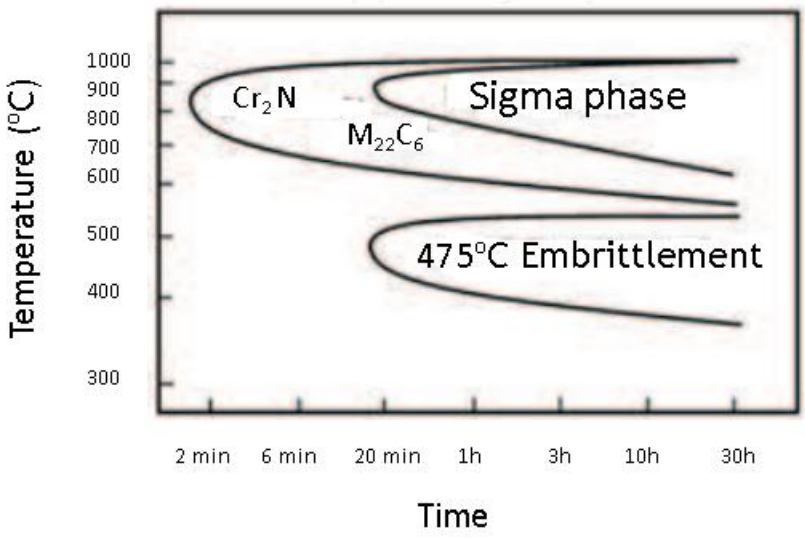

Figure 138. Kinetics of different phase in a duplex stainless steel [106].

8.3.2 Cooling Trajectories

Figure 139 shows the cooling trajectories of the duplex steel during EMspec® tests 1-3. The steels were measured with one thermocouple as a one channel data logger was available at the time of these tests. From 700℃ to 500℃ there is good repeatability of the cooling rates with the trajectories for the three tests overlapping each other. However, as the temperature decreases, it is apparent that test 3 has the slowest cooling rate while test 1 has the fastest.

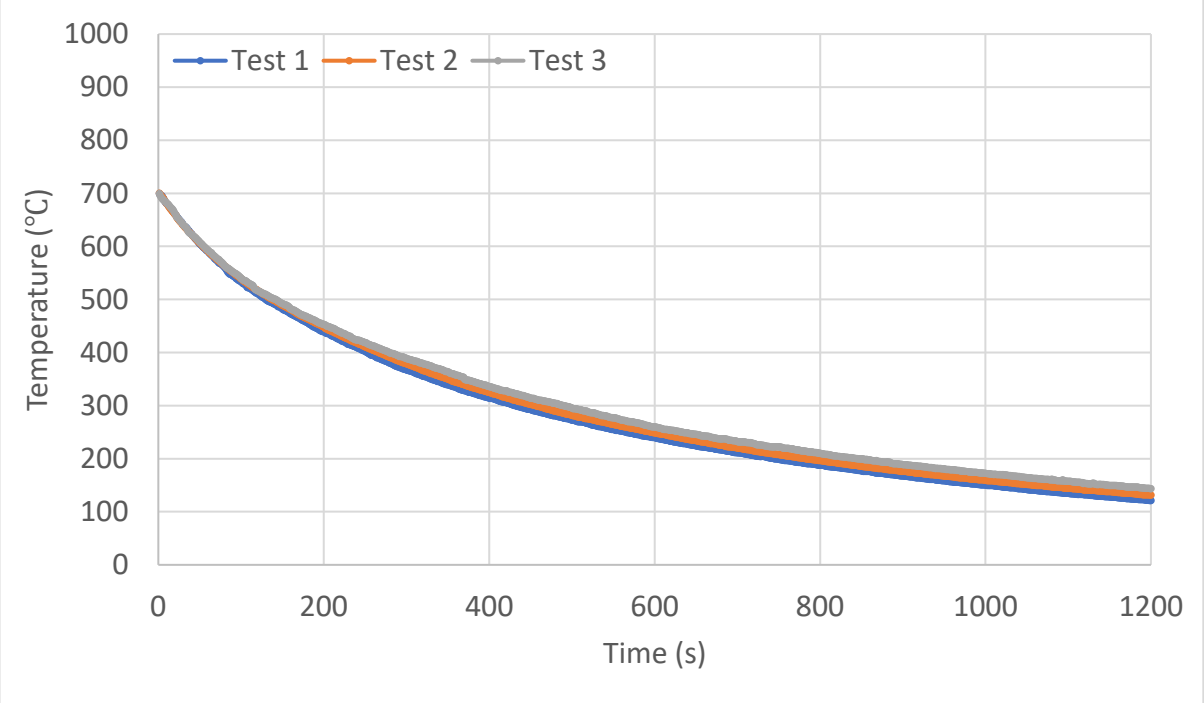

Figure 139. Cooling trajectories for duplex stainless-steel tests 1-3.

8.3.3 EMspec® Sensor Results and Modelling

The EMspec® sensor results with temperature for tests 1-3 for the duplex stainless steel is shown in figure 140. As there is no phase transformation during cooling for a duplex stainless steel, there should just be a ZCF increase when the sample cools through its Curie temperature. Figure 140 shows that the signal for the three tests increases at around 480℃ to 500℃. This suggests that the Curie temperature for these steels after heat treatment is around 480℃ to 500℃. This would be consistent with literature as it is known that high chromium content, as in a duplex stainless steel, decreases the Curie temperature [11]. This is also consistent with a study by Tavarez et al. [107] which showed the Curie temperature of thermally aged duplex stainless steels to range between

500℃ and 600℃. The difference in ZCF peaks between the three tests is likely caused by changed in microstructure as a results of heat treatment. The ZCF peak is noticeably lower for test 3 than it is for tests 1 and 2. This is consistent with the precipitation of higher amount of sigma phase due to the sample being held at 800℃ for 30 minutes. As sigma phase is paramagnetic and forms in the ferritic phase [106], the fraction of ferromagnetic phase will decrease with the formation of sigma phase causing the permeability of the material to decrease, which give a lower peak ZCF as is shown by the test 3 results.

The modelled ZCF is also included in figure 140. The power law was used to calculate an effective permeability with temperature for a 50:50 ferrite austenite phase balance. The modelled data does not agree with the experimental data particularly well. The increase in ZCF seen after cooling through the Curie temperature is higher for the model prediction than it is for the experimental data. Part of the reason for this is because the effective permeability used in the model is for 50:50 austenite ferrite balance while the microstructure of the duplex stainless steel used in this work exhibits a 57:43 ferrite austenite phase balance. This is also thought to be because the power law (described in chapter 5), used to calculate the effective permeability for the 50:50 ferrite austenite phase balance, does not consider the specific microstructure seen in the duplex stainless steel, and more specifically ferrite connectivity, but a random mix of phases. In a study by Hao et al. [37] a FEM, which considers the phase distribution in a two-phase steel microstructure predicts the permeability to increase significantly at around 35% ferrite when the ferrite is starting to become connected [37]. However, the power law permeability increases from zero so there is an offset between power law and FE model for ferrite fractions between 35% and 50%. As the permeability of ferrite increases with temperature, this difference in effective permeability could be higher than at room temperature, which would account for the difference in ZCF peak between the model and the experimental data but also the ZCF values during cooling down to 350℃. The work by Hao et al. [37] also uses approximately equiaxed austenite and ferrite grains while the microstructural phases for the duplex stainless steel used in this work is elongated. Finally, the duplex stainless steel is very highly alloyed with over 20% chromium, which will decrease the magnetic moment of the steel [11] and cause an offset between the experimental and modelled ZCF. This is because the model is for austenite ferrite balances of pure iron.

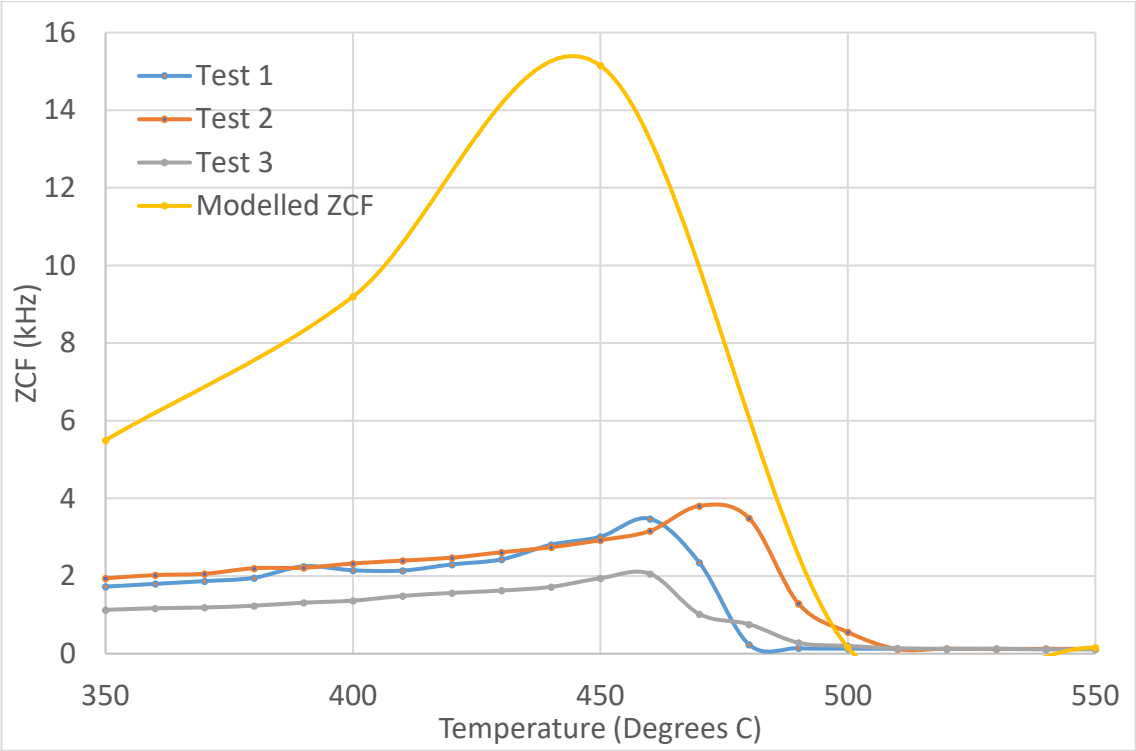

Figure 140. ZCF with temperature for duplex stainless-steel tests 1-3 and modelled ZCF.

8.4 Chapter Summary

The EMspec® sensor has been used to monitor multiple steels during phase transformation on cooling. Phase fraction calculated from dilatometry for the samples has been related to the experimentally measured ZCF. The EMspec® sensor model has been used to predict the ZCF using a combination of phase percentage transformed obtained from dilatometry for the sample being predicted, and power law calculations of effective resistivity and permeability based on measured resistivity data and extrapolated permeability data. The EMspec® sensor was able to detect and monitor the phase transformation for steels including mild steel of 3, 6 and 10mm thickness, 3mm high carbon steel, 10mm medium carbon steel and a 3mm 2.25 Cr- 1Mo steel. The sensor was also able to detect magnetic transformation of a duplex stainless steel while it cooled through its Curie temperature as well as showing sensitivity to the formation of a higher amount of sigma phase in the sample for test 3. The data sets for the mild steels showed good repeatability as did those for the high carbon steel. The medium carbon steel showed variability in the measurements but the EMspec® sensor may have been able to detect two transformations with two ZCF peaks being exhibited by the samples - the first being

consistent with transformation to ferrite and the second to pearlite. Most tests that involved phase transformation showed that the ZCF did not increase due to the increase in phase percentage transformed until the steels were between 30 and 40% transformed which agrees with Hao et al. [37]. The model was not able to solve for the high permeabilities predicted for the transformed percentages during transformation for the 3mm, 6mm and 10mm mild steel. This may be due to a finer mesh being needed to solve for the higher permeabilities, however further simulations are required to confirm model sensitivity to mesh size. The lower permeability duplex stainless steel (50:50 ferrite/austenite) was able to be solved by the EMspec® model, however there is an offset between the experimental and modelled data, and this is due to the nature of the power law calculation and how highly alloyed the steel is. The model agreed well with the experimental results for the high carbon steel and the 2.25Cr-1Mo steel. The EMspec® sensor was shown to be able to detect differences in transformation for mild steel samples of different thicknesses during cooling due to their different transformation temperature range/ transformation percentage and permeability as a result of the different cooling rates of the different thickness samples in air. The EMspec® sensor also showed sensitivity to the phase transformation of steels with different carbon content, as the 3mm mild and 3mm high carbon steel were clearly distinguishable during cooling through transformation and down to room temperature.

8.4.1 Industrial Relevance of this Research

At the Tata Steel hot strip mill in Ijmuiden, there are currently three EMspec® sensors in use on the ROT monitoring various points of transformation on the steel strip. Tata Steel have developed an inhouse model that predicts the transformed ferrite fraction from the EMspec® sensor signal based on the fundamental relationships established in previous work [11, 40, 42]. This model includes several coefficients and fitting constants that are steel grade specific. Tata Steel also have an in-house mill model (Titan) that predicts the transformation behaviour of the steel strip based on composition and process parameters. The EMspec® sensor outputs have been matched against the mill model predictions and has shown promising results for many steel grades [8, 43], however it is known that the mill model does not predict accurately for all steel grades / process parameters and this is why the EMspec® outputs are desired for quality control. The work in this project has contributed to validating a newly developed FEM for the EMspec® sensor which is

described in chapter 5. This model is aimed at predicting the ferrite fraction during dynamic transformation for steels with low carbon contents (<0.2 wt%) and is based on using the relationships established in parallel work for the changes in permeability with temperature for ferrite + austenite microstructures [40, 108]. As previously mentioned, the Tata Steel numeric model requires fitting values that are grade specific, however the newly developed FE model at the University of Warwick does not require fitting values, as it has been established based on the actual sensor design and fundamental physics relationships for permeability and resistivity (the key materials parameters) with temperature. Therefore, in principle this model can be used at any hot strip mill for online ferrite fraction predictions for low carbon grades during dynamic transformation. A real time on-line system for monitoring the ferrite fraction provides advantages for the steel producer when producing complex steel grades such as dual phase steel, where it is important to achieve the right microstructure for the desired mechanical properties such as tensile strength [100]. This research has given key insight into the sensitivity of the EMspec® sensor for monitoring the dynamic transformation of a range of steels and has included austenite to ferrite transformation, austenite to bainite transformation and austenite to pearlite transformation. This shows that the sensor system and model can be applied to monitoring phase transformed fraction of different microstructural phases not just ferrite fraction in ferrite austenite balances during dynamic transformation which opens the door to future industrial applications.

9. Conclusions

The main aim of the work in this thesis was to relate the EM signal measured by the EMspec® sensor to the microstructural state (phase percentage transformed) of a range of steels. It was also essential that non-microstructural effects were considered such as edge effect, lift off, thickness and effect of surrounding structures to give confidence that signals being measured were purely due to the microstructural state of the target steel.

The industrial EMspec® sensor has been used to monitor the phase transformation of a range of steels while dynamically cooling, as well as the magnetic transformation of a duplex stainless steel. The ZCF has been quantitatively related to ferrite percentage transformed obtained via dilatometry. Effective permeabilities and resistivities were calculated using a combination of transformed fraction from dilatometry, measured/literature resistivities of various phases, literature permeabilities of various phases, and power law equations. These permeabilities and resistivities have been used in the EMspec® model to predict ZCF for relation to the experimental data. The main conclusions that can be made from the results presented are as follows:

- The EMspec® sensor can detect and monitor the full phase transformation for various carbon steels including mild steels of 3, 6 and 10mm thickness, a high carbon steel and medium carbon steel. The EMspec sensor is also able to monitor the full transformation to bainite of a 2.25Cr-1Mo steel. Increases in ZCF associated with the phase transformation were recorded for phase transformations to ferrite, pearlite and bainite in a range of steels.

- The EMspec® is sensitive to the changes in phase transformation kinetics of the same grade steel with different cooling rates caused by a difference in sample thickness. The 3mm mild steel transformed at a lower temperature due to having the faster cooling rate than for the 6mm and 10mm samples. This resulted in the ZCF increasing at a lower temperature for the 3mm mild and have a lower peak ZCF due to being at a lower temperature and therefore having a lower permeability. The 10mm mild steel had the highest ZCF peak and this is because of the transformation starting at the highest temperature due to having the slowest cooling rate of the 3 steels. The peak ZCF being the highest for the 10mm mild

steel is consistent with transformation occurring at a higher temperature so the ZCF peaks at a higher temperature which results in a higher permeability.

- The EMspec® sensor can clearly distinguish between steels of different carbon content as they cool and go through phase transformation. A 3mm mild steel and 3mm high carbon steel were compared. It could be seen that the mild steel transforms at a higher temperature than for the high carbon steel which is expected as it has a lower carbon content. The ZCF for the mild steel was higher than for the high carbon steel for two reasons. The first being that the steel transforms at a higher temperature so when the ZCF peaks, the higher temperature plays a part in the permeability being higher than for the high carbon steel. The second reason is because a predominantly ferritic microstructure with some pearlite and bainite (mild steel) is known to have a higher permeability than a fully pearlitic microstructure as shown for the high carbon steel. The 3mm mild steel ZCF remains consistently higher than for the high carbon steel during cooling which further confirms that the mild steel has a higher permeability. This agrees with studies by Zhou et al. [4], Thompson et al. [26], Papaelias et al. [91-93] and Dickinson et al. [97].

- The change in Curie temperature due to a steel being highly alloyed can be detected by the EMspec® sensor. A duplex stainless steel was tested to detect the Curie temperature while the microstructure remained consistently 57:43 ferrite austenite phase balance. The ZCF increase signalling magnetic transformation between 480°C and 500°C for the 3 tests. This suggests a relatively low Curie temperature which would be consistent with the steel being highly alloyed with chromium [11]. This is also consistent with a study by Tavarez et al. [107] who showed that the Curie temperature of a duplex stainless steel was between 500°C and 600°C. The EMspec® sensor is also sensitive to varying levels of sigma phase formation in duplex stainless steels. Tests 1 and 2 were heated to and held at 980°C for 5 minutes and appeared to form small amounts sigma phase. Test 3 was held at 800°C for 30 minutes and showed clear evidence of higher amount of sigma phase. These was reflected in the ZCF with temperature where test 3 had a lower peak ZCF than for tests 1 and 2. Test 3 also had a consistently lower ZCF with decreasing temperature which would be consistent with this sample have a lower

permeability than for the samples used in tests 1 and 2 and this is caused by the greater amount of sigma phase formed.

- The EMspec® signal (ZCF) is sensitive to decarburisation. Test 3 for the 3mm mild steel showed a clearly higher signal for tests 1 and 2 which is consistent with the sample for test 3 showing significant decarburisation while the samples for tests 1 and 2 showed little to none. This was also the case for the high carbon steel where test 2 showed very little evidence of decarburisation while tests 1 and 3 showed evidence of non-continuous decarburisation. The ZCF trajectories during cooling were repeatable for tests 1-3 while test 2 had a lower peak ZCF and during cooling. This is consistent with test 2 having no decarburisation. This agrees with the Papaelias et al. [91-93] who also showed sensitivity of an EM sensor to decarburisation while monitoring the phase transformation for a range of carbon steels.

- When relating the ZCF to phase percentage transformed obtained from dilatometry, the 6mm and 10mm mild steels, the high carbon and the 2.25 Cr-1Mo steel all need to be approximately 30-40% transformed before an increase in ZCF occurs due to the need for ferromagnetic phase connectivity before permeability significantly increases. This agrees well with the literature for room temperature ferrite/austenite phase fractions [37]. For all the steels going through phase transformation during cooling used in this study, the ZCF would generally peak before the steel is fully transformed according to dilatometry. This shows that after a certain amount of phase has transformed the decrease in permeability and resistivity due to decrease in temperature has a more significant effect on ZCF than the increase in permeability due to more ferromagnetic phase forming.

- The modelling data agreed well with the experimental data for steels that consisted of lower permeability phases such as bainite and pearlite. For the 3mm, 6mm and 10mm mild steel the model could not solve for the high permeabilities which may be due to a more refined mesh being required. The model was able to solve for the duplex stainless steel however the modelled data did not agree with the experimental data due to the nature of the calculation of effective permeability. Power law was used however this does not consider the microstructural parameters such as the connectivity of ferrite. There is an offset between

permeabilities calculated from FEM models and microstructure models and from the power law for austenite ferrite phase balances. At lower ferrite fractions (<35%) the effective permeability calculated by the power law increases from 0% as it does not consider the need for ferrite connectivity before there is an influence on permeability [37].

This work shows that the EMspec® sensor can monitor the full transformations of a range of steels during dynamic cooling. The sensor signal can also be quantitatively related to the microstructural state during transformation in the form of phase fraction transformed.

10. Future Works

- To run an FEM microstructure model [40] to establish the relationship for pearlite austenite phase balance and bainite austenite phase balance with permeability to see if the need for connectivity of ferromagnetic phase also applies to ferromagnetic phases with lower permeability such as bainite and pearlite

- Validate the dilatometry phase fraction transformed results by running quench tests on a gleeble. This will require multiple samples of the same steel to be cooled at the cooling rate achieved on the ROT. These samples will be cooled to various temperatures during transformation and then quenched. The remaining austenite will then transform to martensite. The microstructure can then be investigated via optical or scanning electron microscopy to determine the phase fraction at different points during the transformation.

- Run the EMspec® sensor model at a higher mesh to see if this allows the model to solve for higher permeabilities such as that exhibited by the 3mm, 6mm and 10mm mild steels.

- Use the EMspec® sensor with water quench to monitor transformations to martensite and engineer dual phase steel microstructures.

- Apply the EMspec® sensor system with different design for the application of measuring more complex geometries such as rod and bar

- Use the EMspec® system for the application of measuring steel plate, correlating through thickness thermal and microstructure gradients to the EMspec signal

11. References

[1] R. W. K. Honeycombe and H. K. D. H. Bhadeshia, *Steels: Microstructure and Properties*, 2nd ed. London, UK: Edward Arnold, 1995.

[2] C. L. Davis, M. Strangwood, and A. J. Peyton, "Overview of non-destructive evaluation of steel microstructures using multifrequency electromagnetic sensors," *Ironmak. Steelmak.*, vol. 38, no. 7, pp. 510–517, 2011.

[3] L. Zhou, J. Liu, X. J. Hao, M. Strangwood, A. J. Peyton, S. Balamurugan, P. F. Morris and C. L. Davis, "Quantification of the effect of changes in steel microstructural parameters on EM sensor signals," in *NDESAI*, 2011, pp. 208–215.

[4] L. Zhou, J. Liu, X. J. Hao, M. Strangwood, . J. Peyton, and C. L. Davis, "Quantification of the phase fraction in steel using an electromagnetic sensor," *NDT E Int.*, vol. 67, pp. 31–35, 2014.

[5] W. Zhu, W. Yin, A. Peyton, and H. Ploegaert, "Modelling and experimental study of an electromagnetic sensor with an H-shaped ferrite core used for monitoring the hot transformation of steel in an industrial environment," *NDT E Int.*, vol. 44, no. 7, pp. 547–552, 2011.

[6] W. Zhu, H. Yang, A. Luinenburg, F. van den Berg, S. Dickinson, W. Yin and A. J. Peyton, "Development and deployment of online multifrequency electromagnetic system to monitor steel hot transformation on runout table of hot strip mill," *Ironmak. Steelmak.*, vol. 41, no. 9, pp. 685–693, 2014.

[7] A. J. Peyton, W. Yin, C. L. Davis, M. Strangwood, A. J. Douglas, and P. F. Morris, "On-Line Microstructure Analysis of Rod by Induction Spectroscopy," *Ironmak. Steelmak. Process. Prod. Appl.*, vol. 37, no. 2, pp. 135–139, 2010.

[8] P. Hunt, F. Van Den Berg, H. Yang, and A. Peyton, "The Real Time Transformation Control at Hot Strip Mill Key Words Engineering the Sensor," in *Metec & 2nd Estad*, 2015, no. June, pp. 1–9.

[9] A. V Marmulev, G. Herman, J. M. Turon, E. I. Poliak, and L. M. Kaputkina, "Online electromagnetic monitoring of austenite transformation in hot strip rolling and its application to process optimization," vol. 110, no. 3, pp. 205–213, 2013.

[10] R. Hall, M. Strangwood, L. Zhou, and C. Davis, "Dynamic measurement of recovery and recrystallisation in interstitial free steel using a high temperature electromagnetic sensor," *La Metallurgia*, pp. 35–42, 2016.

[11] R. M. Borzoth, *Ferromagnetism*. Wiley, 1993.

[12] H. D. Young, F. W. Sears, R. A. Freedman, and A. L. Ford, *Sears and Zemansky's University Physics: With Modern Physics*. Addison-Wesley, 2012.

[13] W. D. Callister, *Materials Science and Engineering: An Introduction*. John Wiley & Sons, 2007.

[14] R. Hall, "Measurement of Recovery and Recrystallisation in Interstitial Free Steels Using Electromagnetic Sensors," *Univ. Birmingham*, no. September, 2016.

[15] S. Chen, J. Butler, and S. Melzer, "Effect of asymmetric hot rolling on texture,

microstructure and magnetic properties in a non-grain oriented electrical steel," *J. Magn. Magn. Mater.*, vol. 368, pp. 342–352, 2014.

[16] Y. Zhang, Y. Xu, H. Liu, C. Li, G. Cao, Z. Liu and G. Wang, "Microstructure, texture and magnetic properties of strip-cast 1.3% Si non-oriented electrical steels," *J. Magn. Magn. Mater.*, vol. 324, no. 20, pp. 3328–3333, 2012.

[17] P. Ghosh, R. R. Chromik, B. Vashegi, and A. M. Knight, "Effect of crystallographic texture on the bulk magnetic properties of non-oriented electrical steels," *J. Magn. Magn. Mater.*, vol. 365, pp. 14–22, 2014.

[18] C. K. Hou, C. T. Hu, and S. Lee, "Effect of residual aluminium on the microstructure and magnetic properties of low carbon electrical steels," *Mater. Sci. Eng.*, vol. 125, no. 2, pp. 241–247, 1990.

[19] C.-K. Hou and S. Lee, "Effect of Rolling Strain on the Loss Seperation and Permeability of Lamination Steels," *IEEE Trans. Magn.*, vol. 30, no. 2, pp. 212–216, 1994.

[20] Chun-Kan Hou, "The effects of grain size on the magnetic properties of fully processed, continuous-annealed low-carbon electrical steels," *IEEE Trans. Magn.*, vol. 32, no. 2, pp. 471–477, 1996.

[21] P. Baudouin, A. Belhadj, and Y. Houbaert, "Effect of the rapid heating on the magnetic properties of non-oriented electrical steels," *J. Magn. Magn. Mater.*, vol. 238, pp. 221–225, 2002.

[22] C.-K. Hou, C. . Hu, and S. Lee, "The Effect of Titanium and Niobium on Degradation of Magnetic Properties of Lamination Steels," *J. Magn. Magn. Mater.*, vol. 87, pp. 44–50, 1990.

[23] R. PremKumar, I. Samajdar, N. N. Viswanathan, V. Singal, and V. Seshadri, "Relative effect(s) of texture and grain size on magnetic properties in a low silicon non-grain oriented electrical steel," *J. Magn. Magn. Mater.*, vol. 264, no. 1, pp. 75–85, 2003.

[24] A. Chaudhury, R. Khatikar, N. N. Viswanathan, V. Singal, A. Ingle, S. Joshi and I. Samajdar, "Low silicon non-grain-oriented electrical steel: Linking magnetic properties with metallurgical factors," *J. Magn. Magn. Mater.*, vol. 313, no. 1, pp. 21–28, 2007.

[25] C.-K. Hou, "Effect of silicon on the loss seperation and permeability of laminated steels," *J. Magn. Magn. Mater.*, vol. 162, pp. 280–290, 1996.

[26] S. M. Thompson and B. K. Tanner, "The magnetic properties of specially prepared pearlitic steels of varying carbon content as a function of plastic deformation," *J. Magn. Magn. Mater.*, vol. 132, no. 1–3, pp. 71–88, 1994.

[27] B. K. Tanner, J. A. Szpunar, S. N. M. Willcock, L. L. Morgan, and P. A. Mundell, "Magnetic and metallurgical properties of high-tensile steels," *J. Mater. Sci.*, vol. 23, no. 12, pp. 4534–4540, 1988.

[28] P. Ghosh, R. R. Chromik, A. M. Knight, and S. G. Wakade, "Effect of metallurgical factors on the bulk magnetic properties of non-oriented electrical steels," *J. Magn. Magn. Mater.*, vol. 356, pp. 42–51, 2014.

[29] J. W. Wilson, N. Karimian, J. Liu, W. Yin, C. L. Davis, and a. J. Peyton, "Measurement of the magnetic properties of P9 and T22 steel taken from service

in power station," *J. Magn. Magn. Mater.*, vol. 360, pp. 52–58, 2014.

[30] J. Liu, M. Strangwood, A. J. Peyton, and C. L. Davis, "Magnetic Evaluation of Microstrcture Changes in 9Cr-1Mo and 2.25Cr-1Mo Steels using Electromagnetic Sensors," *Metall. Mater. Trans. A*, vol. 44, pp. 5897–909, 2013.

[31] W. Yin, R. Binns, C. Davis, and a J. Peyton, "Analysis of the lift-off effect of spectra for eddy current sensors [J]," *Ieee Trans. Instrum. Meas.*, vol. 56, no. 6, pp. 1779–1784, 2005.

[32] W. Yin, N. Karimian, J. Liu, X. J. Hao, L. Zhou, A. J. Peyton, M. Strangwood and C. L. Davis, "Measurement of electromagnetic properties of power station steels," *NDT E Int.*, vol. 51, pp. 135–141, 2012.

[33] S. Ghanei, M. Kashefi, and M. Mazinani, "Eddy current nondestructive evaluation of dual phase steel," *Mater. Des.*, vol. 50, pp. 491–496, 2013.

[34] S. M. Thompson and B. K. Tanner, "The magnetic properties of plastically deformed steels," *J. Magn. Magn. Mater.*, vol. 83, no. 1–3, pp. 221–222, 1990.

[35] L. Zhou, "Non-Destructive Characterisation of Steel Microstructures using Electromagnetic Sensors," University of Birmingham, 2014.

[36] O. Saquet, J. Chicois, and A. Vincent, "Barkhausen noise from plain carbon steels: analysis of the influence of microstructure," *Mater. Sci. Eng. A*, vol. 269, no. 1–2, pp. 73–82, 2002.

[37] X. J. Hao, W. Yin, M. Strangwood, a. J. Peyton, P. F. Morris, and C. L. Davis, "Modelling the electromagnetic response of two-phase steel microstructures," *NDT E Int.*, vol. 43, no. 4, pp. 305–315, 2010.

[38] J. R. Birchak, C. G. Gardner, J. E. Hipp, and J. M. Victor, "High Dielectric Constant Microwave Probes for Sensing Soil Moisture," *Proc. IEEE*, vol. 62, no. 1, pp. 93–98, 1974.

[39] H. Looyenga, "Dielectric constants of heterogeneous mixtures," *Physica*, vol. 31, no. 3, pp. 401–406, 1965.

[40] L. Zhou, R. Hall, and C. L. Davis, "Measured and modelled low field relative permeability for dual phase steels at high temperature," *J. Magn. Magn. Mater.*, vol. 475, no. August 2018, pp. 38–43, 2019.

[41] D. Ludwigson and F. Schwerer, "The effect of composition on the resistivity of carbon steel sheet," *Metall. Mater. Trans. B*, vol. 2, no. 12, pp. 3500–3501, 1971.

[42] G. N. Maniar, R. Ward, R. Clark-Anderson, C. D. Beachem, D. R. Betner, P. B. Burgess, H. W. Collins, E. P. Dahlberg, J. L. Dassel, M. J. Donoachie Jr, G. A. Fritzlen, P. H. B. Hamilton, D. W. Hemphill, J. A. Hildebrandt, F. L. Jamieson, L. J. Korb, E. R. Kuch, H. P. Langston, R. Mack, L. E. Marsh, D. B. Mazer, J. G. McArdle, J. L. McCall, S. W. McGee, P. J. Mikelonis, P. Patriarca, E. I. Salkovitz, J. E. Scheer, G. M. Slaughter, C. O. Smith, R. Thompson, M. G. H. Wells, D. A. Wilkinson, B. P. Bardes and H. E. Boyer, *Metals Handbook: Volume 1 Properties and Selection: Irons and Steels*, 9th ed. American Society For Metals, 1978.

[43] H. Yang. F. van den Berg, A. Luinenburg, C. Bos, G. Kuiper, J. Mosk, P. Hunt, M. Dolby, M. Flicos, A. Peyton and C. Davis "In-Line Quantitative Measurement of Transformed Phase Fraction by EM Sensors duing ControLled Cooling on the Run-Out Table of a Hot Strip Mill," in *19th World Conference on Non-Destructive*

Testing, 2016, pp. 1–8.

[44] J. Garcia-Martin, J. Gomez-Gil, and E. Vazquez-Sanchez, "Non-Destructive Techniques Based on Eddy Current Testing," *Sensors*, vol. 11, no. 3, pp. 2525–2565, 2011.

[45] W. Zhu, "Electromagnetic Techniques for On-line Inspection of Steel Microstructure," University of Manchester, 2013.

[46] J. Epp, *Materials Characterization Using Non-Destructive Evaluation (NDE) Methods*. Elsevier, 2016.

[47] J. Goldstein, D. E. Newbury, P. Echlin, D. C. Joy, C. E. Lyman, E. Lifshin, L. Sawyer and J. R. Michael, "Quantitative X-ray analysis: the basics," in *Scanning Electron Microscopy and X-ray Analysis*, Springer, 2003, pp. 391–451.

[48] E. Cakmak, H. Choo, K. An, and Y. Ren, "A synchrotron X-ray diffraction study on the phase transformation kinetics and texture evolution of a TRIP steel subjected to torsional loading," *Acta Mater.*, vol. 60, no. 19, pp. 6703–6713, 2012.

[49] W. Solano-Alvarez, H. F. G. Abreu, M. R. Da Silva, and M. J. Peet, "Phase quantification in nanobainite via magnetic measurements and X-ray diffraction," *J. Magn. Magn. Mater.*, vol. 378, pp. 200–205, 2015.

[50] A. Bénéteau, E. Aeby-Gautier, G. Geandier, P. Weisbecker, A. Redjaïmia, and B. Appolaire, "Tempering of a martensitic stainless steel: Investigation by in situ synchrotron X-ray diffraction," *Acta Mater.*, vol. 81, pp. 30–40, 2014.

[51] S. E. Offerman, N. H. Van Dijk, J. Sietsma, S, S. Grigull, E. M. Lauridsen, L. Margulies, H. F. Poulsen, M. T. Rekveldt and S. van der Zwaag, "Grain nucleation and growth during phase transformations," *Science (80-.).*, vol. 298, no. 5595, pp. 1003–1005, 2002.

[52] H. J. Kopineck, R. Löffel, and H. B. Otten, "Industrial on-line texture determination in rolled steel strips," *J. Nondestruct. Eval.*, vol. 12, no. 1, pp. 13–19, 1993.

[53] Yale, "Environmental Health and Safety - X-Ray Diffraction Safety Information." [Online]. Available: http:/ehs.yale.edu/training/x-ray-diffractio-safety.

[54] P. . Shull, *Non-Destructive Evaluation: Theory, Techniques and Applications*. CrC Press, 2016.

[55] L. Cartz, *Non-Destructive Testing*. ASM International, The Materials Information Society, Materials Park, OH, 1995.

[56] J. Wilson, "Investigation of Electromagnetic NDT&E Techniques for Comprehensive Materials Assessment," University of Newcastle Upon Tyne, 2009.

[57] A. Moro, C. Farina, and F. Rossi, "Measurement of Ultrasonic Wave Velocity in Steel for Various Structures and Degrees of Cold-Working.," *NDT Int.*, vol. 13, no. 4, pp. 169–175, 1980.

[58] H. Willems, "Non-Destructive Determination of Hardening Depth in Induction Hardened Components by Ultrasonic Back Scattering," in *Review of Progress in Quantitative Non-Destructive Evaluation*, Springer, 1991, pp. 1707–1713.

[59] H. Ogi, M. Hirao, and T. Honda, "Ultrasonic attenuation and grain-size evaluation

using electromagnetic acoustic resonance," *J. Acoust. Soc. Am.*, vol. 98, no. 1, pp. 458–464, 1995.

[60] A. Vary, "Correlations between ultrasonic and fracture toughness factors," in *Proceedings of the Eleventh National Symposium on Fracture Mechanics*, 1979.

[61] A. Smith, S. E. Kruger, J. Sietsma, and S. van der Zwaag, "Laser-ultrasonic monitoring of ferrite recovery in ultra low carbon steel," *Mater. Sci. Eng. A*, vol. 458, no. 1–2, pp. 391–401, 2007.

[62] S. E. Kruger, A. Moreau, M. Militzer, and T. Biggs, "In-situ, laser-ultrasonic monitoring of the recrystallization of aluminum alloys," *Mater. Sci. Forum*, vol. 426–432, no. 1, pp. 483–488, 2003.

[63] S. Kruger, A. Moreau, and J. Monchalin, "Laser-Ultrasonic Monitoring of Metallurgical Transformations in Advanced Ultra-High Strength Steels 2 . Basics of Ultrasonic Interaction with Steel Microstructure 3 . Austenite Decomposition Monitoring," *Int. Symp. Laser Ultrason. Sci. Technol. Appl.*, 2008.

[64] M. Dubois, A. Moreau, and J. F. Bussière, "Ultrasonic velocity measurements during phase transformations in steels using laser ultrasonics," *J. Appl. Phys.*, vol. 89, no. 11 I, pp. 6487–6495, 2001.

[65] B. Hutchinson, P. Lundin, E. Lindh-Ulmgren, and D. Lévesque, "Anomalous ultrasonic attenuation in ferritic steels at elevated temperatures," *Ultrasonics*, vol. 69, pp. 268–272, 2016.

[66] B. Hutchinson, B. Moss, A. Smith, A. Astill, C. Scruby, G. Engberg and J. Björklund, "Online characterisation of steel structures in hot strip mill using laser ultrasonic measurements," *Ironmak. Steelmak.*, vol. 29, no. 1, pp. 77–80, 2002.

[67] D. O'Sullivan, M. Cotterell, D. A. Tanner, and I. Mészáros, "Characterisation of ferritic stainless steel by Barkhausen techniques," *NDT E Int.*, vol. 37, no. 6, pp. 489–496, 2004.

[68] N. Karimian, "Monitoring of Power Station Steels Using Electromangetic Sensors," University of Manchester, 2014.

[69] C. Stefanita, *Barkhausen noise as a mangetic nondestructive testing technique*. Springer, 2008.

[70] S. Ghanei, M. Kashefi, and M. Mazinani, "Comparative study of eddy current and Barkhausen noise nondestructive testing methods in microstructural examination of ferrite-martensite dual-phase steel," *J. Magn. Magn. Mater.*, vol. 356, pp. 103–110, 2014.

[71] J. Anglada-Rivera, L. R. Padovese, and J. Capó-Sánchez, "Magnetic Barkhausen Noise and hysteresis loop in commercial carbon steel: Influence of applied tensile stress and grain size," *J. Magn. Magn. Mater.*, vol. 231, no. 2–3, pp. 299–306, 2001.

[72] D. H. L. Ng, K. S. Cho, M. L. Wong, S. L. I. Chan, X. Y. Ma, and C. C. H. Lo, "Study of microstructure, mechanical properties, and magnetization process in low carbon steel bars by Barkhausen emission," *Mater. Sci. Eng. A*, vol. 358, no. 1–2, pp. 186–198, 2003.

[73] K. Gurruchaga, A. Martínez-De-Guerenu, M. Soto, and F. Arizti, "Magnetic barkhausen noise for characterization of recovery and recrystallization," *IEEE*

Trans. Magn., vol. 46, no. 2, pp. 513–516, 2010.

[74] M. R. N. Astudillo, M. N. Nicolás, J. Ruzzante, M. P. Gómez, G. C. Ferrari, L. R. Padovese and M. I. L. Pumarega, "Correlation between Martensitic Phase Transformation and Magnetic Barkhausen Noise of AISI 304 Steel," *Procedia Mater. Sci.*, vol. 9, pp. 435–443, 2015.

[75] E. A. Huallpa, P. F. S. Farina, J. Capo, L. R. Padovese, and H. Goldenstein, "The use of Barkhausen noise to study the martensitic phase transformation," *Solid State Phenom.*, vol. 172–174, no. January 2011, pp. 184–189, 2011.

[76] I. Petryshynets, F. Kovac, M. Sopko, J. Marcin, and B. Petrov, "Study of microstructure and texture evolution in grain-oriented steels via coercivity measurements," *IEEE Trans. Magn.*, vol. 50, no. 4, pp. 3–6, 2014.

[77] J. Šternberk, E. Kratochvílová, J. Hřebík, and A. Gemperle, "Coercivity and Microstructure of Low-Alloy Cr□Mo Steel," *Phys. Status Solidi*, vol. 79, no. 2, pp. 523–529, 1983.

[78] S. Habermehl, D. . Jiles, and C. . Teller, "Influence of heat treatment and chemical composition on the magnetic properties of ferrmagnetic steels," *IEEE Trans. Magn.*, vol. Mag 21, no. 5, pp. 1909–1911, 1985.

[79] K. Gurruchaga, A. Martínez-de-guerenu, and F. Arizti, "Monitoring Recovery and Recrystallization in Interstitial Free (IF) Steel by Magnetic Hysteresis Loop Measurements," *Ecndt*, pp. 1–8, 2006.

[80] Y. S. Lukin, S. V. Bakhtin, A. S. Lukin, and A. A. Zaveryukha, "Structure of IF steel in continuous annealing," *Steel Transl.*, vol. 42, no. 4, pp. 365–367, 2012.

[81] J. Sort, A. Concustell, E. Menéndez, S. Suriñach, M. D. Baró, J. Farran and J. Nogués, "Selective generation of local ferromagnetism in austenitic stainless steel using nanoindentation," *Appl. Phys. Lett.*, vol. 89, no. 3, 2006.

[82] A. Mitra, P. K. Srivastava, P. K. De, D. K. Bhattacharya, and D. C. Jiles, "Ferromagnetic properties of deformation-induced martensite transformation in AISI 304 stainless steel," *Metall. Mater. Trans. A Phys. Metall. Mater. Sci.*, vol. 35 A, no. 2, pp. 599–605, 2004.

[83] D. Hennessy, G. Steckel, and C. Altstetter, "Phase transformation of stainless steel during fatigue," *Metall. Trans. A*, vol. 7, no. 3, pp. 415–424, 1976.

[84] S. Takahashi, J. Echigoya, T. Ueda, X. Li, and H. Hatafuku, "Martensitic transformation due to plastic deformation and magnetic properties in SUS 304 stainless steel," *J. Mater. Process. Technol.*, vol. 108, no. 2, pp. 213–216, 2001.

[85] K. Mumtaz, S. Takahashi, J. Echigoya, Y. Kamada, L. F. Zhang, H. Kikuchi, K. Ara and M. Sato, "Magnetic measurements of martensitic transformation in austenitic stainless steel after room temperature rolling," *J. Mater. Sci.*, vol. 39, no. 1, pp. 85–97, 2004.

[86] H. Kim, I. Park, S. Wee, S. Hahn, and H. M, "Eddy current methods for evaluation of the transformed fraction of metals by volage source," *IEEE Trans. Magn.*, vol. 26, no. 2, pp. 505–508, 1990.

[87] W. Yin, a. J. Peyton, M. Strangwood, and C. L. Davis, "Exploring the relationship between ferrite fraction and morphology and the electromagnetic properties of steel," *J. Mater. Sci.*, vol. 42, no. 16, pp. 6854–6861, 2007.

[88] W. Yin, X. J. Hao, a. J. Peyton, M. Strangwood, and C. L. Davis, “Measurement of permeability and ferrite/austenite phase fraction using a multi-frequency electromagnetic sensor,” *NDT E Int.*, vol. 42, no. 1, pp. 64–68, 2009.

[89] R. J. Haldane, W. Yin, M. Strangwood, A. J. Peyton, and C. L. Davis, “Multi-frequency electromagnetic sensor measurement of ferrite/austenite phase fraction-Experiment and theory,” *Scr. Mater.*, vol. 54, no. 10, pp. 1761–1765, 2006.

[90] J. W. Wilson, N. Karimian, J. Liu, W. Yin, C. L. Davis, and A. J. Peyton, “Measurement of the magnetic properties of P9 and T22 steel taken from service in power station,” *J. Magn. Magn. Mater.*, vol. 360, pp. 52–58, 2014.

[91] M. Papaelias, M. Strangwood, a Peyton, and C. Davis, “Measurement and modeling of the electromagnetic response to phase transformation in steels,” *Metall. Mater. Trans. A*, vol. 35, no. March, pp. 965–972, 2004.

[92] M. P. Papaelias, M. Strangwood, a. J. Peyton, and C. L. Davis, “Effect of microstructural variations on smart inductive sensor measurements of phase transformation in steel,” *Scr. Mater.*, vol. 51, no. 5, pp. 379–383, 2004.

[93] C. L. Davis, M. P. Papaelias, M. Strangwood, and A. Peyton, “Measurement of phase transformation in steels using electromagnetic sensors,” vol. 29, no. 6, pp. 469–476, 2002.

[94] X. J. Hao, W. Yin, M. Strangwood, a. J. Peyton, P. F. Morris, and C. L. Davis, “Off-line measurement of decarburization of steels using a multifrequency electromagnetic sensor,” *Stud. Appl. Electromagn. Mech.*, vol. 31, pp. 86–89, 2008.

[95] X. J. Hao, W. Yin, M. Strangwood, a. J. Peyton, P. F. Morris, and C. L. Davis, “Characterization of decarburization of steels using a multifrequency electromagnetic sensor: Experiment and modeling,” *Metall. Mater. Trans. A Phys. Metall. Mater. Sci.*, vol. 40, no. 4, pp. 745–756, 2009.

[96] W. Yin, X. J. Hao, a. J. Peyton, M. Strangwood, and C. L. Davis, “Measurement of decarburisation of steel rods with an electromagnetic sensor using an analytical model,” *NDT E Int.*, vol. 43, no. 8, pp. 667–670, 2010.

[97] S. J. Dickinson, R. Binns, W. Yin, C. Davis, and A. J. Peyton, “The development of a multifrequency electromagnetic instrument for monitoring the phase transformation of hot strip steel,” *IEEE Trans. Instrum. Meas.*, vol. 56, no. 3, pp. 879–886, 2007.

[98] J. W. Wilson, N. Karimian, A. J. Peyton, and C. Davis, “Electromagnetic measurements for the assessment of skin passed steel samples,” *54th Annu. Br. Conf. Non-Destructive Testing, NDT 2015*, pp. 1–8, 2015.

[99] A. . Marmulev, L. . Kaputkina, E. . Poliak, and J. . Turon, “Online Non-Destructive Monitoring of Phase Transformation on Run-Out Table of Csp Hot Strip Mill,” *Mach. Technol. Mater.*, vol. 9, no. August, pp. 27–29, 2013.

[100] M. . Jolfaei, “Electromagnetic Sensor System for Characterisation of Advanced High Strength Steels,” University of Warwick, 2019.

[101] M. Aghadavoudi-Jolfaei, J. Shen, A. Smith, L. Zhou, and C. L. Davis, “Non-destructive measurement of microstructure and tensile strength in varying thickness commercial DP steel strip using an EM sensor,” *J. Magn. Magn. Mater.*,

vol. 473, no. August 2018, pp. 477–483, 2019.

[102] J. Shen, L. Zhou, W. Jacobs, P. Hunt, and C. Davis, “Use of COMSOL® AC/DC module to model a commercial electromagnetic sensor deployed to monitor steel transformation during cooling from high temperatures,” *COMSOL Conf.*, pp. 22–24, 2018.

[103] J. Shen, L. Zhou, and C. Davis, “Final Report on Modelling of the EMspec Sensor,” 2018.

[104] H. K. D. H. Bhadeshia, “Interpretation of the Microstructure of Steels.” [Online]. Available: https://www.phase-trans.msm.cam.ac.uk/2008/Steel_Microstructure/SM.html.

[105] S. Dépinoy, “Microstructural evolution of a 2.25Cr - 1 Mo steel during austenitization and temper : austenite grain growth, carbide precipitation sequence and effects on mechanical properties,” 2015.

[106] A. da Cunha Rocha, A. P. da Rocha Santos, and G. R. Pereira, “Phase Transformations in Duplex Stainless Steels: An Assessment by in Situ X-Ray Diffractions,” in *Stainless Steels and Alloys*, .

[107] S. S. M. Tavares, R. F. de Noronha, M. R. da Silva, J. M. Neto, and S. Pairis, “475 °C Embrittlement in a duplex stainless steel UNS S31803,” *Mater. Res.*, vol. 4, no. 4, pp. 237–240, 2001.

[108] J. Shen, L. Zhou, W. Jacobs, P. Hunt, and C. Davis, “Real-time in-line steel microstructure control through magnetic properties using an EM sensor,” *J. Magn. Magn. Mater.*, vol. 490, no. March, p. 165504, 2019, doi: 10.1016/j.jmmm.2019.165504.

Appendix A. Phase Angle at 8 Frequencies with Temperature 10mm Medium Carbon Steel

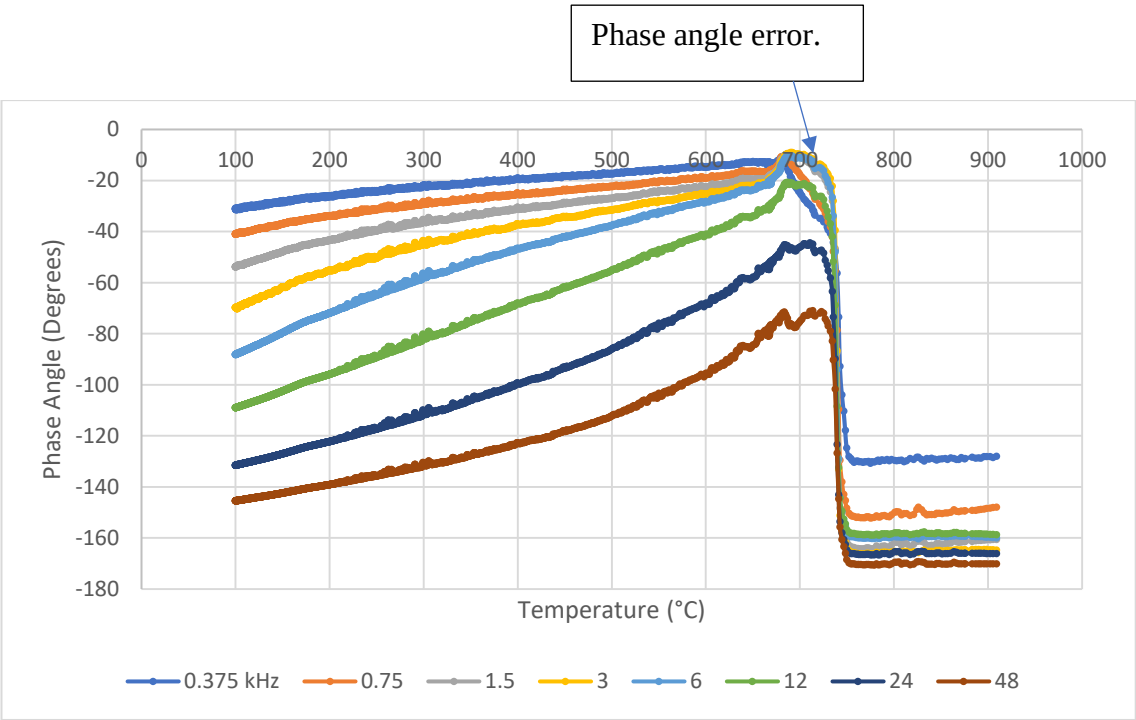

Figure 141. Phase angles at 0.375-48kHz with temperature. Error in phase angle indicated on graph